

Number: 26

Redalyc 3.0

ESCI Web of science

UNIVERSIDAD POLITÉCNICA SALESIANA ECUADOR

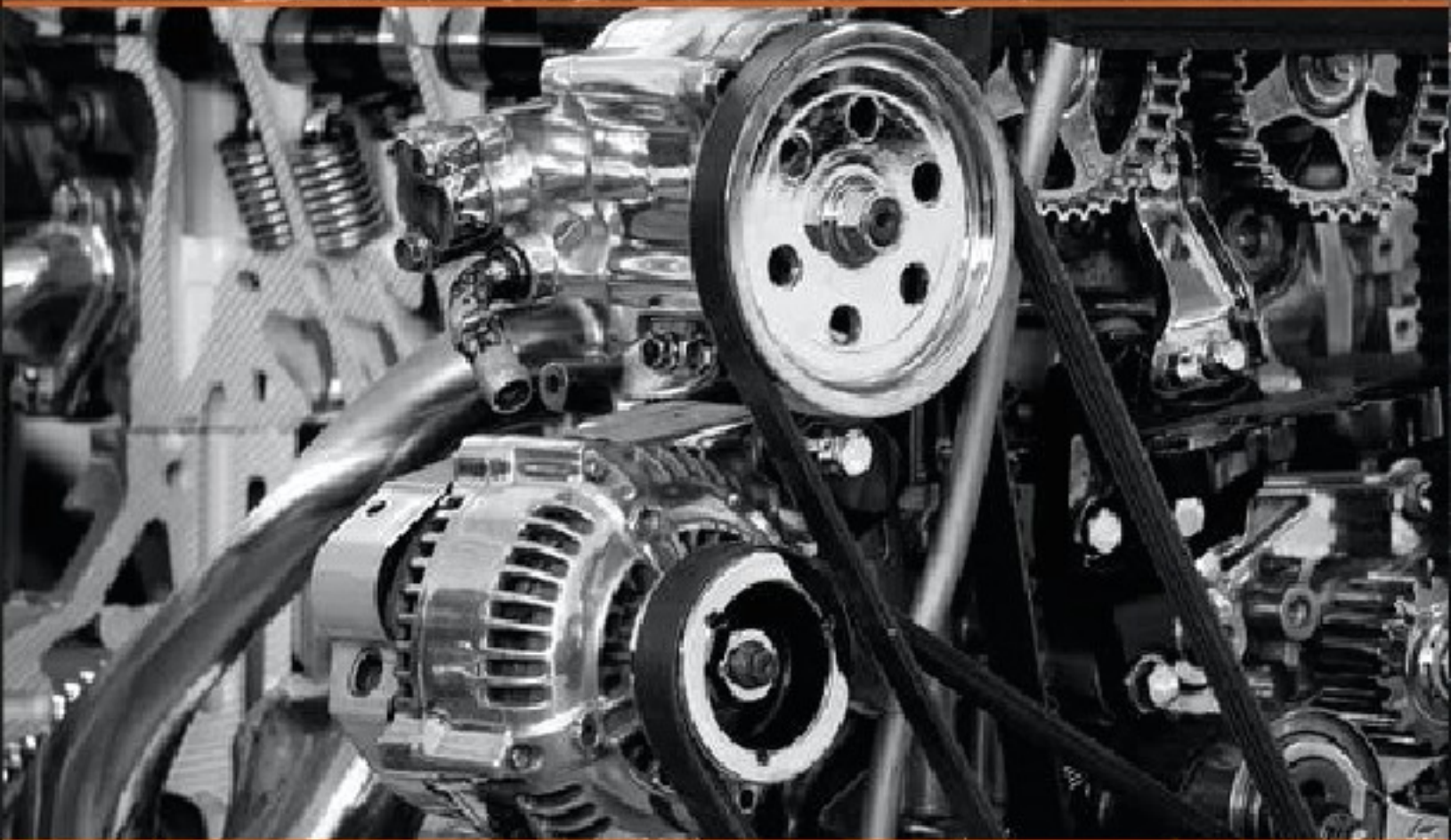
pISSN: 1390-650X

eISSN: 1390-860X

july / december 2021

# INGENIUS

Revista de Ciencia y Tecnología



✚ Rapid Convective Deposition at Nanoscale of Active Composite Materials for the Manufacture of Organic Field-Effect Transistors

**Pag. 9**

✚ Transfer Learning for Binary Classification of Thermal Images

**Pag. 71**

✚ Support to the human talent subsystems, selection and recruitment from an expert system. Case study

**Pag. 41**

✚ Numerical analysis of flow pattern map of R600a in a collector/evaporator of a solar-assisted heat pump

**Pag. 111**

# INGENIUS

INGENIUS • Number 26 • july/december 2021. Semester Journal of Science and Tecnology of the Universidad Politécnica Salesiana of Ecuador. Publication dedicated to studies related to the Sciences of Mechanical Engineering, Electrical Engineering, Electronic Engineering, Mechatronic Engineering, Systems Engineering and Industrial Engineering.

## Editors Board

RAFAEL ANTONIO BALART GIMENO, PHD, Universidad Politécnica de Valencia, España – Editor-in-chief.

JOHN IGNACIO CALLE SIGÜENCIA, PHD, Universidad Politécnica Salesiana, Ecuador – Editor-in-chief.

ESTEBAN MAURICIO INGA ORTEGA, PHD, Universidad Politécnica Salesiana, Ecuador – Associate Editor.

MARLON XAVIER QUINDE ABRIL, MSC, Universidad Politécnica Salesiana, Ecuador – Associate Editor.

TEODIANO FREIRE BASTOS FILHO, PHD, (Universidade Federal do Espírito Santo, Brasil – Associate Editor.

## Scientific board

JUAN LÓPEZ MARTÍNEZ, PHD, Universidad Politécnica de Valencia, España.

ELENA FORTUNATI, PHD, Universidad de Perugia, Italia.

GUSTAVO ROVELO RUIZ, PHD, Hasselt University, Diepenbeek, Bélgica.

FRANKLIN GAVILANEZ ALVAREZ, PHD, American University, Estados Unidos.

PIEDAD GAÑAN ROJO, PHD, Universidad Pontificia Bolivariana, Colombia.

JOSÉ ALEX RESTREPO, PHD, Universidad Simón Bolívar, Venezuela.

SERGIO LUJAN MORA, PHD, Universidad de Alicante, España.

MARTHA ZEQUERA DÍAZ, PHD, Pontificia Universidad Javeriana, Colombia.

GROVER ZURITA, PHD, Universidad Privada Boliviana, Bolivia.

VLADIMIR ROBLES, PHD, Universidad Politécnica Salesiana, Ecuador.

GERMÁN ARÉVALO, PHD, Universidad Politécnica Salesiana, Ecuador.

WILBERT AGUILAR, PHD, Universidad de las Fuerzas Armadas, ESPE, Ecuador.

JACK BRAVO TORRES, PHD, Universidad Politécnica Salesiana, Ecuador.

WALTER OROZCO, PHD, Universidad Politécnica Salesiana, Ecuador.

MARIELA CERRADA, PHD, Universidad Politécnica Salesiana, Ecuador.

JULIO CÉSAR VIOLA, PHD, Universidad Politécnica Salesiana, Ecuador.

SERGIO GAMBOA SÁNCHEZ, PHD, Universidad Nacional Autónoma de México, México.

ROGER ABDÓN BUSTAMANTE PLAZA, PHD, Universidad de Chile, Chile.

CHRISTIAN BLUM, PHD, Consejo Superior de Investigaciones Científicas, España.

SILVIA NOEMI SCHIAFFINO, PHD, Universidad Nacional del Centro de la Provincia de Buenos Aires, Argentina.

ANALÍA ADRIANA AMANDI, PHD, Universidad Nacional del Centro de la Provincia de Buenos Aires, Argentina.

RUBÉN DE JESÚS MEDINA MOLINA, PHD,

Universidad de Los Andes, Venezuela.

JOHNNY JOSUÉ BULLÓN TORREALBA, PHD, Universidad de Los Andes, Venezuela.

RODRIGO PALMA HILLERNS, PHD, Universidad de Chile, Chile.

GERARDO ESPINOZA PÉREZ, PHD, Universidad Nacional Autónoma de México, México.

ALEXANDRE MENDES ABRÃO, PHD, Universidad Federal de Minas Gerais, Brasil.

KAMLA ABDEL RADI ISMAIL, PHD, Universidad Estatal de Campinas Unicamp, Brasil.

ARNALDO DA SILVA, PHD, Universidad Estatal de Campinas Unicamp, Brasil.

ÁLVARO ROCHA, PHD, Universidad de Coimbra, Portugal.

JOSÉ ANTENOR POMILIO, PHD, Universidad Estatal de Campinas Unicamp, Brasil.

LUIS PAULO REIS, PHD, Universidad de Minho, Portugal.

LUÍS FERNANDES, PHD, Escuela Superior Náutica Infante d. Henrique, Portugal.

ANÍBAL TRAÇA DE ALMEIDA, PHD, Universidad de Coimbra, Portugal.

JORGE SÁ SILVA, PHD, Universidad de Coimbra, Portugal.

PEDRO MANUEL SOARES MOURA, PHD, Universidad de Coimbra, Portugal.

SÉRGIO MANUEL RODRIGUES LOPES, PHD, Universidad de Coimbra, Portugal.

RICARDO MADEIRA SOARES BRANCO, PHD, Universidad de Coimbra, Portugal.

CARLOS ALEXANDRE BENTO CAPELA, PHD, Universidad de Coimbra, Portugal.

FILIFE ARAUJO, PHD, Universidad de Coimbra, Portugal.

LUIS MANUEL GUERRA SILVA ROSA, PHD, Universidad de Lisboa, Portugal.

HÉLDER DE JESUS FERNANDES, PUGA, PHD, Universidad de Minho, Portugal.

FILIFE SAMUEL, PEREIRA DA SILVA, PHD, Universidad de Minho, Portugal.

CÉSAR SEQUEIRA, PHD, Universidad de Lisboa, Portugal.

JOSÉ TEIXEIRA ESTÊVÃO FERREIRA, PHD,

Universidad de Coimbra, Portugal.

NUNO LARANJEIRO, PHD, Universidad de Coimbra, Portugal.

LUÍS AMARAL, PHD, Universidad de Lisboa, Portugal.

JORGE HENRIQUES, PHD, Universidad de Coimbra, Portugal.

WILLIAM IPANAQUE, PHD, Universidad de Piura, Perú.

LORENZO LEIJA SALAS, PHD, Centro de Investigación y Estudios Avanzados del Instituto Politécnico Nacional, México.

VALERI KONTOROVICH MAZOVER, PHD, Centro de Investigación y de Estudios Avanzados del Instituto Politécnico Nacional, México.

ALEJANDRO ÁVILA GARCÍA, PHD, Centro de Investigación y de Estudios Avanzados del Instituto Politécnico Nacional, México.

PAOLO BELLAVISTA, PHD, Universidad de Bologna, Italia.

CARLOS RUBIO, PhD, Centro de Ingeniería y Desarrollo Industrial, México.

FERNANDO HERNÁNDEZ SÁNCHEZ, PhD, Centro de Investigación Científica de Yucatán, México.

EMILIO MUÑOZ SANDOVAL, PhD, Instituto Potosino de Investigación Científica y Tecnológica, México.

YASUHIRO MATSUMOTO KUWABARA, PhD, Centro de Investigación y de Estudios Avanzados del Instituto Politécnico Nacional, México.

DAVID ZUMOFFEN, PhD, Centro Internacional Franco Argentino de Ciencias de la Información y de Sistemas, Argentina.

VICENTE RODRÍGUEZ GONZÁLEZ, PhD, Instituto Potosino de Investigación Científica y Tecnológica, México.

ALEJANDRO RODRÍGUEZ ÁNGELES, PhD, Centro de Investigación y de Estudios Avanzados del Instituto Politécnico Nacional, México.

ALISTAIR BORTHWICK, PhD, Universidad de Edimburgo, Reino Unido.

## Reviewers board

FEDERICO DOMINGUEZ, PHD, Escuela Superior Politécnica del Litoral, Ecuador.

ENRIQUE CARRERA, PHD, Universidad de las Fuerzas Armadas, ESPE, Ecuador.

ANDRÉS TELLO, MSc, Universidad de Cuenca, Ecuador.

CRISTIAN GARCÍA BAUZA, PHD, Universidad Nacional del Centro de la Provincia de Buenos Aires, Argentina.

OSVALDO AÑÓ, PHD, Universidad Nacional de San Juan, Argentina.

THALÍA SAN ANTONIO, PHD, Universidad Técnica de Ambato, Ecuador.

VICTOR SAQUICELA, PHD, Universidad de Cuenca, Ecuador.

GONZALO OLMEDO, PHD, Universidad de las Fuerzas Armadas, ESPE, Ecuador.

ROMÁN LARA, PHD, Universidad de las Fuerzas Armadas, ESPE, Ecuador.

GUILLERMO SORIANO, PHD, Escuela Superior Politécnica del Litoral, Ecuador.

MARÍA FERNANDA GRANDA, PHD, Universidad de Cuenca, Ecuador.

RICARDO CAYSSIALS, PHD, Universidad Tecnológica Nacional, Argentina.

LEONARDO SOLAQUE GUZMAN, PHD, Universidad Militar Nueva Granada, Colombia.

JOSÉ DI PAOLO, PHD, Universidad Nacional de Entre Ríos, Argentina.

ASTRID RUBIANO FONSECA, PHD, Universidad Militar Nueva Granada, Colombia.

ROBINSON JIMÉNEZ, PHD, Universidad Militar Nueva Granada, Colombia.

ALFONSO ZOZAYA, PHD, Universidad de Carabobo, Venezuela.

MAURICIO MAULEDOUX, PHD, Universidad Militar Nueva Granada, Colombia.

LUIS MEDINA, PHD, Universidad Simón Bolívar, Venezuela.

ERNESTO CUADROS-VARGAS, PHD, Universidad Católica San Pablo, Perú.

SAMUEL SEPÚLVEDA CUEVAS, PHD, Universidad de la Frontera, Chile.

CARLOS CARES, PHD, Universidad de la Frontera, Chile.

RAFAEL SOTELO, PHD, Universidad de Montevideo, Uruguay.

OMAR LOPEZ, PHD, Universidad de Los Andes, Colombia.

JOB FLORES-GODOY, PHD, Universidad Católica del Uruguay, Uruguay.

LUIS MARIO MATEUS, PHD, Universidad de los Andes, Colombia.

AMADEO ARGÜELLES CRUZ, PHD, Instituto Politécnico Nacional, México.

SANTIAGO BENTANCOURT PARRA, PHD, Universidad Pontificia Bolivariana, Colombia.

GERMÁN ZAPATA, PHD, Universidad Nacio-

nal de Colombia, Colombia.

PEDRO GARCÍA, PHD, Universidad Autónoma de Barcelona, España.

ARTURO CONDE ENRÍQUEZ, PHD, Universidad Autónoma de Nuevo León, México.

ALBERTO CAVAZOS GONZÁLEZ, PHD, Universidad Autónoma de Nuevo León, México.

ERNESTO VÁZQUEZ MARTÍNEZ, PHD, Universidad Autónoma de Nuevo León, México.

MIGUEL DÍAZ RODRIGUEZ, PHD, Universidad de Los Andes, Venezuela.

EFRAÍN ALCORTA GARCÍA, PHD, Universidad Autónoma de Nuevo León, México.

LUIS CHIRINOS GARCIA, PHD, Pontificia Universidad Católica de Perú, Perú.

OSCAR AVILÉS, PHD, Universidad Militar Nueva Granada, Colombia.

DORA MARTÍNEZ DELGADO, PHD, Universidad Autónoma de Nuevo León, México.

DAVID OJEDA, PHD, Universidad Técnica del Norte, Ecuador.

IRENE BEATRÍZ STEINMANN, PHD, Universidad Tecnológica Nacional, Argentina.

MARIO SERRANO, Universidad Nacional de San Juan, Argentina.

CORNELIO POSADAS CASTILLO, PHD, Universidad Autónoma Nuevo León, México.

MARIO ALBERTO RIOS MESIAS, PHD, Universidad de Los Andes, Colombia.

YUDITH CARDINALE VILLARREAL, PHD, Universidad Simón Bolívar, Venezuela.

EDUARDO MATALLANAS, PHD, Universidad Politécnica de Madrid, España.

JOSE EDUARDO OCHOA LUNA, PHD, Universidad Católica San Pablo, Perú.

DANTE ANGEL ELIAS GIORDANO, PHD, Pontificia Universidad Católica de Perú, Perú.

MANUEL PELAEZ SAMANIEGO, PHD, Universidad de Cuenca, Ecuador.

JUAN ESPINOZA ABAD, PHD, Universidad de Cuenca, Ecuador.

PIETRO CODARA, PHD, Universidad de Milan, Italia.

ALBERTO SORIA, PHD, Centro de Investigación y de Estudios Avanzados del Instituto Politécnico Nacional, México.

JOSÉ M. ALLER, PHD, Universidad Politécnica Salesiana, Ecuador.

FERNEY AMAYA F., PHD, Universidad Pontificia Bolivariana, Medellín, Colombia.

SANTIAGO ARANGO ARAMBURO, PHD, Universidad Nacional de Colombia, Colombia.

DIEGO ARCOS-AVILÉS, PHD, Universidad de las Fuerzas Armadas, ESPE, Ecuador.

PABLO AREVALO, PHD, Universidad Politécnica Salesiana, Ecuador.

ROBERTO BELTRAN, MSc, Universidad de las Fuerzas Armadas, ESPE, Ecuador.

LEONARDO BETANCUR, PHD, Universidad Pontificia Bolivariana, Medellín, Colombia.

ROBERTO GAMBOA, PHD, Universidad de Lisboa, Portugal.

PAULO LOPES DOS SANTOS, PHD, Universidad do Porto, Portugal.

PEDRO ANDRÉ DIAS PRATES, PHD, Universidad de Coimbra, Portugal.

JOSÉ MANUEL TORRES FARINHA, PHD, Universidad de Coimbra, Portugal.

CELSO DE ALMEIDA, PHD, Universidad Estatal de Campinas Unicamp, Brasil.

RAMON MOLINA VALLE, PHD, Universidad Federal de Minas Gerais, Brasil.

CRISTINA NADER VASCONCELOS, PHD, Universidad Federal Fluminense, Brasil.

JOÃO M. FERREIRA CALADO, PHD, Universidad de Lisboa, Portugal.

GUILHERME LUZ TORTORELLA, PHD, Universidad Federal de Santa Catarina, Brasil.

MAURO E. BENEDET, PHD, Universidad Federal de Santa Catarina, Brasil.

ARTEMIS MARTI CESCHIN, PHD, Universidade de Brasilia, Brasil.

GILMAR BARRETO, PHD, Universidad Estatal de Campinas Unicamp, Brasil.

RICARDO EMILIO F. QUEVEDO NOGUEIRA, PHD, Universidad Federal de Ceará, Brasil.

WESLEY LUIZ DA SILVA ASSIS, PHD, Universidad Federal Fluminense, Brasil.

ANA P. MARTINAZZO, PHD, Universidad Federal Fluminense, Brasil.

JORGE BERNARDINO, PHD, Universidad de Coimbra, Portugal.

LUIS GERALDO PEDROSO MELONI, PHD, Universidad Estatal de Campinas Unicamp, Brasil.

FACUNDO ALMERAYA CALDERÓN, PHD, Universidad Autónoma de Nuevo León, México.

FREDDY VILLAO QUEZADA, PHD, Escuela Superior Politécnica del Litoral, Ecuador.

JOSE MANRIQUE SILUPU, MSc, Universidad de Piura, Perú.

GERMÁN ARIEL SALAZAR, PHD, Instituto de Investigaciones en Energía no Convencional, Argentina.

JOSÉ MAHOMAR JANANIÁS, PHD, Universidad del BIOBIO, Chile.

ARNALDO JÉLVEZ CAAMAÑO, PHD, Universidad del BIOBIO, Chile.

JORGE ANDRÉS URIBE, MSc, Centro de Ingeniería y Desarrollo Industrial, México.

RICARDO BELTRAN, PHD, Centro de Investigación en Materiales Avanzados, México.

ADI CORRALES, MSc, Centro de Ingeniería y Desarrollo Industrial, México.

JORGE URIBE CALDERÓN, PHD, Centro de Investigación Científica de Yucatán, México

JOSÉ TRINIDAD HOLGUÍN MOMACA, MSc, Centro de Investigación en Materiales Avanzados, México.

JUAN MANUEL ALVARADO OROZCO, PhD, Centro de Ingeniería y Desarrollo Industrial, México.

ARNALDO JÉLVEZ CAAMAÑO, PhD, Universidad del BIOBIO, Chile.

JAVIER MURILLO, PhD, Centro Internacional Franco Argentino de Ciencias de la Información y de Sistemas, Argentina.

LUCAS DANIEL TERISSI, PhD, Universidad Nacional de Rosario, Argentina.

RENE VINICIO SANCHEZ LOJA, MSc, Universidad Politécnica Salesiana, Ecuador.

FREDDY LEONARDO BUENO PALOMEQUE, MSc, Universidad Politécnica Salesiana, Ecuador.

DIEGO CABRERA MENDIETA, MSc, Universidad Politécnica Salesiana, Ecuador.

EDWUIN JESUS CARRASQUERO, PhD, Universidad Técnica de Machala, Ecuador.

CARLOS MAURICIO CARRILLO ROSERO, MSc, Universidad Técnica de Ambato, Ecuador.

DIEGO CARRION GALARZA, MSc, Universidad Politécnica Salesiana, Ecuador.

CARMEN CELI SANCHEZ, MSc, Universidad Politécnica Salesiana, Ecuador.

DIEGO CHACON TROYA, MSc, Universidad Politécnica Salesiana, Ecuador.

PAUL CHASI, MSc, Universidad Politécnica Salesiana, Ecuador.

JUAN CHICA, MSc, Universidad Politécnica Salesiana, Ecuador.

DIEGO MARCELO CORDERO GUZMÁN, MSc, Universidad Católica de Cuenca, Ecuador.

LUIS JAVIER CRUZ, PhD, Universidad Pontificia Bolivariana, Medellín, Colombia.

FABRICIO ESTEBAN ESPINOZA MOLINA, MSc, Universidad Politécnica Salesiana, Ecuador.

JORGE FAJARDO SEMINARIO, MSc, Universidad Politécnica Salesiana, Ecuador.

PATRICIA FERNANDEZ MORALES, PhD, Universidad Pontificia Bolivariana, Medellín, Colombia.

MARCELO FLORES VAZQUEZ, MSc, Universidad Politécnica Salesiana, Ecuador.

CARLOS FLORES VÁZQUEZ, MSc, Universidad Católica de Cuenca, Ecuador.

CARLOS FRANCO CARDONA, PhD, Universidad Nacional de Colombia, Colombia.

CRISTIAN GARCÍA GARCÍA, MSc, Universidad Politécnica Salesiana, Ecuador.

TEONILA GARCÍA ZAPATA, PhD, Universidad Nacional Mayor de San Marcos, Perú.

LUIS GARZÓN MÑOZ, PhD, Universidad Politécnica Salesiana, Ecuador.

NATALIA GONZALEZ ALVAREZ, MSc, Universidad Politécnica Salesiana, Ecuador.

ERNESTO GRANADO, PhD, Universidad Simón Bolívar, Venezuela.

ADRIANA DEL PILAR GUAMAN, MSc, Universidad Politécnica Salesiana, Ecuador.

JUAN INGA ORTEGA, MSc, Universidad Politécnica Salesiana, Ecuador.

ESTEBAN INGA ORTEGA, PhD, Universidad Politécnica Salesiana, Ecuador.

PAOLA INGAVÉLEZ, MSc, Universidad Politécnica Salesiana, Ecuador.

CESAR ISAZA ROLDAN, PhD, Universidad Pontificia Bolivariana.

NELSON JARA COBOS, MSc, Universidad Politécnica Salesiana, Ecuador.

RUBEN JERVES, MSc, Universidad Politécnica Salesiana, Ecuador.

VICTOR RAMON LEAL, PhD, Investigador de PDVSA, Venezuela.

GABRIEL LEON, MSc, Universidad Politécnica Salesiana, Ecuador.

EDILBERTO LLANES, PhD, Universidad Internacional SEK, Ecuador.

LUIS LÓPEZ, MSc, Universidad Politécnica Salesiana, Ecuador.

CARLOS MAFLA YÉPEZ, MSc, Universidad Técnica del Norte, Ecuador.

HADER MARTÍNEZ, PhD, Universidad Pontificia Bolivariana, Medellín, Colombia.

JAVIER MARTÍNEZ, PhD, Instituto Nacional de Eficiencia Energética y Energías Renovables, Ecuador.

ALEX MAYORGA, MSc, Universidad Técnica de Ambato, Ecuador.

JIMMY MOLINA, MSc, Universidad Técnica de Machala, Ecuador.

ANDRES MONTERO, PhD, Universidad de Cuenca, Ecuador.

VICENTE MORALES, MSc, Universidad Técnica de Ambato, Ecuador.

FABIÁN MORALES, MSc, Universidad Técnica de Ambato, Ecuador.

DIEGO MORALES, MSc, Ministerio de Electricidad y Energías Renovables del Ecuador.

YOANDRYS MORALES TAMAYO, PhD, Universidad Técnica de Cotopaxi, Cotopaxi.

OLENA LEONIDIVNA NAIDIUK, MSc, Universidad Politécnica Salesiana, Ecuador.

OSCAR NARANJO, MSc, Universidad del Azuay, Ecuador.

PAUL NARVAEZ, MSc, Universidad Politécnica Salesiana, Ecuador.

HERNÁN NAVAS OLMEDO, MSc, Universidad Técnica de Cotopaxi, Ecuador.

CESAR NIETO, PhD, Universidad Pontificia Bolivariana, Medellín, Colombia.

FABIO OBANDO, MSc, Universidad Politécnica Salesiana, Ecuador.

LUIS ORTIZ FERNANDEZ, MSc, Universidade Federal de Rio Grande del Norte, Brasil.

PABLO PARRA, MSc, Universidad Politécnica Salesiana, Ecuador.

PAULO PEÑA TORO, PhD, Ministerio de Productividad, Ecuador.

PATSY PRIETO VELEZ, MSc, Universidad Politécnica Salesiana, Ecuador.

DIEGO QUINDE FALCONI, MSc, Universidad Politécnica Salesiana, Ecuador.

DIANA QUINTANA ESPINOZA, MSc, Universidad Politécnica Salesiana, Ecuador.

WILLIAM QUITIAQUEZ SARZOSA, MSc, Universidad Politécnica Salesiana, Ecuador.

FLAVIO QUIZHPI PALOMEQUE, MSc, Universidad Politécnica Salesiana, Ecuador.

WASHINGTON RAMIREZ MONTALVAN, MSc, Universidad Politécnica Salesiana, Ecuador.

FRAN REINOSO AVECILLAS, MSc, Universidad Politécnica Salesiana, Ecuador.

NÉSTOR RIVERA CAMPOVERDE, MSc, Universidad Politécnica Salesiana, Ecuador.

JORGE ROMERO CONTRERAS, MSc, Universidad de Carabobo, Venezuela.

FABIAN SAENZ ENDERICA, MSc, Universidad de las Fuerzas Armadas, ESPE, Ecuador.

LUISA SALAZAR GIL, PhD, Universidad Simón Bolívar, Venezuela.

GUSTAVO SALGADO ENRÍQUEZ, MSc, Universidad Central del Ecuador., Ecuador.

JUAN CARLOS SANTILLÁN LIMA, MSc, Universidad Nacional de Chimborazo.

JONNATHAN SANTOS BENÍTEZ, MSc, Universidad Politécnica Salesiana, Ecuador.

ANDRÉS SARMIENTO CAJAMARCA, MSc, Universidad Federal de Santa Catarina, Brasil.

LUIS SERPA ANDRADE, MSc, Universidad Politécnica Salesiana, Ecuador.

CRISTIAN TIMBI SISALIMA, MSc, Universidad Politécnica Salesiana, Ecuador.

MILTON TIPAN SIMBAÑA, MSc, Universidad Politécnica Salesiana, Ecuador.

PAUL TORRES JARA, MSc, Universidad Politécnica Salesiana, Ecuador.

RODRIGO TUFÍÑO CÁRDENAS, MSc, Universidad Politécnica Salesiana, Ecuador.

FERNANDO URGILES ORTÍZ, MSc, Universidad Politécnica Salesiana, Ecuador.

JUAN VALLADOLID QUITOISACA, MSc, Universidad Politécnica Salesiana, Ecuador.

EFRÉN VÁZQUEZ SILVA, PhD, Universidad Politécnica Salesiana, Ecuador.

JULIO VERDUGO, MSc, Universidad Politécnica Salesiana, Ecuador.

MARY VERGARA PAREDES, PhD, Universidad de los Andes, Merida, Venezuela.

JENNIFER YEPEZ ALULEMA, MSc, Universidad Politécnica Salesiana, Ecuador.

JULIO ZAMBRANO ABAD, MSc, Universidad Politécnica Salesiana, Ecuador.

PATRICIA ZAPATA MOLINA, MSc, Universidad Politécnica Salesiana, Ecuador.

### **Publications board**

JUAN CÁRDENAS TAPIA, SDB, PHD  
JAVIER HERRÁN GÓMEZ, SDB, PHD  
JOSÉ JUNCOSA BLASCO, PHD  
JUAN PABLO SALGADO GUERRERO, PHD  
RENÉ UNDA LARA, PHD  
JAIME PADILLA VERDUGO, PHD  
SHEILA SERRANO VINCENTI, MSC  
JORGE CUEVA ESTRADA, MSC  
JOHN CALLE SIGÜENCIA, PHD  
FLORALBA AGUILAR GORDÓN, PHD  
BETTY RODAS SOTO, MSC  
MÓNICA RUIZ VÁSQUEZ, MSC  
PAOLA INGAVÉLEZ GUERRA, PHD  
DAVID ARMENDÁRIZ GONZÁLEZ, MSC  
LUIS ÁLVAREZ RODAS, PHD

### **General Editor**

LUIS ÁLVAREZ-RODAS, PHD

### **Technical board**

ÁNGEL TORRES-TOUKOUMIDIS, PHD  
DRA. MARCIA PEÑA, Style Reviewer,  
Centro Gráfico Salesiano - Editorial Don Bosco  
MARLON QUINDE ABRIL, MSC, Diagramming and layout  
JOEL MONTERO GALÁN

### **Publications Service**

HERNÁN HERMOSA (General Coordination)  
MARCO GUTIÉRREZ (OJS Layout)  
PAULINA TORRES (Style Editing)  
RAYSA ANDRADE (Layout)  
MARTHA VINUEZA (Layout)  
ADRIANA CURIEL AVILA, (Translation)

### **Editorial**

Editorial Abya Yala (Quito-Ecuador),  
Av. 12 de octubre N422 y Wilson,  
Bloque A, UPS Quito, Ecuador.  
Casilla 17-12-719 Teléfonos: (593-2) 3962800 ext. 2638  
email: [editorial@abyayala.org](mailto:editorial@abyayala.org)

Tiraje: 800 ejemplares

Typographic system used in the composition of this document L<sup>A</sup>T<sub>E</sub>X.

# INGENIUS

JOURNAL OF SCIENCE AND TECHNOLOGY

Número 26, july – december 2021

ISSN impreso 1390-650X / ISSN electrónico 1390-860X

The administration of the journal is done through the following parameters:

The journal uses the academic anti-plagiarism system



The articles have an identification code (Digital Object Identifier)



The editorial process is managed through the Open Journal System



It is an open access publication (Open Access) licensed Creative Commons



The politics copyright of use postprint, are published in the Self-Archive Policy Repository

Sherpa/Romeo. The logo for SHERPA/ROMEO, featuring a green circular icon with a white dot inside, followed by the text "SHERPA/ROMEO" in a bold, sans-serif font.

The articles of the present edition can be consulted in  
<http://revistas.ups.edu.ec/index.php/ingenius>



UNIVERSIDAD POLITÉCNICA SALESIANA DEL ECUADOR

INGENIUS Journal, is indexed in the following Databases and scientific information systems:

### SELECTIVE DATABASES



### REVIEWS EVALUATION PLATFORMS



### SELECTIVE DIRECTORIES



### SELECTIVE SERIAL LIBRARY



### SCIENTIFIC LITERATURE SEARCHERS OPEN ACCESS



### OTHER BIBLIOGRAPHICAL DATABASES



# CATALOG OF INTERNATIONAL UNIVERSITY LIBRARIES



UNIVERSITÄT BAMBERG



Dear readers:

The planet has undergone a great devastation due to the COVID-19 pandemics. Many people have died and those who were able to overcome the disease have physical and psychological effects that will mark the rest of their existence. The view becomes more complicated if we analyze the economic, social and work-related impact generated by the presence of the virus. The innovation and development processes have been also affected due to the reduced social interaction which enables a direct understanding of the problems to search for solutions where science and technology have a substantial value.

However, the pandemics has also generated great challenges, and these have been assumed with a lot of commitment and decision by the scientific community; tools have been searched for improving communication and interrelation between people, new educational technologies have been generated, and all the technological background has been put at the service of the society to support education, work, communication and, therefore, research and development.

Research has not stopped, some conditions have changed, but the scientific production alternatives remain current. *INGENIUS*, as other scientific publications, continues to lead the processes in this space that we consider of great value to generate contributions that will serve to support the development of the society.

Seventy-five contributions have been received for this issue, which were reviewed through the corresponding editorial process and ten scientific papers were accepted for publication. The contributions published correspond to thirty-three researchers from Spain, Ecuador, Colombia, Peru and Venezuela. It is important to emphasize that the works are jointly structured by authors from diffe-

rent countries, which provides a fundamental added value, since it demonstrates the capability of constituting international networks that enable generating synergic contributions from different realities, which are of great value for the development of science and technology.

In the area of materials, Del Pozo and Mas-Torrent conducted their research work about manufacturing of organic field effect transistors; Guilcaso, Ramirez and others establish the influence of zinc chromate on the corrosion of steels exposed to saline atmospheres; Aparicio Sortino and Jerez establish the influence of homogenization prior to cold-rolling on the microstructure of a steel; these works contribute to identify variables for the production and manufacturing process which could be very useful.

In the automotive area, Taípe, Llanes and others conduct and experimental analysis to evaluate an engine with provoked ignition for different types of gasoline, a contribution of great interest to establish transportation efficiency parameters.

Matute and Bojorque, Aguilar, Risco and Casaverde together with Triviño, Franco and Ochoa show how computer science and the internet are tools of great importance in many areas, such as selection of human talent within an administrative process, classification of thermal images in industries and convergence in telecommunications.

Other authors such as Tapia and Torres conduct an experimental evaluation of a two-dimensional frame; Dany Ochoa presents a tool for studies of electric grids in dynamic regime and Quitiaquez, Cortez and others show a refrigeration application with solar energy which is validated experimentally; three industrial fields that will serve for future works in industrial development. Progress continues, the planet does not stop, and research and innovation, fundamental pillars for the development, will remain booming to support the new challenges that arise.

John Calle-Siguencia, PhD  
EDITOR IN CHIEF

# TABLE OF CONTENTS

<b>Rapid Convective Deposition at Nanoscale of Active Composite Materials for the Manufacture of Organic Field-Effect Transistors</b> .....	9
Deposición convectiva rápida a escala nanométrica de materiales compuestos activos para la fabricación de transistores orgánicos de efecto de campo Freddy G. del Pozo, Marta Mas-Torrent	
<b>Evaluation of an experimental induced ignition engine under different gasoline</b> .....	17
Evaluación experimental de un motor de encendido provocado bajo diferentes gasolinas Víctor Alfonso Taipe-Defaz, Edilberto Antonio Llanes-Cedeño, César Fabricio Morales-Bayetero, Ana Elizabeth Checa-Ramírez	
<b>Convergence and nuances of Net Neutrality in South America</b> .....	30
Convergencia y matices de la neutralidad en la red en América del Sur Roberto D. Triviño, Antonio Franco-Crespo, Leonardo Ochoa-Urrego	
<b>Support to the human talent subsystems, selection and recruitment from an expert system. Case study</b> .....	41
Apoyo a los subsistemas de talento humano, selección y reclutamiento a partir de un sistema experto. Caso de estudio Karina Matute-Pinos, Rodolfo Bojorque-Chasi	
<b>Evaluation of the dynamic properties of a 2D-frame (MDOF) in a shake table</b> .....	49
Evaluación de las propiedades dinámicas de un pórtico plano (MDOF) en una mesa vibratoria Andrea Tapia Andrade, Wilson Torres Berni	
<b>Influence of the Zinc Chromate coating on the corrosion of ASTM A-500 and galvanized A-500 steel exposed into a salt fog corrosion chamber</b> .....	63
Influencia del recubrimiento de cromato de zinc en la corrosión de los aceros ASTM A-500 y A-500 galvanizado expuestos en una cámara de niebla salina Cristian Guilcaso, Leonidas Ramírez, Augusto Coque, Xavier Vaca, Diego Molina, Isaac Simbaña	
<b>Transfer Learning for Binary Classification of Thermal Images</b> .....	71
Transfer learning en la clasificación binaria de imágenes térmicas Daniel Pérez-Aguilar, Redy Risco-Ramos, Luis Casaverde-Pacherrez	
<b>Simplified Model of a Grid-Connection Interface Based on Power Electronic Converter for Grid Studies in Dynamic Regime</b> .....	87
Modelo simplificado de una interfaz de conexión a la red basada en un convertidor electrónico de potencia para estudios de red en régimen dinámico Danny Ochoa	
<b>Influence of homogenization preceding to cold-rolling on the microstructure of the AA-3003</b> .....	99
Influencia del homogeneizado previo al laminado en frío en la microestructura del AA3003 Gennifer Aparicio-Carrillo, Marco Ciaccia-Sortino, Ricardo Jerez	
<b>Numerical analysis of flow pattern map of R600a in a collector/evaporator of a solar-assisted heat pump</b> .....	112
Análisis numérico de los mapas de patrones de flujo del refrigerante R600a en un colector/evaporador de una bomba de calor asistida por energía solar William Quitiaquez, Eduardo Cortez, Karen Anchapaxi, C.A. Isaza-Roldán, César Nieto-Londoño, Patricio Quitiaquez, Fernando Toapanta-Ramos	
<b>Guidelines</b> .....	122
Normas editoriales	



# RAPID CONVECTIVE DEPOSITION AT NANOSCALE OF ACTIVE COMPOSITE MATERIALS FOR THE MANUFACTURE OF ORGANIC FIELD-EFFECT TRANSISTORS

## DEPOSICIÓN CONVECTIVA RÁPIDA A ESCALA NANOMÉTRICA DE MATERIALES COMPUESTOS ACTIVOS PARA LA FABRICACIÓN DE TRANSISTORES ORGÁNICOS DE EFECTO DE CAMPO

Freddy G. del Pozo<sup>1,\*</sup> , Marta Mas-Torrent<sup>2</sup> 

Received: 24-07-2020, Received after review: 04-12-2020, Accepted: 03-02-2021, Published: 01-07-2021

### Abstract

Organic field-effect transistors based on composite materials has been manufactured using the rapid convective deposition technique. The manufacturing was carried out under environmental conditions (air, light and humidity). All manufactured transistors show a typical field-effect behavior with features of a p-type semiconductor, and exhibit field-effect mobilities around 10-2 cm<sup>2</sup>/V.s, fully comparable with transistors manufactured using thermal evaporation of the same active material. The deposition technique demonstrates that devices may be manufactured with high reproducibility and in all cases with a low threshold voltage of approximately 1V. Therefore, it is demonstrated here that rapid convective deposition can be used to manufacture organic field-effect transistors on large surface areas, showing high reproducibility among devices and high stability at environmental conditions.

**Keywords:** Organic field-effect transistors, Rapid convective deposition, Composite Materials.

### Resumen

Transistores orgánicos de efecto de campo basados en un material compuesto han sido fabricados por medio de la técnica de deposición convectiva rápida. La fabricación fue llevada a cabo bajo condiciones ambientales (aire, luz y humedad). En todos los casos, los transistores fabricados muestran un claro comportamiento de efecto de campo con características de semiconductor tipo-p, y exhiben movilidades en el orden de 10<sup>-2</sup> cm<sup>2</sup>/V.s, totalmente comparables con transistores obtenidos por evaporación térmica del mismo material activo. La técnica de deposición demuestra que se pueden obtener dispositivos con alta reproducibilidad y que en todos los casos muestran una baja tensión umbral de alrededor 1 V. Por lo tanto, se demuestra que la deposición convectiva rápida puede ser usada para la fabricación de transistores orgánicos de efecto de campo sobre áreas amplias, con indicadores de reproducibilidad entre dispositivos y alta estabilidad en condiciones ambiente.

**Palabras clave:** transistores orgánicos de efecto de campo, deposición convectiva rápida, materiales compuestos

<sup>1,\*</sup>Facultad de Ciencia e Ingeniería en Alimentos y Biotecnología, Universidad Técnica de Ambato – Ecuador. Corresponding author ✉: fg.delpozo@uta.edu.ec.

<sup>2</sup>Departamento de Nanociencia Molecular y Materiales Orgánicos, Instituto de Ciencia de Materiales de Barcelona (ICMAB – CSIC)/ CIBER – BBN, 08193 – Bellaterra – España.

Suggested citation: del Pozo, F. G. and Mas-Torrent, M. (2021). «Rapid Convective Deposition at Nanoscale of Active Composite Materials for the Manufacture of Organic Field-Effect Transistors». INGENIUS. N.º 26, (july-december). pp. 9-16. DOI: <https://doi.org/10.17163/ings.n26.2021.01>.

## 1. Introduction

The development of organic electronics, particularly in the past two decades, has been of vital importance and has produced great impacts in the research community and in the electronic industry. Some of the devices with organic architecture, such as the organic light emitting diodes (OLED), currently shine with great success and at the moment are being manufactured in series. Thus, it is now easy to find in our daily life devices such as TVs or cell phones with OLED-based screens [1, 2].

At present, semiconductors have been adopted in a very broad range of applications such as screens, computers, phones, among others, becoming essential in our daily life, and almost without realizing it.

The core of all organic devices are the organic semiconductors (OS) and these may be used as active material of various devices, from single devices (transistors, diodes, sensors) developed in research labs, up to complex circuits. The discovery of organic semiconductors dates back to the 1940s [3]. With the purpose of comparing with silicon-based traditional electronics, organic electronics shows unique features, such as processing from solutions, mechanical flexibility and even a mixture of ionic and electrical conduction, which makes that organic electronics has captured the interest of many research laboratories around the world.

The OS are characterized by being conjugated molecules or even conjugated polymers. Their structure differs significantly from that of the traditional inorganic semiconductors, since the OS are characterized by weak Van der Waals bonds, while covalent bonds prevail in the inorganic semiconductors, and besides, the  $\pi$  electrons of the OS form the valence and conduction bands. It is very important to highlight that OS, as opposed to inorganic semiconductors, do not form a native oxide layer, thus promoting a clean interface between the materials, because the materials that can interact with the OS vary from metals to biological organisms [4].

The research efforts have focused in the manipulation of the chemical structures of different OS, their degree of ordering in nanometric layers, as well as in understanding and controlling the transport processes that occur in the interfaces [5]. However, with the purpose of being able to develop low-cost devices, it is necessary to process the OS with techniques based on their dissolution, to arrive to what is known as printed electronics.

The polymer semiconductors have good solubility in a wide range of organic solvents, however, the semiconductors with small molecules show problems in their solubility [2].

The operating principle of an organic field-effect transistor (OFET) is based on the application of an electric field that causes the formation of a conductive

channel in the interface of the dielectric and the organic semiconductor. The typical and most commonly used configurations are the ones shown in Figure 1, which are known as top contacts and bottom contacts.

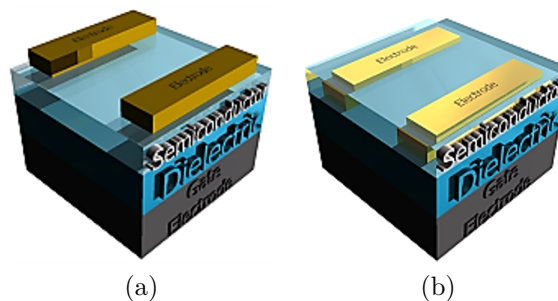


**Figure 1.** Typical configurations used in practice for OFET: (a) top contacts, (b) bottom contacts

In both cases, the organic semiconductor that is deposited on a dielectric layer is in contact with two metallic electrodes, named source and drain; and the gate electrode is typically placed in the bottom part. Then, the current that flows between the source and the drain ( $I_{SD}$ ) may be modulated by the voltage applied to the gate electrode ( $V_G$ ) between the source and the gate, this voltage produces an electric field responsible for the formation of a layer of accumulated charges in the semiconductor/dielectric interface. In addition, depending on the polarity of the voltage applied to the gate ( $V_G$ ), it is possible to control the nature of the charge carriers that accumulate in the interface, thereby holes for p-type semiconductors and electrons for n-type semiconductors [6].

The OS may be deposited on the surfaces in vapor phase or in solution, the processes depend on the vapor pressure and on the solubility of the semiconductor material. The different deposition methods typically result in different morphologies of the resulting films, as well as they increase the variability in the performance of the manufactured devices. However, during past years, new functionalized OS have emerged in which functional groups have been added that have improved the solubility of the rigid conjugated cores. This has enabled to drastically improve the solubility without losing the inherent electrical properties, neither sacrificing its molecular packing [2, 5].

In this way, a very important factor to consider is manufacturing layers at the nanoscale that enables the deposition of OS, functionalized or not, on substrates that further enable the construction of architectures of transistors. One of the most promising OS that has been found is the dibenzo tetrathiafulvalene (DB-TTF), which for this reason is selected for this study [7–10]. From the point of view of manufacturing processes, the organic thin films have been manufactured with processes at low temperatures, among which stands out the centrifugal coating that is widely used in

various research labs. The centrifugal coating enables to have control of the thickness of the manufactured films, most of which are homogeneous and without ruptures; however, such processing method cannot be scaled.

The reason why centrifugal coating cannot be used on large processing surfaces, is the need to use great amounts of solution, which makes centrifugal coating not feasible for application in manufacturing field-effect organic transistors on large areas. For this reason, the development of new manufacturing techniques that reduce the waste of OS solution, which is typically expensive, and likewise enable the deposition of thin layers of organic materials on substrates, is a research topic of continuing interest. Among the unconventional methods, convective self-assembly is widely used for the deposition of coatings on large areas in a small time-scale.

One way to use convective self-assembly, also known as rapid convective deposition, is to use a bar coater such as the one shown in Figure 2, to disperse the OS solution on the desired substrate and cause the self-assembly of the selected molecules on the substrate surface [11, 12].

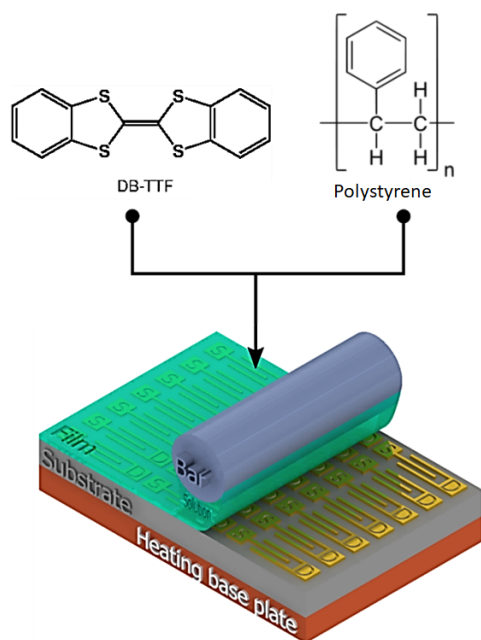


**Figure 2.** Typical graphical scheme of the rapid convective deposition of insulating polymers, semiconductors and/or their mixtures

Despite the promising features of small-molecule semiconductors, manufacturing homogeneous films is complicated, however, in order to overcome such difficulty, the most promising path to this day is creating composite materials, in typical mixtures of a polymeric material as matrix and the organic semiconductor as active material. The application of composite materials has significantly facilitated the processability of

organic semiconductors and, besides, has improved the crystallinity of the films obtained, as well as the stability of the films when facing environmental conditions [2], [13].

## 2. Materials and methods

The silicon substrates were acquired from Fraunhofer IPMS and have an n-type doping, and besides a silicon dioxide layer with a thickness of 230 nm. The gold electrodes have a height of 30 nm, and were deposited on a layer of indium thin oxide (ITO) with a thickness of 10 nm; the ITO layer acts as a bonding layer. The dibenzo tetrathiafulvalene (DB-TTF) thermally evaporated films were prepared at a low evaporation velocity of about  $0.5 \text{ \AA/s}$  on Si/SiO<sub>2</sub> substrates with ITO/Au contacts, the thickness of the films was determined as 110 nm by means of an AFM analysis. The thin films of the active composite material were produced by adapting a commercial coater to the requirements of the experiment. DB-TTF and polystyrene for GPC Mw 10000 (PS10k) were acquired from Sigma-Aldrich and used without any subsequent purification.

In this study, polystyrene for GPC Mw 10000 (PS10k) is used together with the DB-TTF organic semiconductor. Two-percent solutions in chlorobenzene anhydrous of both the insulating polymer and the semiconductor were prepared. Likewise, using a 1:3 proportion, semiconductor solution *versus* insulating polymer solution were prepared in separate vials such that, in all cases, the mixtures do not exceed a volume of 500  $\mu\text{l}$ . Heavily doped n-type silicon, and with a thickness of 200 nm of native silicon oxide (dielectric) were used as substrate and gate electrode, respectively. The substrates employed for coatings were acquired from Si-mat, in which the electrodes were designed using photolithography; such electrodes consist of a layer of 4 nm of Cr (bonding layer) and 40 nm of Au, both metals deposited by thermal evaporation. Prior to the coating process, the substrates are cleaned with acetone and isopropanol, both HPLC grade solvents. At last, the substrates are dried under a nitrogen stream.

Prior to the experiments, the coating equipment was preheated to 105 °C. The substrates with prefabricated electrodes were previously cleaned. The substrates have to be arranged carefully in the coating machine; a small amount of solution, around 30  $\mu\text{l}$ , is used to make the coating. The solution is deposited, and the meniscus dragged at a constant speed of 10 mm/s; during the process of rapid convective deposition, the substrate is always maintained static and at 105 °C. Immediately after the coating process, the coated substrates are carefully removed from the equipment and placed in Petri boxes, and then subjected to a stage of vacuum curing ( $P_{\text{abs}} = 7 \text{ kPa}$ ) and at 60 °C for a period of at least 2 h, with the purpose of

removing any remain of solvent. After the curing, the transistor characteristics are measured at environmental temperature and in darkness.

The optical microscopy photographs were obtained using an Olympus BX51 microscope equipped with polarizer and analyzer. The study of the cross section of the films was performed using a FIB-SEM Neon40 Crossbeam™ workstation from Carl Zeiss. The topography of the surface of the films deposited was studied thanks to the use of an SPM 5500LS from Agilent Technologies; the processing of the topography data was carried out using the software Gwyddion. The measurements of x-rays diffraction were taken with a diffractometer from Rigaku, equipped with a rotating anode.

The electrical measurements were carried out with a Keithley 2612AB with an interface programmed in MATLAB®, typically in a Süss test station with pointed probes and in darkness.

### 3. Results and discussion

Figure 3 shows an image of a DB-TTF:PS10k film obtained by optical microscopy in a mixture ratio 1:3 deposited in an architecture of bottom contacts; it may be observed a film well-formed and free of ruptures on all the area photographed. It is important to note that even though it is an architecture of bottom contacts, the deposited film is homogeneous.



**Figure 3.** Photograph obtained by optical microscopy of a typical film of the DB-TTF and PS10k composite material in a 1:3 ratio; the angle between the polarizer and the analyzer is  $0^\circ$

Since crystallinity is one of the main characteristics of the small and semiconductor DB-TTF molecule, Figure 4 shows the image obtained by polarized optical microscopy in which it is shown, and it may be clearly inferred the formed crystalline structures (spherulites); these are embedded in the film deposited by rapid convective deposition, and crystalline networks form together with paths, also crystalline, for transportation of holes between the electrodes.

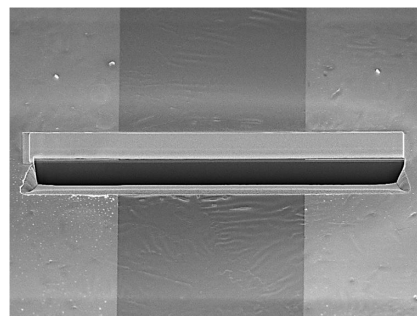
When composite materials are used, parameters such as the polymer nature, the relationship between

the polymer and the active material, in combination with the mechanical parameters of the deposition process, turn the systems complex. In the field of organic semiconductors, all the phases of the OS are obtained even though they do not reach thermodynamic equilibrium, thus the phases obtained must modify the extrinsic parameters. These crystalline phases observed will be named according to the kinetic polymorphs. Even though the DB-TTF shows complex polymorphism it is obtained a crystalline kinetic phase, and as shown in Figure 4 it is observed the gamma kinetic phase that has plate-like shape, which are easily observable along the electrodes of the device analyzed. Since the deposition technique promotes a rapid crystallization, it tends to form the most favorable kinetic crystalline phase [14–16].

Figures 5 and 6 show the frames obtained by FIB-SEM, technique widely used for the study of cross sections of devices and which, similarly, enables the study of the interfaces between materials, thanks to a focused beam of  $\text{Ga}^+$  ions that is used for obtaining the image and even used for nanostructuring. With the purpose of calibrating and obtaining a clean cut, 100 nm of Pt are evaporated on the sample, as observed in Figure 5, together with the hole made.

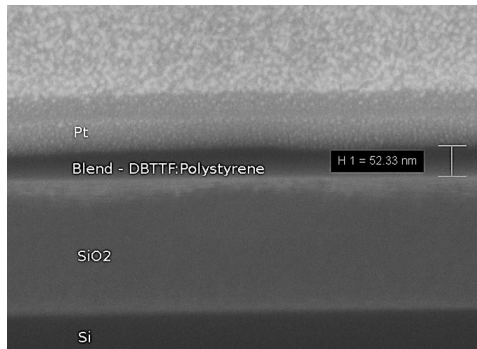


**Figure 4.** Photograph obtained by optical microscopy of a typical film of the DB-TTF and PS10k composite material in a 1:3 ratio; the angle between the polarizer and the analyzer is  $90^\circ$



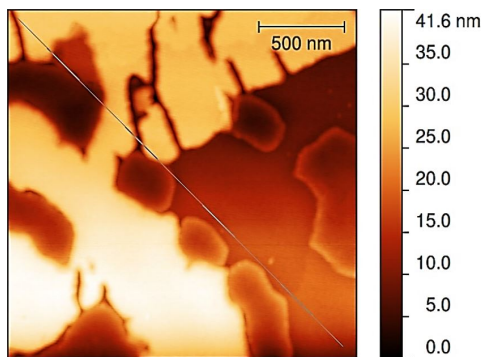
**Figure 5.** Image obtained by FIB-SEM of a typical device manufactured from a film of the DB-TTF and PS10k composite material in a 1:3 ratio. Mag = 6.89 kX, EHT = 5.00 kV, FIB Probe = 30 kV:10 pA, FIB Imaging = SEM, vacuum =  $1.72 \times 10^{-6}$  mbar

On the other hand, Figure 6 shows the cross section of the sample, after the internal rotation of the FIB-SEM; in addition, note the Pt, SiO<sub>x</sub>, Si, and that thanks to this technique it is possible to measure a thickness of 52.33 nm of the film deposited on the substrate with bottom contacts.



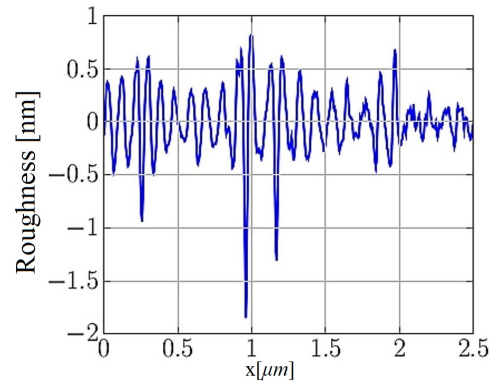
**Figure 6.** Image obtained by FIB-SEM of the cross section of a typical device manufactured from a film of the DB-TTF and PS10k composite material in a 1:3 ratio. Mag = 6.89 kX, EHT = 5.00 kV, FIB Probe = 30 kV:10 pA, FIB Imaging = SEM, vacuum = 1.72e-6 mbar.

Figure 7 was obtained by AFM, in which it is shown structures that are non-periodical and non-structured in a particular region of the deposited film. In addition, it is observed a variability in its topography with a maximum of 41.6 nm.



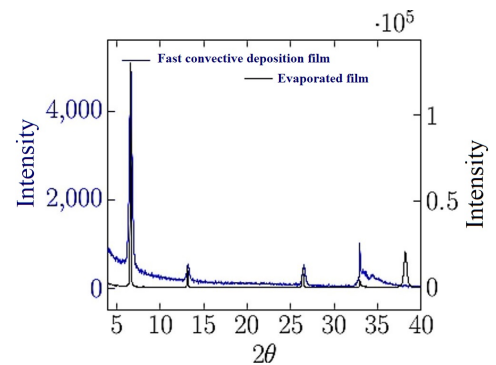
**Figure 7.** Image obtained by AFM of a typical device manufactured from a film of the DB-TTF and PS10k composite material in a 1:3 ratio

Figure 8 shows the roughness as a function of the position, obtained along the diagonal profile shown in Figure 7. Thus, the deposited film shows a relatively low roughness with a maximum of 2.0 nm at the approximate position of positive 1 μm in the x-axis. The smooth surface indicates that it is possible to have a clean interface with the potential of being used in the future for other applications, such as organic field-effect transistors with electrolytic gate electrodes and even in the development of sensors [17].



**Figure 8.** Roughness (nm) as a function of the position in the x-axis [μm] extracted from the diagonal profile shown in Figure 7, for a typical device manufactured from a film of the DB-TTF and PS10k composite material in a 1:3 ratio.

Due to the crystalline nature of the DB-TTF active material, the study by x-rays diffraction is essential, since knowledge of the crystalline structure is key to be able to determine and understand the electrical characteristics of a material. Figure 9 shows the diffractogram of the film, obtained both by rapid convective deposition and by thermal evaporation of the pure DB-TTF material, with the purpose of verifying the formation of crystalline networks, and ruling out that an amorphous film is obtained.



**Figure 9.** X-rays diffractogram for a thermally evaporated film of DB-TTF, and for a typical film of the DB-TTF and PS10k composite material in a 1:3 ratio

Then Figure 9 shows the coincidences at the peaks, which are observed at 6.72°, 13.48°, 20.22°, 27.08° and 41.22°. Thus, the formation of the gamma crystalline phase can be appointed as reported by Brillante *et al.* [18], however the crystalline structure of the gamma phase has not been resolved yet. Notably, the unit cell of the gamma phase contains two DB-TTF molecules, although the increment of volume per molecule in this phase *versus* the alpha-polymorph indicates that the gamma-polymorph is a less stable phase [14].

Figures 10 and 11 show the output and transfer characteristics for a typical device based on the DB-TTF:PS10k (1:3) active composite material. The figure

of merit in the output characteristic shown in Figure 10 exhibits characteristics that are reproducible between devices and which show a quasi-ideal behavior in its linear and saturation response.

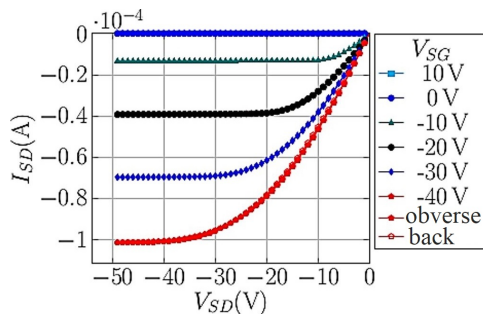


**Figure 10.** Output characteristic of the OFET of a typical film of the DB-TTF and PS10k composite material in a 1:3 ratio. Device  $L = 75 \text{ } \mu\text{m}$ ,  $W = 75000 \text{ } \mu\text{m}$

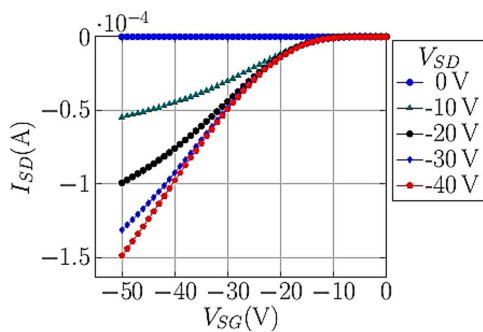


**Figure 11.** Transfer characteristic of a typical film of the DB-TTF and PS10k composite material in a 1:3 ratio. Device  $L = 75 \text{ } \mu\text{m}$ ,  $W = 75000 \text{ } \mu\text{m}$

Then, the device analyzed electrically shows typical characteristics of field effect, observed in the output characteristics of Figure 10, in which it is clear that the voltage applied at the gate modulates the current measured between the source and drain electrodes; similarly, it is observed how the source-drain current tends to saturate as it gets closer to the voltage applied to the gate electrode. It is also important to mention the minimum hysteresis formed during the current-voltage mapping in the positive direction (obverse sweeping) and in the opposite direction (reverse sweeping). A distinctive characteristic of the existence of traps if the hysteresis of the device, where there is a significant difference between the obverse and reverse sweepings, this may occur when charges are trapped and then released, respectively, which may happen altogether due very polar dielectrics [5].

Table 1 summarizes values of mobility and threshold voltage extracted at the saturation regime for various lengths of the channel; despite the significant difference in the length of the channel, the mobility remains between the same values, suggesting the manufacturing

homogeneity between different devices selected. The threshold voltage indicates that transistors need very low voltage to turn on, and the transfer characteristic shown in Figure 11 suggests that there are at least four orders of magnitude between the off and on states in the manufactured organic field effect transistors.

Since the OFETs are considered and viewed as elements in technological applications, the low-cost manufacturing and the stability at environmental conditions are crucial factors to be considered [19]. In this way, and with the purpose of testing the stability along time under controlled conditions, a transistor was subjected to various measurements inside an incubator ( $T = 25 \text{ } ^\circ\text{C}$ ). Thereby, Figure 12 shows the logarithmic transfer characteristic measured at discrete times; such plot suggests that the stability has been significantly improved, since thermally evaporated DB-TTF films are extremely sensitive to environmental conditions [12], [20], [7].

**Table 1.** Summary of mobility and threshold voltage data as a function of the length of the transistor channel

Length of channel [ $\mu\text{m}$ ]	Movility [ $\text{cm}^2/\text{V}\cdot\text{s}$ ]	Threshold voltage [V]
25	$9,75\text{e-}3$	-1,81
50	$1,42\text{e-}2$	0,38
75	$1,02\text{e-}2$	1,18
10	$1,27\text{e-}2$	-1,11

All devices are manufactured from a typical film of the DB-TTF and PS10k composite material in a 1:3 ratio.

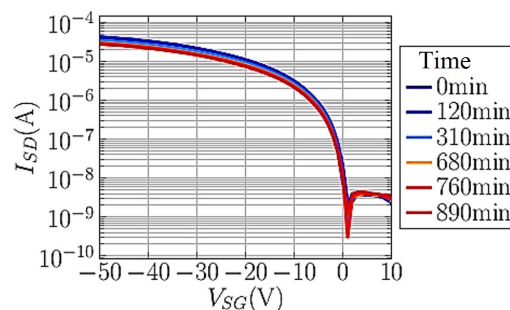


**Figure 12.** Logarithmic transfer characteristic for a device manufactured from a typical film of the DB-TTF and PS10k composite material in a 1:3 ratio

## 4. Conclusions

Organic field effect transistors have been successfully manufactured from a composite material based on a TTF as active material, using a methodology based in the rapid convective deposition from a dissolution of the composite material. Polystyrene was chosen

as bonding matrix to achieve environmental stability. All the devices were manufactured and measured at environmental conditions of light and humidity, thus exhibiting a drastic improvement in their stability compared with the manufactured by thermal evaporation. The mobilities of the devices manufactured oscillate in  $10^{-2}$  cm<sup>2</sup>/V.s con un  $\pm 10^{-3}$  cm<sup>2</sup>/V.s.s, and such mobility is perfectly comparable with the devices manufactured by thermal evaporation from pure DB-TTF. Therefore, it is demonstrated that the manufacturing technique applied to a composite material provides a promising path for manufacturing devices of low cost and high stability.

## Acknowledgements

Freddy del Pozo wants to thank the Group NANOMOL of the Instituto de Ciencia de Materiales de Barcelona (CSIC) for hosting me during my doctoral studies. Also thanks to the Secretaría de Educación Superior, Ciencia, Tecnología e Innovación (Senescyt) for the funding provided through the doctoral scholarship. To the Universidad Técnica de Ambato and its authorities. Thanks to the Dirección de Investigación y Desarrollo (DIDE) of the Universidad Técnica de Ambato for the project «Deposition of organic semiconductor layers at the nanoscale for manufacturing organic field-effect transistors» approved with resolution 0911-CU-P-2016. To doctor Puigdollers and to the Centro de Nanoestructuración of the Universidad Politécnica de Catalunya.

## References

- [1] P. K. L. Chan, “The motivation for and challenges to scaling down organic field-effect transistors,” *Advanced Electronic Materials*, vol. 5, no. 7, p. 1900029, 2019. [Online]. Available: <https://doi.org/10.1002/aelm.201900029>
- [2] S. Riera-Galindo, F. Leonardi, R. Pfattner, and M. Mas-Torrent, “Organic semiconductor/polymer blend films for organic field-effect transistors,” *Advanced Materials Technologies*, vol. 4, no. 9, p. 1900104, 2019. [Online]. Available: <https://doi.org/10.1002/admt.201900104>
- [3] C. Wang, H. Dong, L. Jiang, and W. Hu, “Organic semiconductor crystals,” *Chemical Society Reviews*, vol. 47, pp. 422–500, 2018. [Online]. Available: <http://dx.doi.org/10.1039/C7CS00490G>
- [4] M. Fahlman, S. Fabiano, V. Gueskine, D. Simon, M. Berggren, and X. Crispin, “Interfaces in organic electronics,” *Nature Reviews Materials*, vol. 4, no. 10, pp. 627–650, Oct. 2019. [Online]. Available: <https://doi.org/10.1038/s41578-019-0127-y>
- [5] Z. A. Lamport, H. F. Haneef, S. Anand, M. Waldrip, and O. D. Jurchescu, “Tutorial: Organic field-effect transistors: Materials, structure and operation,” *Journal of Applied Physics*, vol. 124, no. 7, p. 071101, 2018. [Online]. Available: <https://doi.org/10.1063/1.5042255>
- [6] M. Mas-Torrent and C. Rovira, “Role of molecular order and solid-state structure in organic field-effect transistors,” *Chemical Reviews*, vol. 111, no. 8, pp. 4833–4856, 2011, pMID: 21417271. [Online]. Available: <https://doi.org/10.1021/cr100142w>
- [7] K. Shibata, K. Ishikawa, H. Takezoe, H. Wada, and T. Mori, “Contact resistance of dibenzotetrathiafulvalene-based organic transistors with metal and organic electrodes,” *Applied Physics Letters*, vol. 92, no. 2, p. 023305, 2008. [Online]. Available: <https://doi.org/10.1063/1.2834374>
- [8] B. Noda, H. Wada, K. Shibata, T. Yoshino, M. Katsuhara, I. Aoyagi, T. Mori, T. Taguchi, T. Kambayashi, K. Ishikawa, and H. Takezoe, “Crystal structures and transistor properties of phenyl-substituted tetrathiafulvalene derivatives,” *Nanotechnology*, vol. 18, no. 42, p. 424009, sep 2007. [Online]. Available: <https://doi.org/10.1088/0957-4484/18/42/424009>
- [9] M. Mas-Torrent, P. Hadley, S. T. Bromley, X. Ribas, J. Tarrés, M. Mas, E. Molins, J. Veciana, and C. Rovira, “Correlation between crystal structure and mobility in organic field-effect transistors based on single crystals of tetrathiafulvalene derivatives,” *Journal of the American Chemical Society*, vol. 126, no. 27, pp. 8546–8553, 2004, pMID: 15238013. [Online]. Available: <https://doi.org/10.1021/ja048342i>
- [10] M. Mas-Torrent, P. Hadley, S. T. Bromley, N. Crivillers, J. Veciana, and C. Rovira, “Single-crystal organic field-effect transistors based on dibenzo-tetrathiafulvalene,” *Applied Physics Letters*, vol. 86, no. 1, p. 012110, 2005. [Online]. Available: <https://doi.org/10.1063/1.1848179>
- [11] T. Chonsut, A. Rangkasikorn, S. Wirunchit, A. Kaewprajak, P. Kumnorkaew, N. Kayunkid, and J. Nukeaw, “Rapid convective deposition; an alternative method to prepare organic thin film in scale of nanometer,” *Materials Today: Proceedings*, vol. 4, no. 5, Part 2, pp. 6134–6139, 2017, international Conference on Science and Technology of the Emerging Materials (July 27-29, 2016), Pattaya, Thailand. [Online]. Available: <https://doi.org/10.1016/j.matpr.2017.06.106>

- [12] F. G. D. Pozo, S. Galindo, R. Pfattner, C. Rovira, and M. Mas-Torrent, "Deposition of composite materials using a wire-bar coater for achieving processability and air-stability in Organic Field-Effect Transistors (OFETs)," in *Organic Field-Effect Transistors XIV; and Organic Sensors and Bioelectronics VIII*, I. Kymissis, R. Shinar, L. Torsi, I. McCulloch, and O. D. Jurchescu, Eds., vol. 9568, International Society for Optics and Photonics. SPIE, 2015, pp. 17–22. [Online]. Available: <https://doi.org/10.1117/12.2186521>
- [13] L. J. Richter, D. M. DeLongchamp, and A. Amassian, "Morphology development in solution-processed functional organic blend films: An in situ viewpoint," *Chemical Reviews*, vol. 117, no. 9, pp. 6332–6366, 2017, pMID: 28414244. [Online]. Available: <https://doi.org/10.1021/acs.chemrev.6b00618>
- [14] A. Tamayo, S. Riera-Galindo, A. O. F. Jones, R. Resel, and M. Mas-Torrent, "Impact of the ink formulation and coating speed on the polymorphism and morphology of a solution-sheared thin film of a blended organic semiconductor," *Advanced Materials Interfaces*, vol. 6, no. 22, p. 1900950, 2019. [Online]. Available: <https://doi.org/10.1002/admi.201900950>
- [15] A. M. Hiszpanski, R. M. Baur, B. Kim, N. J. Tremblay, C. Nuckolls, A. R. Woll, and Y.-L. Loo, "Tuning polymorphism and orientation in organic semiconductor thin films via post-deposition processing," *Journal of the American Chemical Society*, vol. 136, no. 44, pp. 15 749–15 756, 2014, pMID: 25317987. [Online]. Available: <https://doi.org/10.1021/ja5091035>
- [16] H. Chung and Y. Diao, "Polymorphism as an emerging design strategy for high performance organic electronics," *Journal of Materials Chemistry C*, vol. 4, pp. 3915–3933, 2016. [Online]. Available: <http://dx.doi.org/10.1039/C5TC04390E>
- [17] A. Kyndiah, F. Leonardi, C. Tarantino, T. Cramer, R. Millan-Solsona, E. Garreta, N. Montserrat, M. Mas-Torrent, and G. Gomila, "Bioelectronic recordings of cardiomyocytes with accumulation mode electrolyte gated organic field effect transistors," *Biosensors and Bioelectronics*, vol. 150, p. 111844, 2020. [Online]. Available: <https://doi.org/10.1016/j.bios.2019.111844>
- [18] A. Brillante, I. Bilotti, R. G. Della Valle, E. Venuti, S. Milita, C. Dionigi, F. Borgatti, A. N. Lazar, F. Biscarini, M. Mas-Torrent, N. S. Oxtoby, N. Crivillers, J. Veciana, C. Rovira, M. Leufgen, G. Schmidt, and L. W. Molenkamp, "The four polymorphic modifications of the semiconductor dibenzo-tetrathiafulvalene," *CrytEngComm*, vol. 10, pp. 1899–1909, 2008. [Online]. Available: <http://dx.doi.org/10.1039/B810993A>
- [19] P. A. Bobbert, A. Sharma, S. G. J. Mathijssen, M. Kemerink, and D. M. de Leeuw, "Operational stability of organic field-effect transistors," *Advanced Materials*, vol. 24, no. 9, pp. 1146–1158, 2012. [Online]. Available: <https://doi.org/10.1002/adma.201104580>
- [20] M. Mas-Torrent and C. Rovira, "Tetrathiafulvalene derivatives for organic field effect transistors," *Journal of Materials Chemistry*, vol. 16, pp. 433–436, 2006. [Online]. Available: <http://dx.doi.org/10.1039/B510121B>



# EVALUATION OF AN EXPERIMENTAL INDUCED IGNITION ENGINE UNDER DIFFERENT GASOLINE

## EVALUACIÓN EXPERIMENTAL DE UN MOTOR DE ENCENDIDO PROVOCADO BAJO DIFERENTES GASOLINAS

Víctor Alfonso Taípe-Defaz<sup>1</sup> , Edilberto Antonio Llanes-Cedeño<sup>1\*</sup> ,  
 César Fabricio Morales-Bayetero<sup>1,2</sup> , Ana Elizabeth Checa-Ramírez<sup>1</sup>

Received: 09-07-2020, Received after review: 04-12-2020, Accepted: 03-02-2021, Published: 01-07-2021

### Abstract

The internal combustion engine with provoked ignition is a thermal machine that enables obtaining mechanical power from the chemical energy of a fuel. The objective of this work was to evaluate the performance of an internal combustion engine through the balance of energy and exergy, under the individual use of the three types of gasoline sold in Ecuador (Super, Extra and Ecopais). The experimental methodology consisted of starting the engine with the individual use of gasoline until reaching its maximum power at engine speed, and taking measurements of temperature, specific fuel consumption and air-fuel ratio during 3 minutes. Results show an energy efficiency of 11.31% for the Super gasoline, 10.75% for the Extra gasoline and 10.39% for the Ecopais gasoline. Regarding exergy efficiency, 58.81% was established for the Super gasoline, 58.89% for the Extra gasoline and 59.19% for the Ecopais gasoline. Results enable us to conclude that there is an exergy potential for improvement that may be an opportunity to increase energy efficiency.

**Keywords:** energy balance, exergy, energy consumption, ignition motor induced.

### Resumen

El motor de combustión interna de encendido provocado es una máquina térmica que permite obtener una potencia mecánica a partir de la energía química de un combustible. El presente trabajo tuvo como objetivo evaluar el desempeño de un motor de combustión interna mediante el balance de energía y exergía, bajo el uso individual de las tres gasolinas comercializadas en el Ecuador (Súper, Extra y Ecopaís). La metodología experimental consistió en la puesta en marcha bajo el uso individual de las gasolinas hasta alcanzar su máxima potencia a una velocidad de giro del motor, donde se tomaron mediciones de temperatura, consumo específico del combustible y la relación aire combustible para un tiempo de tres minutos. Los resultados muestran una eficiencia energética de 11,31 % para gasolina Súper, 10,75 % para gasolina Extra y 10,39 % para gasolina Ecopaís. En lo relacionado a la eficiencia exergética se estableció un 58,81 % para la gasolina Súper, 58,89 % para la gasolina Extra y un 59,19 % para la gasolina Ecopaís. Los resultados permiten concluir que existe un potencial exergético de mejoramiento que puede ser una oportunidad para aumentar la eficiencia energética.

**Palabras clave:** balance de energía, exergía, consumo energético, motor de encendido provocado.

<sup>1,\*</sup>Grupo de Investigación Eficiencia, Impacto Ambiental e Innovación en la Industria y el Transporte, Facultad de Ingeniería y Ciencias Aplicadas, Carrera de Mecánica, Universidad Internacional SEK, Quito - Ecuador. Autor para correspondencia ✉: antonio.llanes@uisek.edu.ec.

<sup>2</sup>Universidad Técnica del Norte, Ibarra - Ecuador.

Suggested citation: Taípe-Defaz, V. A.; Llanes-Cedeño, E. A.; Morales-Bayetero, C. F. and Checa-Ramírez, A. E. (2021). «Evaluation of an experimental induced ignition engine under different gasoline». INGENIUS. N.º 26, (july-december). pp. 17-29. DOI: <https://doi.org/10.17163/ings.n26.2021.02>.

## 1. Introduction

Internal combustion engines (ICE) have great applications in energy generation and cogeneration systems, and in the automotive industry. Therefore, testing and studying the performance of these engines is very important to contribute to a larger growth of its scope of application and operation quality [1, 2].

In general, ICEs have a larger delivery and activity in the transportation sector, in which the use of fuels and the increase of emissions are related with industrial processes that drive a strong economic activity of marketing and insurance of goods and supplies [3, 4]. In Ecuador, the transport sector represents 49 % of the total energy consumption, where 98.3 % comes from diesel and gasolines, representing 25 % of the emission of greenhouse gases due to the combustion of gasolines [5].

The ICE is the most efficient and reliable energy plant in the transport (gasoline and diesel engines) and heavy machinery (diesel engine) sector. It is expected that ICEs are present until: (i) fuel shortage becomes a serious problem; (ii) less polluting and more efficient new technologies are developed as replacement; or (iii) emissions regulations, established by environmental agencies to improve quality of air, become unreachable for engine and vehicle manufacturers [6].

Since the last century, the automotive industry has been analyzing the design of engines with the purpose of reducing emissions of greenhouse gases –carbon dioxide ( $\text{CO}_2$ ), nitrogen oxides ( $\text{NO}_x$ ), carbon monoxide ( $\text{CO}$ )– and particulate matter (PM), main responsible for the degradation of the environment [7, 8]. In addition, ICEs are designed to guarantee a specific output power combined with the greatest possible efficiency [9]. The improvements have also increased through the use of fuels with better properties; one of the important factors that determine the quality of gasolines is the so-called octane rating [10]. It is defined as a quantification of the quality and antiknocking capability of gasolines; its main feature is identifying the combustion process within the engine: a high-octane rating represents a better antiknocking capability.

For example, in South America the gasolines with higher octane rating are Argentina and Peru with 98, followed by Brazil with 95 and Colombia with 92 [11]. Three types of gasolines are sold in Ecuador, which come from domestic refineries. According to the INEN 935 REGULATION, these are classified based on their octane-rating in two types:

- Super Gasoline, with a minimum octane rating of 92.
- Extra Gasoline and Ecopais, with a minimum octane rating of 87.

The Ecopais gasoline is defined as a biofuel which

contains a mixture of 95 % of premixed naphtha and 5 % of ethanol [12].

The development of the automotive industry has an impact on the energy shortage [13], however, the increasing demand of biofuels as an alternative to mitigate the emission of gases and reduce the consumption of oil-based fuels is only a part of the solution [14], therefore, it is necessary to evaluate the performance of the engine through energy and exergy analyses.

The energy analysis is based on the first law of thermodynamics, as an efficient way to know the energy distribution characteristics reflected in the conversion, transfer, usage and energy loss of the fuel in terms of quantity. With this characteristic as a guide, specific measures may be used to reduce energy loss. However, the energy analysis does not reflect the difference in energy quality, term which is indeed considered for the exergy analysis; the latter is based on the second law of thermodynamics, the exergy study may evaluate the energy quality to achieve a total reusability of the energy lost [15].

With respect to the energy analysis of the ICEs, up to 55 % of the input energy is yielded to the environment through exhaust gases and various heat exchange processes between the engine configuration of the engine, the refrigerant and the lube oil [16]. Figure 1 indicates the performance percentages of an ICE.

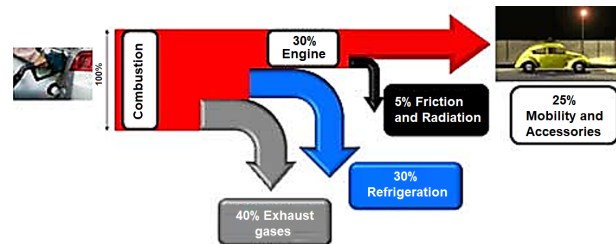


Figura 1. Sankey Diagram in ICE [17]

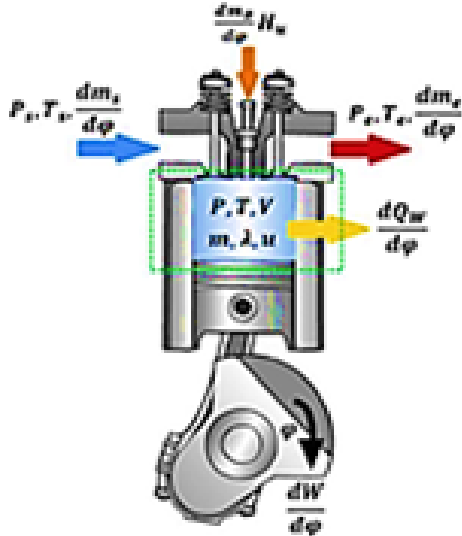
El MCI es un motor térmico que transforma la energía química en energía mecánica, generalmente, disponible en un eje de salida giratorio. La energía química del combustible se transforma primero en energía térmica mediante la combustión u oxidación con el aire en el interior del motor, luego de la combustión, los reactantes se transforman en productos como dióxido de carbono ( $\text{CO}_2$ ), agua ( $\text{H}_2\text{O}$ ) y monóxido de carbono ( $\text{CO}$ ). La energía térmica incrementa la presión y la temperatura de los gases en el interior del motor, el gas a alta presión se expande contra los mecanismos mecánicos del motor [18].

La Universidad Internacional SEK, con el objetivo de reforzar los conocimientos y habilidades de los estudiantes en Ingeniería Automotriz, adquirió un banco experimental para MCI, específicamente de encendido provocado (MEP). Del mismo se desconoce su comportamiento energético a partir del uso de las gasolinas comercializadas en el Ecuador.

Por lo mencionado el actual estudio de investigación tiene como objetivo general: evaluar el desempeño de un motor de encendido provocado experimental mediante el balance de energía y exergía, bajo el uso individual de las tres gasolinas comercializadas en el Ecuador, para la valoración y evaluación de su rendimiento.

## 2. Materiales y métodos

La Figura 2 indica que las paredes de la cámara de combustión conforman los límites del sistema. Al utilizar la primera ley de la termodinámica se obtiene la descomposición de la energía del sistema, la Ecuación (1) que acompaña a la Figura 2 corresponde a decir que «el cambio de la energía del sistema ( $E_{sis}$ ), asumiendo que no hay pérdidas de energía en deformaciones del volumen de control, se reduce al cambio de la energía interna del sistema ( $U$ )» [19].



1. Energy of the system ( $E_{sis}$ )
2. Energy supplied to the system by the fuel ( $Q_{comb}$ )
3. Inlet load ( $m_{adm} * h_{adm}$ )
4. Mechanical work ( $W$ )
5. Heat dissipated through the refrigerant ( $Q_{ref}$ )
6. Heat of the exhaust gases ( $m_{esc} * h_{esc}$ )
7. Equivalent heat of the chamber gases that escape through the interstices between the segments ( $m_{fug} * h_{fug}$ )

**Figura 2.** Thermodynamic model of an ICE [20, 21]

$$\frac{dE_{sis}}{dt} = \frac{dU}{dt} = \frac{dQ_{comb}}{dt} + \frac{dQ_{refr}}{dt} + \frac{dW}{dt} + \frac{dm_{adm}}{dt} h_{adm} + \frac{dm_{esc}}{dt} h_{esc} + \frac{dm_{fug}}{dt} h_{fug} \quad (1)$$

For the practical purposes of calculating the energy balance of the engine, Equation (1) may be rewritten as shown in equation (2) [21]:

$$Q_{comb} + m_{adm} h_{adm} = W + Q_{refr} \frac{dU}{dt} + m_{esc} h_{esc} + m_{fug} h_{fug} \quad (2)$$

Regarding the scope, the present study is experimental, because it is based on the management of parameters that measure the performance of the engine, such as torque, rotational speed, engine power, volumetric flow and specific consumption of fuel under strictly controlled circumstances, with the objective of explaining how or why a particular situation or circumstance arises [22].

The engine under study is a 1 cylinder four-stroke CT 150 air-cooled EPI, with carburetor. With an approximate weight of 15 kg, dimensions  $L \times W \times H$  ( $420 \times 300 \times 320$  mm), approximate power of 2.2 kW, oil volume 0.6 L, magnetic ignition voltage, compression ratio 7:1, thermal probe for measuring the temperature of exhaust gases from 0 to 1000 °C, driven by a pulley of diameter 125 mm, and SPA 1250 v-belt (see Figure 3).



**Figura 3.** CT 150 engine

The following instruments and materials (integrated in the experimental bench as illustrated in Figure 4) were used for conducting the research:



**Figura 4.** Experimental bench. Air-cooled gasoline engine with 1 cylinder, and HM 365 universal drive and brake unit

- Air-cooled gasoline engine with one cylinder.
- HM 365 universal drive and brake unit
- Asynchronous motor with frequency converter
  - power: 2200 W
  - maximum speed: 3000 min<sup>-1</sup> approx.
  - maximum torque: 12 Nm approx.
- Operation with v-belt
  - v-belt length: 1157 mm, 1180 mm, 1250 mm
  - type of v-belt: SPA
  - diameter of the v-belt pulley: 125 mm
- Resistive load: 72 Ω, 2400 W
- Measurement ranges
  - torque: ± 15 Nm
  - speed: 0... 5000 min<sup>-1</sup>
- 400 V, 50 Hz, 3 phases
- 400 V, 60 Hz, 3 phases
- 230 V, 60 Hz, 3 phases
- Super, Extra and Ecopais Gasolines (see Table 1, fundamental features)

**Tabla 1.** Properties of the fuels

Parameters	Super	Extra	Ecopais
Octane Rating (OR)	92	87	87
Sulphur content (%)	0,065	0,065	0,065
Gum content (mg/100 ml)	4	3	3
Aromatic content (% vol.)	35	30	30
Olefin content (% vol.)	18	18	18
Final point of evaporation (°C)	220	220	220
Density (kg/m <sup>3</sup> )	722	723	749
LCV (kJ/kg)	48345	45124	44739

Note: Taken from the study conducted by Rocha-Hoyos, *et al.* [23]

The following steps were implemented to obtain the power curve:

- Start the engine at full load.
- Adjust the torque potentiometer (M) to progressively brake the engine (n) (reducing the rpm).

- Record the torque (M) and the number of revolutions (n) in a table (9 readings).
- Repeat the procedure for a second reading to be able to calculate the average.
- Apply Equation (3) for obtaining the power:

$$P = \frac{2\pi nM}{60} \text{ (W)} \quad (3)$$

- Plot power (y axis) *vs.* rpm (x axis).

The following steps were implemented to obtain the consumption curve:

- The engine is adjusted to operate at constant revolutions (2500 rpm), and it is measured the time at which 5.1 cm<sup>3</sup> are consumed (which corresponds to a descent of 1 cm in the scale of the measuring tube, thus determining the volumetric flow Q) for a fixed torque in the equipment.
- Values are recorded for different engine torques (always maintaining the engine at 2500 rpm), the results are recorded in a table.
- Make a table that records the power, the mass flow  $\dot{m} = Q\rho_{fluid}$  (where Q is the volumetric flow and  $\rho_{fluid}$  is the density of the fuel) and the specific consumption ( $b_e$ ) obtained by means of Equation (4):

$$b_e = \frac{\dot{m}}{P} \quad (4)$$

- Plot  $b_e$  (y axis) and P (x axis).

## 2.1. Calculation of the thermal balance

The energy balance of the ICEs is basically a study of the first law of thermodynamics, which is also called energy balance, heat balance or thermal balance [20]. The analysis of the thermal balance is an efficient way to know the energy flow, enables the designer to evaluate the variation of internal energy as a function of the energy transfers as heat or work through the boundaries, and the enthalpies associated with the mass flow that crosses these boundaries, and then presenting a highly potential method which reduces fuel consumption in the engines [24]. The thermal balance enables carrying out the following equality: Energy that enters the system = Energy that exits the system.

From another point of view, Equation (5) is fulfilled for a process with flow and steady state.

$$\sum Q = \sum H_{input} - \sum H_{output} \quad (5)$$

Where:

$\sum Q$ : sum of heat evacuated to the environment

$\sum H_{output}$ : sum of enthalpies that exit the system    Where:

$\sum H_{input}$ : sum of enthalpies that enter the system

$P_{max}$ = Maximum power of the engine

$\dot{Q}_c$ = heat released by the fuel

In the light of the above, the sum of heats that cross the system is equal to the difference between the sum of enthalpies that enter the system and the sum of enthalpies that exit the system [19]. On the other hand, the change of enthalpy is a measure of the amount of energy absorbed or delivered in a thermodynamic system, i.e., is the change produced by a transformation in which it is possible to receive or provide energy (such as in the present case study, mechanical energy), and thus the enthalpy may be considered as numerically equal to the heat exchanged with the environment. In order to solve the thermal balance, the following general calculations are taken into account.

## 2.2. Exergy balance

The exergy is established as the analysis of the performance of the system based on the second law of thermodynamics. The exergy is the amount of «energy available» in the system. The exergy analysis is used to define the type, location and extent of the energy losses in different parts of an ICE [25]. The exergy is defined as the maximum amount of useful theoretical work, which may be obtained when a system reaches thermodynamic equilibrium with the environment. The destruction of exergy or the irreversibilities are accompanied by the generation of entropy. The main objective of an exergy analysis is to conceptualize the optimal design for a system, the design parameters and operation have considerable effects in the exergy balance during the operation of engine [26].

Three main sources of destruction of exergy may be identified: irreversibilities in the cylinder, mechanical irreversibilities and other forms of irreversibility. The effects of the heat transfer of the gases to the cylinder wall, the combustion and the viscosity are explained in the cylinder. Mechanical irreversibilities are caused by friction, which may be calculated by the difference between the indicated braking power. Other irreversibilities explain the sum of various irreversible processes, such as the pumping losses, the mixing process of air and fuel, the choking and the heat transfer from the wall to the cooling system [27].

The exergy balance is determined according to the following methodology:

Exergy associated to the fuel heat (Equation (10)):

$$E\chi_c = \dot{m}_c LCV \quad (10)$$

Where:

$E\chi_c$ = Exergy of the fuel (kW)

LCV = lower calorific value of the fuel (kJ/kg)

### 2.1.1. Mass flow of fuel (Equation 6)

$$\dot{m}_c = \rho \frac{v}{\Delta t} \quad (6)$$

Donde:

$\dot{m}_c$  = mass flow of fuel (kg/s)

$\rho$  = fuel specific density (kg/m<sup>3</sup>)

$V$  = fuel volume (m<sup>3</sup>)

$\Delta t$  = flow time (180 s)

### 2.1.2. Heat released by the fuel (Equation (7))

$$\dot{Q}_c = \dot{m}_c \cdot PCI \quad (7)$$

Where:

$\dot{Q}_c$  = Heat released by the fuel (kW)

$PCI$  = lower calorific value of the fuel (kJ/kg)

### 2.1.3. Flow of exhaust gases (Equation (8))

$$\dot{m}_g = \dot{m}_{air} + \dot{m}_{fuel} \quad (8)$$

Donde:

$\dot{m}_{air}$  = flow of air (kg/s)

$\dot{m}_{fuel}$  = mass flow of fuel (kg/s)

The energy efficiency of the system is determined according to Equation (9).

$$\eta_{energy} = \frac{P_{max}}{\dot{Q}_c} \quad (9)$$

$$\dot{E}\chi_g = \dot{m}_g \left\{ C_P T_0 \left[ \left( \frac{T}{T_0} - 1 \right) - \ln \left( \frac{T}{T_0} \right) \right] \right\} \quad (11)$$

Where:

$\dot{E}_{\chi_g}$  = Exergy associated to the flow of gas (kW)

$\dot{m}_g$  = Flow of gas (kg/s)

$C_P$  = Specific heat at constant pressure (kJ/kg K)

$T_0$  = Reference temperature (K)

$T$  = Temperature of the exhaust gases (K)

The exergy efficiency is determined from Equation (12):

$$\eta_{exergy} = \frac{\sum E_{inputflows} - \sum E_{outputflows}}{\sum E_{inputflows}} \quad (12)$$

The specific heat of air at a temperature T (K), is given by Equation (13):

$$c_{par,T} = C_0 + C_1T + C_2T^2 + C_3T^3 + C_4T^4 \quad (J/kgK) \quad (13)$$

For a temperature between 200 and 800 K.

Where:

$$\begin{aligned} c_0 &= 1,0189 \times 10^3 \\ c_1 &= -1,3784 \times 10^{-1} \\ c_2 &= 1,9843 \times 10^{-4} \\ c_3 &= 4,2399 \times 10^{-7} \\ c_4 &= -3,7632 \times 10^{-10} \end{aligned}$$

The specific heat of the combustion gases at constant pressure is given by Equation (14):

$$c_{p,g,T} = c_{par,T} + \frac{f}{1+f} \theta_{C_p,T} \quad (J/kgK) \quad (14)$$

Where:

$$f = \frac{\dot{m}_{comb}}{\dot{m}_{ar}} \quad (15)$$

$$\theta_{C_p,T} = C_{P_0}T + C_{P_1}T^2 + C_{P_3}T^3 + C_{P_4}T^4 + C_{P_5}T^5 \quad (16)$$

For a temperature between 200 and 800 K.

$$\begin{aligned} c_{p0} &= -3,5949 \times 10^2 \\ c_{p1} &= 4,5164 \times 10^0 \\ c_{p2} &= 2,8116 \times 10^{-3} \\ c_{p3} &= -2,1709 \times 10^{-5} \\ c_{p4} &= 2,8689 \times 10^{-8} \\ c_{p5} &= -1,2226 \times 10^{-11} \end{aligned}$$

### 2.3. Experimental design

The software Statgraphics Centurion XVI is used for the analysis and comparison of results, performing a simple ANOVA for the different treatments (combinations) shown in Table 2. Three repetitions of each treatment were carried out, as established by the NTE INEN 2205 [28] regulation in its section 6 about testing methods, where item 6.1.5.4 states «Record and average a minimum of three readings in each test». The fuel with three levels (Extra, Super and Ecopais) is the independent variable, while energy and exergy efficiency are the dependent variables.

An ANOVA analysis was used to determine if there is a significant difference among the experimental groups, applying tests of multiple comparison of means, for this case the Least Significant Difference (LSD) in a 95 % of confidence [29, 30].

**Table 2.** Treatments for the analysis of significant

Number of treatments	Engine	Fuels
T1	Motor CT 150	Super
T2	Motor CT 150	Extra
T3	Motor CT 150	Ecopais

### 3. Results and discussion

Table 3 shows the results of the nine measurements of revolutions and torque, variables required for calculating power and for plotting P vs. n.

Figure 5 indicates the power as a function of the turning speed of the engine, it is observed that as the turning speed increases, the power generated also increases, but only up to reaching its maximum power. The maximum power generated with the use of the Super gasoline is 1174.17 W, which corresponds to an engine turning speed of 3199 rpm. The maximum power generated with the use of the Extra gasoline is 1142.46 W, which corresponds to an engine turning speed of 3121.5 rpm.

At last, the maximum power generated with the use of the Ecopais gasoline is 1183.35 W, which corresponds to an engine turning speed of 3224 rpm. In summary, it is obtained that for speeds under 3000 rpm there are no differences in the behavior of the power, as opposed to speeds between 3000 and 3600 rpm where the Super and Ecopais gasolines show the best results. These results are compatible with the works [31] and [32], where power tests with the Extra and Super gasolines were carried out, obtaining the same behavior trend as in the present study.

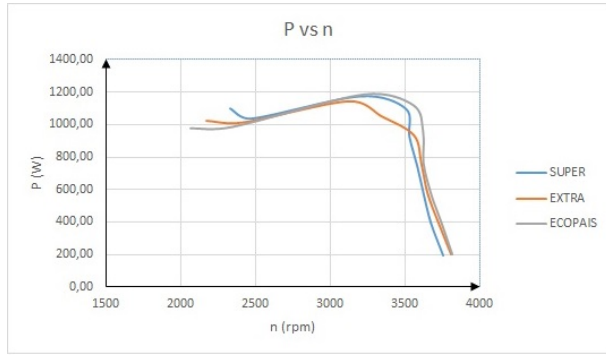


Figura 5. Curves of power vs. rpm

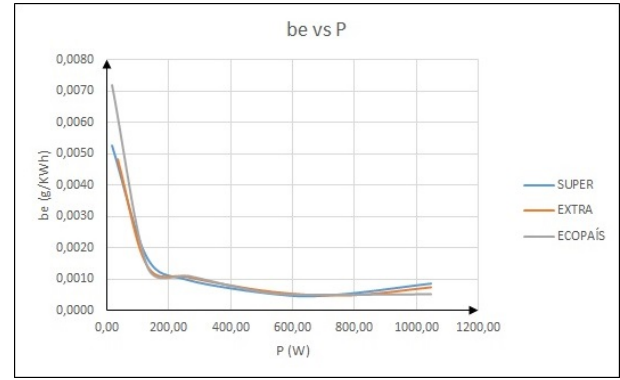


Figura 6. Curves of specific consumption vs. power

Tabla 3. Values of revolutions, torque and power

Super			Extra			Ecopais		
n (rpm)	M (Nm)	P(W)	n (rpm)	M (Nm)	P(W)	n (rpm)	M (Nm)	P(W)
3753	0,5	196,51	3808,5	0,495	197,42	3815	0,5	199,75
3671	1,03	395,96	3724	1,005	391,93	3743	1,005	393,93
3624	1,5	569,26	3650,5	1,505	575,33	3671,5	1,5	576,72
3579,5	1,995	747,81	3609	2,005	757,76	3623	2,01	762,59
3528	2,505	925,48	3559,5	2,5	931,87	3621	2,5	947,98
3501,5	3	1100,03	3342	3	1049,92	3554	3,005	1118,38
3199	3,505	1174,17	3121,5	3,495	1142,46	3224	3,505	1183,35
2474,5	4,005	1037,81	2412,5	4,005	1011,81	2340	4,01	982,63
2333	4,5	1099,4	2169	4,5	1022,12	2067,5	4,505	975,37

Table 4 shows the results of the six power and mass flow measurements, parameters required for calculating specific consumption ( $b_e$ ).

Figure 6 indicates the fuel specific consumption as a function of the power generated; as power increases the fuel specific consumption reduces to approximately 600 W, and then a slight increase starts to occur from this value with the greatest consumptions occurring at low revolutions. This result is compatible with the one obtained by Alzate and Agudelo [3], where tests were carried out in the operating regime from 1100 rpm to 3600 rpm; from 1100 rpm to 2000 rpm the fuel specific consumption diminished progressively down to its minimum value, a from then on it successively grew as a function of the increase in the engine turning speed. In summary, it may be concluded that the behavior of the specific consumption for the three gasolines is not significant, similar to the results obtained in the study

by Quimbita and Guallichico [32], where it is observed a fuel specific consumption of 47.44 g/kWh for the Super gasoline, 43.17 g/kWh for the Extra gasoline and 49.96 g/kWh for the Ecopais gasoline.

Table 5 shows the results of the measurements required for calculating the thermal balance of the ICE at maximum power, carried for the Super, Extra and Ecopais gasolines; and Table 6 indicates the variables obtained when applying the methodology described in the section of the method. As indicated in Table 4, the energy efficiency for the Super gasoline is 11.31 %, and the exergy efficiency is 58.81 %, for the Extra gasoline 10.75 % and 58.89 %, and for the Ecopais gasoline 10.39 % and 59.19 %, respectively; this is due to the fact that there is an amount of exergy being destroyed in the exhaust gases that can be used to generate work.

**Tabla 4.** Tabulated values of power, mass flow and specific consumption for the different gasolines tested

Super			Extra			Ecopais		
P(W)	m(kg/h)	be (g/kwh)	P(W)	m(kg/h)	be (g/kwh)	P(W)	m(kg/h)	be (g/kwh)
18,33	0,096	0,0053	36,652	0,1777	0,0048	15,708	0,1132	0,0072
130,9	0,22	0,0017	130,9	0,1891	0,0014	130,8997	0,1817	0,0014
261,8	0,254	0,001	264,417	0,2824	0,0011	264,4174	0,2938	0,0011
562,87	0,277	0,0005	534,071	0,3222	0,0006	526,2168	0,3003	0,0006
748,75	0,373	0,0005	785,398	0,3836	0,0005	785,3982	0,4045	0,0005
1047,2	0,89	0,0008	1047,198	0,7808	0,0007	1047,1976	0,5567	0,0005

**Tabla 5.** Tabulated average values for calculating energy and exergy efficiency at maximum power

$M_{max}$ (Nm)	$P_{max}$ (W)	Consumption (m <sup>3</sup> )	$Q$ (m <sup>3</sup> /s)	$P_c$ (kg/m <sup>3</sup> )	$\dot{m}_c$ (kg/s)	$\dot{m}_{aire}$ (kg/s)	$\dot{m}_{gas}$ (kg/s)	$\bar{T}_e$ (°C)	$\bar{T}_s$ (°C)	PCI (kJ/kg)
<b>Gasolina Super</b>										
3,505	1174,17	53,55	2,97 E-07	722	0,0002148	0,002071	0,002286	22,77	543	48345,66
<b>Gasolina Extra</b>										
3,495	1142,46	58,65	3,26 E-07	723	0,0002356	0,002046	0,002282	23,72	543,5	45124,76
<b>Gasolina Ecopais</b>										
3,505	1183,35	61,2	3,40 E-07	749	0,0002547	0,00206	0,002315	23,77	541,5	44739,17

Note: The values of LCV were taken from the study by Rocha-Hoyos *et al.* [23]

**Tabla 6.** Average results of energy and exergy efficiency calculated at maximum power

$P_{max}$ (W)	$\dot{Q}_c$ (kW)	$\eta_{ener}$ %	$E\chi_g$ (kW)	$E\chi_c$ (kW)	$E\chi_k$ (kW)	$\eta_{ener}$ %
<b>Gasolina Super</b>						
1174,17	10,38	11,31	0,64	10,38	3,63	58,81
<b>Gasolina Extra</b>						
1142,46	10,63	10,75	0,65	10,63	3,72	58,89
<b>Gasolina Ecopais</b>						
1183,35	11,39	10,39	0,66	11,39	3,99	59,19

Note: The exergy due to the conduction and convection heat transfers has been denoted as  $E\chi_k$ , estimated as 35 % of  $E\chi_c$  according to Li *et al.* [7].

Having an exergy efficiency greater than an energy efficiency, implies that there is an exergy potential for improvement through which it is possible to take advantage of part of that exergy being destroyed and transform it into work, thus achieving an increase in the thermal efficiency [33].

The results obtained are compatible with the work by Gonzalez *et al.*, [33], where it was obtained an exergy efficiency of 14.77 % which is greater than the energy efficiency of 12.79 %, concluding that this difference is due to the increase of 43.19 % in the engine turning speeds.

On the other hand, according to Llerena [34], an energy efficiency of 39 % and an exergy efficiency of

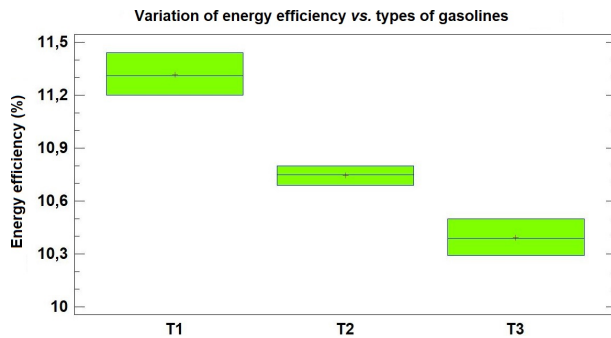
79 % were obtained at the beginning of the study, and later a reduced exergy efficiency of 56 % was achieved due to the use of the exhaust gases that escape from the turbine to generate vapor (cogeneration), thus enabling an increase of 67 % in the energy efficiency.

Table 7 and Figure 7 represent the multiple range test and the box and whisker plot for the energy efficiency as dependent variable. It is concluded that there is a significant difference between the gasolines, and the Super gives the best result.

**Table 7.** Analysis of significant differences for the energy efficiency

Fuel	Cases	Mean	Homogeneous Groups
T3 (Ecopais)	3	10,39	X
T2 (Extra)	3	10,75	X
T1 (Super)	3	11,31	X

Note: Method: 95.0 percentage of LSD



**Figure 7.** Comparative graph of the energy efficiency for the different types of gasoline

On the other hand, Table 8 and Figure 8 show the multiple range test and the box and whisker plot for the exergy efficiency as dependent variable, where it is concluded that there is a significant difference between the gasolines, with the Ecopais gasoline giving the best result; however, there is no significant difference between the Extra and the Super gasolines.

**Table 8.** Analysis of significant differences for the exergy efficiency

Fuel	Cases	Mean	Homogeneous Groups
T1 (Super)	3	58,8	X
T2 (Extra)	3	58,89	X
T3 (Ecopais)	3	59,19	X

Note: Method: 95.0 percentage of LSD

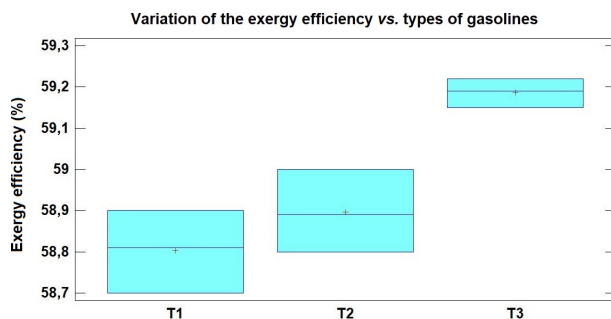


**Figure 8.** Comparative graph of the exergy efficiency for the different types of gasoline

For a better visualization of the results of the energy part, values of energy flow are presented in Table 9, as well as Figures 9, 10 and 11, which represent the Sankey diagrams for the three types of gasoline used. These diagrams represent the quantitative distribution of the energy flows that enter and exit the system, as well as the losses due to heat transfer and emission of exhaust gases.

**Table 9.** Values of energy flow

Energy flow (kW)			
Gasoline	Super	Extra	Ecopais
Fuel	10,38	10,63	11,39
Exhaust Gases	5,58	5,77	6,22
Losses due to convection	3,63	3,72	3,99
Shaft power	1,17	1,14	1,18

With the results obtained it may be concluded that the amount of energy loss in the engine under study when using the Super gasoline is 9.21 kW (88.73 %) as indicated in Figure 9, whereby it was determined that the engine has an energy efficiency of 11.31 % and an exergy efficiency of 58.81 %.

On the other hand, the amount of energy loss in the engine under study when using the Extra gasoline is 9.49 kW (89.28 %) as indicated in Figure 10, whereby it was determined that the engine has an energy efficiency of 10.75 % and an exergy efficiency of 58.89 %.

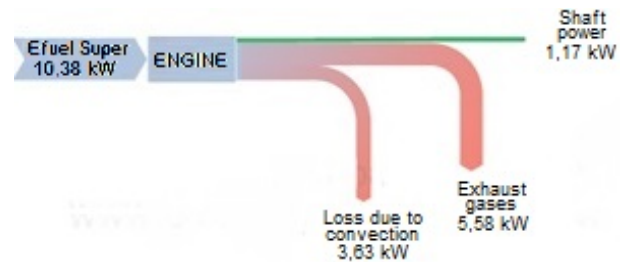


**Figure 9.** Sankey Diagram-Super Gasoline

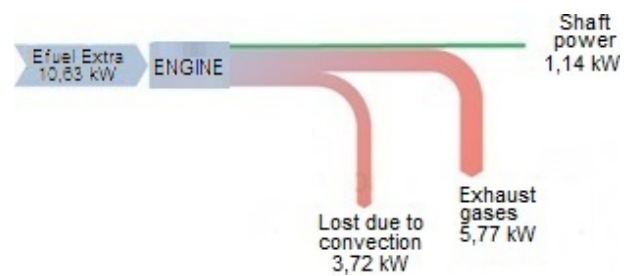


**Figure 10.** Sankey Diagram-Extra Gasoline

At last, the amount of energy loss in the engine under study when using the Ecopais gasoline is 10.21 kW (89.64 %) as indicated in Figure 11, whereby it was determined that the engine has an energy efficiency of 10.39 % and an exergy efficiency of 59.19 %.

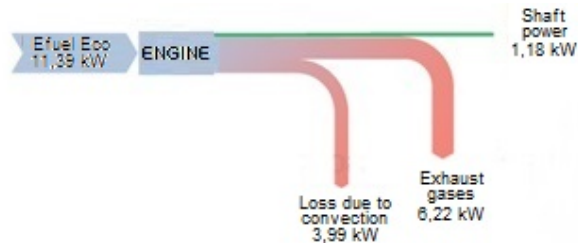


**Figura 11.** Sankey Diagram-Ecopais Gasoline

With the results presented it may be concluded that there are variations in the energy and exergy efficiency in the motor under study when using the three gasolines, the best efficiency of 11.31 % is obtained for the Super gasoline. It is also observed that the largest energy loss of 10.21 kW (89.64 %) exists in the engine for the Ecopais gasoline, this energy loss occurs in the emission of exhaust gases and in the conduction and convection heat transfers, consistent with the results of Llanes-Cedeño, Carguachi-Caizatoa, and Rocha-Hoyos [19], and at the same time this represents a high exergy potential for improvement which may be used to generate work and simultaneously achieve an increase in the energy efficiency of the engine when using the Ecopais gasoline, these results are compatible with the ones obtained by Valle *et al.* [35], where energy losses of 8.57 kW (66.35 %) of a total of 12.92 kW (100 %) were obtained.

#### 4. Conclusions

The static engine which was studied when using different gasolines, shows an energy efficiency of 11.31 % for the Super gasoline, 10.75 % for the Extra gasoline and 10.39 % for the Ecopais gasoline. Regarding exergy efficiency, it was determined as 58.81 % for the Super gasoline, 58.89 % for the Extra gasoline and 59.19 % for the Ecopais gasoline. The exergy efficiency is much greater than the energy efficiency in each of the cases, thus existing an exergy potential for improvement that may take advantage of the exergy being destroyed to transform it into work, and thus achieve an increase in the energy efficiency.

The maximum power of the engine is directly proportional to the energy efficiency, therefore, it may be concluded that the best energy efficiency of the engine was obtained when consuming the Super gasoline, with a maximum power generated of 1183.35 W at 3224 rpm and an energy efficiency of 11.31 %.

Based on the methodology applied, energy efficiencies in the range from 10.39 % to 11.31 % were determined, which are very low compared to the real thermal efficiencies of an internal combustion engine which oscillate between 25 % and 30 %.

#### Referencias

- [1] A. Filho, M. Rodrigues, J. Santos, C. Cunha, and J. a. Donatelli, "Balanço Energético e Exergético de uma Pequena Central Termelétrica Equipada com um Motor de Combustão Interna a Diesel," in *Conference: Iberian Latin American Congress on Computational Methods in Engineering At: Cartagena das Índias, Colombia*, 11 2019. [Online]. Available: <https://bit.ly/3bPazB4>
- [2] E. A. Llanes-Cedeño, Y. Guardia-Puebla, A. de la Rosa-Andino, S. Cevallos-Carvajal, and J. C. Rocha-Hoyos, "Detección de fallas en motores de combustión mediante indicadores de temperatura y presión de inyección," *INGENIUS*, no. 22, pp. 38–46, 2019. [Online]. Available: <https://doi.org/10.17163/ings.n22.2019.04>
- [3] J. D. Ramírez Alzate and A. Arcila Agudelo, *Validación experimental de la relación de compresión para varios combustibles a utilizar en un motor de combustión interna*. Universidad Tecnológica de Pereira, 2017. [Online]. Available: <https://bit.ly/3r5PqJ6>
- [4] E. A. Llanes Cedeño, V. D. Zambrano León, A. S. Cevallos Carvajal, E. R. Mena Mena, and J. C. Rocha Hoyos, *Teoría de selección y dimensionamiento del parque automotor*. Universidad de las Fuerzas Armadas – ESPE, 2017. [Online]. Available: <https://bit.ly/3q7pLYI>
- [5] Ministerio de Electricidad y Energía Renovable, *Balance Energético Nacional 2017*. Gobierno de la República del Ecuador, Ministerio e Electricidad y Energía Renovable, 2017. [Online]. Available: <https://bit.ly/37ZUQOm>
- [6] Erdiwansyah, R. Mamat, M. S. M. Sani, K. Sudhakar, A. Kadarohman, and R. E. Sardjono, "An overview of Higher alcohol and biodiesel as alternative fuels in engines," *Energy Reports*, vol. 5, pp. 467–479, 2019. [Online]. Available: <https://doi.org/10.1016/j.egy.2019.04.009>
- [7] Y. Li, M. Jia, S. L. Kokjohn, Y. Chang, and R. D. Reitz, "Comprehensive analysis of exergy destruction sources in different engine combustion regimes," *Energy*, vol. 149, pp. 697–708, 2018. [Online]. Available: <https://doi.org/10.1016/j.energy.2018.02.081>
- [8] P. Tamilselvan, N. Nallusamy, and S. Rajkumar, "A comprehensive review on performance, combustion and emission characteristics of biodiesel fuelled diesel engines," *Renewable and Sustainable Energy Reviews*, vol. 79, pp. 1134–1159, 2017. [Online]. Available: <https://doi.org/10.1016/j.rser.2017.05.176>

- [9] N. Dolatabadi, M. Forder, N. Morris, R. Rahmani, H. Rahnejat, and S. Howell-Smith, "Influence of advanced cylinder coatings on vehicular fuel economy and emissions in piston compression ring conjunction," *Applied Energy*, vol. 259, p. 114129, 2020. [Online]. Available: <https://doi.org/10.1016/j.apenergy.2019.114129>
- [10] E. A. Llanes Cedeño, J. C. Rocha-Hoyos, D. B. Peralta Zurita, and J. C. Leguísamo Milla, "Evaluación de emisiones de gases en un vehículo liviano a gasolina en condiciones de altura. Caso de estudio Quito, Ecuador," *Enfoque UTE*, vol. 9, pp. 149–158, 06 2018. [Online]. Available: <https://doi.org/10.29019/enfoqueute.v9n2.201>
- [11] E. Castillo Rivera, L. Mora Díaz, E. Gutiérrez Gualotuña, O. Martínez Valdez, P. Tafur Escanta, A. Soria Amancha, A. Villavicencio Poveda, G. Torres Rodríguez, and R. Baldeón López, "Análisis, estudio y modelamiento matemático para la caracterización energética de las gasolinas comerciales en función de los parámetros de calidad referentes a las normas ASTM," *Aporte Santiaguino*, no. 1, pp. 122–137, 2019. [Online]. Available: <https://doi.org/10.32911/as.2019.v12.n1.612>
- [12] M. A. William Fernando, C. P. Galarza Valarezo, and A. López Hidalgo, "Evaluación del consumo específico de combustible y emisiones de gases de escape, con el uso del combustible Eco-país en un motor de combustión interna alternativo," Master's thesis, Universidad del Azuay – Facultad de Ciencia y Tecnología – Escuela de Ingeniería en Mecánica Automotriz, 2017. [Online]. Available: <https://bit.ly/3kB8dd5>
- [13] M. Mofijur, M. G. Rasul, J. Hyde, and M. M. K. Bhuyia, "Role of Biofuels on IC Engines Emission Reduction," *Energy Procedia*, vol. 75, pp. 886–892, 2015, clean, Efficient and Affordable Energy for a Sustainable Future: The 7th International Conference on Applied Energy (ICAE2015). [Online]. Available: <https://doi.org/10.1016/j.egypro.2015.07.211>
- [14] Q. Wang, W. Sun, L. Guo, L. Fan, P. Cheng, H. Zhang, and Y. Sun, "Effects of EGR and combustion phasing on the combustion and emission characteristic of direct-injection CI engine fueled with n-butanol/diesel blends," *Energy Procedia*, vol. 160, pp. 364–371, 2019, 2nd International Conference on Energy and Power, ICEP2018, 13–15 December 2018, Sydney, Australia. [Online]. Available: <https://doi.org/10.1016/j.egypro.2019.02.169>
- [15] X. Wang, B. gang Sun, and Q. he Luo, "Energy and exergy analysis of a turbocharged hydrogen internal combustion engine," *International Journal of Hydrogen Energy*, vol. 44, no. 11, pp. 5551–5563, 2019, the 6th International Conference on Energy, Engineering and Environmental Engineering. [Online]. Available: <https://doi.org/10.1016/j.ijhydene.2018.10.047>
- [16] R. Morgan, G. Dong, A. Panesar, and M. Heikal, "A comparative study between a rankine cycle and a novel intra-cycle based waste heat recovery concepts applied to an internal combustion engine," *Applied Energy*, vol. 174, pp. 108–117, 2016. [Online]. Available: <https://doi.org/10.1016/j.apenergy.2016.04.026>
- [17] M. Razmara, M. Bidarvatan, M. Shahbakhti, and R. D. Robinett, "Optimal exergy-based control of internal combustion engines," *Applied Energy*, vol. 183, pp. 1389–1403, 2016. [Online]. Available: <https://doi.org/10.1016/j.apenergy.2016.09.058>
- [18] K. Venkata Sundar Rao, S. N. Kurbet, and V. V. Kuppast, "A review on performance of the IC engine using alternative fuels," *Materials Today: Proceedings*, vol. 5, no. 1, Part 1, pp. 1989–1996, 2018, international Conference on Processing of Materials, Minerals and Energy (July 29th – 30th) 2016, Ongole, Andhra Pradesh, India. [Online]. Available: <https://doi.org/10.1016/j.matpr.2017.11.303>
- [19] E. A. Llanes-Cedeño, J. B. Carguachi-Caizatoa, and J. C. Rocha-Hoyos, "Evaluación energética y exergética en un motor de combustión interna ciclo Otto de 1.6 L," *Enfoque UTE*, vol. 9, pp. 221–232, 12 2018. [Online]. Available: <https://doi.org/10.29019/enfoqueute.v9n4.365>
- [20] P. Sun, Z. Liu, X. Yu, C. Yao, Z. Guo, and S. Yang, "Experimental study on heat and exergy balance of a dual-fuel combined injection engine with hydrogen and gasoline," *International Journal of Hydrogen Energy*, vol. 44, no. 39, pp. 22301–22315, 2019. [Online]. Available: <https://doi.org/10.1016/j.ijhydene.2019.06.149>
- [21] C. A. Romero Piedrahita, "Contribución al conocimiento del comportamiento térmico y la gestión térmica de los motores de combustión interna alternativos," Ph.D. dissertation, Universitat Politècnica de València, 2009. [Online]. Available: <https://doi.org/10.4995/Thesis/10251/4923>
- [22] R. Hernandez Sampieri, *Metodología de la investigación: las rutas cuantitativa, cualitativa y mixta*. McGraw-Hill Interamericana, 2018. [Online]. Available: <https://bit.ly/2O8xoHE>
- [23] J. C. Rocha-Hoyos, L. E. Tipanluisa, V. D. Zambrano, and A. A. Portilla, "Estudio de

- un motor a gasolina en condiciones de altura con mezclas de aditivo orgánico en el combustible,” *Información tecnológica*, vol. 29, pp. 325–334, 10 2018. [Online]. Available: <http://dx.doi.org/10.4067/S0718-07642018000500325>
- [24] Q. he Luo and B. gang Sun, “Experiments on the effect of engine speed, load, equivalence ratio, spark timing and coolant temperature on the energy balance of a turbocharged hydrogen engine,” *Energy Conversion and Management*, vol. 162, pp. 1–12, 2018. [Online]. Available: <https://doi.org/10.1016/j.enconman.2017.12.051>
- [25] M. Krishnamoorthi and R. Malayalamurthi, “Availability analysis, performance, combustion and emission behavior of bael oil - diesel - diethyl ether blends in a variable compression ratio diesel engine,” *Renewable Energy*, vol. 119, pp. 235–252, 2018. [Online]. Available: <https://doi.org/10.1016/j.renene.2017.12.015>
- [26] V. Karthickeyan, “Effect of combustion chamber bowl geometry modification on engine performance, combustion and emission characteristics of biodiesel fuelled diesel engine with its energy and exergy analysis,” *Energy*, vol. 176, pp. 830–852, 2019. [Online]. Available: <https://doi.org/10.1016/j.energy.2019.04.012>
- [27] C. H. Rufino, A. J. T. B. de Lima, A. P. Mattos, F. U. M. Allah, J. L. L. Bernal, J. V. Ferreira, and W. L. R. Gallo, “Exergetic analysis of a spark ignition engine fuelled with ethanol,” *Energy Conversion and Management*, vol. 192, pp. 20–29, 2019. [Online]. Available: <https://doi.org/10.1016/j.enconman.2019.04.035>
- [28] INEN, “Vehículos automotores. Bus urbano. Requisitos, NTE INEN 2 205:2010,” Instituto Ecuatoriano de Normalización, Norma Técnica Ecuatoriana, Tech. Rep., 2010. [Online]. Available: <https://bit.ly/3bPTIU1>
- [29] V. Kolanjiappan, “Reduction of amine and biological antioxidants on NOx emissions powered by mango seed biodiesel,” *Revista Facultad de Ingeniería Universidad de Antioquia*, no. 84, pp. 46–54, Sep. 2017. [Online]. Available: <http://doi.org/10.17533/udea.redin.n84a06>
- [30] Y. Guardia-Puebla, J. Márquez-Delgado, V. Sánchez-Girón, E. A. Llanes-Cedeño, J. C. Rocha-Hoyos, and D. B. Peralta-Zurita, “Mejoras a la asignatura diseño estadístico de experimentos para estudiantes de la carrera de Ingeniería Mecánica,” *Revista Espacios*, vol. 39, no. 30, 2018. [Online]. Available: <https://bit.ly/3b5M5UK>
- [31] A. Guzmán, E. Cueva, A. Peralvo, M. Revelo, and A. Armas, “Estudio del rendimiento dinámico de un motor Otto utilizando mezclas de dos tipos de gasolinas Extra y Súper,” *Enfoque UTE*, vol. 9, pp. 208–220, 12 2018. [Online]. Available: <https://doi.org/10.29019/enfoqueute.v9n4.335>
- [32] A. I. Quimbita Panchi and E. X. Guallichico Sun-tasig, “Determinación del potencial energético y mecánico del motor Mazda F2 al utilizar los tipos de gasolina comercial empleados en el Ecuador,” Master’s thesis, Universidad de las Fuerzas Armadas – ESPE, 2017. [Online]. Available: <https://bit.ly/3kCcddd>
- [33] E. V. Torres González, R. Lugo Leyte, H. D. Lugo Méndez, L. E. Méndez Cruz, J. A. González Andrade, and I. E. Hernández Mora, “Evaluación del desempeño de un motor de gasolina mediante el análisis energético y exergético,” in *Memorias del XXXVII Encuentro Nacional de la AMIDIQ, Jalisco, México*, 2016, pp. 49–54. [Online]. Available: <https://bit.ly/2NU95NV>
- [34] O. Rosendo Llerena, “Análisis energético, exergético y económico de un sistema de cogeneración: Caso para una planta azucarera de San Pablo,” *INGENIUS*, no. 19, pp. 29–39, 2018. [Online]. Available: <https://doi.org/10.17163/ings.n19.2018.03>
- [35] A. Erazo, M. Ribeiro Batista, C. E. Tuna, C. L. Vorobieff, and J. Silveira, “Análisis energético, exergético y ecológico aplicado en un motor de combustión interna de pequeño porte accionado con biogas,” in *XI Latin-American Congress on Electricity Generation and Transmission*, 2015. [Online]. Available: <https://bit.ly/3r6qMs0>



# CONVERGENCE AND NUANCES OF NET NEUTRALITY IN SOUTH AMERICA

## CONVERGENCIA Y MATICES DE LA NEUTRALIDAD EN LA RED EN AMÉRICA DEL SUR

Roberto D. Triviño<sup>1,\*</sup> , Antonio Franco-Crespo<sup>2</sup> , Leonardo Ochoa-Urrego<sup>3</sup> 

Received: 08-07-2020, Received after review: 04-12-2020, Accepted: 03-02-2021, Published: 01-07-2021

### Abstract

The Internet has become the ultimate platform for convergence, closely associated with network, technology, and media, due to its open and nondiscriminatory architecture. Convergence in telecommunications is propelled by ideas, ideologies, and policies progressively and cyclically, bringing further technological advancement, market, business, and policy changes. As a response to convergence, net neutrality seeks to regulate the relationship between Internet service providers and users to avoid discriminatory practices and ensure the openness of the Internet as a platform for innovation, economic development, and access to information for all. The objective of this work is to analyze the development of convergence in the telecommunications sector and the progress of net neutrality policies in South America, with five specific cases using a qualitative empirical approach. Within the findings, we identify different approaches for legislating net neutrality, controversies concerning the levels of commitment to the principles, ambiguity for effective enforcement of the rules, and commercial arrangements that in practice violate net neutrality.

**Keywords:** internet, net neutrality, convergence, telecommunications, South America

### Resumen

El Internet se ha convertido en la plataforma definitiva para la convergencia, estrechamente asociada con las redes, la tecnología y los medios, debido a su arquitectura abierta y no discriminatoria. La convergencia en las telecomunicaciones es impulsada por ideas, ideologías y políticas de manera progresiva y cíclica, lo que genera más avances tecnológicos, cambios en el mercado, los negocios y las políticas. Como respuesta a la convergencia, la neutralidad en la red busca regular la relación entre los proveedores de servicios de Internet y los usuarios para evitar prácticas discriminatorias y asegurar un Internet abierto como plataforma de innovación, desarrollo económico y acceso a la información para todos. El objetivo de este trabajo es analizar el desarrollo de la convergencia en el sector de las telecomunicaciones y el avance de las políticas de neutralidad en la red en América del Sur, con cinco casos específicos utilizando un enfoque empírico cualitativo. Dentro de los hallazgos, se identifican diferentes enfoques para legislar la neutralidad en la red, controversias sobre los niveles de compromiso con los principios, ambigüedad para la aplicación efectiva de las reglas y acuerdos comerciales que en la práctica violan la neutralidad de la red.

**Palabras clave:** Internet, neutralidad en la red, convergencia, telecomunicaciones, América del Sur

<sup>1,\*</sup>Departamento de Eléctrica y Electrónica, Universidad de las Fuerzas Armadas, Sangolquí, Ecuador.  
 Autor para correspondencia ✉: rdtrivino@espe.edu.ec.

<sup>1</sup>Programa de Doctorado en Gestión Tecnológica, Escuela Politécnica Nacional, Quito, Ecuador.

<sup>2</sup>Facultad de Ciencias Administrativas, Escuela Politécnica Nacional, Quito, Ecuador.

<sup>3</sup>Facultad de Ciencias Administrativas, Económicas y Contables, Universidad Central, Bogotá, Colombia.

Suggested citation: Triviño, R. D.; Franco-Crespo, A. and Ochoa-Urrego, L. (2021). «Convergence and nuances of Net Neutrality in South America». INGENIUS. N.º 26, (july-december). pp. 30-40. DOI: <https://doi.org/10.17163/ings.n26.2021.03>.

## 1. Introducción

Convergence, in general, refers to the trend or phenomenon where two or more independent technologies, services, or networks integrate and form a new outcome [1]. The term is often thought of as something new, but regulatory and technological convergence has been ongoing in the history of telecommunications. A discussion of convergence in telecommunications in isolation is difficult because is closely associated, with technological, media and network convergence as is shown in Figure 1. Thus, convergence in network, technologies, and media is at the basis of change in innovative offers and new business models in the telecommunications sector; but also, has been facilitated by the opening up of markets to competition, the digitalization of content, the emergence of Internet Protocol, and the adoption of high-speed broadband. This evolution leads to move the classic telecommunication and broadcast environments towards an open and integrated programmable broadband network environment.

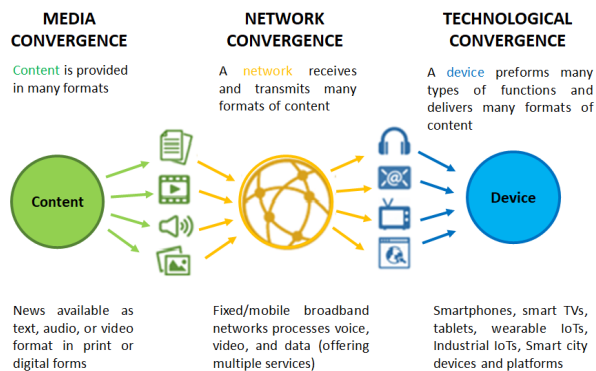


**Figure 1.** Relationships between technological, media, and network convergences [1]

On the other hand, the growing role of the Internet in the economy and society has enhanced the process of convergence and its rate of change. Although large telecom operators have played a role in the process, new market players have moved rapidly, and often in an unpredictable way, adopting different market models from traditional telecommunication firms. Traditional services (voice and video) are delivered over IP networks and the development of new platforms is facilitating the provision of converged services. In the last years new digital content distributors, such as Over the Top - OTT providers (e.g., Video: Netflix, Amazon video and HBOGo; Audio: Spotify, Deezer; Message: WhatsApp, and Line), now coexist and compete with traditional providers and network access operators, to deliver content and services on Internet [2]. Moreover, a growing number of operators are also focusing on mobile content to offer music, video, or access to applications and online services from mobile devices.

These changes are often taking place as a result of an increasing number of users creating and exchanging their own content on a multiplicity of devices.

Convergence is happening today in South America and tests traditional business models, generates competition between platforms, pressures traditional operators, changes consumer behavior and demand for services, leading to dynamic technology management processes. In turn, these technological and market changes put pressure on regulatory agencies as a challenge to adapt them to the new converging service environment, due to the one-to-one relationship with a regulatory entity is no longer clear, and it may create a new sector where a regulatory entity has not been identified.

In the era of convergence and expansion of network services, it is important to study the impact of policies related to the Internet. Issues such as universal access to network services, freedom to communicate, diversity of the content market, competitiveness, innovation, and the promotion of economic benefits are mayor concerns underlying the debate in the new environment in South America.

Thus, the growing convergence between the telecommunications, communication and media sectors, together with the possibility to (1) transmit different services, content, and applications over the same networks, without major costs for infrastructure owners, operators, or users, and (2) the transmission to different types of terminals without privileging or discriminating content or formats, is precisely the essence of the origin of the debate on Net Neutrality – NN. The term was introduced by Wu [3], and refers to the principle that all Internet data should be treated equally without any discrimination or restriction, independent of the origin and destination, type, content, device, service, or application [3, 4].

The purpose of the NN rules is to ensure that the network infrastructure is neutral by prohibiting internet service providers – ISP block, slow-down, or prioritize traffic [3]. Moreover, traffic management measures should be reasonable, transparent, non-discriminatory, and proportionate, based on objective technical differences, according to legal provisions in place in some countries [5].

The NN has emerged as an important convergence policy tied to technological innovation, economic development, and information access. In the last years, many governments have analyzed the role of those who control the access infrastructure and Internet traffic for their benefits and defined the NN differently in their policies, laws, and regulations [6]. The debate centers on the potential consequences of network owners exercising additional control over traffic in their networks [7].

The analysis of the NN debate and the role of regulators has reached national levels. Country regula-

tors have taken varied positions about NN generating controversies and pressures about what should be considered reasonable Internet traffic management - ITM in a converging world, the type of regulation that should be applied, and control mechanisms to enforce the regulation. All this, have forced government authorities to analyze the conditions offered by ISPs, the responsibilities with their customers, but also its rights to remain free of responsibility for the content, and services that may be considered illegal by third parties [8]. On the other hand, the controversies are concentrated on the degree of freedom that a provider must have to implement ITM techniques, which can discriminate specific data over their networks. Although it may seem a purely technical problem, the ITM is more complex, it might lead to discriminatory practices, in case providers block or degrade online services that compete with their services, also has enormous social, legal and economic implications, which may limit the freedom of expression, access to information, competitiveness, and innovation [9].

The changes caused by the convergence are not unknown to the countries of South America, several countries in the region have already adopted laws that ensure the principle of NN. Thus, the objective of this work is to discuss the progress on NN as a convergence policy and its developments in five South American countries to see where they stand on the NN debate. Even though there are a few studies about NN implementation for countries in South America [9, 10] they are neither comprehensive nor up-to-date. As the States must guarantee the validity of this principle through appropriate legislation, we compare the differences between the regulations/laws in each of the researched countries.

## 2. Materials and methods

This study relies on an approach that is largely empirical, based on qualitative tools to support the tracing of the NN initiatives in five countries from South America. These countries have been selected in order to generate a rich array of findings from a limited number of cases. The methodology employed for data gathering includes document analysis and archival research comprising: reports and other documents that depict the historical evolution of the NN; content of websites and other relevant documents produced within the context of each initiative studied here. We use a qualitative approach, because there is a need to explore and describe the phenomenon of the convergence, NN and the development of the principle in South America.

### 2.1. The Telecom Convergence

Historically, in the traditional telecom world, distinct communication networks and their underlying tech-

nologies provided voice, data, radio, and television services. The initial concept of telecommunications, which was based on telephony and diffusion of video and audio, is being replaced by a completely new approach where different types of separate networks for different services have converged to a single network.

Today, communication networks are shifting towards IP based solutions that, together with broadband and developments in terminal devices, allow access to IP based applications on a multitude of devices, in a multilayered process that can be termed convergence.

Telecommunication networks have grown over the last century to become the global infrastructure that it is today. In 2019, there were over 5.19 billion unique mobile phone users worldwide, and Internet has grown to also become a global communications infrastructure that reaches 59% of the world population (4.54 billion people). That same year, South America was the subregion that had the largest Internet penetration rate, with 73% of the population having access to this service [11].

Convergence between traditional telecommunication operators and content providers (e.g. audio and video streaming), has introduced an increasing number of new products and services available on the Internet, and users access them according to their own needs at any time and anywhere. Convergence is encouraging competition, mobility, collaboration, interoperability, content creation, and product and service innovation. At the same time, however, it poses new challenges for businesses, consumers, and governments in the South American region, which fall into three major categories: (1) disruptions of the traditional communications industry, (2) increased choice and new vulnerabilities for consumers, and (3) regulatory boundaries have become less clear.

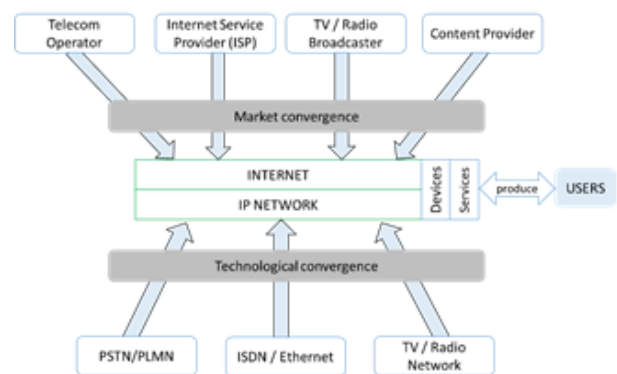


**Figure 2.** . Convergence of telecommunication to IP base networks and services

Digitalization, technological innovation, and increased connectivity have fused previously separated value chains (e.g., telecommunications/broadcasting)

into mixed-value chains of access, which include content distribution service and device providers [12]. Convergence has encouraged the upgrading and remixing of new configurations of products and services and the nature of media consumption. Even, the emerge of the OTT players has profound implications for the telecoms and broadcasting industries, these new business models have removed the old boundary between fixed/wireless and cellular connectivity, and between broadcasting and Internet services.

On the other hand, the users now have greater control over what they want to access, where, and when on the Internet. They are taking a more active role, creating their content and services (e.g. using YouTube, Instagram, Twitter, or developing apps). The increased availability of broadband and convergence has resulted in the “on-demand” market, which is connecting consumers and producers directly and customizing goods and services.

Before convergence, regulators use to deal only with a few traditional players in specific sectors, but now has eliminated the traditional segmentation of telecom services, with a more integrated value chain, new participants and competition on a global scale; also has given rise to new models for content and services, where users have gained the ability to access them over different networks and devices, and interact with multiple providers using the Internet, as a result, there are new players from different sectors to deal with, reducing regulators’ ability to impose and enforce regulations (see Figure 2). This requires a review of the regulatory approach and levels of intervention, together with greater institutional coordination and flexibility.

Consequently, changes in the telecommunications sector, particularly the exponential growth of Internet traffic, create tensions between regulation and the competitive supply of services in certain segments of the network. In other words, as broadband speeds increase and the networks become more capable of delivering added-value services, policymakers will have to rethink their traditional approaches to deal with issues related to, for example, adapting their management models to convergence trends, treatment of bundles and convergent offers, and Internet openness [12], a function that involves ensuring effective competition, managing scarce resources and protecting consumers’ rights.

## 2.2. Net neutrality

The Internet’s decentralized nature and openness to new devices, applications, and services have played an important role in advancing convergence and in its success in fostering the free flow of information, innovation, creativity, and economic growth. This openness responds to the continuously evolving interaction and independence from the Internet’s various technical com-

ponents, which enable collaboration and innovation while continuing to act independently of one another. At the international level, the roles, openness, and competencies of the global multi-stakeholder institutions that govern standards for different layers of Internet components have served to expand the decentralized networks that the Internet is made up of today. At the national level, multi-stakeholder arrangements for governing the Internet are also advisable. Moreover, is important to maintain technology neutrality and appropriate quality for all broadband networks and services to ensure an open and dynamic Internet environment [12].

Broadband networks are a key platform for innovation, economic opportunities, and civic engagement. The extent to which these networks are open to facilitating these objectives has thus become the main concern for all stakeholders and requires a review of the regulatory approach and levels of intervention, together with greater institutional coordination and flexibility. In the actual increasingly converged environment, ISPs have become gateways for content and applications, as they control content providers’ final access to consumers. In this scenario, the role played by those who manage the access infrastructure generates a great debate on the application of the principles of openness and non-discrimination at the transport level, and if it should be regulated or not [7], [13] as a means to protect access, innovation and competition on the internet [14].

Around the world, government authorities have been forced to analyze the conditions offered by ISPs and the responsibilities they have with their customers and the free competition. Thus, NN has advanced from thwarted regulatory proposal to actual regulatory action in several advanced and developing nations [15], where have incorporated issues relating not only to traffic management but also to topics such as transparency in the provision of services, the blocking of harmful content, data protection, privacy and service quality. About it, until 2015 both the regulatory frameworks of the European Union and the Open Internet rules proposed by the Federal Communications Commission - FCC of the United States - USA, had also protected this principle, and indicated that NN is a subject of great importance and have a broad regulation scope to guarantee the Internet’s open state [8], [16]. However, in December 2017, the FCC voted to repeal the 2015 NN rules. This decision came into effect in June 2018, rolling back the 2015 rules: blocking, throttling, and paid prioritization.

## 2.3. Net neutrality in South America

NN is becoming increasingly important as the global debate intensifies and governments worldwide implement and withdraw regulations. Many countries in South

America already have implemented similar rules. These countries have a middle or middle-high percentage of Internet penetration, variable uses focused in big cities, predominant mobile Internet (two or more mobile operators offering content), and content and application providers - CAPs charged by ISPs in violation of NN that could result in lower prices to users and higher adoption of Internet applications and services [17].

Given the multilayered convergence of networks and services, policymakers in South America could have incentives to apply diverse rules when increasing access is a priority. Thus, they are reassessing their policy and regulatory frameworks to adjust them to current and future developments, and appear to be inclined to layout principles to ensure NN. Based on the rationales given by the initial countries to do so, they see NN as essential to stimulate competition, promote innovation and ensure that consumers can access any lawful content or service provided over the Internet [18]. On NN issues in South America, we concentrate in five countries. Notably, Argentina, Chile, Brazil, Colombia, and Ecuador, have taken decisions to prohibit blocking, throttling, and paid prioritization by ISPs; while others are carrying out consultations or still debating on the topic [12].

### 2.3.1. Chile

In 2010, Chile was among the first countries to enact a specific law to protect NN. The Network Neutrality Act, Law No. 20.453/2010, specifies the NN principle and its exceptions in Article 24H, paragraph A, that (1) promotes transparency by asking for the publication of the characteristic of Internet access, speed, and quality; (2) guarantees of the service; and (3) prohibits blocking, interfering, discriminating or disrupting any content, application or legal service [15]. In this sense, ISPs must offer to each user connectivity and Internet access without distinguishing arbitrarily content or applications based on source or ownership, considering the different configurations in the access contracts [9], [19].

The Act adopts a flexible view of traffic discrimination, letting providers take actions for network and traffic management, but without affect free competition. In 2013, the Secretariat of the Ministry of Transport and Telecommunication - SUBTEL, promulgated Decree No. 368 [20] which forbids the arbitrary blocking of the Internet's content, but according to article 7, traffic shaping is regulated, but not forbidden [9]. ISPs only can affect the quality or execute actions for the traffic shaping and net management, as long as those actions do not affect the free competition, privacy and it is informed through a clear publication.

It is important to mention that, despite the existence of the Law and decree, since 2013 several telecom companies were accused by civil organizations of slow-

ing down applications, and specific contents without justify these practices [9]. There is evidence of the absence of control of the obligations from the law, either due to a lack of technical capacity or political will [21]. In a 2015 report in counterpart, statistics about the level of compliance of the law were presented [22]; it showed around 40 charges between 2011 and 2015 but did not indicate to what type of noncompliance it refers [19].

In recent years non-observance issues are maintained [23], especially with mobile operators that offer access to specific applications and contents with zero rating - ZR, as a sales strategy. For content providers, these strategies undermine free competition and the NN, however, regulatory agents mention that commercial aspects such as ZR offers do not arbitrarily distinguish contents, based on source or owner, and therefore does not apply discrimination since users can still access content and Internet. This interpretation seems to favor the idea that technical aspects must meet the Law, and on the contrary, commercial aspects would be outside the scope of the obligations [19]. So, the SUBTEL only requires to telecom companies and ISPs to eliminate from their plans the so-called free access to applications and content [23, 24].

Since 2018, based on the rollback of the NN rules in the USA, the debate continues and the SUBTEL has set up working groups with the multi-stakeholders to analyze the ZR, OTT services and implications of the USA decision considering that is a power in terms of content generation, as well as hosting 80% of the world's information and data [24, 25].

### 2.3.2. Colombia

The legislation that addresses the NN is contained in the Article 56 of the Law No. 1450, Chapter II and established the ISPs may not block, interfere with, discriminate against, or restrict the right of any Internet user to use, send, receive or offer any licit content, application or service on the Internet [9], [15] regardless on the origin or ownership. The law also sets the way to make offers according to the needs of the market segments, based on the use and consumption profiles of users, and this shall not be understood as discrimination. Other aspects specify the right of users to (1) use any class of legal devices in the network; (2) be offered parental control services for content that violates the law; (3) the transparency of the information about characteristics and guarantees of the service; (4) have mechanisms to preserve the privacy of users against viruses and network security; and only block access to specific content upon express request of the user [26].

In addition to the Law, Resolution 3502 of Colombia's regulator, passed in 2011 generating criticisms from users, experts, and civic organizations who found in the text of the rule, inaccuracies, gaps, and ambi-

guities that could give operators a way of avoiding certain aspects of the NN. For some critics [27] the controversies in that process were due to the absence of the participation from civil society and academia, and therefore the vision of the operators influenced its development. The resolution itself allows providers to offer Internet access services for a price according to the needs of the market, that is, to offer plans based on contents and applications the ISPs want to offer, through third parties, ZR, or vertical integration. Also allows the implementation of reasonable and non-discriminatory traffic management by establishing quality of services - QoS levels and prioritize traffic types according to latency and delay for access to the Internet, and clarify the conditions for content blocking due to security reasons which meet technical requirements or standards adopted [28]. Aspects banned or controlled in other NN laws [29].

The exception on Internet plans limited by content makes the resolution itself not faithful, ambiguous, and directly contradicts the Law since to limit content, applications, or services according to market deals or consumption profiles is to discriminate or prioritize the data, and make available a "reduced Internet" [19], [27]. Finally, Resolution 3502 regulates the relationship of consumers with ISPs, but not with content or application providers [15].

The Colombian Ministry of ICT started in 2016 multi-stakeholder consultations to develop a new policy and regulatory framework for telecommunications and broadcasting to deal with convergence in communications markets [9]. Nowadays, Colombia has formulated the project "The role of OTT services" within the initiatives of the Regulatory Agenda 2018-2019 to review regulatory trends for the digital economy, where shall analyze and complement the regulatory framework on NN that allow offers and market prices oriented to costs, protection of consumers interests, as well as updating the operating license conditions of existing operators and service providers [30].

### 2.3.3. Brazil

In 2014, after almost five years of debate, the Brazilian Congress passed the Marco Civil da Internet - MCI, Law No. 12.965/2014 which, among consolidating rights, duties, and principles for the use and development of the Internet in Brazil, enshrined the principle of NN and privacy of Internet users [8]. Its importance lies not only in its principles but also in the way in which it was drafted, based on an open, public, and collaborative consultation process, implemented across the country that helped to construct the text of the Law.

The law sets (1) the of transparency of information, by asking providers for clear and complete information on service contracts, including details of the data

protection, mitigation, and network management; (2) non-blocking, by affirming that the providers must treat, on an isonomic basis any data packages, regardless of content, origin and destination, service, terminal or application; and (3) for anticompetitive practices, by offering services in non-discriminatory commercial conditions [15].

The law goes on to prohibit traffic discrimination or degradation, which can only be implemented as a result of essential technical requirements, and prioritization of emergency services. The Decree No. 8.771/2016 defines the "essential technical requirements" as network security issues, and exceptional situations of congestion or interruption; while "emergency services" as communications destined to the emergency services providers, or communications to inform the population in situations of disaster, emergency risk or state of public calamity [31]. The Decree also sought to regulate that commercial relations between the infrastructure operator - IO and the actors of the logical layer cannot "compromise the public and unrestricted character of Internet access", "prioritize data packages due to commercial arrangements" or privilege applications offered by the IO [19].

The MCI is considered one of the most advanced laws in the world and shows a major effort to adapt fundamental rights and freedoms to the digital world, incorporating aspects to eliminate ambiguities and violations towards the NN that have the potential to stop innovation and competition. As a novelty, the decree prohibits ZR strategies, includes a tripartite system to supervise, and determines that content companies must have legal headquarters in Brazil [32]. However, when in 2018 consumer associations and other civil society organizations evaluate ZR practice as negative and claim that violate NN, private operators and regulatory agents have claimed that NN was specifically limited to the logical level and infrastructure of the Internet, so the market practices do not violate NN [33, 34].

### 2.3.4. Ecuador

The new Telecommunications Act in Ecuador - LOT, enacted in 2015, embraces the opportunities of convergence and stipulates in its Article 12 that the state will "propel the establishment and exploitation of telecommunication networks and services that promote the convergence of services, in conformity with public interests and with the dispositions of the Act and its normative" [12], [15]; also included clauses specifically addressing the NN and its promotion (Article 3 and 4); and the rights that subscribers, customers, and users of telecommunications services have, indicating that they can access to any application or permitted service available on the Internet (Article 22).

The Act prohibits blocking, throttling, prioritizing or restricting the user's right to use, send, receive or offer any legal content, applications, or service through the Internet, their networks, or other ICT technologies. Also forbids to limit the right to incorporate or use any class of equipment or device on the network, whenever legal, except for cases established under the legal framework and those in which the competent authority decides, or when the client, subscriber or user expressly demands the limitation or blocking of content. Providers are allowed to carry technical actions to manage their networks when considered necessary, and within the exclusive scope of its activities to guarantee the provision of service [35].

According to the new Act, the regulator body AR-COTEL will be responsible for regulations and norms that allow the provision of multiple services on the same network to drive, in an effective manner, the convergence of services and assist with the technological development in the country, following the principle of NN [12]. However, the LOT has omissions such as: not defining what NN is, using the concept issued by the ITU, which is ambiguous and not very applicable. It also ignores the meaning of the principle and allows the Art. 66 of the Law, in which service providers establish "tariff plans constituted by one or several services, or products of service." Besides, unlike the policy that previously defined the NN (TEL-477-16) [36], which included the concepts of non-discrimination, these have not been included in the Law; all those aspects violate the NN and leaves users defenseless against the potential abuses from providers [37]. As an example, there was a lawsuit against mobile operators for offering unlimited and free WhatsApp service, but these offers did not include the voice call functionality that normally is integrated. Regarding the situation, the Minister of Telecommunications stated that this practice of not including that function in WhatsApp's ZR packages went against the principle of NN and will investigate the facts and take actions [38]. However, even today mobile operators still offer unlimited use of some services and certain applications along with their limited data plans.

### 2.3.5. Argentine

In 2014, the Law 27.078 "Argentine Digital Law" passed, this new law governs telecommunication in the country and replaces the National Law of Telecommunications 19.798 / 72 and Decree 764/00 [36], [39]. The law was an important update and established the state must ensure quality, accessibility, and affordability to the Internet. It also must guarantee the ICT services and ensure their conditions of quality, affordability, and at fair and reasonable prices, encouraging competition between service providers so that consumers can choose the best for them. Article 1 established

and guarantee NN as an objective, while Article 56 states the rights of users to access, use, send, receive, or offer any content, application, service, or protocol without any restriction, discrimination, distinction, blocking, interference, obstruction, or degradation, [40] and Article 57 prohibits ICT operators (1) to block or discriminate access or use of any content, application, or service except by court order; (2) set the price of Internet access by virtue of its content, services, or applications; and (3) arbitrarily limit the user's right to use any hardware or software to access the Internet, as long as those actions do not affect or harm the network.

Although the law was modified in 2015 by the Decree of Necessity and Urgency 267/2015, the changes did not modify the provisions of articles 56 and 57 about NN. However, it generated controversies and criticisms, due to the Law itself ensures ICT services that in practice should be Internet, content, or application providers, but in its disaggregation, it seems to only refer to ISPs. Also, neither the zero-rating aspects are specified nor do procedures to ensure NN [11], issues that undermining free competition.

Since 2017 mobile operators have been offering free traffic for some applications and services, within this strategy providers paid third-party services to position their offer, and even one of them, integrated vertically, favored its content. This practice is an obstacle for other existing applications it creates an entry barrier for new ones, affecting competition and innovation [40]. Finally, it is important to note that in 2018 there was a lawsuit between operators claiming that a video ZR application of one of them, during the Soccer World Cup, violated the NN. The regulatory agent concluded that the promotion of that application was tolerable as long as it is applied to other similar applications as well [40]. This implies that the Argentine regulator is not independent or impartial, being more permeable to the interests and competition of companies.

## 3. Results and Discussion

The NN is an example of a response to convergence since it is a principle to regulate the relationship between ISPs and users to avoid discriminatory practices over services or applications. Although regulations/laws related to NN have been introduced in South America, their implementation may vary for fixed or mobile networks. Table 1 shows the list of differences among the regulations/laws in the five countries.

The review shows that the different rules in South America focus on access, transparency of information, the arbitrary non-discrimination of the content or services, and the exceptions to the principle. However, most of the time, the ITM practices or terms of services are not clear, as is mentioned in [23], [36].

**Table 1.** Policies Comparison among countries

Article	Countries				
	CH	BR	CO	EC	AR
NN definition and concepts	•	•	–	–	–
Guarantees to access/use of services/ content	•	•	•	•	•
Prohibits to block or discriminate access/use	•	•	•	•	•
Transparency of the Information	•	•	•	•	•
Use of HW to access	•	•	•	•	•
Set price by content, service or market	–	▲	•	•	▲
Implement ITM techniques	•	▲	•	•	•
Exceptions (technical requirements, emergency)	–	•	–	–	–
Zero Rating	▲	▲	–	–	–
Control of the obligations	•	•	–	–	•

• Specified, – Not Specified, ▲ Prohibits

The integration of multiple legal devices in the network is allowed as long as they do not affect its quality. However, the laws seek to establish exceptions to allow ITM and QoS to users, pending between reasonableness criteria and exceptions explicitly placed in policies. Thus, allow ISPs to interfere with Internet traffic arbitrarily and discriminate or even block new services or platforms (Industry 4.0, OTT, or IoT devices) for commercial or technical reasons. Thus, ITM practices should be transparent since they can significantly affect end-users [41].

The level of compliance with the laws has problems with repeated transgressions [22]. ZR is an example of how NN may be affected, especially in the mobile Internet service, through which companies offer access to specific applications without constituting an expense in the user’s data plan [42]. Since it is not possible to do so without the necessary discrimination of data by origin, destination, or content, this practice acts against the basic NN principles [33], [38]. These plans are offered in the five analyzed countries, creating captive consumers, even when in some of them, this practice is banned [34], [42].

#### 4. Conclusions

Nowadays, convergence plays an important role in society. It can influence how governments develop ap-

propriate policy while looking for social welfare and enterprises competition with new value-added products and services. However, convergence has raised several issues like interoperability, interconnection, neutrality, policy and regulatory framework, consumer rights protection, and nondiscrimination universal access.

Although in South America each nation has a specific market need to deal with, they must adapt. We identified that the five countries demonstrate different approaches to legislating NN and offer the opportunity to examine the relationship between forms of NN legislation and the extent to which it is compromised by traffic management measures or commercial aspects (e.g., ZR).

In theory, ZR constitutes a violation of NN. By extension, ZR may also impede innovation, competition and free speech. Even when it could help to overcome cost barriers to realize the valued goal of increasing Internet penetration in the region, also could locking users into ‘walled gardens’ of content. Thus, regulatory agencies should be cautions that any commercial arrangements should be designed in a manner that ensures the least possible intrusion into the principle of non-discriminatory pricing. On the other hand, this particular topic within NN represent a thorny public policy challenge and needs further research in the region.

Finally, the development of the approaches to implement the NN principle and the number of nations adopting this principle confirms its importance. Regarding the limitations of this research, the data on the NN policies in the five countries examined here represents a snapshot in time, and the available insights are accordingly restricted. Longitudinal studies are needed to assess the impacts of the NN rules on access, innovation, and competition over time. What is also required are studies on ITM practices that should be transparent, regardless of regulations, and large-scale studies that probe the habits of mobile internet users. These would help us better understand the effect of the NN rules, ZR practices, Internet patterns of use, and propose a new regulatory approach in the region.

#### References

- [1] S. E. Park, “Technological convergence: Regulatory, digital privacy, and data security issues,” Congressional Research Service, Tech. Rep., 2019. [Online]. Available: <https://bit.ly/306086z>
- [2] M. Gendler, “Neutralidad de la red y servicios over the top: una compleja relación en el ecosistema de telecomunicaciones,” *PAAKAT: Revista de Tecnología y Sociedad*, vol. 0, no. 17, 2019. [Online]. Available: <http://dx.doi.org/10.32870/Pk.a9n17.362>

- [3] T. Wu, “Network neutrality, broadband discrimination,” *Journal on Telecommunications and High Technology Law*, vol. 2, no. 1, 2003. [Online]. Available: <https://bit.ly/3rqaESO>
- [4] ITU, “Trends in telecommunication reform,” International Telecommunication Union (ITU), Tech. Rep., 2013. [Online]. Available: <https://bit.ly/3bVcbct>
- [5] V. Stocker, G. Smaragdakis, and W. Lehr, “The state of network neutrality regulation,” *ACM SIGCOMM Computer Communication Review*, vol. 50, no. 1, pp. 45–59, Mar. 2020. [Online]. Available: <https://doi.org/10.1145/3390251.3390258>
- [6] J. Barata Mir, “El concepto de net neutrality y la tensión entre regulación pública y autorregulación privada de las redes,” *IDP. Revista de Internet, Derecho y Política*, no. 13, pp. 44–52, 2012. [Online]. Available: <https://bit.ly/3e62Ykk>
- [7] J. Krämer, L. Wiewiorra, and C. Weinhardt, “Net neutrality: A progress report,” *Telecommunications Policy*, vol. 37, no. 9, pp. 794–813, 2013, papers from the 40th Research Conference on Communication, Information and Internet Policy (TPRC 2012) Special issue on the first papers from the ‘Mapping the Field’ initiative. [Online]. Available: <https://doi.org/10.1016/j.telpol.2012.08.005>
- [8] European Union, *Official Journal of the European Union L 310*, 2015, vol. 58. [Online]. Available: <https://bit.ly/3qaPAgX>
- [9] P. A. Vargas-Leon, *Net Neutrality: An Overview of Enacted Laws in South America*. Cham: Springer International Publishing, 2016, pp. 109–126. [Online]. Available: [https://doi.org/10.1007/978-3-319-26425-7\\_10](https://doi.org/10.1007/978-3-319-26425-7_10)
- [10] O. V. Carboni and C. Labate, “América latina por una red neutral: o principio da neutralidade em chile e brasil,” *Revista FAMECOS*, vol. 25, no. 2, p. ID28507, abr. 2018. [Online]. Available: <https://doi.org/10.15448/1980-3729.2018.2.28507>
- [11] We are social. (2020) DIGITAL 2020. [Online]. Available: <https://bit.ly/2Ohytgu>
- [12] OECD and IDB, *Broadband Policies for Latin America and the Caribbean: A Digital Economy Toolkit*. OECD Publishing, Paris, 2016. [Online]. Available: <http://dx.doi.org/10.1787/9789264251823-en>
- [13] R. Hahn and W. Scott, “The economics of net neutrality,” *The Economists’ Voice*, vol. 3, no. 6, pp. 1–7, 2006. [Online]. Available: <https://bit.ly/3bW0bHL>
- [14] B. Van Schewick, *Internet Architecture and Innovation*. MIT Press, 2012. [Online]. Available: <https://bit.ly/3kI8xqd>
- [15] R. Triviño, A. Franco, and L. Ochoa, “Net neutrality regulation in south america: A progress review,” *Latin-American Journal of Computing - LAJC*, vol. 6, no. 1, pp. 17–26, 2019. [Online]. Available: <https://bit.ly/3uPQzXF>
- [16] FCC. (2015) Open internet advisory committee. [Online]. Available: <https://bit.ly/2PvLrrw>
- [17] G. Robb and R. Hawthorne, “Net neutrality and market power: The case of south africa,” *Telecommunications Policy*, vol. 43, no. 9, p. 101814, 2019. [Online]. Available: <https://doi.org/10.1016/j.telpol.2019.03.003>
- [18] M. Zukerfeld and B. Califano, “Discutiendo la neutralidad de la red: de los discursos dominantes a las prácticas en contextos periféricos / debating net neutrality: From dominant discourses to practices in peripheral contexts,” *Commons. Revista de Comunicación y Ciudadanía Digital*, vol. 8, no. 1, pp. 5–43, jun. 2019. [Online]. Available: <http://dx.doi.org/10.25267/COMMON.2019.v8.i1.01>
- [19] P. Viollier, O. Castro, C. Brito, and S. Pereira da Silva, *Neutralidad de red en América Latina: Reglamentación, aplicación de la ley y perspectivas*. Derechos Digitales America Latina, 2017. [Online]. Available: <https://bit.ly/3bZ15TJ>
- [20] Ministerio de Transportes y Telecomunicaciones, *Reglamento que regula las características y condiciones de la neutralidad de la red en el servicio de acceso a internet*. Biblioteca del Congreso Nacional de Chile. Santiago de Chile, Chile, 2011. [Online]. Available: <https://bit.ly/3uL3fyS>
- [21] J. Huerta, “La neutralidad de la red en chile: ¿mucho sofisticación para la subtel?” *Digital Rights Latin American and the Caribbean*, no. 30, 2013. [Online]. Available: <https://bit.ly/30aO9ow>
- [22] P. Huichalaf. (2015) La neutralidad de la red: El caso chileno. [Online]. Available: <https://bit.ly/3e8gJz0>
- [23] R. Layton, “Which open internet framework is best for mobile app innovation?: An empirical inquiry of net neutrality rules around the world,” Ph.D. dissertation, 2017, PhD supervisor: Prof. Knud Erik Skouby, Aalborg University, Denmark. [Online]. Available: <https://doi.org/10.5278/vbn.phd.engsci.00181>
- [24] M. Correa Pérez, “Zero-rating y la neutralidad de la red en Chile,” *Revista*

- chilena de derecho y tecnología*, vol. 7, pp. 107–135, 06 2018. [Online]. Available: <http://dx.doi.org/10.5354/0719-2584.2018.48961>
- [25] SUBTEL. (2017) Subtel establece mesa de trabajo para analizar implicancias del fin de la neutralidad de red en EE.UU. [Online]. Available: <https://bit.ly/3bZkT9B>
- [26] Congreso de la República de Colombia, *Plan Nacional de Desarrollo: 2010-2014. Todos por un nuevo país*. Departamento Nacional de Planeación, 2011. [Online]. Available: <https://bit.ly/3e38BQd>
- [27] Fundación karisma, *¿Cómo se contrata en América Latina el acceso a Internet y que tiene que ver con la neutralidad de la red?* Fundación Karisma, 2016. [Online]. Available: <https://bit.ly/3sM0yv5>
- [28] Comisión de Regulación de Comunicaciones. (2011) Neutralidad en internet. [Online]. Available: <https://bit.ly/3qlKFf5>
- [29] J. Casasbuenas G. (2016) Neutralidad en internet: Factor que potencia el cierre de la brecha social digital. [Online]. Available: <https://bit.ly/3bbtE1a>
- [30] Comisión de Regulación de Comunicaciones, *El rol de los servicios OTT en el sector de las comunicaciones en Colombia, impactos y perspectivas regulatorias*. Comisión de Regulación de Comunicaciones, República de Colombia, 2018. [Online]. Available: <https://bit.ly/3qdyZt7>
- [31] Camara dos Deputados. (2016) Legislação informatizada - decreto n 8.771, de 11 de maio de 2016 - publicação original. [Online]. Available: <https://bit.ly/3bfBZkc>
- [32] O. V. Carboni and C. Labate, “América latina por una rede neutral: o principio da neutralidade em chile e brasil,” *Revista FAMECOS*, vol. 25, no. 2, p. ID28507, abr. 2018. [Online]. Available: <https://doi.org/10.15448/1980-3729.2018.2.28507>
- [33] UNESCO, *Assessing Internet Development in Brazil. Using UNESCO’s Internet Universality ROAM-X Indicators*. United Nations Educational, Scientific and Cultural Organization – UNESCO, 2019. [Online]. Available: <https://bit.ly/2O2X74q>
- [34] J. Omari, “Is facebook the internet? ethnographic perspectives on open internet governance in brazil,” *Law & Social Inquiry*, vol. 45, no. 4, pp. 1093–1112, 2020. [Online]. Available: <https://doi.org/10.1017/lsi.2020.5>
- [35] Asamblea Nacional, *Ley orgánica de Telecomunicaciones*. Asamblea Nacional de la República del Ecuador, 2015. [Online]. Available: <https://bit.ly/3rlrFgw>
- [36] B. Califano, “Políticas de internet: la neutralidad de la red y los desafíos para su regulación,” *Revista Eptic*, vol. 15, no. 3, pp. 19–37, 2013. [Online]. Available: <https://bit.ly/3kJCLcx>
- [37] A. Delgado. (2015) Ecuador: la ley de telecomunicaciones afecta la neutralidad de la red. [Online]. Available: <https://bit.ly/3bg5a6P>
- [38] A. J. Carrillo, *Protección a la neutralidad de la red en Ecuador*, 2017. [Online]. Available: <https://bit.ly/3riDvYG>
- [39] M. A. Gendler, “La neutralidad de la red: Debates y acciones en argentina,” in *XXXI Congreso ALAS Uruguay 2017. Las encrucijadas de América Latina. La sociología en tiempos de cambio*, 2017. [Online]. Available: <https://bit.ly/2PzdNBb>
- [40] L. Enzo Lufrano, “El primero te lo regalan: zero-rating de las operadoras móviles de la argentina,” *Revista Questión*, vol. 1, no. 62, p. e163, 2019. [Online]. Available: <https://doi.org/10.24215/16696581e163>
- [41] T. Garrett, L. E. Setenareski, L. M. Peres, L. C. E. Bona, and E. P. Duarte, “Monitoring network neutrality: A survey on traffic differentiation detection,” *IEEE Communications Surveys Tutorials*, vol. 20, no. 3, pp. 2486–2517, 2018. [Online]. Available: <https://doi.org/10.1109/COMST.2018.2812641>
- [42] G. T. Hoskins, “Beyond zero sum: the case for context in regulating zero rating in the global south,” *Internet Policy Review*, vol. 8, no. 1, 2019. [Online]. Available: <https://doi.org/10.14763/2019.1.1392>



# SUPPORT TO THE HUMAN TALENT SUBSYSTEMS, SELECTION AND RECRUITMENT FROM AN EXPERT SYSTEM. CASE STUDY

## APOYO A LOS SUBSISTEMAS DE TALENTO HUMANO, SELECCIÓN Y RECLUTAMIENTO A PARTIR DE UN SISTEMA EXPERTO. CASO DE ESTUDIO

Karina Matute-Pinos<sup>1,\*</sup> , Rodolfo Bojorque-Chasi<sup>2</sup> 

Received: 10-11-2020, Received after review: 04-02-2021, Accepted: 25-02-2021, Published: 01-07-2021

### Abstract

Human talent management is a key factor in the success of organizations. The inclusion of people with disabilities in the work environment has helped to enhance their qualities and harness their talent. Many of the human talent management systems lack guidelines for the recruitment and selection of a person with a disability, this is why this work shows the study carried out on these two processes indicating the factors that influence the allocation or not of a position, where for each candidate it is considered the level and type of disability, level of education, experience, training among other aspects, focusing on the task of applying supervised learning techniques that enable us to classify a candidate with a disability as suitable or not for a job, and unsupervised learning techniques such as clustering that helps us define hidden patterns in the data, if any. The result obtained from the study presents some classifications techniques and the selection of the most appropriate one for the available dataset. It is not sought to integrate people through their disabilities, but quite the opposite, to integrate people based on the potential of all their abilities.

**Palabras clave:** aprendizaje automático, inteligencia artificial, minería de datos, sistemas expertos

### Resumen

La gestión de talento humano es un factor fundamental en el éxito de las organizaciones. La inclusión en el entorno laboral de las personas con discapacidad ha ayudado a potenciar sus cualidades y a aprovechar su talento. Muchos de los sistemas de gestión de talento humano carecen de directrices para el reclutamiento y selección de una persona con discapacidad, es por eso por lo que el presente trabajo muestra el estudio realizado a estos dos procesos indicando los factores que influyen en la asignación o no de un cargo, donde de cada candidato es considerando el nivel y tipo de discapacidad, nivel de estudios, experiencia, capacitación entre otros aspectos, enfocándose en la tarea de aplicar técnicas de aprendizaje supervisado que permitan clasificar a un candidato con discapacidad para un puesto de trabajo como apto o no y técnicas de aprendizaje no supervisado como el *clustering* que ayuda a definir patrones ocultos en los datos si los hubiera. El resultado obtenido del estudio presenta varias técnicas de clasificación y la selección de la más adecuada para el conjunto de datos en cuestión, igualmente mediante técnicas de aprendizaje no supervisado se determina cuántos clústeres representativos se identifican en los datos. No se busca que se integren las personas a través de las discapacidades, sino todo lo contrario, que se integren las personas por medio de la potencialidad de todas sus capacidades.

**Keywords:** automatic learning, artificial intelligence, data mining, expert systems

<sup>1,\*</sup>Maestría en Administración de Empresas, Universidad Politécnica Salesiana, Ecuador.

Corresponding author ✉: [kmatute@est.ups.edu.ec](mailto:kmatute@est.ups.edu.ec).

<sup>2</sup>Universidad Politécnica Salesiana, Ecuador.

## 1. Introduction

In recent years different organisms and Governments have considered as an important point in their administration, improving the quality of life of the people with disabilities, such as the case of the Government of Ecuador whose Development Plan points out as one of its goals «To increase the number of people with disabilities and/or substitutes inserted in the labor system for 2021» [1] and thus based on the current Constitution, the Labor Code and the Organic Law of Dissabilities an integration has been achieved that contributes to the inclusion of people with disabilities in the society. In the working environment, selection mechanisms have been gradually created in which processes have been adjusted to enable the participation of people with disabilities seeking gender equity and diversity of disability [2].

The human resources data provide a valuable source of information for discovering knowledge and for developing systems to assist in the decision making when recruiting personnel. Nowadays, organizations have to struggle effectively in terms of cost, quality, service and innovation.

The success of these tasks depends upon having available enough adequate people with the adequate skills, deployed in the appropriate places at the adequate moment, which is known as human talent management. Managing the talent of an organization has become a challenge for human resources professionals, this task implies many managerial decisions to select the right person for the right job at the right moment. At times, these decisions are very uncertain and difficult; and depend on various factors, such as human experience, knowledge, preference and judgement [3]. The talent is considered as the capability of any individual to make a significant difference in the current and future performance of the organization [4].

The recruitment becomes difficult when analyzing the labor inclusion process of people with disabilities. According to the World Health Organization (WHO), in developing countries between 80 % and 90 % of the people with disabilities at working age are currently unemployed, and in industrialized countries the estimation is between 50 % and 70 %.

The barriers for entering the labor market for people with disabilities vary according to the type of disability, and thus, in the process of labor insertion of a person with disability, it is required to take measures that guarantee the access and permanence of this person at the workplace, respecting individuality and type of disability [5]. When a candidate fulfills the adequate profile for a position, the company should manage and perform the necessary changes to the workplace, thus helping to develop the abilities of this person.

In the National Council for the Equality of Disabilities (CONADIS, Consejo Nacional para la Igualdad de

Discapacidades) of Ecuador, by June 2020 there were registered [6] 481 392 people with disabilities of which 13 % are occupationally active without considering substitutes, 56.20 % of which have physical disability, followed by 17.12 % with hearing disability, 14.31 % with visual disability, 8.88 % with intellectual disability and, finally, 3.50 % with psychosocial disability. The private sector has 46 496 people with disability on its payroll and the public sector 18 333 people. See Figure 1.

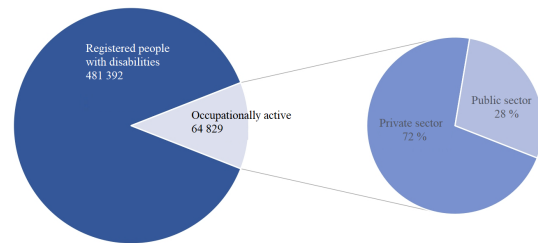


**Figure 1.** People with disabilities registered in the CONADIS

According to [7], the recruiting process has improved through the implementation of information technologies, which enable simplifying the process of posting vacancies and resumes, listing jobs and seeing possible candidates. However, the recruiting process remains being imperfect and the study mentions three reasons:

1. Some steps of the recruiting process are not automated. As a result, recruiters have to manually process a large number (sometimes hundreds, or even thousands) of resumes to select the best potential employee.
2. In general, recruiters do not take into consideration all possible alternatives for the employee.
3. Recruiters are only guided by their subjective opinion, and thus there is no guarantee that the selected candidate is really the best possible option for the employer.

The contracting and selection of personnel directly affects the quality of the employees. Various studies have been carried out about resumes, interviews, evaluation centers, tests about knowledge of the job, job sample, tests, cognitive tests and personality tests in human resources management, to help organizations to make better decisions in the selection of personnel. In fact, the existing selection approaches are focused on the job duties and the analysis of such duties which are defined through activities and specific tasks based on their static properties [8]. The abovementioned processes generate an important amount of data regarding recruitment, the present study attempts to

take advantage of automatic learning techniques on these databases.

Automatic learning consists in the application of statistical techniques to databases for learning hidden patterns, projections or predictions of observations, by means of the application of algorithms valuable information may be automatically extracted from data of a specific domain [9].

The present work is organized as follows, section two presents different works related with the area of artificial intelligence and its application in human resources management, different concepts are introduced when it is considered opportune. Section three presents the working methodology, detailing the applied techniques. Section four shows the relevant results that were obtained and, finally, section five exposes the conclusions of the present work.

### 1.1. Related works

Organizations are starting to adopt and capitalize the functionality of artificial intelligence in their recruiting processes [10]. The applications of expert systems or systems to assist decision making for selecting and recruiting personnel are increasing [8,9,11–14].

For job application and selection, artificial intelligence may use behavioral and physiological (for example, biometrics) features as part of the general decision-making process [10]. Some implementation examples are the use of multimedia tools [15], on-line candidate monitoring systems [16], automatic learning systems [17], systems for supporting decision making which help in the entire process of categorizing and identifying disabilities [9], however, at present the richness of data mining is not being exploited.

Nowadays, there are countless artificial intelligence techniques such as data mining, data analytics and the discovery of information in databases that, by means of automatic learning techniques, provide organizations the tasks of prediction and classification, to support decision making, including human talent management.

Data mining refers to the extraction of patterns or useful rules from an extensive data source, through automatic or semiautomatic exploration and from data analysis [18]. For this work, the application of automatic learning techniques constitutes the data mining process, according to the literature there is the consensus of classifying automatic learning techniques in supervised learning, unsupervised learning and reinforcement learning [19].

The present work focuses on the task of applying supervised learning techniques such as classification and unsupervised learning techniques such as clustering to the database collected in the project of educational and labor inclusion of people with disabilities of the Universidad Politécnica Salesiana.

The supervised techniques enable classifying a candidate with disability as suitable or not for a job post. From the computational point of view, it is a classification task, however, the disability condition biases the data to a very reduced population, first, there is no enough data about them and the sample is limited to the domain of the city of Cuenca-Ecuador.

Classifying is a supervised learning task, where the class or classification objective is known. In data mining, there are various techniques used for classification such as decision trees, Bayesian techniques, fuzzy logic, support vector machines, neural networks, genetic algorithms and the nearest-neighbors algorithm. In the present study various techniques are applied to determine the one that best fits the collected information about the candidates with disabilities.

Clustering consists in finding hidden patterns in the data, natural groupings that are not perceptible in the high dimensionality environment exhibited by modern datasets [19], seventy features in our case. Due to the high dimensionality, the work seeks to determine correlations between the different features in order to eliminate those that show a high correlation index. Similarly, dimensionality reduction techniques were tested.

It is important to mention a research area with strong growth perspective in the field of automatic learning for supporting human resources management, it is natural language processing, and as a current disruptive technology the chatbots handle tasks such as interviews to candidates, personnel training, customer service and any task that requires communication between people and an intelligent agent [20]. In the personnel recruitment area, it is important to mention that the chatbots are capable of handling a significant amount of information that interviewers often overlook [21].

## 2. Materials and methods

The work [22] was used as base line; such work consists of 120 data samples, with 70 features regarding age, sex, level of education, work experience, foreign language proficiency, type of disability and the transversal skills of each candidate. The original study utilizes a rule-based system validated by experts. Our proposal incorporates as a novelty the learning from the original dataset to predict if a candidate is suitable or not for a position, and thus, through supervised learning techniques the system does not require the validation of experts.

Data dispersion is the most relevant feature of the dataset, i.e., the available matrix is missing information, and such information cannot be considered as 0 in the analysis process because this could bias the results of the analysis. Table 1 shows a summary of the different features of the dataset.

**Table 1.** Features of the dataset

Type of information	Description
<b>Descriptive information</b>	Descriptive details of each candidate, the most relevant feature in this case is the age and the type of disability
<b>Information about adaptations</b>	Makes reference to the use of auxiliary devices by the candidate, as well as the need to be supported by an interpreter or have developed skills such as the sign language
<b>Education</b>	Level of education of the candidate
<b>Information about the position</b>	Various features that provide information about the details of the position
<b>Information about the experience</b>	Features that collect the past working experience of the candidate
<b>Optimal parameters to apply for a position</b>	Desirable parameters for applying to a position
<b>Parameters obtained by the candidate</b>	Assessment of each candidate in the different parameters
<b>Domain of other languages</b>	Details about the domain of other languages
<b>Training</b>	Features that collect information about trainings received

For this work it was proceeded to impute the data and eliminate those features that do not provide enough information to the system, either because the data collected represented an insignificant amount of the population under study or because the feature presented text type descriptions that do not provide information to the system. After this process, a complete matrix was available.

In order to validate the elimination of features, it was carried out an analysis of the similarities between the original dataset, the one that contains the sparse data; and the dataset after the imputation. Different similarity metrics were used according to study [23], being relevant for our study the Pearson and Jaccard similarities for the complete dataset (with sparsity features), and only the Pearson similarity for the modified dataset.

It may be seen in Equation (1) how the similarity between candidate  $u$  and candidate  $v$  is calculated in a sparse matrix, where  $i$  represents the  $i$ th feature and  $r$  the value of the feature. In addition, let  $I'$  be the set of all common features between  $u$  and  $v$ .

$$S_{PC}(u, v) = \frac{\sum_{i \in I'} (r_{ui} - \bar{r}_u)(r_{vi} - \bar{r}_v)}{\sqrt{\sum_{i \in I'} (r_{ui} - \bar{r}_u)^2} \sqrt{\sum_{i \in I'} (r_{vi} - \bar{r}_v)^2}} \quad (1)$$

Equation (2) is used to calculate the Jaccard similarity, in this case it is important to determine if there is intersection between the features of  $u$  and  $v$  without regard of the difference in magnitude between their values.

$$S_{Jac}(u, v) = \left| \frac{I_u \cap I_v}{I_u \cup I_v} \right| \quad (2)$$

Results show that the average of similarity between users within one group of candidates with the same

disability is around 0.1, for both Pearson and Jaccard similarities, although it is slightly lower for the latter.

With the modified dataset it does not make sense to apply Jaccard similarity because it will always be equal to one, since it is a complete matrix, however, with Pearson similarity it is obtained an improvement of 0.25 in the similarity average between users within a group of candidates with the same disability, which evidences that eliminating some features simplified the system and improved the results.

Using the new dataset, it was proceeded to generate a color map to determine correlations between the features of the candidates. Figure 2 presents the color map between the most relevant features, where the intersection of each row and column represents the correlation coefficient in the interval  $[-1, 1]$  where values close to  $-1$  mean a strong inversely proportional correlation and values close to  $1$  mean a strong directly proportional correlation, values close to  $0$  mean that there is no correlation.

**Figure 2.** Color map of the correlations between the most relevant features of the dataset

In this initial analysis it is noteworthy the direct relationship existing between experience and level of disability of the candidate (moderate, mild). On one hand, private companies have a direct relationship with the mild level of disability, and public companies have a direct relationship with the moderate level of disability.

In addition it was proceeded to visualize if there are relationships between the different features through a scatter plot. Figure 3 enables appreciating the dispersion of points between the different pairs of features of the dataset, the diagonal shows the histogram of each feature.

After the statistical analysis it was proceeded to apply data analytics, where this work has two objectives, the first is generating a classification model for

the correct allocation of a person to a position. Second, through clustering techniques it is attempted to discover the cohesion of the groups of candidates. In the first case, classification techniques such as logistic regression, support vector machines and the nearest neighbors algorithm, will be compared. In the second case, the k-means clustering algorithm will be used.

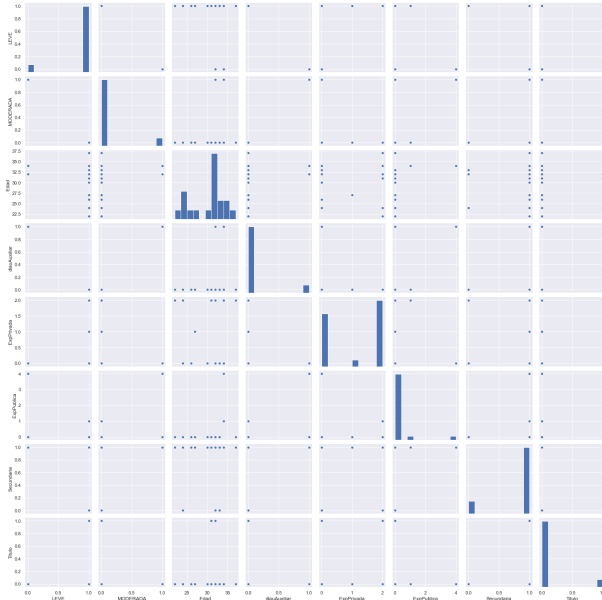


Figure 3. Scatter plots between pairs of features

### 3. Results and Discussion

#### 3.1. Classification

When designing the model, different classifications techniques were used, including, a binary logistic regression scheme, since the objective is to attempt predicting if a person is suitable or not for the position. The logistic regression was tested with linear, quadratic and cubic hypotheses; techniques such as Support Vector Machines with Gaussian kernel and the k-nearest neighbors algorithm (KNN) for results with 3 and 5 neighbors, were also implemented.

In order to validate the results, the dataset was divided in five random sets for training and testing, in a proportion of 80 % and 20 %, respectively. Results show the average of the five random testing sets. The metric used to compare the quality of the prediction is the precision according to Equation (3), where TP represents the number of classifications made correctly (true positives) and FP the number of incorrect classifications (false positives).

$$Precision = \frac{TP}{TP + FP} \tag{3}$$

The results of the different models are shown in Table 2. Even though the best results are obtained

with SVM, the difference in precision with logistic regression is not significant, and thus logistic regression may be used for simplifying the model.

Table 2. Results of classification techniques

Technique	Parameters	Precision
<b>Logistic regression</b>	Función lineal	0,805
<b>Logistic regression</b>	Función cuadrática	0,815
<b>Logistic regression</b>	Función cúbica	0,818
<b>SVM</b>	Gaussian Kernel	0,821
<b>KNN</b>	3 neighbors	0,791
<b>KNN</b>	5 neighbors	0,798

#### 3.2. Clustering

The most famous and well-known hard clustering technique is the k-means algorithm [24,25] or hard c-means, which has the following advantages:

- a. It is conceptually simple, versatile and easy to implement.
- b. It exhibits linear complexity with respect to the number of elements and clusters.
- c. It is guaranteed that the algorithm ends with a quadratic convergence rate [26].

To measure the clustering quality, it was used the cohesion measure  $J_c$  given by Equation (4), where  $X$  represents the sample of the candidate under consideration and  $C$  represents the centroid to which it belongs.

$$J_c = \sum_{j=1}^c \sum_{i=1}^n \|X_i - C_j\|^2 \tag{4}$$

The k-means algorithm uses parameter K as the indicator of the groups to be classified, however, the challenge is determining what number of groups should there exist to express the best representation of them. For the dataset of the candidates, it was determined the clustering quality from  $K = 2$  to  $K = 10$ . In Figure 4 it can be seen, through the Elbow method [26], that there is no clear determination of the groups of candidates; it might be considered the value  $K = 3$  as well as the value  $K = 6$  as inflection points where the clustering quality stabilizes according to the curve. This indicates that the information that is being collected in the system requires more work, both in quantity and in the quality of the features.

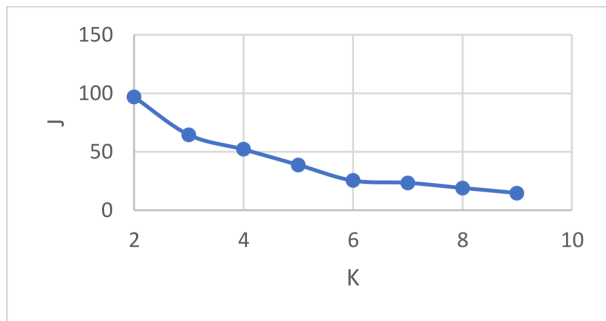


Figure 4. Elbow method for  $k = 2$  hasta  $k = 10$

## 4. Conclusions

This study enables visualizing the correlations existing between different variables of the dataset, with the novel contribution of incorporating automatic learning techniques, supervised learning to support selection processes of human talent with disability as well as unsupervised learning to determine in the high dimensional space the number of groups existing in the data.

Based on the study conducted it could be observed that the most determinant factor for a person with disability to get a job is the experience, i.e, having previously worked in some place; in the dataset there is a direct correlation between the candidates that were considered suitable and the previous experience, however, the candidates that although being suitable have not been located, have as a common factor not having such experience; this evidences that for the case study, the main feature which determines that a person with disability gets a position is this experience, factor that may be considered discriminatory because it is attentive against equality of opportunities. The dataset used for this work is considered the most comprehensive of its type for selection of personnel with disability, however, the present study has demonstrated that more relevant features are required. It should be mentioned that the study also find limitations in the number of samples, at present the dataset comprises 120 samples which restricts us to the application of automatic learning techniques, for the future it would be interesting to have available a much larger dataset to apply deep learning techniques.

Various studies demonstrate that the level of education improves the opportunity of finding a job [27], situation which is not fulfilled in the dataset used here. Such studies also demonstrate that people with disabilities have a lower level of education, compared to the general population, and this element is easily verifiable in our case study. Academic preparation determines that people with disabilities are disadvantaged for the tasks demanded by the market due to reasons that go beyond the disability itself. Both the training and level of education have significant influence on the

job opportunities, because the skills and knowledge within a specific area are acquired in this training process [28]. Current systems continue being discriminatory for these people, because most organizations privilege experience and this induces a poor assessment of the attitudes of these people. This situation is reflected in the quality of the prediction systems and in the inability to discover clear clustering patterns in the data provided.

It is considered that a novel field of study in recruiting processes is the application of chatbots in the personnel selection interviews, because they enable eliminating subjective elements that experts consider as confusion variables that guide the interview in one direction or another, subjective factors such as the personal image perceived by the interviewer and the mood, are elements that are difficult to measure and therefore might be eliminated with an adequate selection of experimental and control groups [29].

While it is true that public policies have contributed to the labor inclusion of people with disabilities, it is necessary that companies supported by technology narrow the currently existing gap, and likewise eliminate the stereotypes that hinder recognizing and enhancing the qualities of people with disabilities thus hindering exploiting their talent.

## Acknowledgement

The authors express the gratitude to the research group in artificial intelligence and assistive technologies (GIATA, Grupo de investigación de inteligencia artificial y tecnologías de asistencia) and to the UNESCO Chairs, who provided the data that was used in this study.

## References

- [1] Consejo Nacional de Planificación, *Plan Nacional de Desarrollo 2017-2021-Toda una Vida*. Secretaría Nacional de Planificación y Desarrollo, Senplades. Quito – Ecuador, 2017. [Online]. Available: <https://bit.ly/3isgCNb>
- [2] Asamblea Nacional, *Ley Orgánica de Discapacidades*. Registro Oficial N.º 796. República del Ecuador, 2012. [Online]. Available: <https://bit.ly/3cXWwch>
- [3] H. Jantan, A. Hamdan, and Z. Othman, “Human talent prediction in HRM using C4.5 classification algorithm,” *International Journal on Computer Science and Engineering*, vol. 2, pp. 2526–2534, 2010. [Online]. Available: <https://bit.ly/3aIbF1x>
- [4] L. Morton, “Talent management value imperatives: Strategies for execution,” in *Con-*

- ference Board, 2005. [Online]. Available: <https://bit.ly/2S4TyN0>
- [5] Ministerio de Relaciones Laborales, *Manual de Buenas Prácticas para la inclusión laboral de personas con discapacidad*. Dirección de Atención a Grupos Prioritarios. Consejo Nacional de Discapacidades. Ecuador, 2013. [Online]. Available: <https://bit.ly/32S8PD4>
- [6] Consejo Nacional para la Igualdad de Discapacidades. (2020) Estadísticas de discapacidad. [Online]. Available: <https://bit.ly/3vn30JT>
- [7] E. Kalugina and S. Shvydun, “An effective personnel selection model,” *Procedia Computer Science*, vol. 31, pp. 1102–1106, 2014, 2nd International Conference on Information Technology and Quantitative Management, ITQM 2014. [Online]. Available: <https://doi.org/10.1016/j.procs.2014.05.365>
- [8] C.-F. Chien and L.-F. Chen, “Data mining to improve personnel selection and enhance human capital: A case study in high-technology industry,” *Expert Systems with Applications*, vol. 34, no. 1, pp. 280–290, 2008. [Online]. Available: <https://doi.org/10.1016/j.eswa.2006.09.003>
- [9] G. Harih and N. Vujica-Herzog, “Towards an expert system for assigning optimal workplaces to workers with disabilities,” in *Advances in Social and Occupational Ergonomics*, R. H. Goossens and A. Murata, Eds. Cham: Springer International Publishing, 2020, pp. 57–66. [Online]. Available: [https://doi.org/10.1007/978-3-030-20145-6\\_6](https://doi.org/10.1007/978-3-030-20145-6_6)
- [10] P. van Esch, J. S. Black, and J. Ferolie, “Marketing AI recruitment: The next phase in job application and selection,” *Computers in Human Behavior*, vol. 90, pp. 215–222, 2019. [Online]. Available: <https://doi.org/10.1016/j.chb.2018.09.009>
- [11] R. Storey Hooper, T. P. Galvin, R. A. Kilmer, and J. Liebowitz, “Use of an expert system in a personnel selection process,” *Expert Systems with Applications*, vol. 14, no. 4, pp. 425–432, 1998. [Online]. Available: [https://doi.org/10.1016/S0957-4174\(98\)00002-5](https://doi.org/10.1016/S0957-4174(98)00002-5)
- [12] M. Nussbaum, M. Singer, R. Rosas, M. Castillo, E. Flies, R. Lara, and R. Sommers, “Decision support system for conflict diagnosis in personnel selection,” *Information & Management*, vol. 36, no. 1, pp. 55–62, 1999. [Online]. Available: [https://doi.org/10.1016/S0378-7206\(99\)00007-5](https://doi.org/10.1016/S0378-7206(99)00007-5)
- [13] S. M. C. Loureiro, J. Guerreiro, and I. Tussyadiah, “Artificial intelligence in business: State of the art and future research agenda,” *Journal of Business Research*, vol. 129, pp. 911–926, 2021. [Online]. Available: <https://doi.org/10.1016/j.jbusres.2020.11.001>
- [14] H. J. Wilson and P. R. Daugherty, “Collaborative intelligence: Humans and AI are joining forces,” *Harvard Business Review*, 2018. [Online]. Available: <https://bit.ly/3npoJOx>
- [15] S. T. Hunter, N. D. Shortland, M. P. Crayne, and G. S. Ligon, “Recruitment and selection in violent extremist organizations: Exploring what industrial and organizational psychology might contribute.” *The American psychologist*, vol. 72, pp. 242–254, Apr 2017. [Online]. Available: <https://doi.org/10.1037/amp0000089>
- [16] A. Eckhardt, S. Laumer, C. Maier, and T. Weitzel, “The transformation of people, processes, and it in e-recruiting,” *Employee Relations*, vol. 36, no. 4, pp. 415–431, Apr. 2021. [Online]. Available: <https://doi.org/10.1108/ER-07-2013-0079>
- [17] N. Herbst, S. Becker, S. Kounev, H. Koziolk, M. Maggio, A. Milenkoski, and E. Smirni, *Metrics and Benchmarks for Self-aware Computing Systems*. Cham: Springer International Publishing, 2017, pp. 437–464. [Online]. Available: [https://doi.org/10.1007/978-3-319-47474-8\\_14](https://doi.org/10.1007/978-3-319-47474-8_14)
- [18] M. J. A. Berry and G. S. Linoff, *Data Mining Techniques: For Marketing, Sales, and Customer Relationship Management*. John Wiley & Sons, 2004. [Online]. Available: <https://bit.ly/3tXJh37>
- [19] P.-N. Tan, M. Steinbach, and V. Kumar, *Introduction to data mining*. Pearson Education, 2013. [Online]. Available: <https://bit.ly/3voKVeG>
- [20] J. Hill, W. Randolph Ford, and I. G. Farreras, “Real conversations with artificial intelligence: A comparison between human-human online conversations and human-chatbot conversations,” *Computers in Human Behavior*, vol. 49, pp. 245–250, 2015. [Online]. Available: <https://doi.org/10.1016/j.chb.2015.02.026>
- [21] A. M. Rahman, A. A. Mamun, and A. Islam, “Programming challenges of chatbot: Current and future prospective,” in *2017 IEEE Region 10 Humanitarian Technology Conference (R10-HTC)*, 2017, pp. 75–78. [Online]. Available: <https://doi.org/10.1109/R10-HTC.2017.8288910>
- [22] M. Rodas-Tobar, C. Bernal-Bravo, M. Andrés-Romero, A. Pinos-Figueroa, P. Vidal-Mogrovejo, A. León-Pesántez, V. Robles-Bykbaev, and F. Pesántez-Avilés, “An expert system to support the provisioning of staff with disabilities in industry,” in *2018 IEEE Biennial Congress of Argentina (ARGENCON)*,

- 2018, pp. 1–6. [Online]. Available: <https://doi.org/10.1109/ARGENCON.2018.8646043>
- [23] R. X. Bojorque Chasi, “Clustering de sistemas de recomendación mediante técnicas de factorization matricial,” Ph.D. dissertation, 2020. [Online]. Available: <https://doi.org/10.20868/UPM.thesis.58156>
- [24] J. MacQueen, “Some methods for classification and analysis of multivariate observations,” in *Proceedings of the fifth Berkeley symposium on mathematical statistics and probability*, 1967. [Online]. Available: <https://bit.ly/3xrH16A>
- [25] S. Zahra, M. A. Ghazanfar, A. Khalid, M. A. Azam, U. Naeem, and A. Prugel-Bennett, “Novel centroid selection approaches for kmeans-clustering based recommender systems,” *Information Sciences*, vol. 320, pp. 156–189, 2015. [Online]. Available: <https://doi.org/10.1016/j.ins.2015.03.062>
- [26] M. A. Syakur, B. K. Khotimah, E. M. S. Rochman, and B. D. Satoto, “Integration k-means clustering method and elbow method for identification of the best customer profile cluster,” in *IOP Conference Series: Materials Science and Engineering*, vol. 336, 2017. [Online]. Available: <https://doi.org/10.1088/1757-899x/336/1/012017>
- [27] T. Boman, A. Kjellberg, B. Danermark, and E. Boman, “Employment opportunities for persons with different types of disability,” *Alter*, vol. 9, no. 2, pp. 116–129, 2015. [Online]. Available: <https://doi.org/10.1016/j.alter.2014.11.003>
- [28] M. A. Espinoza Mina and D. Gallegos Barzola, “Inserción laboral de las personas con discapacidad en Ecuador,” *Espacios*, vol. 39, no. 51, 2018. [Online]. Available: <https://bit.ly/3sXKMwS>
- [29] M. Reynolds, “Ai coach helps chatbots seem more human,” *New Scientist*, vol. 235, no. 3135, p. 14, 2017. [Online]. Available: [https://doi.org/10.1016/S0262-4079\(17\)31407-0](https://doi.org/10.1016/S0262-4079(17)31407-0)



# EVALUATION OF THE DYNAMIC PROPERTIES OF A 2D-FRAME (MDOF) IN A SHAKE TABLE

# EVALUACIÓN DE LAS PROPIEDADES DINÁMICAS DE UN PÓRTICO PLANO (MDOF) EN UNA MESA VIBRATORIA

Andrea Tapia Andrade<sup>1,\*</sup> , Wilson Torres Berni<sup>1</sup> 

Received: 14-11-2020, Received after review: 22-02-2021, Accepted: 04-03-2021, Published: 01-07-2021

## Abstract

At present, the study of structural dynamics is mainly theoretical with access to certain simulations through software, however, this project attempts that the student may understand and physically observe the dynamic responses of experimental models. These models correspond to 2D - frames with multiple degrees of freedom that are subjected to acceleration in the base; this acceleration is generated by a Shake Table II, and the results obtained will be compared with theoretical results. These theoretical results were obtained based on modal decomposition and Newmark's method for calculating the dynamic response, considering the linear variation in the acceleration of each floor. The application developed, ATH Dynamic Responses, provided the theoretical responses through a graphical interface friendly for the user. The experimental models are constituted by two materials: stainless steel for frame legs and acrylic sheets for floors; these were tested on a Shake Table II<sup>®</sup>. The data was acquired using accelerometers that were placed in each floor and in the shake table, and they were corrected both by baseline and with the low pass filter. The results obtained show that the instrumentation with the Shake Table II and the data acquisition with accelerometers provide results similar to the theoretical ones regarding dynamic responses and modal properties.

**Keywords:** modal decomposition, structural dynamics, experimental model, Shake Table, Newmark, filter

## Resumen

Hoy en día, el estudio de la dinámica estructural es fundamentalmente teórico con acceso a ciertas simulaciones vía *software*, sin embargo, este proyecto intenta que el estudiante pueda entender y observar de manera física las respuestas dinámicas de modelos experimentales. Estos modelos corresponden a pórticos planos de múltiples grados de libertad, que están sometidos a aceleración en la base, la cual es generada por una mesa vibratoria. Los resultados obtenidos se compararán con teóricos. Estos fueron obtenidos basándose en la descomposición modal y en el método de Newmark para el cálculo de la respuesta dinámica, considerando variación lineal en la aceleración de cada piso. La aplicación generada, ATH Dynamic Responses, proporcionó las respuestas teóricas, mediante una interfaz gráfica amigable para el usuario. Los modelos experimentales están constituidos por dos materiales: acero inoxidable (parantes) y láminas de acrílico (pisos), y fueron ensayados sobre una mesa vibratoria. La adquisición de datos se realizó mediante acelerómetros que se colocaron en cada piso y sobre la mesa vibratoria, fueron corregidos, tanto por línea base como con el filtro pasa bajo. Los resultados obtenidos muestran que la instrumentación con una mesa vibratoria y adquisición de datos con acelerómetros proporcionan valores muy similares a los teóricos en cuanto a respuestas dinámicas y propiedades modales.

**Palabras clave:** descomposición modal, dinámica estructural, modelo experimental, mesa vibratoria, Newmark, filtro

<sup>1,\*</sup>Carrera de Ingeniería Civil, Universidad Politécnica Salesiana, Quito, Ecuador  
 Autor para correspondencia ✉: [atapiaa@est.ups.edu.ec](mailto:atapiaa@est.ups.edu.ec).

Suggested citation: Tapia Andrade, A. and Torres Berni, W. (2021). «Evaluation of the dynamic properties of a 2D-frame (MDOF) in a shake table». INGENIUS. N.º 26, (july-december). pp. 49-62. DOI: <https://doi.org/10.17163/ings.n26.2021.05>.

## 1. Introduction

Ecuador has a significant seismic activity, the last earthquake that affected the country with great intensity occurred on April 16th, 2016 with a magnitude of momentum  $M_w$  of 7.8, it happened in the coastal provinces of Manabí and Esmeraldas [1], causing material damages, collapsing of buildings and nearly seven hundred people dead.

The earthquake was caused by the subduction of the Nazca oceanic plate below the South American plate; the friction between both plates produces an accumulation of elastic energy, which is relaxed when there is a sudden rupture and the seismic event occurs [2].

This has motivated engineers to develop a philosophy which is centered in preventing life losses, controlling the collapse of all structures [3]. As a result, every building should be designed considering seismic solicitation; the analysis of the structure when facing this type of load is the main problem that structural dynamics seeks to solve.

In most cases, the study of structural dynamics is carried out theoretically, without being able to physically observe the behavior of structures in the event of an earthquake or acceleration in the base. Therefore, this project is focused on constructing experimental models with multiple degrees of freedom and made of appropriate materials, which means slabs very rigid compared with the bending columns, where the model will concentrate the deformation of the structure. In addition, both columns and floors are considered axially rigid, in the analytical model, it will be considered that floors concentrate the mass, and that frame legs are the ones that collaborate with the rigidity, i.e., that it behaves as a shear building [4].

Experimental techniques, such as placing triaxial accelerometers or the use of dynamic excitation equipment that reproduce earthquakes to scale [5], have been implemented to obtain dynamical responses and modal properties in experimental models and real structures. A shake table, known as Shake Table II [6], was used in the project. This device is an earthquake simulator for small physical-academic models (maximum mass = 7.5 kg), that will enable generating floor accelerations in the form of pulsations, sinusoidal sweeps and seismic records (scaled) [6]. The Shake Table II enables reproducing floor accelerations in two directions (x,y), however, for the project it was used 2-D models and unidirectional acceleration, each floor will move in only one direction [7].

Dynamic properties of experimental structures have been determined in [7,8] and [9] using the same method, however, these are centered only in maximum displacements and others only in obtaining frequencies; besides, they are limited to two floors. In the project it will be analyzed how frequencies and dampings are obtained

and, besides, models according to their construction mode, have the possibility of stacking until becoming a model of six floors, and the unique limitation is the maximum weight withstood by the shake table.

## 2. Materials and methods

The project consists of the theoretical foundation, which includes the concepts about structural dynamics used to develop the Matlab script; and the experimental part, where it is established the type of material to be used, the geometrical features, the acceleration of the base, the acceleration of each floor, the operation of the shake table, and the way to acquire and process the responses.

### 2.1. System with multiple degrees of freedom

From the point of view of structural dynamics, a system with multiple degrees of freedom (MDOF) is one that requires more than one coordinate to describe its movement. The degrees of freedom may also determine the directions of acceleration of the concentrated masses. In the project, the direction of the earthquake will be uniaxial, and hence, the number of degrees of freedom will be one per floor [10].

Experimental models are modular and may become systems from one to six degrees of freedom, the tests were carried out with systems of one, two, and three degrees of freedom. Figure 1 shows the model with three degrees of freedom.

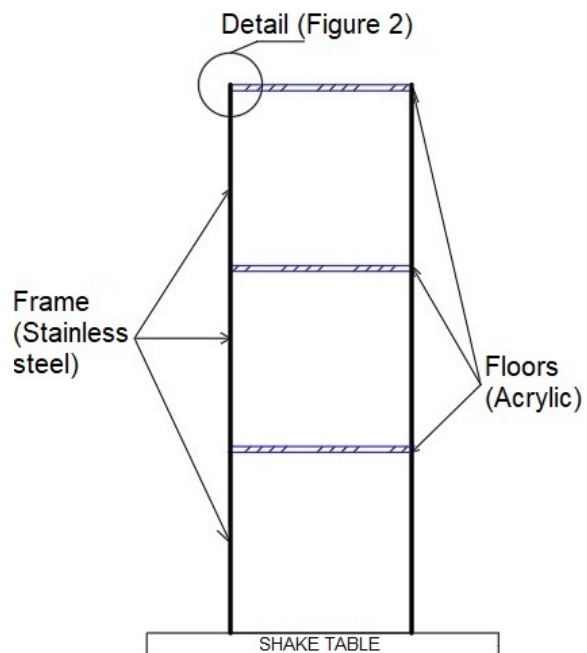


Figure 1. Model with three degrees of freedom

### 2.2. Shear building

A shear building is characterized as an array that concentrates the mass in each floor, and besides they should act as diaphragms infinitely rigid to bending and axial load. Therefore, in the model, only the columns should collaborate with the rigidity [4].

The preceding considerations enable simplifying the structure and solving the problem as an MDOF, where the slabs are infinitely rigid, and enable assuring that there will be no rotations between frame legs and floors. In the experimental model, the rotation was controlled according to the connection between the frame leg and the acrylic, because the connection is not fixed at a point but in an area, as observed in Figure 2. Regarding axial deformation, it will be negligible due to the physical features of the floors.

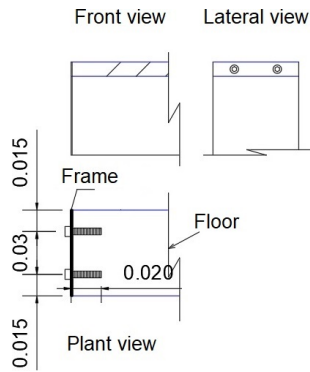


Figure 2. Detail of the connection

In the experimental model it should be taken into account that columns add mass, and therefore it was considered that the slab concentrates half of the mass of each column that is above and below it, as shown in Figure 3.

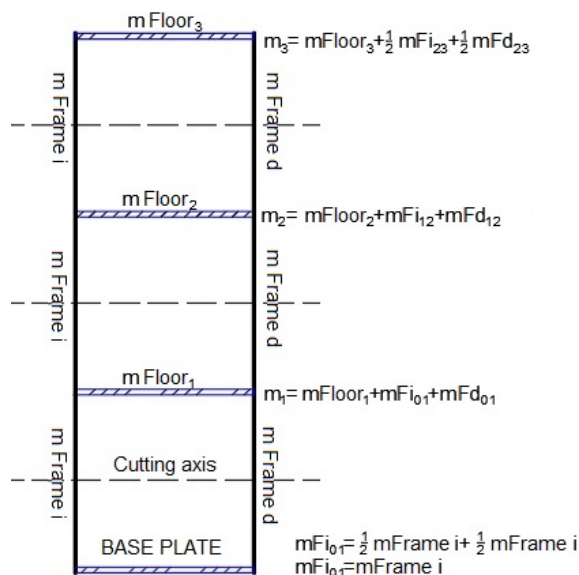


Figure 3. Distribution of mass of the structure

Where:  $mFi_{ij}$  and  $mFd_{ij}$  is the mass of the frame leg from degree of freedom  $i$  to degree of freedom  $j$ .

Cutting axis: helps to quantify how the mass of each floor was concentrated.

### 2.3. Inertia force

It relates the external forces that act on the mass of the structure with the accelerations of the dynamic degrees of freedom, as shown in Equation (1) [11].

$$\{F_i\} = [M] \times \{\ddot{x}\} \quad (1)$$

Where  $\{F_i\}$  is the vector of inertial force,  $[M]$  is the mass matrix and  $\{\ddot{x}\}$  is the vector of acceleration of the degrees of freedom.

The mass matrix (2) is an estimation of the mass of the whole structure, this matrix is also known as «matrix of concentrated mass» [12].

$$[M] = \begin{bmatrix} m_1 & 0 & 0 & 0 \\ 0 & m_2 & 0 & 0 \\ 0 & 0 & m_3 & 0 \\ 0 & 0 & 0 & m_4 \end{bmatrix} \quad (2)$$

### 2.4. Elastic force

It relates the external forces on the rigidity of the structure with the displacements of the dynamic degrees of freedom, as shown in Equation 3 [11].

$$\{F_s\} = [K] \times \{x\} \quad (3)$$

Where  $\{F_s\}$  is the vector of elastic force,  $[K]$  is the rigidity matrix and  $\{x\}$  is the vector of displacement of the degrees of freedom.

The rigidity matrix ((4) includes properties of the columns, such as length, area and modulus of elasticity [12].

$$[K] = \begin{bmatrix} k_{11} & k_{12} & \cdots & k_{1N} \\ k_{21} & k_{22} & \cdots & k_{2N} \\ \vdots & \vdots & \vdots & \vdots \\ k_{N1} & k_{N2} & \cdots & k_{NN} \end{bmatrix} \quad (4)$$

### 2.5. Damping force

It is a mechanism with which energy may be dissipated from the structure; according to this, the external forces that act on the damping are related with the velocities of the dynamic degrees of freedom as shown in Equation ??5 [11].

$$\{F_d\} = [C] \times \{\dot{x}\} \quad (5)$$

Where  $\{F_d\}$  is the vector of damping force,  $[C]$  is the damping matrix and  $\{\dot{x}\}$  is the vector of velocity of the degrees of freedom.

Classical damping will be supposed for obtaining the damping matrix. The classical damping matrix

may be used in this type of models, if the damping mechanisms are similar in all the structure, i.e., a MDOF structure which in turn is constituted by the same structural system and similar materials, along the entire height [11].

One of the procedures within classical damping is modal damping. The analysis provides the damping of a specific number of modes, as indicated in expression (6) [13] y [14].

$$\{\phi_n\}^T \times [C] \times \{\phi_n\} = 2 \times \xi_n \times \omega_n \quad (6)$$

Where  $C$  is the damping matrix,  $\phi_n$  is the vector of each modal form,  $\xi_n$  is the damping factor,  $\omega_n$  the natural frequency, and  $n$  is the number of modes.

### 2.5.1. Damping factor

An important feature is the damping of the structure, which is defined based on the damping factor; for this reason, it should be obtained applying the bandwidth method described in the following [15].

#### a) Bandwidth

It is a method to obtain the damping factor in the frequency domain; this technique is widely used in professional practice, in which a structure should be excited by simultaneous or individual pulsations at different frequencies [16].

With the purpose of applying the method it should be considered the effect of the movement of the base, whereby it is proceeded to find the ratio between the amplitudes of the Fourier transform of the acceleration records of each slab with respect to the records of the base. This is known as transmissibility [11], which is indicated in expression (7).

$$Tr = \frac{\alpha_o(\omega)}{\alpha_b(\omega)} \quad (7)$$

Where  $Tr$  is transmissibility,  $\alpha_o(\omega)$  amplitude of the acceleration of each floor in the frequency domain and  $\alpha_b(\omega)$  is amplitude of the acceleration of the base in the frequency domain.

From the calculation of the transmissibility, plots with respect to the frequency are obtained and the damping factor is determined by means of the difference between two frequencies called medium power points at the frequency corresponding to each mode. The medium power points are the frequencies located at  $\frac{1}{\sqrt{2}}$  of the maximum amplitude of the transmissibility, as indicated in Figure 4, and this will enable applying Equation (8) [17].

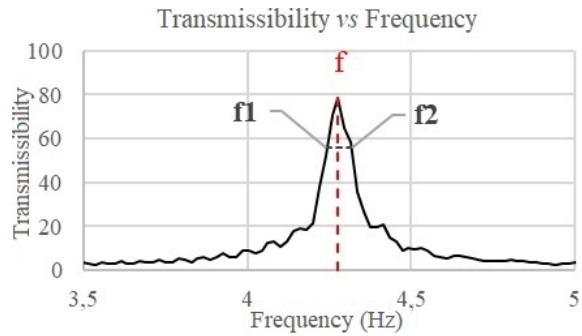


Figure 4. Bandwidth

$$\xi = \frac{f_2 - f_1}{2 \times f} \quad (8)$$

Where  $f$  is the frequency with maximum amplitude (Hz),  $f_1$  and  $f_2$  are the medium power frequencies (Hz).

### 2.6. Equation of motion

Based on the forces detailed in the previous sections, the equation of the MDOF system will be established, taking into account Newton's second law of motion, it is obtained Equation (9).

$$[M] \times \{\ddot{u}\} + [C] \times \{\dot{u}\} + [K] \times \{u\} = -[M] \times \{\iota\} \times \{\ddot{x}_o\} \quad (9)$$

Where  $\{\iota\}$  is the positioning vector,  $\{\ddot{x}_o\}$  the floor acceleration for each time instant and  $u$  is the relative coordinate of each degree of freedom with respect to the base.

Figure 5 presents the forces acting on the system.

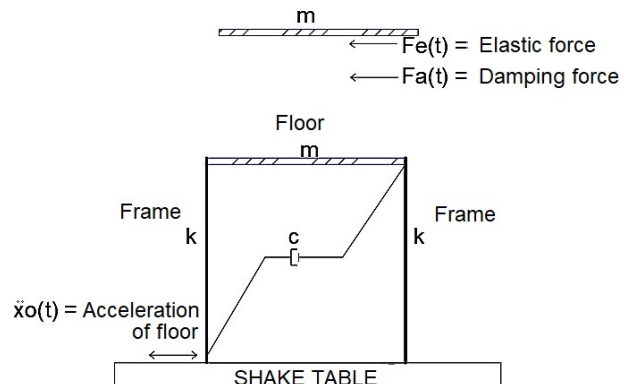
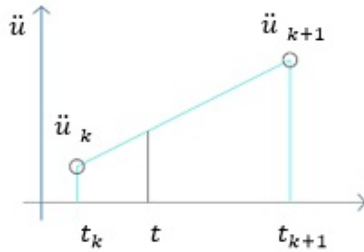


Figure 5. Acting forces

### 2.7. Newmark's method

It is a method very versatile for calculating the response of a dynamic system. In 1959, N. M. Newmark developed a family of methods depending on the law of variation between consecutive time instants [11]; the linear acceleration method was the one used here, as shown in Figure 6.



**Figure 6.** Linear acceleration

The matrix representation of the method applied for obtaining the responses of acceleration, velocity and position in time for a system with one degree of freedom, is shown in expression (10), where the response at instant  $k + 1$  only depends on the response at instant  $k$  [11].

$$\begin{pmatrix} u_{k+1} \\ \dot{u}_{k+1} \\ \ddot{u}_{k+1} \end{pmatrix} = [A] \times \begin{pmatrix} u_k \\ \dot{u}_k \\ \ddot{u}_k \end{pmatrix} + [B] \times \ddot{x}_{o_{k+1}} \quad (10)$$

Where  $[A]$ ,  $[B]$  are constant matrices that depend on the frequency, damping, rigidity and time interval, and  $\ddot{x}_{o_{k+1}}$  is floor acceleration at instant  $k + 1$  [12] and [18]

### 2.7.1. Stability of the method

There are two types of methods depending on their stability: conditionally stable and unconditionally stable [11].

Conditionally stable procedures depend on the passage of time and unconditionally stable procedures are independent of the passage of time [11].

Newmark's method based on linear acceleration is conditionally stable, and must comply with expression (11) to make possible its application.

$$\frac{\Delta t}{T} < 0,551 \quad (11)$$

Where  $\Delta t$  is the time interval and  $T$  is the period of the system.

## 2.8. Modal analysis

It enables calculating the response of the structure based on the vibration modes. For this purpose, it is important to define its dynamic properties: frequency, damping and modal shapes for each mode [19].

This analysis is very useful because it enables decomposing the responses of a structure in models of one degree of freedom, and combine them to obtain the response of the MDOF system.

### 2.8.1. Vibration frequencies and modes

In the damped system with multiple degrees of freedom, it should be established natural frequencies and modal shapes, considering it as a system subject to free vibration and without damping, such that in expression (9) the terms floor acceleration and damping become zero, thus resulting in expression (12).

$$[M] \times \ddot{u} + [K] \times \{u\} = 0 \quad (12)$$

Solving this differential equation yields expression (13), which is the base for solving the eigenvalues and eigenvectors problem [11].

$$[[K] - [M] \times \{\omega^2\}] \times \{\phi\} = 0 \quad (13)$$

Equation (13) corresponds to a system of simultaneous homogeneous equations, which by definition only has a non-trivial solution, therefore, the determinant of the coefficient matrix is zero, as indicated in Equation (14) [20].

$$|[K] - [M] \times \{\omega^2\}| = 0 \quad (14)$$

When expanding the determinant, it is obtained a polynomial of order  $2n$  ( $n$ : number of vibration modes), where  $\omega^2$  is the variable. This equation is known as «equation of frequencies». The solutions are called eigenvalues, and their square roots correspond to the natural frequencies  $\omega$  of the system [21].

In order to determine the eigenvectors or vibration modes  $\phi$ , the natural frequencies  $\omega$  are substituted in equation (13), and such equation is solved.

### 2.8.2. Orthogonality of the modes

The previous analysis enables demonstrating that the vibration modes corresponding to different frequencies fulfill the orthogonality condition, which is shown in the following equation (15) [11].

$$\begin{aligned} \{\phi_i\}^T \times [M] \times \{\phi_j\} &= 0 \\ \{\phi_i\}^T \times [K] \times \{\phi_j\} &= 0 \end{aligned} \quad (15)$$

$i \neq j$  Where  $i, j$ : vibration modes

Where  $\phi_i$  y  $\phi_j$  are modal shapes for the modes  $i$  and  $j$ ,  $[M]$  the mass matrix and  $[K]$  the rigidity matrix.

From this it is obtained that the system may be solved for each vibration mode as a separate system, without the influence of one mode with respect to the other, and the response of the entire system is defined based on expression (16).

$$\begin{aligned} \{x\} &= \{\phi_1\} \times q_1(t) + \{\phi_2\} \times q_2(t) + \dots + \{\phi_n\} \times q_n(t) \\ \{\dot{x}\} &= \{\phi_1\} \times \dot{q}_1(t) + \{\phi_2\} \times \dot{q}_2(t) + \dots + \{\phi_n\} \times \dot{q}_n(t) \\ \{\ddot{x}\} &= \{\phi_1\} \times \ddot{q}_1(t) + \{\phi_2\} \times \ddot{q}_2(t) + \dots + \{\phi_n\} \times \ddot{q}_n(t) \end{aligned} \quad (16)$$

Where  $\phi_i$  is modal shape, and  $q$ ,  $\dot{q}$  and  $\ddot{q}$  are the modal coordinates of position, velocity and acceleration, respectively, for the  $i$ -th mode.

Replacing the response  $\{x\}$ ,  $\{\dot{x}\}$  and  $\{\ddot{x}\}$  based on the sum of the modes, and pre-multiplying by the transpose of the modal shapes matrix, it is obtained equation (17).

$$[\Phi]^T [M] [\Phi] \times \ddot{q}_n + [\Phi]^T [C] \times [\Phi] \times \dot{q}_n + [\Phi]^T \times [K] \times [\Phi] \times q_n = -[\Phi]^T \times [M] \times \{\iota\} \times \ddot{x}_o \quad (17)$$

Based on equation (17) and the property of orthogonality, it may be defined equation (18) for each vibration mode.

$$[\phi_n]^T [M] [\phi_n] \times \ddot{q}_n + [\phi_n]^T [C] \times [\phi_n] \times \dot{q}_n + [\phi_n]^T \times [K] \times [\phi_n] \times q = -[\phi_n]^T \times [M] \times \{\iota\} \times \ddot{x}_o \quad (18)$$

The relative dynamic responses (position, velocity and acceleration) are obtained at each time instant for each modal coordinate, using equation (18) and with the help of Newmark's method of linear acceleration.

## 2.9. Design of the program

### 2.9.1. Matlab programming language

The ATH Dynamic responses program has been developed in the software Matlab, which is a programming

language with a friendly working environment. It enables working in console mode (it only presents results based on expressions introduced) and in routine mode (programs with coded commands and enables to make and store programs) [10] and [22].

The most important Matlab feature is that it enables handling vectors and matrices directly, and besides the coding is not complex [10].

The project was made in routine mode, since a program with coded commands was run and a GUIDE created, which enabled improving the graphical user interface.

### 2.9.2. ATH Dynamic responses program

The ATH Dynamic responses program is based on Newmark's numerical method considering linear acceleration for calculating the response of systems with 1 DOF in modal analysis.

Geometrical features, rigidity of the frame legs and mass considered as concentrated in each floor should be entered into the program. Based on this it is obtained relative dynamic responses (position, velocity and acceleration) and modal properties of the physical model (frequencies, modes and percentage of participative mass).

In order to understand the functionality of the program, Figure 7 indicates its flow diagram.

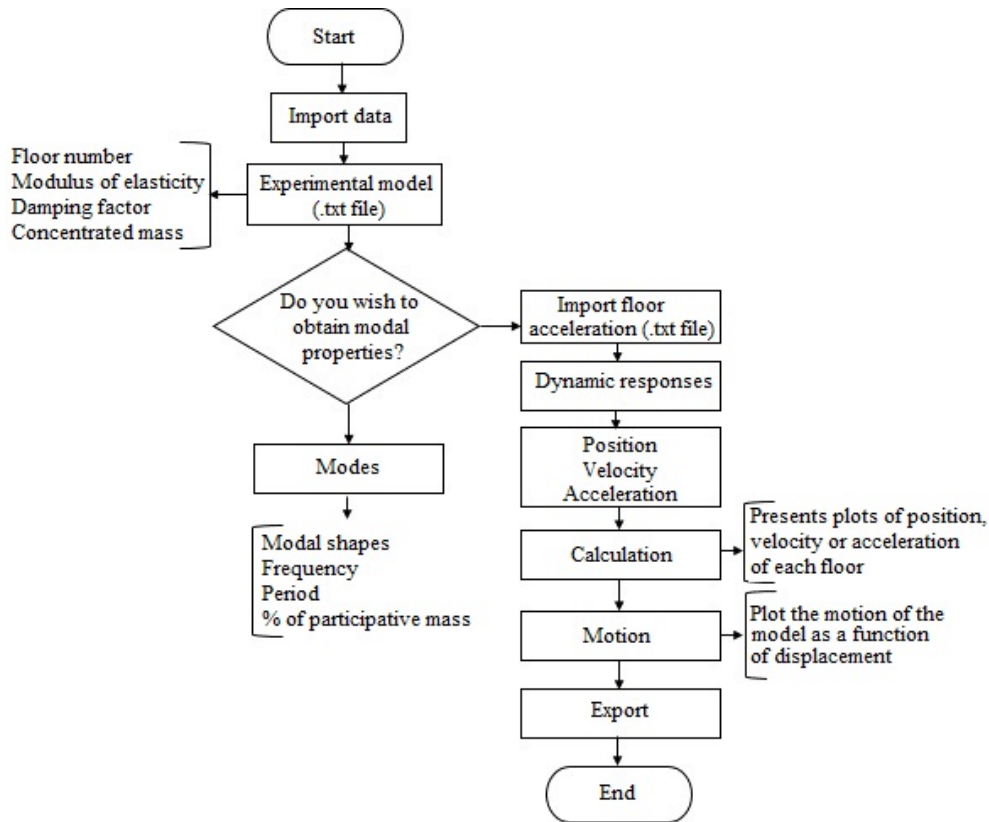


Figure 7. Flow diagram of the ATH Dynamic responses program

### 2.10. Data processing

The data obtained by the accelerometers need to be corrected by baseline and by filtering unwanted frequencies. To achieve this, it was used a low pass Butterworth filter [23], with a cut-off frequency of 16 Hz. The AB signal program [24] was used for this purpose.

### 2.11. Instrumentation

In general, the instrumentation to measure the dynamic response of a structure consists of the installation of sensors that record dynamic responses (velocity, acceleration and displacement) [25].

The purpose of the instrumentation is registering the response in front of displacement, internal motions, earthquakes and observing the behavior of structures or models [24].

The acquisition of the project data was carried out by means of PCB Piezotronics accelerometers [25], which have the frequencies and sensitivities shown in Table 1.

Table 1. Properties of the accelerometers

Type	Frequency	Sensitivity
Normal accelerometer	2 Hz – 5 kHz	100 m V/g
Normal accelerometer	1 Hz – 5 kHz	100 m V/g
Miniature accelerometer	1 Hz – 4 kHz	100 m V/g

### 2.12. Shake Table II

The test in a shake table is the most direct way to simulate the dynamic behavior of structures. The models will be limited to be not very heavy, of scaled dimensions and not very rigid [26].

Shake Table II was originally developed by the University Consortium on Instructional Shake Tables (UCIST) [6]. It is a mechanical device, which consists of an upper plate of  $45.7 \times 45.7 \text{ cm}^2$  where the model is anchored, a lower plate of  $60.9 \times 45.7 \text{ cm}^2$  and a DC motor with a power of 400 W. The table withstands a load of 7.5 kg and an acceleration of 2.5 g and enables motions with displacements up to  $\pm 7.62 \text{ cm}$  [6].

**2.13. Materials**

The equipment used for carrying out this project is constituted by a Shake Table II [6] and accelerometers PCB Piezotronics [25], described in sections 2.11 and 2.12.

The experimental models are constituted by acrylic and stainless steel. The features and dimensions of the materials are specified in Tables 2 and 3.

**Table 2.** Specifications of the materials for frame legs and floors

Material	Thickness (m)	Width (m)	Length (m)	I (m <sup>4</sup> )	E (kN/m <sup>2</sup> )
Frame Stainless Steel	7E <sup>-4</sup>	0,06	0,3	1,715E <sup>-12</sup>	1,80E <sup>+11</sup>
Floor acrylic	0,01	0,06	0,31		

**Table 3.** Mass of frame legs and floors

	Material	Mass (g)
Floors	Acrílico	232-234
Frame model 1	Acero inoxidable	102
Frame model 2	Acero inoxidable	204
Frame model 3	Acero inoxidable	299

Figure 8 presents drawings of the experimental models that were built. Figure 9 indicates the dimensions of the model with 3 degrees of freedom and, besides, how the mass concentration for the theoretical model was made, based on the experimental model, and Figure 10 shows an image of the real model.

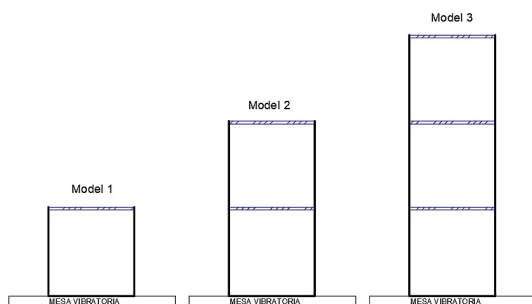


**Figure 8.** Models of one, two and three floors

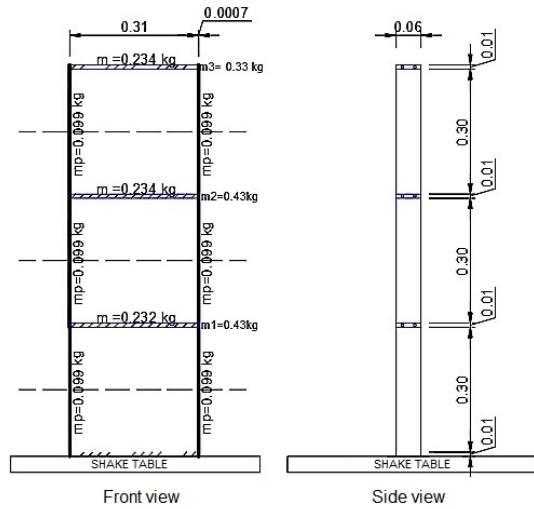


**Figure 9.** Dimensions of the model with 3 degrees of freedom and mass concentration



**Figure 10.** Experimental model of the model with 3 degrees of freedom

**3. Results and discussion**

Results show frequencies, damping factors, absolute accelerations of the experimental models and their comparison with the theoretical results provided by the ATH Dynamic responses program.

### 3.1. Experiment 1. Determining the frequencies and damping factors of each model

The frequencies were obtained theoretically using the ATH Dynamic responses program and verified with the SAP2000 software [27]. For obtaining the experimental frequency and the damping factor, a sweep of frequencies was performed with the Shake Table II.

It was carried out a baseline and filtering correction process, as explained in section 2.10. Based on this, the fast Fourier transform available in Matlab [23] was used, and transmissibility vs. frequency plots were obtained, as shown in Figures 11, 12 and 13, where the abscissa of each peak in the plot corresponds to the frequency of each mode and, besides, it enables

obtaining the damping factor applying equation (8). The percentage error in the analytical frequency was obtained with respect to the experimental acceleration.

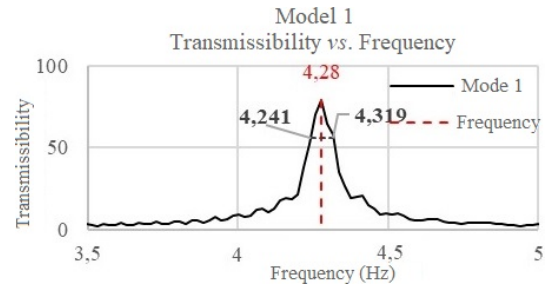
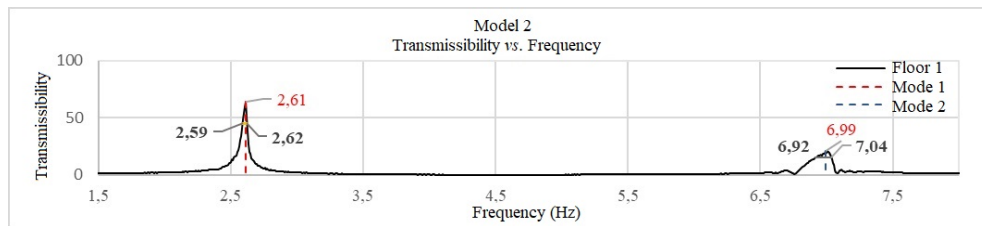
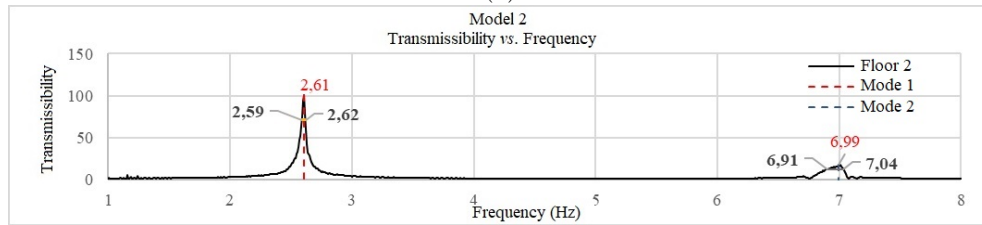


Figure 11. Frequency and bandwidth for the model

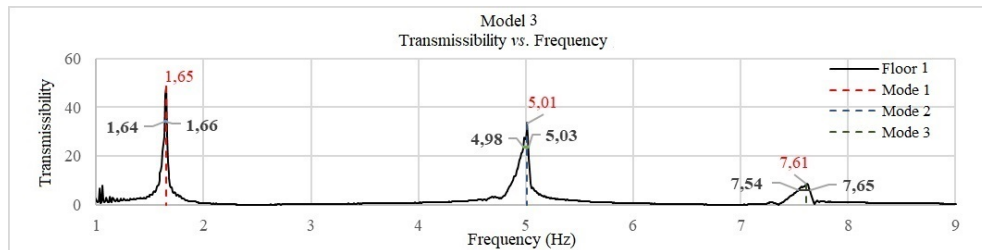


(a)

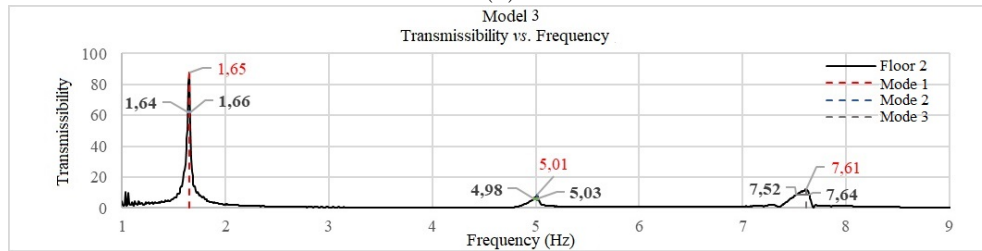


(b)

Figure 12. Frequency and bandwidth for model 2 (a) floor 1 and (b) floor 2



(a)



(b)

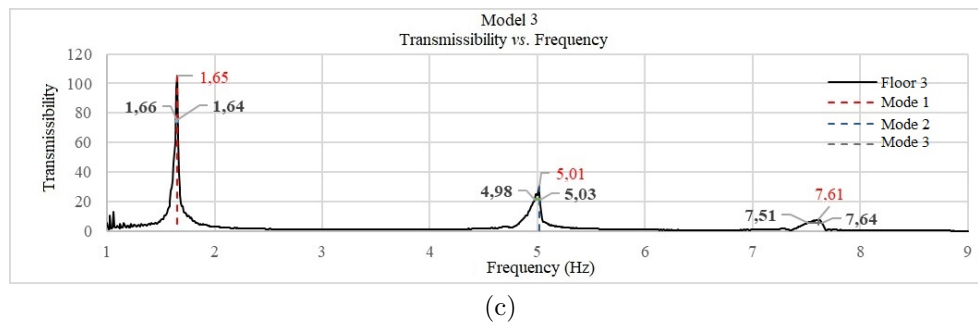


Figure 13. Frequency and bandwidth for model 3 (a) floor 1, (b) floor 2 and (c) floor 3

### 3.1.1. Frequencies and damping factor for model 1

Figure 11 shows the plots that enabled obtaining the theoretical frequency and the damping factor, and Table 4 displays these values.

The peak of Figure 11 shows that the experimental frequency for model 1 is 4.28 Hz.

Table 4. Frequency and damping for model 1

Mode	ATH Dynamic responses		Damping	
	f (Hz)	Exp. f (Hz)	% error	$\xi$ (%)
1	4,58	4,28	6,55	1,44

### 3.1.2. Frequencies and damping factor for model 2

Figures 12 (a) and (b) show the plots that enabled obtaining the frequencies and damping factors for the two modes, and Table 5 presents the results.

The peaks of Figures 12 (a) and (b) are the experimental frequencies, which for mode 1 is 2.61 Hz and for mode 2 6.99 Hz.

Table 5. Frequency and damping for model 2

Mode	ATH Dynamic responses		Damping	
	f (Hz)	Exp. f (Hz)	% error	$\xi$ (%)
1	2,61	2,60	0,38	0,57
2	6,53	6,99	7,07	0,85

### 3.1.3. Frequencies and damping factor for model 3

Figures 13 (a), (b) and (c) show the plots that enabled obtaining the frequencies and damping factors for the 3 modes, and Table 6 presents the results.

The peaks of Figures 13 (a), (b) and (c) are the experimental frequencies, which for mode 1 is 1.65 Hz, for mode 2 5.01 Hz and for mode 3 7.61 Hz.

Table 6. Frequency and damping for model 3

Mode	ATH Dynamic responses		Damping	
	f (Hz)	Exp. f (Hz)	% error	$\xi$ (%)
1	1,91	1,65	13,61	0,55
2	5,25	5,01	4,57	0,49
3	7,36	7,6	3,26	0,85

## 3.2. Experiment 2. Dynamical response of the model to floor acceleration

The dynamical response was obtained when subjecting the experimental models to a scaled seismic record. The seismic record used was El Centro and its scaling was carried out using the software of the Shake Table II; the record was scaled based on maximum displacement of 4 cm.

The results presented in the following correspond to absolute accelerations, since these are the ones provided directly by the accelerometers, and they were compared with the absolute accelerations obtained from the ATH Dynamic response program, based on expression (19):

$$\ddot{x} = \ddot{u} + \ddot{x}_o \quad (19)$$

Where  $\ddot{x}$  is absolute acceleration,  $\ddot{u}$  relative acceleration and  $\ddot{x}_o$  acceleration in the base.

### 3.2.1. Base acceleration record for Model 1: El Centro earthquake

Figure 14 shows the experimental acceleration and the theoretical acceleration for model 1, and Table 7 the maximum theoretical and experimental accelerations.

Table 7. Maximum accelerations for model 1

Acceleration (m/s <sup>2</sup> ) Floor 1		
Theoretical	Experimental	% error
8,707	7,657	13,711

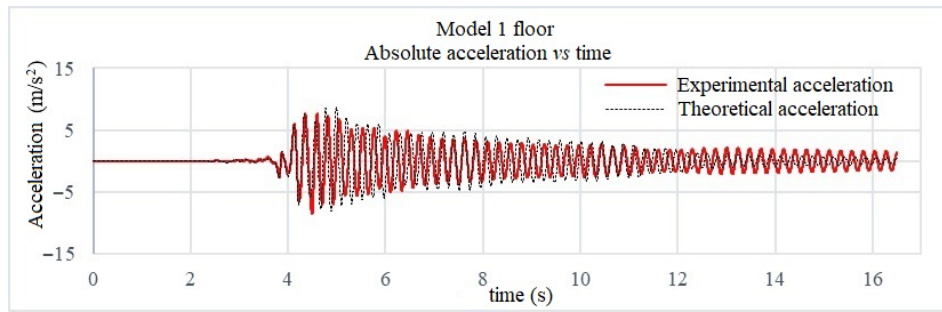


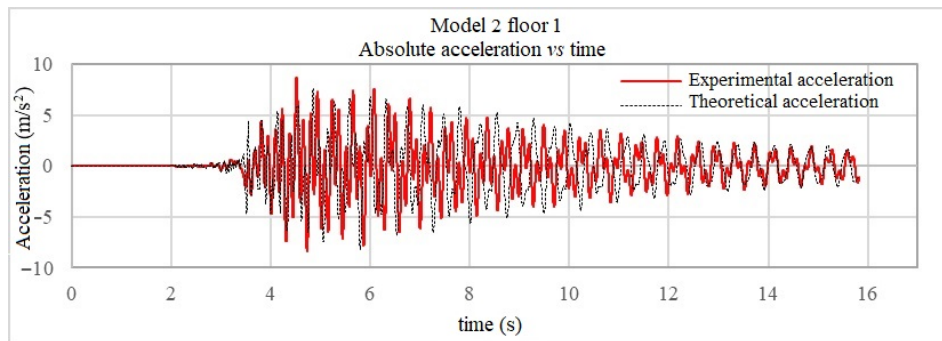
**Figure 14.** Experimental and theoretical absolute acceleration for model 1, with acceleration in the base of the El Centro earthquake

**3.2.2. Base acceleration for Model 2: El Centro earthquake**

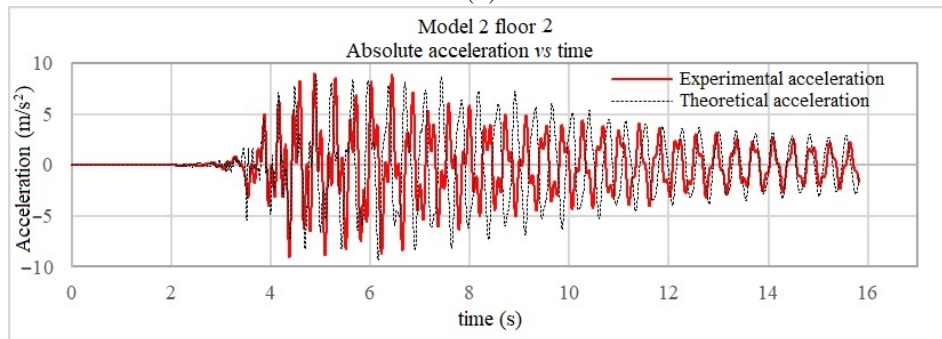
Figures 15 (a) and (b) show the experimental acceleration and the theoretical acceleration for model 2, and Table 8 the maximum theoretical and experimental accelerations.

**Table 8.** Maximum accelerations for model 2

	Acceleration (m/s <sup>2</sup> )		
	Theoretical	Experimental	% error
Piso 1	7,585	8,678	12,586
Piso 2	8,989	9,021	0,353



(a)



(b)

**Figure 15.** Experimental and theoretical absolute acceleration for model 2, with acceleration in the base of the El Centro earthquake: (a) floor 1, (b) floor 2

**3.2.3. Base acceleration for Model 3: El Centro earthquake**

Figures 16 (a), (b) and (c) show the experimental acceleration and the theoretical acceleration for model 3, and Table 9 the maximum theoretical and experimental accelerations.

**Table 9.** Maximum accelerations for model 3

	Acceleration (m/s <sup>2</sup> )		
	Theoretical	Experimental	% error
Piso 1	5,225	5,033	3,824
Piso 2	5,297	5,698	7,043
Piso 3	5,967	5,845	2,095

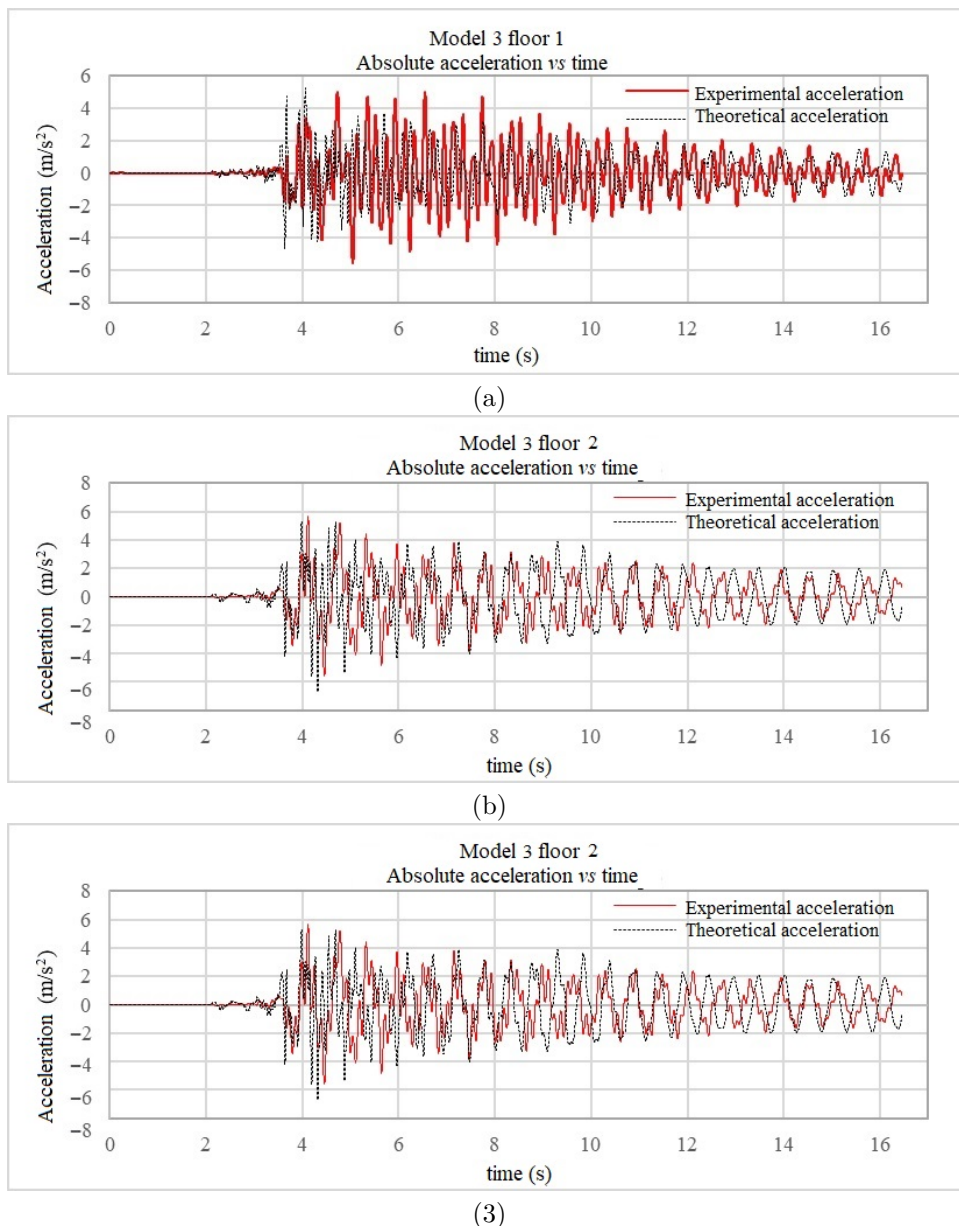


**Figure 16.** Experimental and theoretical absolute acceleration for model 3, with acceleration in the base of the El Centro earthquake: (a) floor 1, (b) floor 2, (c) floor 3

When graphically comparing the models, it was observed that the experimental acceleration has larger amplitude in most of the cases, however, in general the shapes of the experimental and theoretical plots are similar.

#### 4. Conclusions

Based on the experimental results and the theoretical results of the models, it may be argued that the method which uses the Fourier transform to obtain the frequencies is appropriate, because the results are similar between experimental and theoretical frequencies.

The damping factor obtained by means of the bandwidth is consistent in terms of the values obtained per floor, since each floor provided similar values of damping factor per mode, and such factors were useful for theoretical modeling, and thus being able to obtain the damping matrix and the dynamical responses.

The experimental modeling of the model helped us to observe in a real manner how a model behaves when a sinusoidal acceleration or an acceleration of a scaled earthquake is applied, and enabled verifying the values obtained analytically with respect to the experimental ones.

As future work, it may be implemented to obtain the dynamical properties of three-dimensional systems

that exhibit irregularity in plant and elevation.

A mismatch may be observed between experimental and theoretical responses regarding absolute accelerations, due to the consideration of the time 0 in which the experimental models were at rest.

## References

- [1] INEC, *Reconstruyendo las cifras luego del sismo. Memorias*. Instituto Nacional de Estadísticas y Censos. Ecuador, 2017. [Online]. Available: <https://bit.ly/3gEu4Al>
- [2] Instituto Geofísico. (2020) Cuatro años después del terremoto de Pedernales: un testimonio sobre el peligro sísmico en el Ecuador. [Online]. Available: <https://bit.ly/3dW198V>
- [3] MIDUVI, *Norma ecuatoriana de la construcción. NEC-SE-DS. Cargas Sísmicas. Diseño Sismoresistente*. Ministerio de Desarrollo Urbano y Vivienda. Ecuador, 2014. [Online]. Available: <https://bit.ly/3xpr2FY>
- [4] D. Gutiérrez Calzada, *Sistema de múltiples grados de libertad. Análisis modal espectral*. Universidad Autónoma del Estado de México. México, 2018. [Online]. Available: <https://bit.ly/3dSSQe2>
- [5] D. Henao Ángel, “Identificación de las propiedades dinámicas de una estructura sometida a vibración ambiental empleando análisis espectral,” Master’s thesis, 2013. [Online]. Available: <https://bit.ly/3sQd7Fu>
- [6] QUANSER, “SHAKE TABLE II bench-scale single-axis motion simulator,” QUANSER INNOVATE EDUCATE, Tech. Rep., 2020. [Online]. Available: <https://bit.ly/3tWivbj>
- [7] B. A. Guaygua Quillupangui, V. N. Colcha Guachamín, and E. L. Tibán Guacolante, “Estudio comparativo del comportamiento dinámico de modelos estructurales teóricos y modelos estructurales experimentales,” 2018. [Online]. Available: <https://bit.ly/3gJDR8i>
- [8] P. X. Villalba Nieto, A. I. Cepeda Aveiga, and N. A. Hipocuro Simbaña, “Análisis de las frecuencias fundamentales de modelos estructurales con excitaciones sísmicas,” 2019. [Online]. Available: <https://bit.ly/3dXrBio>
- [9] L. W. Morales Gubio, P. E. Chimarro Quishpe, and M. G. Coronel Armas, “Análisis de una estructura de un edificio de 9 piso a escala en Quito, sometido a cargas sísmicas en la mesa de vibración,” 2018. [Online]. Available: <https://bit.ly/32Ts5A4>
- [10] J. E. Hurtado Gómez, *Introducción de la dinámica de estructuras*. Universidad Nacional de Colombia, sede Manizales, 2000. [Online]. Available: <https://bit.ly/3ezgOKC>
- [11] A. K. Chopra, *Dinámica de Estructuras*. Pearson Educación de México, 2014. [Online]. Available: <https://bit.ly/3dROhkd>
- [12] Y. Bai and Z.-D. Xu, *Structural Dynamics for Structural Engineers*. John Wiley & Sons, Inc., 2019. [Online]. Available: <https://bit.ly/3tYARsf>
- [13] R. R. Craig and A. J. Kurdila, *Fundamentals of Structural Dynamics*. John Wiley & Sons, Inc., 2006. [Online]. Available: <https://bit.ly/2S6J6EK>
- [14] O. Möller, M. Rubinstein, and J. P. Ascheri, “Análisis del amortiguamiento proporcional a la rigidez tangente en sistemas dinámicos no lineales,” *Asociación Argentina de Mecánica Computacional*, vol. XXX, no. 14, pp. 1277–1293, 2011. [Online]. Available: <https://bit.ly/3evo9L8>
- [15] D. J. Inman, *Vibration with Control*. John Wiley & Sons, Inc, 2017. [Online]. Available: <https://bit.ly/3vidqKE>
- [16] R. Boroschek and F. Hernández, “Corrección de sobreestimación del amortiguamiento en el método de ancho de banda del espectro de potencia,” in *X Chilean Conference of seismology and earthquake engineering. ACHISINA*, 2010. [Online]. Available: <https://bit.ly/32Uy2wp>
- [17] M. Paz, *Dinámica estructural teoría y cálculo*. Editorial Reverté, 1992. [Online]. Available: <https://bit.ly/32Pw94l>
- [18] P. L. Sierra, O. Möller, J. P. Ascheri, and M. Poliotti, “Dinámica estructural, comparación y análisis de la propagación de vibraciones en estructuras,” in *XXIII Congreso de Métodos Numéricos y sus Aplicaciones (ENIEF 2017)*, 2017. [Online]. Available: <https://bit.ly/32Wc780>
- [19] M. Rodríguez, “Análisis modal operacional: Teoría y práctica,” 2005. [Online]. Available: <https://bit.ly/3gPU5wm>
- [20] H. Garzón Molano, “Instrumentación geotécnica. aplicación y soporte para la toma de decisiones,” 2018. [Online]. Available: <https://bit.ly/3aF31Ru>
- [21] L. E. García Reyes, *Dinámica estructural aplicada al diseño sísmico*. Universidad de los Andes. Bogotá – Colombia, 1998.
- [22] R. Aguiar Falconi, *Dinámica de estructuras con MatLab*. Centro de Investigación Científica, CEINCI – Universidad de las Fuerzas Armadas, ESPE, 2006. [Online]. Available: <https://bit.ly/3dU0dlC>

- [23] MathWorks. (2021) Matlab para inteligencia artificial. 1994-2021 The MathWorks, Inc. [Online]. Available: <https://bit.ly/2S9ay4I>
- [24] B. D. Erazo Silva and P. A. Vargas Yépez, “Desarrollo de un software para procesamiento y corrección de registros, y generación de espectros de respuesta sísmica,” 2020. [Online]. Available: <https://bit.ly/3u0ZafB>
- [25] DataLights. (2020) Soluciones de control e iluminación. Datalights, Cia. Ltda. [Online]. Available: <https://bit.ly/3aH2T3U>
- [26] L. Bustos, F. Zabala, J. Santalucía, and A. Masanet, “Estudio del comportamiento dinámico de un modelo de mampostería encadenada mediante un ensayo en mesa vibratoria,” in *JUBILEO, XXIX Jornadas Sudamericanas de Ingeniería Estructural, Argentina*, 2020. [Online]. Available: <https://bit.ly/2QZYP7W>
- [27] Computers and Structures. (2021) Sap 2000 computer software for structural and earthquake engineering. [Online]. Available: <https://bit.ly/2S75M7Q>



# INFLUENCE OF THE ZINC CHROMATE COATING ON THE CORROSION OF ASTM A-500 AND GALVANIZED A-500 STEEL EXPOSED INTO A SALT FOG CORROSION CHAMBER

## INFLUENCIA DEL RECUBRIMIENTO DE CROMATO DE ZINC EN LA CORROSIÓN DE LOS ACEROS ASTM A-500 Y A-500 GALVANIZADO EXPUESTOS EN UNA CÁMARA DE NIEBLA SALINA

Cristian Guilcaso<sup>1,\*</sup> , Leonidas Ramírez<sup>2</sup> , Augusto Coque<sup>3</sup> , Xavier Vaca<sup>2</sup> ,  
 Diego Molina<sup>1</sup> , Isaac Simbaña<sup>2</sup> 

Received: 13-11-2020, Received after review: 04-02-2021, Accepted: 09-03-2021, Published: 01-07-2021

### Abstract

In this research work it has been analyzed the influence of the Zinc chromate coating on the corrosion of ASTM A-500 and galvanized A-500 steels exposed in a salt spray corrosion chamber, according to the ASTM B117 Standard. Two surface cleaning methods were used prior to applying the coating, considering the SSPC-SP-3 and SSP-SP-5 standards, namely a mechanical cleaning and a blast cleaning. The samples were put into the chamber with exposure times of 200, 250 and 350 h. Different equipment were used for recording the information that was used to calculate the corrosion rate. Through visual assessments according to the ASTM-D610 and ASTM D-714 standards, the corrosion degree and the blistering frequency, respectively, were determined. The materials without coating and coated after the two surface cleaning methods were compared. The results obtained have demonstrated that galvanized steel exhibited a lower corrosion rate.

**Keywords:** ASTM-500, anticorrosive coatings, salt spray corrosion chamber

### Resumen

En esta investigación se ha analizado la influencia del recubrimiento de cromato de zinc en la corrosión del acero ASTM A-500 y A-500 galvanizado expuesto en una cámara de niebla salina acorde a la norma ASTM B117. Se realizaron dos métodos de limpieza superficial antes de la aplicación del recubrimiento, según la normas SSPC-SP-3 y SSPC-SP-5, una limpieza mecánica y otra con chorro presurizado. Las probetas se introdujeron en la cámara con tiempos de exposición de 200, 250 y 350 h. Se utilizaron diferentes equipos para registrar información que fue utilizada en el cálculo de la velocidad de corrosión. Con evaluaciones visuales, utilizando las normas ASTM D-610 y ASTM D-714, se determinó el grado de corrosión de las probetas y la frecuencia de ampollas, respectivamente. Se comparó los materiales sin recubrimiento y los dos métodos de limpieza superficial. Los resultados obtenidos han demostrado que el acero galvanizado presentó una menor velocidad de corrosión.

**Palabras clave:** ASTM-500, recubrimientos anticorrosivos, cámara de niebla salina

<sup>1,\*</sup>Facultad de Ingeniería Civil y Mecánica, Universidad Técnica de Ambato, Ambato, Ecuador.

Autor para correspondencia ✉: erojas@ups.edu.ec.

<sup>2</sup>Carrera de Ingeniería Mecánica, Universidad Politécnica Salesiana, Quito, Ecuador.

<sup>3</sup>Carrera de Ingeniería Industrial, Universidad Politécnica Salesiana, Quito, Ecuador.

Suggested citation: Guilcaso, C.; Ramírez, L.; Coque, A.; Vaca, X.; Molina, D. and Simbaña, I. (2021). «Influence of the Zinc Chromate coating on the corrosion of ASTM A-500 and galvanized A-500 steel exposed into a salt fog corrosion chamber». INGENIUS. N.º 26, (july-december). pp. 63-70. DOI: <https://doi.org/10.17163/ings.n26.2020.06>.

## 1. Introduction

The ASTM A-500 steel, as rectangular or circular tube, is commonly used in the construction industry, as well as in the automotive industry, due to its mechanical properties and ease of welding [1]. This steel may be treated with different methods according to the particular requirement, for instance, increasing its ductility by reducing its resistance. A common application of the steel is for manufacturing bodies of vehicles, automobiles and even trucks, both cargo and for public transportation. The design of the body of a public transportation vehicle should be carried out considering the worst-case scenario in a collision, where it must be reduced the severity of the accident for the passengers and the driver [2]. One of the main agents that may cause deformation and rupture failures is the corrosion, which affects the structure of the steel and, hence, its mechanical properties. The application of an anticorrosive coating may extend the useful life of a structural element. However, it should be applied correctly, or otherwise the corrosion may be accelerated by exhibiting delaminations or blisters. Corrosion generates mass loss, mainly by reducing the area of the cross section, and even a very small reduction may decrease the resistance of the material and generate a failure [3, 4].

The most commonly used anticorrosive treatment is galvanized, because the Zn provides cathodic protection to steel thus preventing damages produced by rust and, besides, it is a low-cost element. By means of an electrochemical galvanized coating, a steel improves its corrosion resistance and even its mechanical properties by slightly modifying its composition [5]. The Zn has recyclable and non-toxic properties, and this is why more than five million tons are used yearly in anticorrosive applications, generating savings around 2200 million USD in repairs or replacements of rusty elements [6].

In order to improve the corrosion resistance of a steel immersed in Zn, different elements may be added considering the appropriate content. Kania *et al.* [7] characterized the microstructure and analyzed the corrosion resistance of a Zn coating obtained in an immersion of Zn-AlNiBi. The authors used steel with low content of Si, 0.021 %, in samples of  $50 \times 100 \times 2$  mm submerged for 180 s in the solution studied, at 450 °C. The samples were placed inside a salt spray chamber (SSCC) with NaCl at 5 % at a temperature of  $35 \pm 2$  °C and pH between 6.8 and 7.2, from 24 to 1000 h. The mass of the samples was measured every 24 h and the results indicate that this new coating is a better anticorrosive agent than pure Zn, because the presence of corrosion was reduced 30 %, having final masses of 140.34 and 108.24 g/m<sup>2</sup>, respectively. When the coating is inspected, Bi is observed on the surface, but it is not visualized Al or Ni, and thus authors

recommend using Bi as additive instead of Pb which is environmentally harmful.

Before considering a coating to be applied at large scale in the industrial sector, various experimental tests should be carried out and the most viable alternative to analyze the corrosion rate is by means of an SSCC. Vera *et al.* [8] evaluated anticorrosive coatings in steel exposed to a marine environment, comparing field tests with an accelerated corrosion. It was used A-36 steel of  $100 \times 100 \times 3$  mm subject to blast cleaning, and a Zn-rich coating and an epoxy enamel coating were applied. The tests in the sea were conducted in Chile for 24 months, and SO<sub>2</sub> was collected to dissolve it in Na<sub>2</sub>CO<sub>3</sub> at 5 %. The loss in thickness was between 71.9 and 222.2 μm, depending on climatic conditions, and thus it was estimated a corrosion rate of 131.4 μm/year. Using an algorithm, authors determined that similar conditions in an SSCC should be implemented at 37 °C, with a humidity of 100 % and NaCl at 3.5 % during 3000 h of exposure (125 days), reducing the time to the sixth part.

The electroplating of nanocrystalline Zn in steel to improve its corrosion resistance was analyzed by Li *et al.* [6]. The experiment used a solution of NaCl at 3.5 % and the electroplating was carried out with a bath of ZnSO<sub>4</sub> with a low carbon steel, then the samples were washed and dried. By means of a scanning electron microscope (SEM), it was visualized that the rust spot reduced from 5 μm to 40 nm, and consequently the application of this coating increased corrosion resistance almost 40 times.

Stojanović *et al.* [9] evaluated the protection to corrosion of a system with two coatings in a simulated marine environment. Naval steel plates of  $120 \times 70 \times 3$  mm were subject to blast cleaning to apply two layers of anticorrosive coating, each of 150 μm, and further an anti-fouling coating. The plates were exposed for 1440 h in an SSCC at 38.08 % and a pH of 8, where two groups were selected, one for immersion and another for agitation. Results indicate that the plates that were agitated in the solution produce more microorganisms and, as a result, a greater corrosion; in addition, the second coating did not have the appropriate adherence, and thus authors recommend analyzing the chemical composition of the anticorrosive coatings

The corrosive behavior of the ASTM-SA213-T22 steel coated with Cr<sub>2</sub>O<sub>3</sub> in a saline environment at 700 °C was analyzed by Goyal *et al.* [10]. The samples were of  $22 \times 15 \times 3$  mm and coated with commercial Cr<sub>2</sub>O<sub>3</sub> with a thickness between 250 and 255 μm. A furnace was used to generate heat corrosion with Na<sub>2</sub>SO<sub>4</sub> at 60 % for 1 h, and the final mass of the samples was considered. The base material showed a larger corrosion rate compared with the Cr<sub>2</sub>O<sub>3</sub> coating that had a perfect adherence, causing that the mass of the material remained at 94.5 %.

This research is aimed at determining the influence of a zinc chromate coating in the corrosion of ASTM A-500 and galvanized A-500 steels, used for manufacturing bodies of public transportation vehicles. In this way, it will be established if it is required this prior treatment. The document is distributed as follows. The Materials and methods section describes the steps of the experimental process considering different standards for conducting it. Results presents figures and the comparative analysis of the samples after their exposure to the SSCC. At last, the Conclusions explain the results obtained and define which steel had the lowest corrosion.

## 2. Materials and methods

Figure 1 summarizes the procedure considered for the experimental development, and for obtaining the results of this research.

### 2.1. Preparation of the material

The material used was a tube of ASTM A-500 carbon steel obtained by means of cold seamless welding, used for manufacturing vehicle bodies. Using a matrix of experimental design, it was established that it is required eight samples of each material, and for such purpose, they were cut by means of an abrasive wheel using a grinder, thus getting plates of  $100 \times 50 \times 2$  mm.

### 2.2. Surface cleaning

The Society for Protective Coatings (SSPC) has regulated specific surface cleaning procedures required before applying an anticorrosive coating. Two surface cleaning methods have been chosen for this research, the first corresponds to a mechanical cleaning, according to standard SSPC-SP-3 [11], using sandpaper to remove rust layers. Afterwards, it is required a rotating wire brush as electrical tool to clean the surface and remove all debris. It is important to mention that, due to the geometry of both the material and tools, it is possible that there may remain debris hidden in the irregularities of the material.

The standard SSPC-SP-5 [12] was considered for the second surface cleaning method, which consists of using a pressurized liquid to remove all particles on the surface of the material. This method assures a total cleaning, free of delaminations, since a pressurized stream enables removing even dust and grease, such achieving a better adherence of the coating.

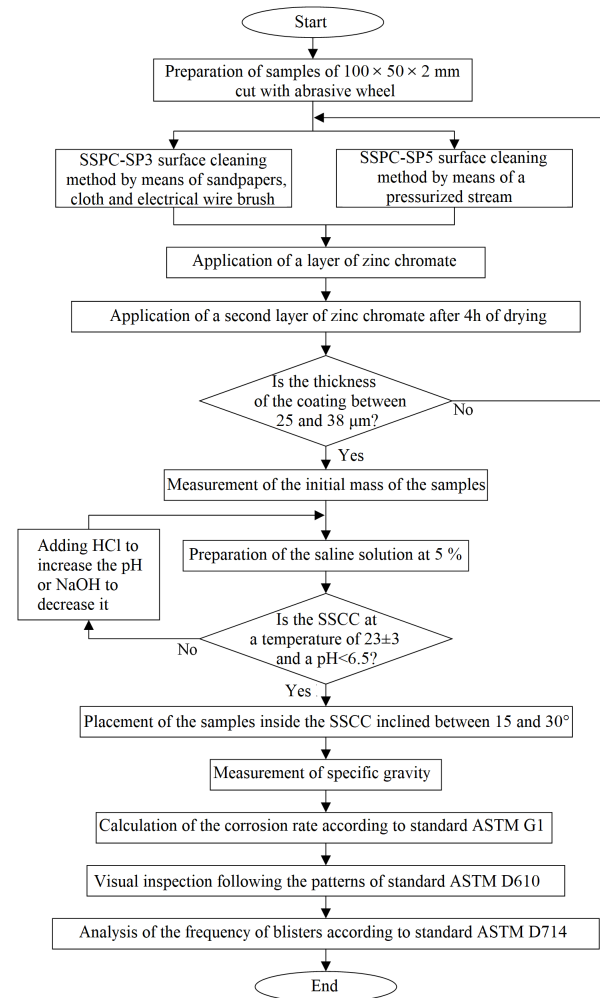


Figure 1. Flow diagram for the experimental development

### 2.3. Coating

A zinc chromate coating was applied on the eight samples of A-500 and galvanized steel, four to be cleaned with SSPC-SP-3 and the remaining four with SSPC-SP-5. This coating consists of resins and pigments that provide corrosion resistance in the presence of different atmospheric agents; in addition, it is one of the most widely used commercially.

The coating was diluted in thinner in a 4 to 1 proportion for its application using a blowtorch. According to the manufacturer, the thickness of the coating must be between 25 and 38  $\mu\text{m}$ , and thus two layers were applied with a drying time between them of 4 h at 20  $^{\circ}\text{C}$ . The Elecometer 456 was used for measuring the thickness of the coating.

### 2.4. Test in the SSCC

The ASTM B-117 standard [13] was used for the experimentation in the SSCC, which indicates preparation, procedures, prediction and results under a controlled

corrosive environment. It was used a saline solution at 5 %, with 12.72 kg of NaCl in a volume of 240 liters of distilled water.

Among the measuring instruments that were used, it is important to mention the HANNA HI9125 waterproof pH meter, to verify that the pH is less than 6.5 at an average temperature of 23 °C. If the pH value decreases, NaOH may be added, otherwise, when the pH is high, HCl is added until obtaining the required value. By means of a flow meter, 2 ml/h of NaCl were collected from the SSCC every 24 hours. An MA887 digital salinity refractometer was used as a salinity meter to determine the specific gravity of NaCl. The mass of the samples, of the base material and of the material with the coating, was measured before entering them in the SSCC, where they were placed at an inclination of 20 to 30°.

For the zinc chromate coating, the average time for the test was estimated in 250 h. Different exposure times inside the SSCC were established, having 200, 250 and 350 h to determine how this exposure time influences steel corrosion. After each period, the weight of the samples was measured again to calculate the mass loss between the initial and the final values.

### 2.5. Corrosion rate

According to the ASTM G-1 [14] standard, this parameter is defined as the thickness loss of a steel per unit time to analyze the damage produced by corrosion after the exposure. The corrosion rate ( $\dot{C}$ ) is a function of the material, as well as of the exposure time, and may be obtained as:

$$\dot{C} = (K \cdot W) \cdot (A \cdot t \cdot \delta)^{-1} \quad (1)$$

Where  $K$  remains constant at a value of  $8.76 \times 10^4$  mm/year,  $W$  is the mass loss expressed in g,  $A$  is the area of the sample in  $\text{cm}^2$ ,  $t$  are the exposure hours and  $\delta$  if the steel density in  $\text{g/cm}^3$ .

### 2.6. Visual evaluation

The ASTM D-610 standard [15] was considered for evaluating the corrosion degree on a coated surface, to determine if the coating shall be repaired or replaced. According to this standard, a scale from 1 to 10 has been established as a function of the surface area of corrosion, where 10 is used to indicate rust stains which are 0.01 % smaller than the total area, while if the corroded area is larger than 33 %, it is assigned a value of 1. This number should come along with a letter to indicate the corrosion visual pattern, stained ( $S$ ), punctuated ( $P$ ) or general ( $G$ ).

This visual evaluation is reinforced with a second inspection, which consists of evaluating the blisters produced by corrosion on the coating according to the ASTM D-714 standard [16]. A number between 0 and

10 has been assigned for identifying blisters, where 10 corresponds to a surface without imperfections, 8 indicates small blisters which are difficult to detect with the naked eye and the smaller numbers indicate increasingly bigger blisters. In addition, this number comes along with a letter that represents the frequency of presence of blisters per unit area, indicating if this frequency is few ( $F$ ), medium ( $M$ ), medium dense ( $MD$ ) or dense ( $D$ ).

## 3. Results and discussion

### 3.1. Corrosion rate

When considering the difference between the initial and final mass of the samples, it was possible to calculate the corrosion per year. In the following, values of corrosion rate obtained with Equation (1) are presented for the base material and for the samples with the SSPC-SP-3 and SSPC-SP-5 surface cleaning methods.

The samples of ASTM A-500 steel and of galvanized steel without the zinc chromate coating exhibited a corrosion rate of 1.672 and 0.535 mm/year after 200 h of exposure in the SSCC, as shown in Figure 2a. On the other hand, with the SSPC-SP-3 mechanical cleaning, the values were 0.129 and 0.044 mm/year for the A-500 and galvanized steel, respectively, for the same exposure time. At last, for the A-500 and galvanized steel samples that were subject to blast cleaning according to the SSPC-SP-5 standard, corrosion rates of 0.051 and 0.034 mm/year were obtained. The values of corrosion rate tend to grow as the exposure time increases, however, the rust on the surface of the samples may create an additional coating and this value may decrease.

After 250 h of exposure, the A-500 samples with the surface cleaning methods and zinc chromate coating decreased the value of corrosion rate, yielding 0.083 and 0.014 mm/year for methods SP-3 and SP-5, respectively, while the base material increased its corrosion to 2.092 mm/year. With the same exposure time, the galvanized steel showed opposite results, where the base material decreased its corrosion to 0.436 mm/year and the SP-3 and SP-5 methods increased in 0.058 and 0.002 mm/year, respectively, with respect to an exposure of 200 h.

At last, with an exposure time of 350 h, the base material samples of A-500 and galvanized steel had a corrosion of 1.594 and 0.142 mm/year. For the SSPC-SP-3 surface cleaning, these steels showed a corrosion rate of 0.139 and 0.103 mm/year, respectively. In addition, with the SP-5 surface cleaning method, the samples recorded values of 0.033 and 0.029 mm/year for the A-500 and galvanized steel, respectively.

The values obtained are more closely grouped for the SSPC-SP-5 cleaning, having a standard deviation of 0.0185 and 0.0036 mm/year for the A-500 and the

galvanized steel, respectively. These steels had a standard deviation for the SSPC-SP-3 method of 0.0299 and 0.03378 mm/year, respectively, and besides, 0.2679 and 0.2044 mm/year without treatment.

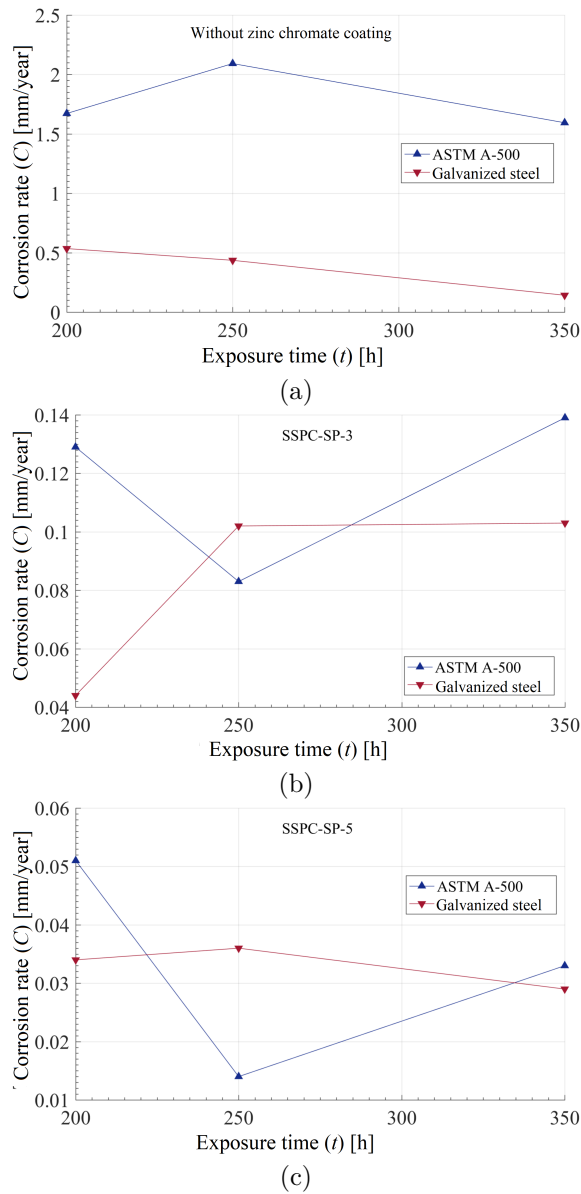


**Figure 2.** Corrosion rate for samples a) without coating, b) SSPC-SP-3 cleaning, c) SSPC-SP-5 cleaning

### 3.2. Visual evaluation

By means of an SEM microscope, it was visualized the morphology of the corrosion products in the A-500 samples. Figure 3a shows a sample without coating exposed for 300 h, where it is observed a formation generated by corrosion which is known as lepidocrocite. Figure 3b presents the analysis of the morphology of the sample with an exposure time of 350 h, where it is identified semicrystalline goethite shaped like clouds,

as well as very thin sheets of lepidocrocite, with a contour similar to roots.

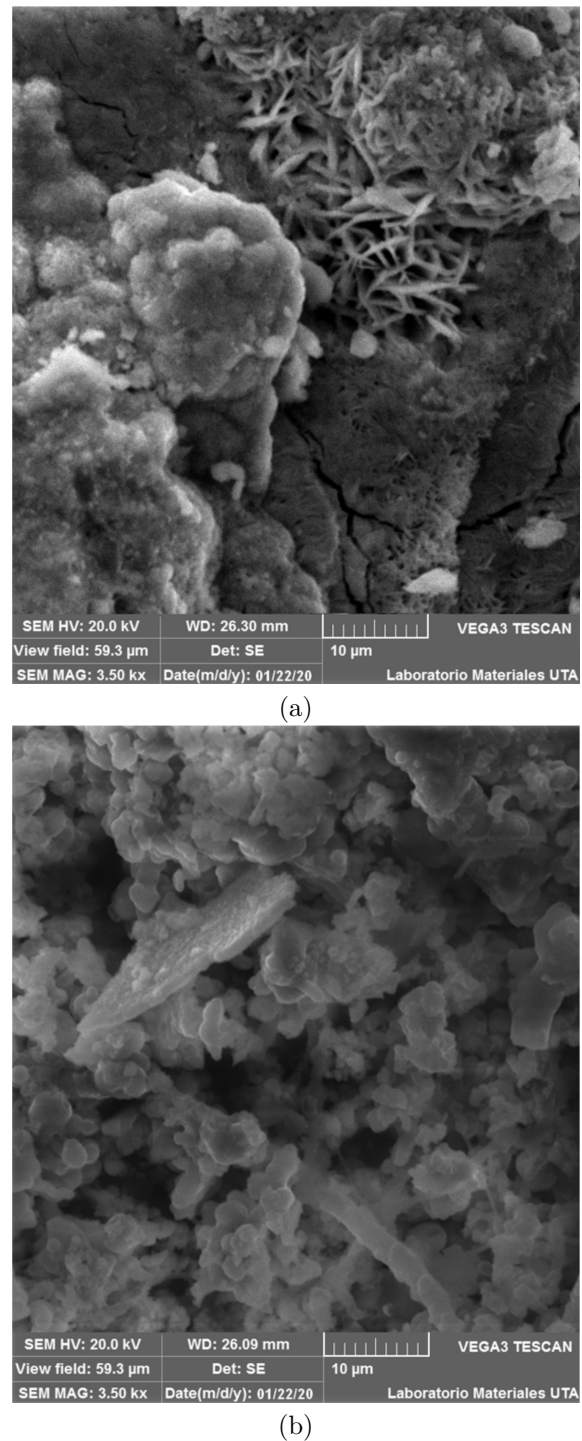


**Figure 3.** Microstructure of the ASTM A-500 steel without coating exposed in the SSCC a) 300 h, b) 350 h.

Figure 4a indicates the results of the corrosion existing in the ASTM A-500, while Figure 4b shows the corroded galvanized steel, after 200, 250 and 350 h of exposure in the SSCC. The samples appear as surfaces with a lot of corrosion, visible to the naked eye,

and even with significant accumulations, verifying the calculated values of corrosion rate.

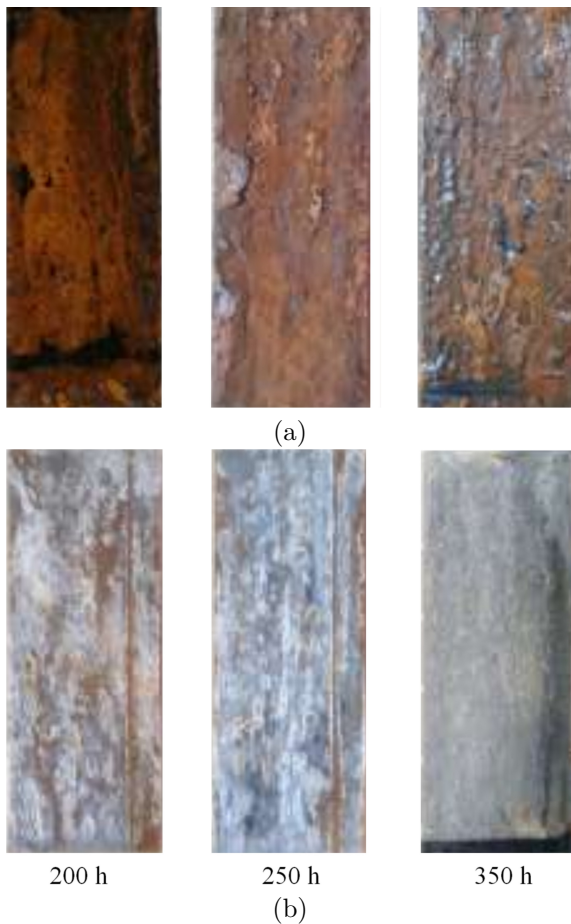


**Figure 4.** Samples of base material exposed to the SSCC a) ASTM A-500, b) galvanized steel

The patterns of the ASTM D-610 standard were used as reference to perform an evaluation of the percentage of surface corroded. In addition, this visual evaluation was complemented indicating the frequency and size of the blisters present in the samples according to the D-714 standard.

Figure 5a shows the coated A-500 samples with SSPC-SP-3 surface cleaning, where corrosion stains in about 3 % have been indicated corresponding to 5 S after 200 h. For the sample exposed for 250 h, a corrosion of 5 G has been considered and the sample that was in the SSCC for 250 h was evaluated as 3 G.

The frequency of the blisters was measured for the samples with exposure time of 200 and 350 h, indicating an evaluation of 6 M and 2 M, respectively. On the other hand, for the sample exposed for 250 h this frequency was larger, assigning it a value of 6 MD with visible blisters.

The ASTM A-500 samples with SSPC-SP-5 cleaning prior to the application of the zinc chromate, are indicated in Figure 5b, after exposure times of 200, 250 and 350 h, respectively. For the sample that was

exposed for 200 h, it was assigned a corrosion of 4 G, while the samples with exposure time of 250 and 350 h, were evaluated as 5 G.

None of the samples evidenced the existence of blisters, indicating that the coating had a good adherence.

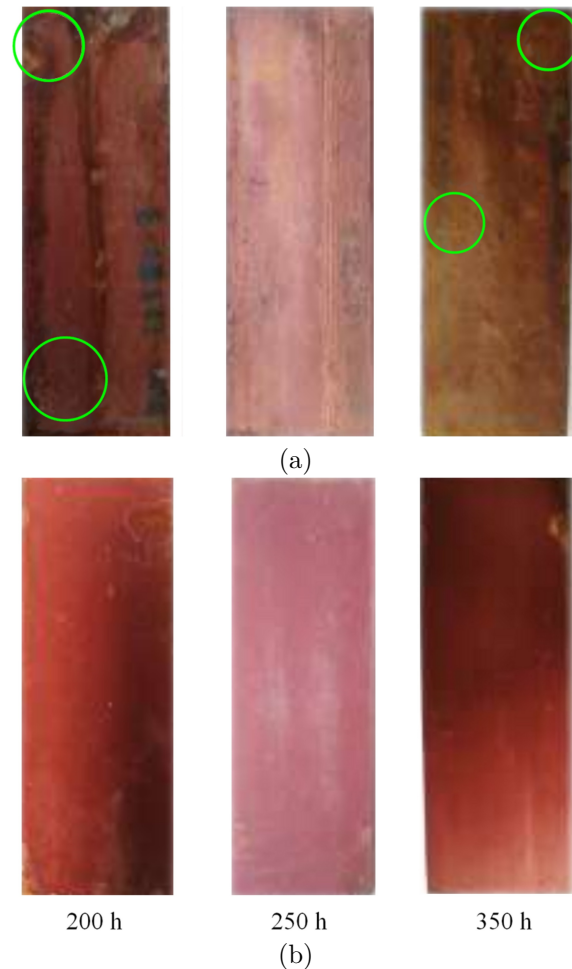


**Figure 5.** ASTM A-500 samples exposed to 200, 250 and 350 h, a) SSPC-SP-3, b) SSPC-SP-5

Figure 6a presents the galvanized steel samples cleaned with the SSPC-SP-3 method and coated with zinc chromate. In the sample that was in the SSCC for 200 h, there was evidence of corrosion stains, yielding 5 S and there were no blisters on its surface. For the sample exposed for 250 h, a general corrosion is visible, yielding 6 G and small blisters were visualized, thus assigning it a 6 M. Regarding the sample with exposure time of 350 h, a corrosion of 4 S has been assigned due to visible stains, and it had 6 F because the frequency of blisters is low, although such blisters are significant. The galvanized steel samples with SSPC-SP-5 cleaning are shown in Figure 6b.

In the galvanized steel sample with exposure time of 250 h it was not possible to visualize signals of corrosion and there are small blisters, having a frequency of 8 M. Regarding the samples exposed for 200 and

350 h, they show small corrosion stains, thus they have been assigned 5 S and none of them has shown blisters on its surface.

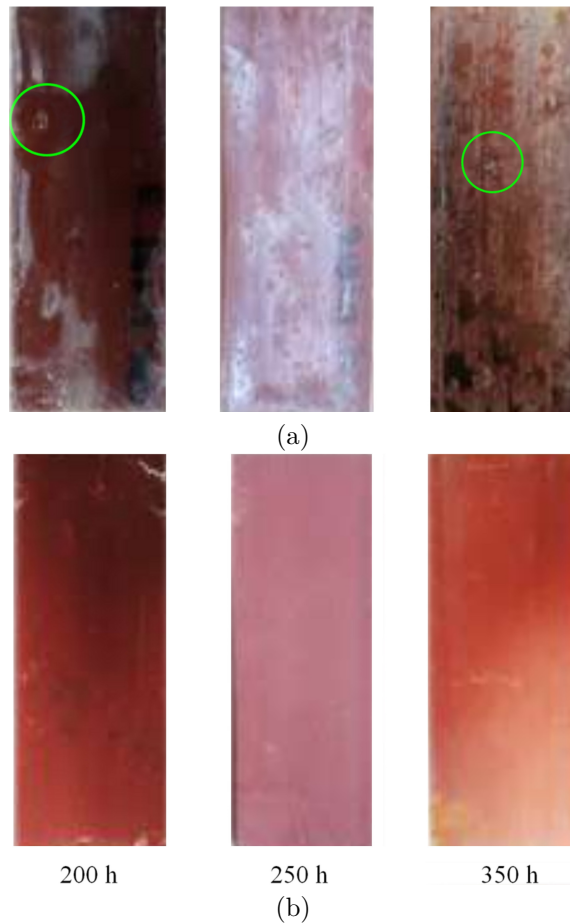


**Figure 6.** Samples of galvanized ASTM A-500 exposed for 200, 250 and 350 h, a) SSPC-SP-3, b) SSPC-SP-5

#### 4. Conclusions

The values obtained of corrosion rate for the samples indicate that the corrosion affects more during the initials hours of exposure. For the A-500 steel after 200 and 250 h of exposure, there was a corrosion rate of 1.672 and 1.594 mm/year, respectively. For the galvanized steel without coating, the values obtained were 0.535 and 0.142 mm/year for similar times. This trend remained during the tests with samples cleaned using SSPC-SP3 and SSPC-SP5 for both materials.

The A-500 steel without treatment had a maximum corrosion rate of 2.092 mm/year, in the sample exposed for 250 h in the SSCC, which is 3.9 times higher than the largest value reached for the galvanized steel. With the SSPC-SP-3 method, the A-500 steel and the galvanized steel reached a maximum of 0.139 and 0.103 mm/year, for a difference of 25.9 %. With the cleaning according to the SSPC-SP-5 standard, the

highest corrosion rate was 0.051 and 0.036 mm/year for the A-500 and the galvanized steel, respectively. Then, in the steels without coating it is evident that the galvanized is an anticorrosive protection, although it continues exhibiting higher values than with coating. The corrosion may be considered similar for both materials, but the SSPC-SP-5 methods yields lower corrosion in the samples.

When considering the analysis between the two surface cleaning methods, according to the ASTM D-610 standard, it was obtained that the A-500 and the galvanized steel cleaned with the SSPC-SP-3 method exhibited a general surface corrosion and stained between 5 S and 5 G to 6 G. This evaluation was reduced in the samples treated with the SSPC-SP-5 cleaning, considering the samples with a general 4 G corrosion.

The ASTM D-714 standard was used for complementing the visual evaluation and determining the frequency and size of the blisters. In the A-500 and galvanized steel samples cleaned according to the SSPC-SP-3 standard, maximum and minimum evaluations of 2 M, 6 MD and 6 M, 6 S, respectively, were obtained. Therefore, it may be stated that the zinc chromate coating adheres similarly in both materials and provides an anticorrosive protection 7.7 and 8.2 times higher compared to the A-500 and galvanized steel without coating, respectively.

#### References

- [1] M. Morrison, "A ductile fuse for special concentrically braced frames," in *Ninth International Conference on Advances in Steel Structures (ICASS2018)At: Hong Kong*, 2018. [Online]. Available: <https://bit.ly/3xJJqcW>
- [2] K. B. Yu., G. Stradanchenko S., S. A. Yu., S. Garmider A., and B. Kalmykova Yu., "Effect of the bus bodywork on impact strength properties in roll-over," *ARPJ Journal of Engineering and Applied Sciences*, vol. 11, no. 17, pp. 10 205–10 208, 2016. [Online]. Available: <https://bit.ly/3vsZf5F>
- [3] C. Cui, A. T. O. Lim, and J. Huang, "A cautionary note on graphene anti-corrosion coatings," *Nature Nanotechnology*, vol. 12, no. 9, pp. 834–835, Sep. 2017. [Online]. Available: <https://doi.org/10.1038/nnano.2017.187>
- [4] K. K. Toledo, H.-S. Kim, Y.-S. Jeong, and I.-T. Kim, "Residual compressive strength of short tubular steel columns with artificially fabricated local corrosion damage," *Materials*, vol. 13, no. 4, 2020. [Online]. Available: <https://doi.org/10.3390/ma13040813>
- [5] V. N. Tseluikin and A. A. Koreshkova, "Corrosion resistance of composite coatings based on zinc,"

- Chemical and Petroleum Engineering*, vol. 52, no. 7, pp. 560–562, Nov. 2016. [Online]. Available: <https://doi.org/10.1007/s10556-016-0232-3>
- [6] Q. Li, H. Lu, J. Cui, M. An, and D. Li, “Electrodeposition of nanocrystalline zinc on steel for enhanced resistance to corrosive wear,” *Surface and Coatings Technology*, vol. 304, pp. 567–573, 2016. [Online]. Available: <https://doi.org/10.1016/j.surfcoat.2016.07.056>
- [7] H. Kania, M. Saternus, J. Kudláček, and J. Svoboda, “Microstructure characterization and corrosion resistance of zinc coating obtained in a zn-alnibi galvanizing bath,” *Coatings*, vol. 10, no. 8, 2020. [Online]. Available: <https://doi.org/10.3390/coatings10080758>
- [8] R. Vera, E. Cruz, M. Bagnara, R. Araya, R. Henríquez, A. Díaz-Gómez, and P. Rojas, “Evaluation of anticorrosive coatings on carbon steel in marine environments: Accelerated corrosion test and field exposure,” *International Journal of Electrochemical Science*, vol. 13, pp. 898–914, 2018. [Online]. Available: <https://doi.org/10.20964/2018.01.66>
- [9] I. Stojanović, A. Farkas, V. Alar, and N. Degiuli, “Evaluation of the corrosion protection of two underwater coating systems in a simulated marine environment,” *Advances in Surface Engineering*, vol. 71, no. 12, pp. 4330–4338, Dec. 2019. [Online]. Available: <https://doi.org/10.1007/s11837-019-03669-4>
- [10] K. Goyal, H. Singh, and R. Bhatia, “Hot-corrosion behavior of Cr<sub>2</sub>O<sub>3</sub>-CNT-coated ASTM-SA213-T22 steel in a molten salt environment at 700<sup>circ</sup>C,” *International Journal of Minerals, Metallurgy, and Materials*, vol. 26, no. 3, pp. 337–344, Mar. 2019. [Online]. Available: <https://doi.org/10.1007/s12613-019-1742-8>
- [11] SSPC, “Sspc-sp-3, surface preparation specification: Power tool cleaning,” The Society for Protective Coatings, Tech. Rep., 2003. [Online]. Available: <https://bit.ly/3u4JX6Z>
- [12] —, “Sspc-sp-5, white metal blast cleaning,” The Society for Protective Coatings, Tech. Rep., 1999. [Online]. Available: <https://bit.ly/3e3L2q1>
- [13] ASTM, “Astm b117 - 19 standard practice for operating salt spray (fog) apparatus,” ASTM International, West Conshohocken, PA, Tech. Rep., 2019. [Online]. Available: <http://doi.org/10.1520/B0117-19>
- [14] —, “Astm g1 - 03(2017)e1 standard practice for preparing, cleaning, and evaluating corrosion test specimens,” ASTM International, West Conshohocken, PA, Tech. Rep., 2017. [Online]. Available: <http://doi.org/10.1520/G0001-03R17E01>
- [15] —, “Astm d610 - 08(2019) standard practice for evaluating degree of rusting on painted steel surfaces,” ASTM International, West Conshohocken, PA, Tech. Rep., 2019. [Online]. Available: <http://doi.org/10.1520/D0610-08R19>
- [16] —, “Astm d714 - 02(2017) standard test method for evaluating degree of blistering of paints,” ASTM International, West Conshohocken, PA, Tech. Rep., 2017. [Online]. Available: <http://doi.org/10.1520/D0714-02R17>



# TRANSFER LEARNING FOR BINARY CLASSIFICATION OF THERMAL IMAGES

## TRANSFER LEARNING EN LA CLASIFICACIÓN BINARIA DE IMÁGENES TÉRMICAS

Daniel Pérez-Aguilar<sup>1,\*</sup> , Redy Risco-Ramos<sup>1,\*</sup> , Luis Casaverde-Pacherrez<sup>1</sup> 

Received: 13-11-2020, Received after review: 17-12-2020, Accepted: 22-02-2021, Published: 01-07-2021

### Abstract

The classification of thermal images is a key aspect in the industrial sector, since it is usually the starting point for the detection of faults in electrical equipment. In some cases, this task is automated through the use of traditional artificial intelligence techniques, while in others, it is performed manually, which can lead to high rates of human error. This paper presents a comparative analysis between eleven *transfer learning* architectures (AlexNet, VGG16, VGG19, ResNet, DenseNet, MobileNet v2, GoogLeNet, ResNeXt, Wide ResNet, MNASNet and ShuffleNet) through the use of fine-tuning, in order to perform a binary classification of thermal images in an electrical distribution network. For this, a database with 815 images is available, divided using the 60-20-20 hold-out technique and cross-validation with 5-Folds, to finally analyze their performance using Friedman test. After the experiments, satisfactory results were obtained with accuracies above 85 % in 10 of the previously trained architectures. However, the architecture that was not previously trained had low accuracy; with this, it is concluded that the application of *transfer learning* through the use of previously trained architectures is a proper mechanism in the classification of this type of images, and represents a reliable alternative to traditional artificial intelligence techniques.

**Keywords:** fine-tuning, Friedman test, pre-training, thermal images, transfer learning

### Resumen

La clasificación de imágenes térmicas es un aspecto clave en el sector industrial, debido a que suele ser el punto de partida en la detección de fallos en equipos eléctricos. En algunos casos, esta tarea se automatiza mediante el uso de técnicas tradicionales de inteligencia artificial, mientras que en otros, es realizada de manera manual, lo cual puede traer consigo altas tasas de error humano. Este artículo presenta un análisis comparativo entre once arquitecturas de *transfer learning* (AlexNet, VGG16, VGG19, ResNet, DenseNet, MobileNet v2, GoogLeNet, ResNeXt, Wide ResNet, MNASNet y ShuffleNet) mediante el uso de fine-tuning, con la finalidad de realizar una clasificación binaria de imágenes térmicas en una red de distribución eléctrica. Para ello, se dispone de una base de datos con 815 imágenes, divididas mediante la técnica tipo hold-out 60-20-20 y validación cruzada con 5-folds, para finalmente analizar su rendimiento mediante el test de Friedman. Luego de los experimentos, se obtuvieron resultados satisfactorios con exactitudes superiores a 85 % en diez de las arquitecturas previamente entrenadas. Sin embargo, la arquitectura que no se entrenó previamente presentó una exactitud baja; concluyéndose que la aplicación de *transfer learning* mediante el uso de arquitecturas previamente entrenadas es un mecanismo adecuado en la clasificación de este tipo de imágenes, y representa una alternativa confiable frente a técnicas tradicionales de inteligencia artificial.

**Palabras clave:** imágenes térmicas, fine-tuning, preentrenamiento, test de Friedman, transfer learning

<sup>1,\*</sup>Laboratorio de Sistemas Automáticos de Control, Universidad de Piura, Perú.  
 Autor para correspondencia: ✉: daniel.perez.a@alum.udel.edu.pe

Suggested citation: Pérez-Aguilar, D.; Risco-Ramos, R. and Casaverde-Pacherrez, L. (2021). «Transfer Learning for Binary Classification of Thermal Images». INGENIUS. N.º 26, (july-december). pp. 71-86. DOI: <https://doi.org/10.17163/ings.n26.2021.07>.

## 1. Introduction

At present, artificial intelligence (AI) is a booming discipline that has redefined many of the processes carried out in industry, showing very diverse applications, which include object recognition through artificial vision, voice recognition and synthesis, reading comprehension, translation systems, language comprehension, etc. [1]. AI is not a new term, since it has existed for many years; however, what has changed in recent times is the computational power, which can be used to compute much more complex models in shorter time [2]. AI is defined as a set of algorithms whose purpose is creating machines that emulate the capabilities of human beings. Seen in another way, it is a software that may be trained for recognizing patterns and performing predictions, in some cases more accurately than human beings [3]. Terms such as Machine Learning (ML) and Deep Learning are found within AI [4].

Machine Learning (ML) or automatic learning, is a branch of AI that seeks generalizing behaviors of a set of input data, i.e., their objective is to predict future behaviors based on finding patterns within big data sets [5]. Likewise, Deep Learning (DL) is a part of Machine Learning [6], whose objective is that systems automatically mimic the behavior and reasoning of people; in other words, that humans are involved as little as possible in the process. This objective is based on the use of artificial neural networks (ANN), which simulate the synopsis of the human brain [7]. Figure 1 displays the traditional structure of an artificial neural network, which includes the input layer, the hidden layers and the output layer.

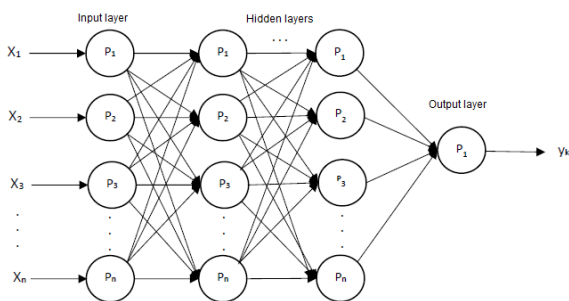


**Figure 1.** Structure of an artificial neural network [8]

In addition, it should be pointed out that within ANNs there are the convolutional neural networks (CNNs), which are an advanced and high potential type of the classical artificial neural network model, designed to address more complex problems, and generally used in image classification [9].

Regarding data separation, the holdout technique [10] is one of the most commonly used, and consists of dividing the data in three subsets: 60 % for training, 20 % for validation and the remaining 20 % for testing the

model, as observed in Figure 2. However, this type of technique cannot be considered enough to evaluate the performance of the models, and consequently literature suggests to apply a k-folds cross-validation [11] by randomly dividing the data set in k subsets, of which k-1 are used to train the model, and one to validate it. This mechanism must be repeated k times in each iteration, using different validation subsets, as seen in Figure 3. Finally, it is recommended to perform a statistical comparison of the results of each model [12], by means of parametric techniques such as ANOVA, or non-parametric ones such as Friedman Test [13].

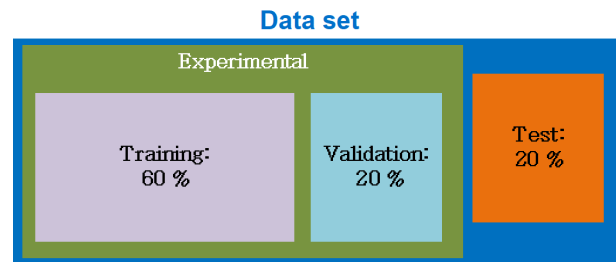


**Figure 2.** Holdout technique for separation

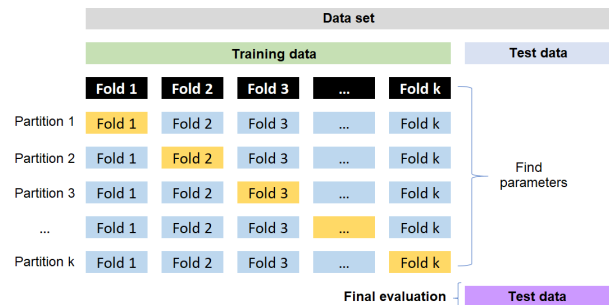


**Figure 3.** K-folds cross-validation

Some research works show that the application of artificial intelligence is useful in the electricity sector through the use of thermal images to automate their classification [14]. This type of images is captured by means of infrared cameras, thus involving another relevant term: thermography, a technique that enables capturing infrared radiation of the electromagnetic spectrum, whose main advantage is not requiring physical contact with the object or piece under study, with which machinery operation does not stop [15]. Figure 4 shows an example of the thermal image of a high-voltage equipment captured from the ground.

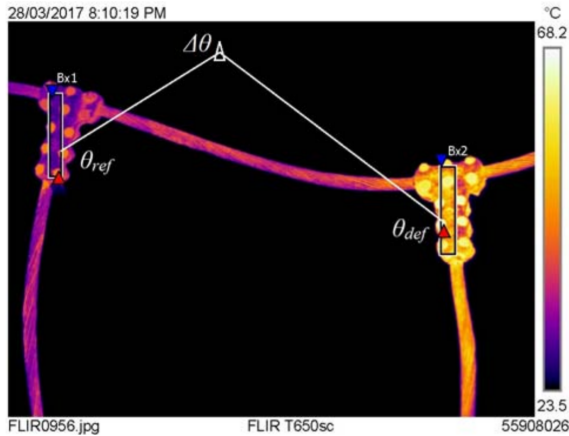


**Figure 4.** Thermal image of a high-voltage equipment [15]

Hereafter, the most relevant research works about the use of traditional artificial intelligence techniques for classification of thermal images are described. A clear example is the proposal of an automatic recognition system for classifying thermographic images of an electric power distribution network [16], where it was implemented a CNN and the JSEG or J segmentation algorithm, which consists of reducing the number of colors and their fusion based on the similarity of the regions of the image [17]. Similarly, a research work carried out in the Chongqing Technology Department, China [18], addresses computer vision using infrared thermal images captured without disturbing the operation of electrical substations. For this purpose, they trained a multi-layer perceptron (MLP), which is a type of artificial neural network constituted by various layers of intermediate or hidden neurons, used for solving problems that cannot be linearly separated [19].

A semiautomatic approach is proposed in [20] to evaluate the thermal condition of the electrical installations of a building through the analysis of infrared images, using a multilayer perceptron (MLP) and principal components analysis (PCA); the latter is a statistical technique whose purpose is simplifying the complexity of the sample through the selection or extraction of the most representative features of the input data [21]; whereas, an intelligent diagnosis method is described in [22], for classifying different conditions of electrical equipment using data obtained from infrared images using the K-means algorithm, which is in charge of grouping the images of electrical equipment to determine and classify clusters or groups with similar features [23].

The aforementioned research works are focused on training a model from scratch or in the traditional way for a specific scenario; however, at present there are techniques that simplify this process, such as transfer learning (TF), which is part of deep learning and consists of using a pretrained network, i.e., reusing the architecture and weights of a model trained with great amounts of input data, and apply them to different

scenarios with other data sets, seeking to carry out classifications more rapidly and using lower computational load [24]. An example of the databases used to train these models is ImageNet, which contains more than fourteen millions of images [25].

One of the paradigms of transfer learning is fine-tuning the model, which seeks to adapt it to a new application domain [26]; for this purpose, it is taken the pretrained model and some parameters such as the learning rate are varied, with the objective of achieving significant improvements in the predictions [27].

The literature review reveals that there are different transfer learning applications in sectors such as (i) health, through the classification of pathologies in neurological images [28], detection of objects such as guns or knives in X-ray images [29] or cervical [30], among others. (ii) In the agroindustry, as observed in [31], which presents a comparison of the ResNet, GoogLeNet, VGG16, AlexNet and DenseNet transfer learning architectures, with the purpose of classifying a data set that contains images of flowers, demonstrating that the pretrained VGG16 architecture obtains accuracy levels larger than the others. (iii) In the food sector, as described in [32], where it is indicated that CNNs are the most frequently used image classification techniques; this research is focused in classifying food with the purpose of obtaining a healthier lifestyle, for which they use a database with 500 images, in addition to the pretrained architectures VGG16, VGG19, ResNet and InceptionV3, with the latter achieving the best results.

However, when studying applications of thermal images and transfer learning techniques in the electric sector, it is found a scarcity of them. One of the most representative is the case of [33], where it is proposed a mechanism for classifying thermal images of rotor bearing systems; for this purpose, they modify a convolutional neural network with the use of transfer learning, nevertheless they do not specify the TF architecture used. On the other hand, in [34] it is sought to automate the supervision of the state of industrial machinery through the use of thermal images and a CNN, indicating that a drawback of the latter is the need for great amounts of data for training; as a consequence, it is proposed the use of the VGG16 architecture as a method for reusing layers of the neural network.

Based on what has been pointed out in previous paragraphs, there is an evidence that the advantages of transfer learning are not being fully exploited in the electrical sector, since there is no study that applies different architectures with the same data set, and thus the objective of the present study is to propose an alternative to the traditional use of artificial intelligence techniques through the analysis of eleven transfer learning architectures and the self-tuning paradigm, applied to the binary classification of thermal images in an electric power distribution network.

## 2. Materials and methods

Figure 5 represents the methodology followed in this research, which starts with the collection of field data through the capture of thermal images; afterwards, it is carried out the design of a base architecture which includes different pretrained transfer learning architectures, each of which is trained and tested to finally compare the results obtained. All this process was conducted with the help of the Google Collaboratory online service, through the use of Jupyter Notebooks [35].

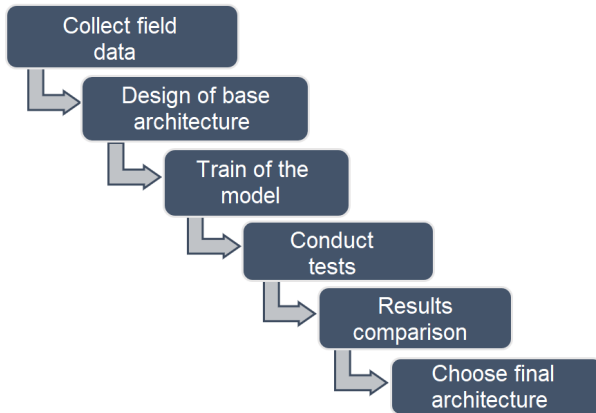


Figure 5. Methodology

### 2.1. Database

The database used in this work corresponds to 815 thermal images, belonging to a Peruvian electric power distribution company, classified in two categories, electric substations and transmission lines. This data set is larger than the ones used in [18], [20], [22], [36] and [37]. The images were captured using the TP8S infrared camera, whose specifications are seen in Table 1.

Table 1. Technical specifications of the TP8S camera [38]

Feature	Description
Type of detector	FPA (384 × 288 pixels, 35 m)
Spectral range	8-14 m
Thermal sensitivity	0.08 °C a 130 °C
Field of vision	22° × 16° / 35 mm
Electronic focus	Automatic or motorized
Zoom	Continuous from ×1 a ×10

The procedure that the electric distribution company has been executing includes five stages which are described in detail in the following and are shown in Figure 6. (i) First, an external company is hired for the capture of thermal images, specifically transmission lines and electric substations, which is carried out weekly or monthly. (ii) The service company delivers all images to a specialist certified in thermal image analysis. (iii) The specialist should manually classify

the images and divide them between transmission lines or equipment in electric substations, since they require different types of analyses. (iv) Then the specialist proceeds to analyze each image to determine, based on knowledge and experience, if there is an evidence of failures due to the detection of a hotspot. (v) Finally, if the specialist detects a hotspot, he/she prepares the corresponding report and takes the appropriate corrective actions.

The present study focused in automating stage 3 of the process using transfer learning techniques.

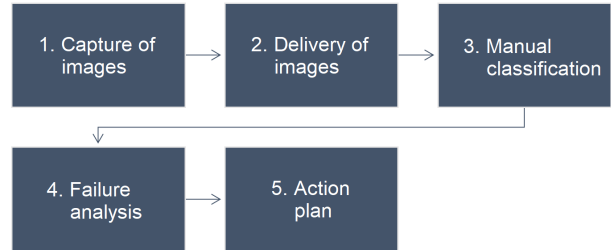


Figure 6. Process for classifying the thermal images

The images have a resolution of 384 × 288 pixels. Figure 7 shows some examples of typical images corresponding to transmission lines equipment, and Figure 8 shows some images corresponding to electrical substations, which represent the two classes of the model.



Figure 7. Typical image of transmission lines equipment

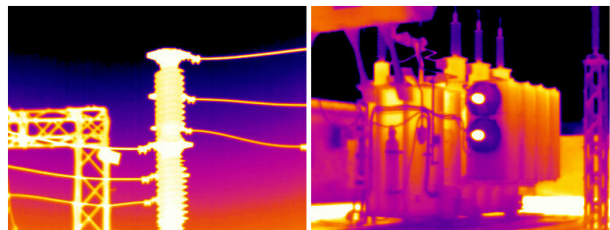


Figure 8. Typical image of electrical substations equipment

### 2.2. Data set

A total of 815 thermal images were used for carrying out the experiments; these images were divided in three data sets with a split of 60-20-20, known as holdout separation (See Figure 2). The 60 % of the images were considered as training data and 20 % as

validation data, while the remaining 20 % includes the data for testing the model (see Table 2), i.e., that the model is trained and validated in parallel and finally tested with new images that have not been previously considered. It is indicated in [39] that the models that generalize appropriately show similar accuracy and loss metrics in training and validation, thus preventing overfitting.

**Table 2.** Distribution of the data sets

Class	Train	Validation	Test
Line	206	68	68
Substation	283	95	95
TOTAL	489	163	163

### 2.3. Architectures

Eleven architectures of previously trained models were considered in this study, through the use of the TorchVision package, which is part of PyTorch, an open-source automatic learning library; as indicated in [40], the PyTorch models are faster and easier to implement and train. The architectures used were:

#### 2.3.1. AlexNet

Convolutional neural network constituted by eight layers [41], five of which are max-pooling, and the three remaining are fully connected. This architecture was trained with the ReLU (Rectified Linear Units) activation function and the ImageNet database. As it is observed in Figure 9, the input to the network are images of  $224 \times 224$  pixels, which are transformed in each of the layers up to the obtaining the output, the classification of one thousand categories.

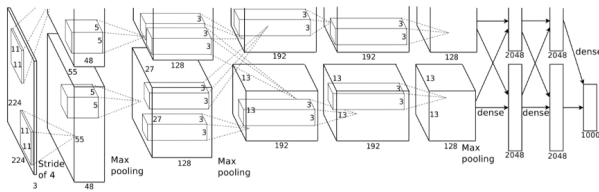


**Figure 9.** AlexNet architecture [41]

#### 2.3.2. VGG16

Network constituted by 16 layers, which was also trained with the ImageNet database [42], assuming improvements compared to the AlexNet architecture since it replaces the large kernels filters by a set of  $3 \times 3$  filters. The VGG16 architecture is shown in Figure 10.

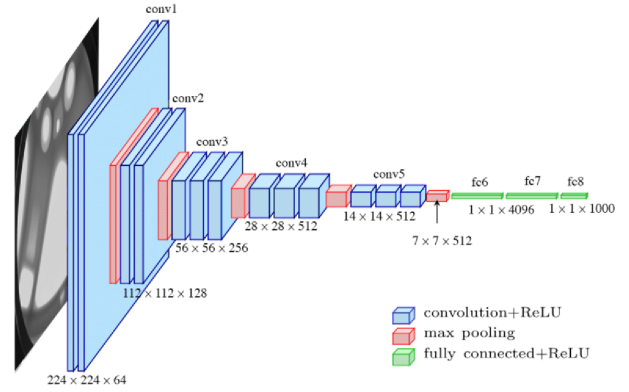


**Figure 10.** VGG16 architecture [42]

#### 2.3.3. VGG19

Convolutional neural network constituted by 16 convolutional layers [43], three fully-connected, five MaxPool and one SoftMax, with an approximate of 143 million of parameters. The VGG19 architecture is shown in Figure 11.

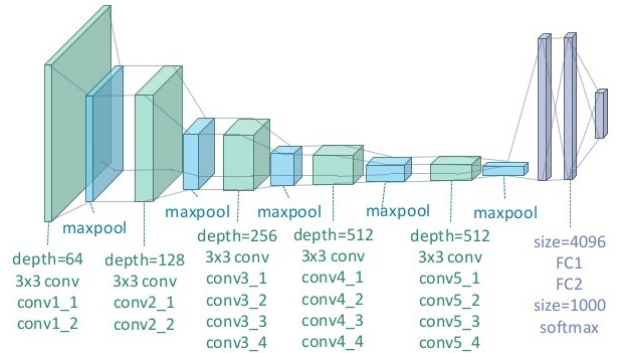


**Figure 11.** VGG19 architecture [43]

#### 2.3.4. ResNet

Architecture that seeks that the increase of layers is performed different to the traditional way [44], and thus it adds a residual connection with an identity layer that is directly passed to the next layer, considerably improving the training of the model. A traditional block of the ResNet architecture is shown In Figure 12.

#### 2.3.5. DenseNet

CNN in which every layer obtains additional inputs from all previous layers and passes its own feature maps to all further layers [45], i.e., that all outputs from previous layers are concatenated with further layers, seeking to have a smaller number of parameters and an accuracy greater than the one achieved with networks such as ResNet. The DenseNet architecture is shown in Figure 13.

### 2.3.6. GoogLeNet

Neural network developed by Google with the purpose of classifying images. This CNN is based on the Inception architecture [46], and thus it uses modules that give the possibility of choosing among different sizes of convolutional filter in each of the blocks. An example of the Inception module is shown in Figure 14.

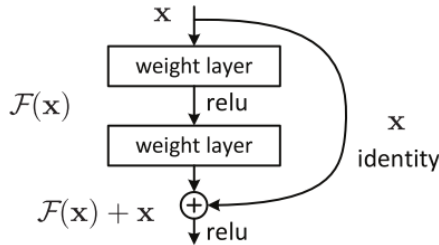


Figure 12. Block of the ResNet architecture [44]

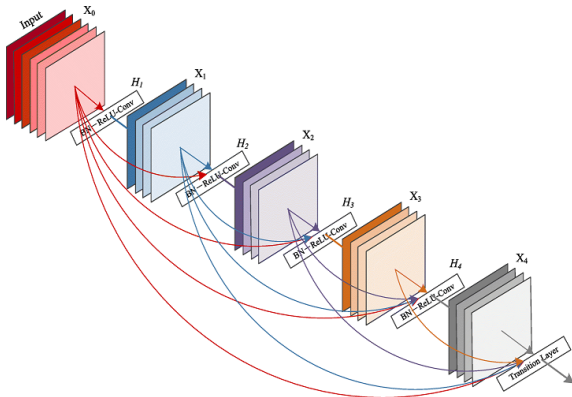


Figure 13. Block of the DenseNet architecture [45]

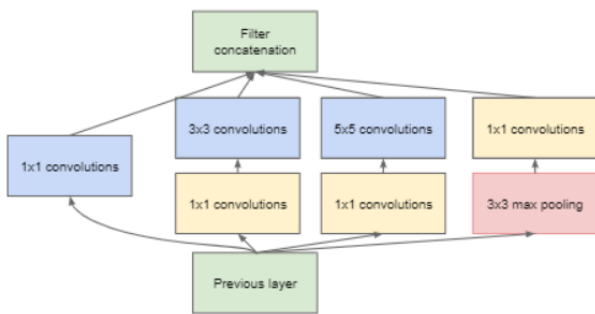


Figure 14. Inception module with reduced dimension [47]

### 2.3.7. MobileNet v2

is based on the use of depthwise separable convolutions and uses an inverted residual structure [48], where the input and output of the residual block are thin bottleneck layers opposed to traditional residual models that use expanded representations in the input, as it is shown with detail in Figure 15.

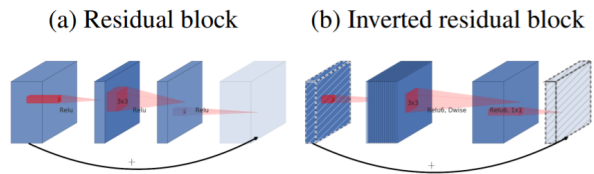


Figure 15. Blocks of the MobileNet v2 architecture [48]

### 2.3.8. ResNeXt

A variant of ResNet that seeks to increase the number of paths or routes parallel to the residual connection [49], i.e., that ResNeXt is a CNN with multiple branches, as seen in Figure 16, with shows a block with a cardinality of 32.

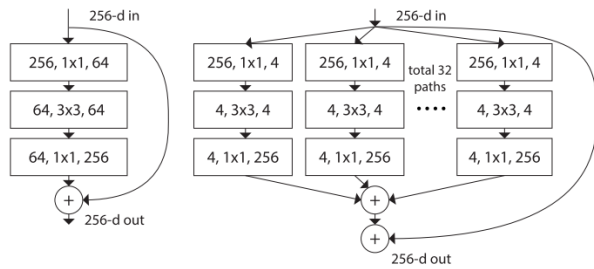


Figure 16. Block of the ResNeXt architecture [49]

### 2.3.9. Wide ResNet

A neural network that represents a variation to the traditional ResNet architecture [50], reducing the depth of the model and increasing the width of the residual networks. The characteristic blocks of this CNN are: basic, bottleneck, basic-wide and wide-dropout. Figure 17 shows the details of the latter.

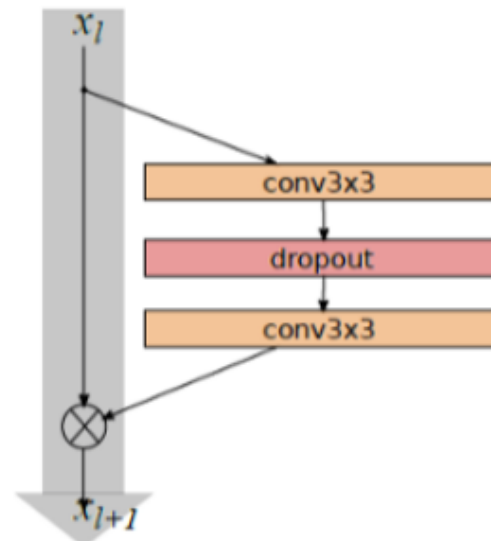


Figure 17. Wide-dropout block [50]

### 2.3.10. MNASNet

Is a convolutional neural network that, similar to the MobileNet [51], is designed and optimized for mobile devices and seeks that the model obtains an equilibrium between latency and accuracy. Figure 18 shows an example of the design of a convolutional layer with a  $5 \times 5$  kernel.

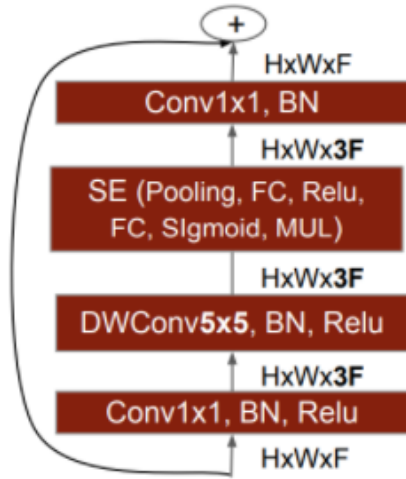


Figure 18. Convolutional layer of MNASNet [51]

### 2.3.11. ShuffleNet

A CNN whose main component is a new channel reorganization operation [52], seeking that the information flows more easily in them. Figure 19 shows a ShuffleNet unit, that is a central element within this architecture.

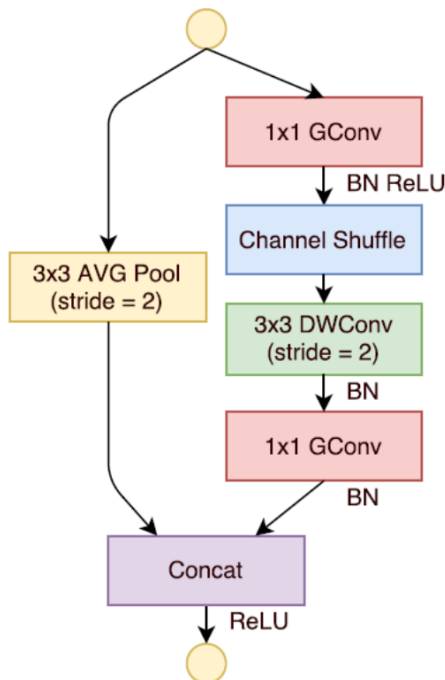


Figure 19. ShuffleNet unit [52]

At last, Table 3 shows information provided in the TorchVision [53] web site; it summarizes the features of these architectures related with the size in megabytes and the number of parameters used in training the model, highlighting that ShuffleNet is the only architecture that currently does not allow the use of the pretraining configuration parameter, i.e., its size is zero megabytes.

Table 3. Features of the architectures used

Nº	Architecture	Size (mb)	Parameters (millions)
1	AlexNet	233	61.1
2	VGG16	528	138.36
3	VGG19	548	143.67
4	ResNet	230	60.19
5	DenseNet	77.4	20.01
6	GoogLeNet	49.7	13
7	MobileNet v2	13.6	3.5
8	ResNeXt	340	44.55
9	Wide ResNetx	243	126.89
10	MNASNet	16.9	4.38
11	ShuffleNet	0*	7.39

### 2.4. Model

Figure 20 shows the design of the base architecture to be used. The first section corresponds to the input layer, in which images of  $328 \times 288$  pixels were included. Afterwards, the eleven architectures were added in the «Transfer learning model architecture» section, highlighting that the classification layer of each of them was edited to perform a binary classification, since they were originally designed to classify an approximate of one thousand images. At last, there is the output layer that corresponds to the predictions of the model.

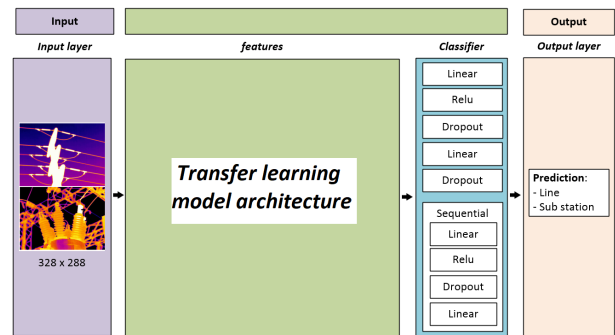


Figure 20. Base architecture

Since no research works were found that compare this number of architectures applied to thermography, and with the purpose of carrying out a fair comparison between the models, the same hyperparameters were

considered in all tests conducted. They were selected based on empirical experiments, as proposed in [54–56], based on the values in Table 4. According to the results of the initial experiments, there is a breaking point at approximately epoch 20, in which the training and validation curves show a separation trend, evidencing problems of overfitting (see Figure 21). It is concluded that the models obtain better results according to the hyperparameters shown in Table 5, and these data were used to execute the remaining tests.

**Table 4.** Empirical experiments with hyperparameters

Hyperparameter	Value
Learning rate	$10^{-2}$ , $10^{-3}$ , $10^{-4}$ y $10^{-5}$
Images per Batch	16, 32, 64 y 128
Number of epochs	5, 10, 20, 30, 50 y 100
Cost function	Cross Entropy, Multi Margin Loss y MSE
Optimizer	Adagrad, Adam, Adamax, RMSprop y SGD

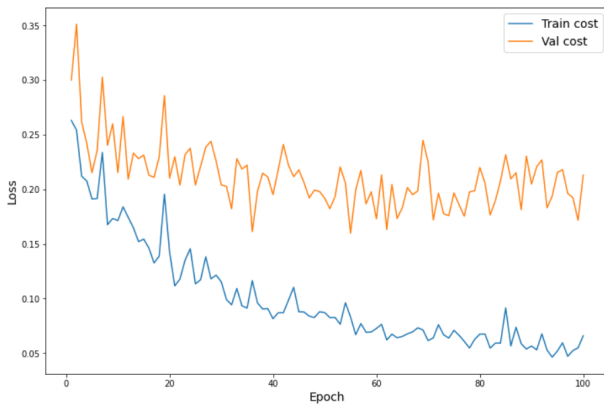


**Figure 21.** Experiment with 100 epochs

**Table 5.** Final configuration of hyperparameters

Hyperparameter	Value
Learning rate	0.0001
Images per Batch	32
Number of epochs	20
Cost function	Multi Margin Loss
Optimizer	Adam

Models improved their performance when the input data is normalized calculating the standard deviation and the mean of the data sets. In addition, the data set (815 images) is larger than in research works such as [18], [20], [22], [36] and [37], in which the maximum number of images used is 500. The literature suggests as a good practice the application of techniques that contribute to improve the quality of the training, and for this reason it was used Data Augmentation [57, 58] through the random horizontal flip, random vertical

flip and random rotation transformations. Figure 22 shows some results of the transformations used.

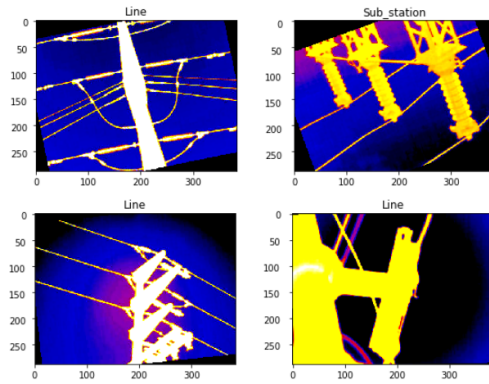


**Figure 22.** Images with data augmentation

### 3. Results and discussion

The eleven architectures were trained using the values of Table 5, obtaining the accuracy results shown in Table 6. On the other hand, Table 7 shows the loss rate for each architecture. Based on the results, it is seen that DenseNet yields a higher accuracy, while VGG16 shows the lowest loss rate. An additional point to be considered is that ShuffleNet yields the worst results since it was the only architecture without pre-training, evidencing that the pretrained architectures yield better results.

**Table 6.** Accuracy of the architectures

Architecture	Train	Validation	Test
DenseNet	96.52	92.02	98.15
VGG19	93.66	90.18	96.31
Wide ResNetx	94.68	90.18	96.31
MobileNet v2	94.68	88.95	95.70
VGG16	95.91	91.41	95.09
ResNeXt	94.06	92.02	95.09
ResNet	93.66	84.66	94.47
AlexNet	95.50	91.41	93.86
GoogLeNet	95.09	88.95	93.86
MNASNet	71.41	69.93	79.14
ShuffleNet	62.78	68.09	76.68

**Table 7.** Loss rate of the architectures

Architecture	Train	Validation	Test
VGG16	0.130571	0.195825	0.106733
VGG19	0.175259	0.257767	0.124051
MobileNet v2	0.179914	0.283927	0.124497
DenseNet	0.134446	0.198757	0.126488
AlexNet	0.127838	0.226890	0.134585
GoogLeNet	0.205683	0.242438	0.164706
ResNet	0.220600	0.295843	0.175979
ResNeXt	0.215153	0.241967	0.179627
Wide ResNetx	0.246464	0.271462	0.19046
MNASNet	0.507049	0.529690	0.395779
ShuffleNet	0.647315	0.579723	0.524782

Research works such as [59], point out that the accuracy and loss rate metrics exhibit a high degree of subjectivity, and consequently it is proposed the use of statistical techniques to evaluate the results of the architectures, specifically F1-score, whose calculation mechanism is observed in (1). Precision and recall are obtained from (2) and (3), respectively, where TP represents true positives, FP false positives and FN the false negatives. The results are shown in detail in Table 8, demonstrating that the VGG16 architecture achieves the first place with the highest F1-score, corresponding to 95.11 %.

$$F1_{score} = 2 \times \frac{precision \times recall}{precision + recall} \quad (1)$$

$$Precision = \frac{TP}{TP + FP} \quad (2)$$

$$Precision = \frac{TP}{TP + FN} \quad (3)$$

**Table 8.** Comparison between architectures: F1-score

Architecture	Precision	Recall	F1-score
VGG16	96.12	94.12	95.11
ResNeXt	92.86	93.79	93.32
MobileNet v2	93.62	92.54	93.08
ResNet	92.36	93.48	92.92
VGG19	92.25	92.85	92.55
DenseNet	93.48	91.59	92.53
Wide ResNetx	93.13	91.8	92.46
AlexNet	93.03	89.91	91.44
GoogLeNet	92.11	89.39	90.73
MNASNet	85.71	86.11	85.91
ShuffleNet	29.14	50.00	36.82

The holdout separation mechanism may not be enough when comparing different models, and with the purpose of eliminating this source of variability other experiments were conducted by means of 5-folds cross-validation (see Figure 23) as suggested in [60], followed by a statistical comparison of the results of each model, as it is performed in [12]. The results of the cross-validation may be observed in Table 9.

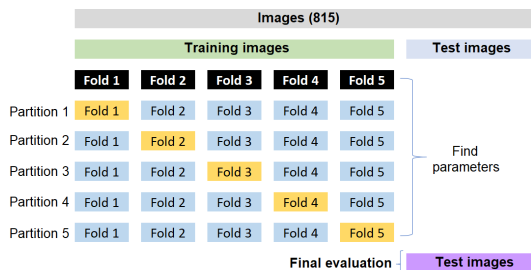


**Figure 23.** 5-folds cross validation

**Table 9.** Results – 5-folds cross validation

Architecture	Fold 1	...	Fold 5	Average
VGG16	93.87	...	98.16	96.81
VGG19	93.87	...	98.77	95.83
AlexNet	90.18	...	99.38	95.34
ResNeXt	94.48	...	98.16	94.6
DenseNet	88.34	...	98.16	94.36
MobileNet v2	90.18	...	96.32	93.99
ResNet	93.87	...	95.09	93.74
GoogLeNet	88.96	...	93.86	93.5
MNASNet	86.51	...	98.15	92.52
Wide ResNetx	84.66	...	94.48	89.82
ShuffleNet	68.09	...	72.39	70.06

Regarding the statistical tests to evaluate the performance of the architectures, first every model was executed 30 times, as it was done in [12]. Afterwards, residue and normal probability analyses were carried out; according to the former, it is evidenced that it might be applied a parametric test since the residues exhibit a similar dispersion (see Figure 24). However, when analyzing the normal probability plot to verify that the residues approximately fit a normal distribution, it is observed that there are data outside the confidence interval, with a Shapiro-Wilk coefficient equal to 0.932994 and a p-value equal to 0 (see Figure 25). Similarly, it was carried out a data transformation using the square root, but these are still outside the confidence interval.

Since populations do not fit a normal distribution, it cannot be applied a parametric test; for this reason, it is necessary to use a non-parametric test, specifically Friedman test, in which it is not required to meet the normality or homoestacity (equality of variances) condition. By means of this analysis shown in Table 10, it is obtained a p-value equal to zero, i.e., there is a difference between the populations, showing that VGG16 is better than the other architectures.

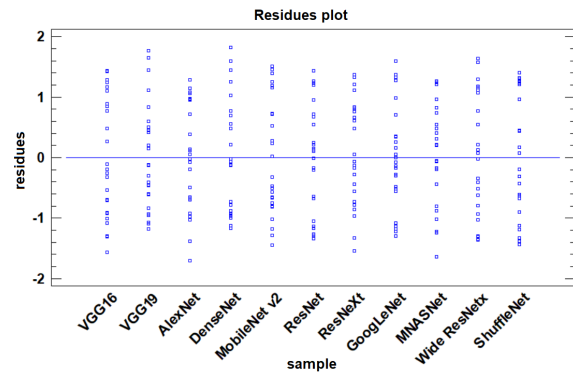


**Figure 24.** Residues plot

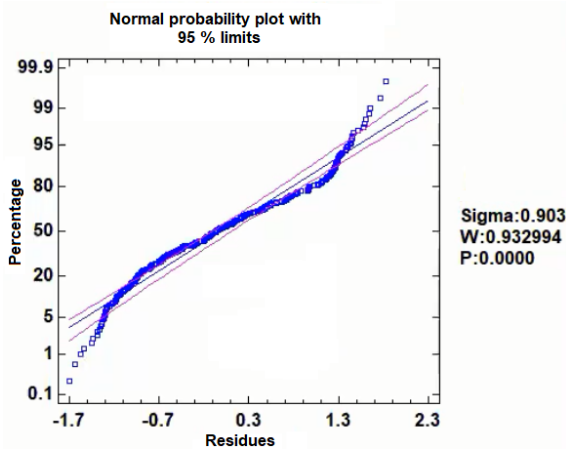


Figure 25. Normal probability plot

Table 10. Statistical results –Friedman test

Ranking	Architecture	Average range
1	VGG16	10.68
2	AlexNet	9.28
3	VGG19	9.28
4	DenseNet	6.48
5	MobileNet v2	6.32
6	ResNeXt	6.06
7	ResNet	5.78
8	GoogLeNet	5.16
9	MNASNet	3.96
10	Wide ResNetx	2.00
11	ShuffleNet	1.00

This same result is evidenced in the analysis of means, in which it is seen that the confidence interval that has been constructed both with the Fisher LSD (Figure 26) and Tukey HSD (Figure 27) methods, is better for the case of VGG16 since it does not intersect the corresponding to other architectures. In the case of the analysis of medians it is observed that the VGG16 architecture is better than most of the others, but it shows a small intersection with the AlexNet and VGG19 architectures (see Figure 28).

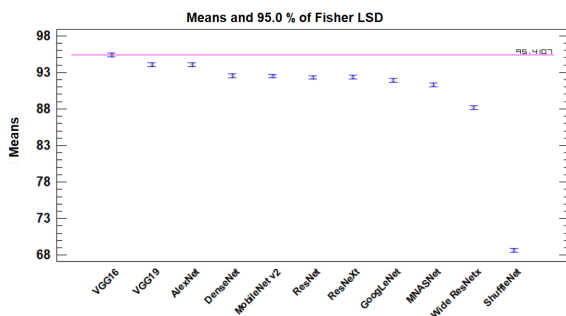


Figure 26. Plot of means – Fisher LSD

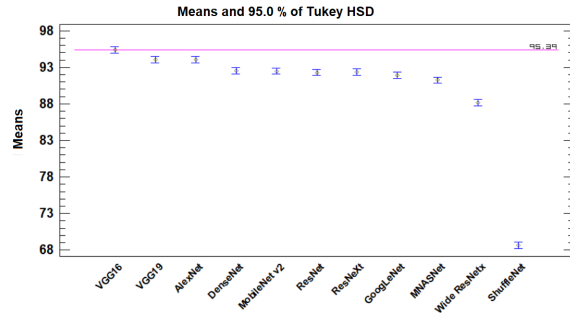


Figure 27. Plot of means – Tukey HSD

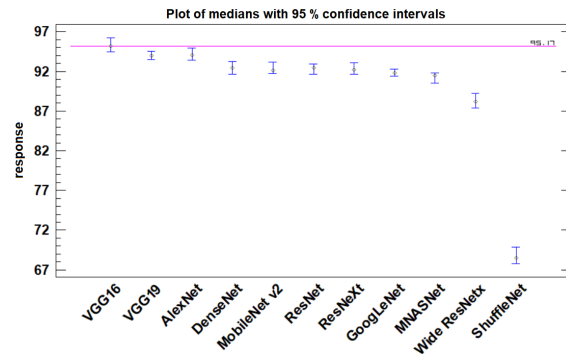


Figure 28. Plot of medians

In addition, it was performed the multiple comparison analysis by means of the multiple range test (see Table 11), where if the “X” of homogeneous groups are in the same column the architectures behave similarly, observing that VGG16 is better and different than the other architectures.

Table 11. Multiple range test

Architecture	Mean	Homogeneous groups
ShuffleNet	686.560	X
Wide ResNetx	881.820	X
MNASNet	912.540	X
GoogLeNet	919.068	XX
ResNet	923.080	X
ResNeXt	923.704	X
MobileNet v2	924.816	X
DenseNet	925.336	X
AlexNet	940.500	X
VGG19	940.652	X
VGG16	953.756	X

The present paper is not intended to obtain a «better» model but presenting an alternative mechanism in front of traditional artificial intelligence techniques. However, the results corresponding to the model with better performance, i.e., VGG16, are presented for academic purposes; the original architecture of this model is seen in Figure 10, and the resulting final architecture is shown with details in Figure 29.

It is seen in this architecture that the input is represented by images of  $328 \times 288$  pixels, which enter the VGG16 pretrained convolutional neural network, constituted by thirteen convolutional layers followed by three fully connected layers, the first two of which have 4096 channels and the last one 1000 channels; therefore, this was edited to be able to perform a binary classification (2 channels). The hidden layers use the ReLU activation function and besides different  $3 \times 3$  kernels. Finally, the output corresponds to the classification between both classes, i.e., lines and substations.

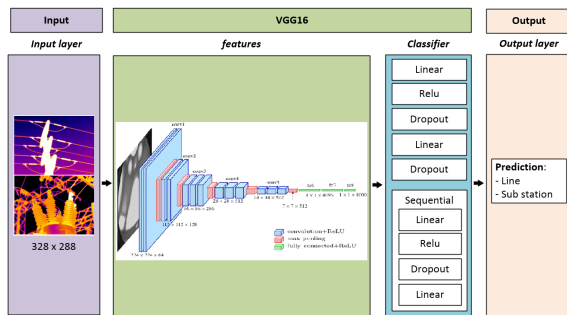


Figure 29. Proposed transfer learning architecture for classifying thermal images

Precisions of 95.91 % and 91.41 % in training and validation, respectively, were obtained with this model (Figure 30). This architecture was tested with new images belonging to the test data set, obtaining an accuracy of 94.43 % for the category lines, and 92.81 % for substations. This may be seen in the confusion matrix shown in Figure 31.

The accuracy of the model was graphically represented through the receiver operating characteristic (ROC) curve, whose area under the curve (AUC) shows a value of 94 %, which indicates a high performance of the proposed architecture in the classification of thermal images (see Figure 32).

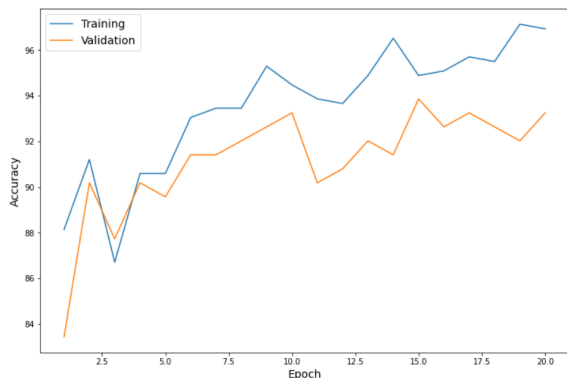


Figure 30. Accuracy: training and validation of the model

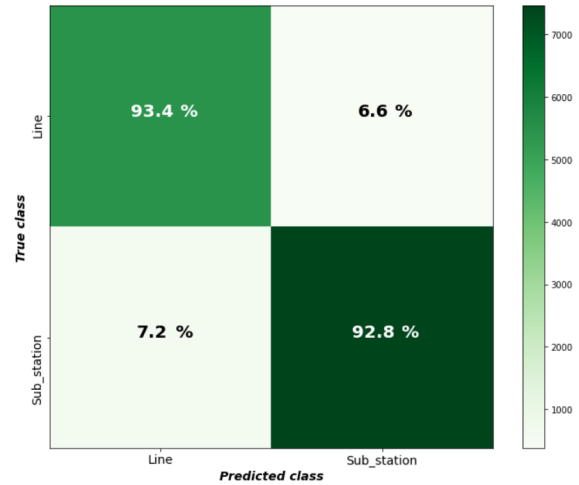


Figure 31. Confusion matrix

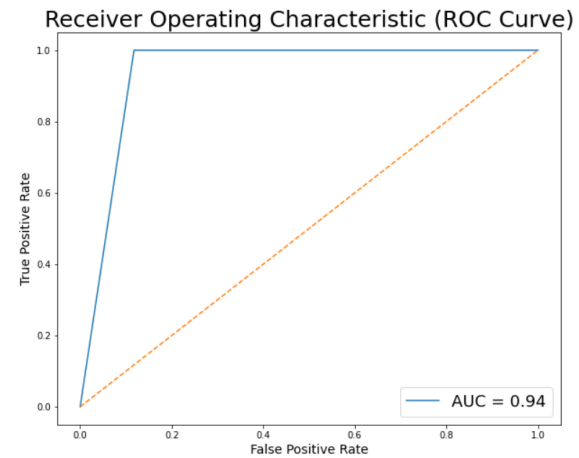


Figure 32. ROC curve

At last, Figure 33 shows some examples of the predictions by the model. The real classification is represented in the left side of the title of each image, and in the right side the one obtained by the model.

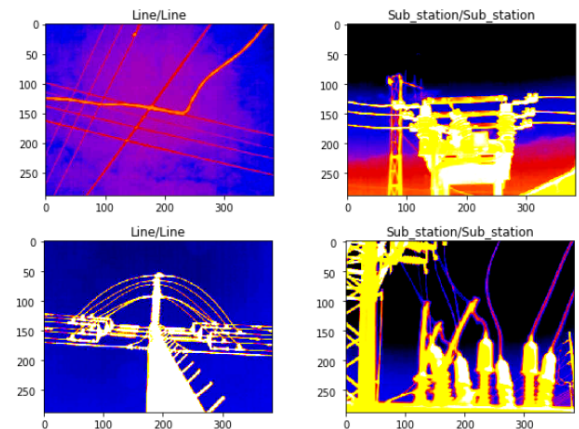


Figure 33. Predictions by the model

## 4. Conclusions

In this work, it is analyzed the performance of eleven pretrained networks that use the transfer learning paradigm based in fine-tuning the model, for binary classification of thermal images. The final objective is not finding a «better» model, but presenting alternatives to traditional artificial intelligence techniques, seeking to save computational time and load.

The models yield accuracies between 79.14 % and 98.15 %, and values of F1-score between 85.91 % and 95.11 % in the pretrained architectures; these results are an indication that the use of transfer learning techniques represents a reliable alternative as a mechanism for classifying thermal images in the electric sector; however, it is recommended to perform a specific analysis in each particular case of application.

The use of data augmentation, transformations and normalization of the images, are important aspects to improve the performance of the model; whereas the division of the data set in the training, validation and test subsets using the holdout technique helped to prevent overfitting, generalize the model and, therefore, carry out more accurate predictions. However, with the purpose of performing a fairer comparison, the study also included applying a 5-folds cross-validation, and moreover a statistical analysis by means of Friedman Test.

## Acknowledgement

Daniel Pérez-Aguilar acknowledges the financial support of the CONCYTEC-World Bank Project, through its executive unit, the Fondo Nacional de Desarrollo Científico, Tecnológico y de Innovación Tecnológica (FONDECYT), within the call E033-2018-01-BM under Contract N° 06-2018-FONDECYT/BM, for the research work Transfer learning in binary classification of thermal images, executed as part of the doctoral program in Engineering with focus on Process Automation, Control and Optimization, carried out in the Automatic Control Systems Laboratory of the Universidad de Piura, Peru.

## References

- [1] M. Haenlein and A. Kaplan, “A brief history of artificial intelligence: On the past, present, and future of artificial intelligence,” *California Management Review*, vol. 61, no. 4, pp. 5–14, 2019. [Online]. Available: <https://doi.org/10.1177/0008125619864925>
- [2] M. Flasiński, *Introduction to artificial intelligence*. Springer International Publishing, 2016. [Online]. Available: <http://doi.org/10.1007/978-3-319-40022-8>
- [3] M.-H. Huang and R. T. Rust, “Artificial intelligence in service,” *Journal of Service Research*, vol. 21, no. 2, pp. 155–172, 2018. [Online]. Available: <https://doi.org/10.1177/1094670517752459>
- [4] Z. Aung, I. S. Mikhaylov, and Y. T. Aung, “Artificial intelligence methods application in oil industry,” in *2020 IEEE Conference of Russian Young Researchers in Electrical and Electronic Engineering (EIConRus)*, 2020, pp. 563–567. [Online]. Available: <https://doi.org/10.1109/EIConRus49466.2020.9039330>
- [5] T. P. Carvalho, F. A. A. M. N. Soares, R. Vita, R. da P. Francisco, J. ao P. Basto, and S. G. S. Alcalá, “A systematic literature review of machine learning methods applied to predictive maintenance,” *Computers & Industrial Engineering*, vol. 137, p. 106024, 2019. [Online]. Available: <https://doi.org/10.1016/j.cie.2019.106024>
- [6] S. Wan, L. Qi, X. Xu, C. Tong, and Z. Gu, “Deep learning models for real-time human activity recognition with smartphones,” *Mobile Networks and Applications*, vol. 25, no. 2, pp. 743–755, Apr. 2020. [Online]. Available: <https://doi.org/10.1007/s11036-019-01445-x>
- [7] V. Golodov, A. Zavei-Boroda, S. Ivanov, and K. Nikolskaya, “Development of a deep learning neural network for human movements analysis,” in *2017 Second Russia and Pacific Conference on Computer Technology and Applications (RPC)*, 2017, pp. 72–74. [Online]. Available: <https://doi.org/10.1109/RPC.2017.8168071>
- [8] E. A. Galindo, J. A. Perdomo, and J. C. Figueroa-García, “Estudio comparativo entre máquinas de soporte vectorial multiclase, redes neuronales artificiales y sistema de inferencia neuro-difuso autoorganizado para problemas de clasificación,” *Información tecnológica*, vol. 31, pp. 273–286, 02 2020. [Online]. Available: <http://dx.doi.org/10.4067/S0718-07642020000100273>
- [9] A. Brunetti, D. Buongiorno, G. F. Trotta, and V. Bevilacqua, “Computer vision and deep learning techniques for pedestrian detection and tracking: A survey,” *Neurocomputing*, vol. 300, pp. 17–33, 2018. [Online]. Available: <https://doi.org/10.1016/j.neucom.2018.01.092>
- [10] I. Yildiz, P. Tian, J. Dy, D. Erdoğan, J. Brown, J. Kalpathy-Cramer, S. Ostmo, J. Peter Campbell, M. F. Chiang, and S. Ioannidis, “Classification and comparison via neural networks,” *Neural Networks*, vol. 118, pp. 65–80, 2019. [Online]. Available: <https://doi.org/10.1016/j.neunet.2019.06.004>

- [11] Y. Jung, “Multiple predicting k-fold cross-validation for model selection,” *Journal of Nonparametric Statistics*, vol. 30, no. 1, pp. 197–215, 2018. [Online]. Available: <https://doi.org/10.1080/10485252.2017.1404598>
- [12] F. Pacheco, J. Valente de Oliveira, R.-V. Sánchez, M. Cerrada, D. Cabrera, C. Li, G. Zurita, and M. Artés, “A statistical comparison of neuroclassifiers and feature selection methods for gearbox fault diagnosis under realistic conditions,” *Neurocomputing*, vol. 194, pp. 192–206, 2016. [Online]. Available: <https://doi.org/10.1016/j.neucom.2016.02.028>
- [13] D. W. Zimmerman and B. D. Zumbo, “Relative power of the Wilcoxon test, the Friedman test, and repeated-measures ANOVA on ranks,” *The Journal of Experimental Education*, vol. 62, no. 1, pp. 75–86, 1993. [Online]. Available: <https://doi.org/10.1080/00220973.1993.9943832>
- [14] C. Lile and L. Yiqun, “Anomaly detection in thermal images using deep neural networks,” in *2017 IEEE International Conference on Image Processing (ICIP)*, 2017, pp. 2299–2303. [Online]. Available: <https://doi.org/10.1109/ICIP.2017.8296692>
- [15] A. Dragomir, M. Adam, M. Andruçcă, A. Munteanu, and E. Boghiu, “Considerations regarding infrared thermal stresses monitoring of electrical equipment,” in *2017 International Conference on Electromechanical and Power Systems (SIELMEN)*, 2017, pp. 100–103. [Online]. Available: <https://doi.org/10.1109/SIELMEN.2017.8123307>
- [16] F. Fambrini, Y. Iano, D. G. Caetano, A. A. D. Rodríguez, C. Moya, E. Carrara, R. Arthur, F. C. Cabello, J. V. Zubem, L. M. Del Val Cura, J. a. B. Destro Filho, J. R. Campos, and J. H. Saito, “Gpu cuda jseg segmentation algorithm associated with deep learning classifier for electrical network images identification,” *Procedia Computer Science*, vol. 126, pp. 557–565, 2018, knowledge-Based and Intelligent Information & Engineering Systems: Proceedings of the 22nd International Conference, KES-2018, Belgrade, Serbia. [Online]. Available: <https://doi.org/10.1016/j.procs.2018.07.290>
- [17] X. W. X. L. Z. J. Wenzhen Yang, Jiali Luo and Z. Pan, “Image tactile perception with an improved jseg algorithm,” *International Journal of Performability Engineering*, vol. 14, no. 1, p. 77, 2018. [Online]. Available: <https://doi.org/10.23940/ijpe.18.01.p9.7788>
- [18] I. Ullah, F. Yang, R. Khan, L. Liu, H. Yang, B. Gao, and K. Sun, “Predictive maintenance of power substation equipment by infrared thermography using a machine-learning approach,” *Energies*, vol. 10, no. 12, 2017. [Online]. Available: <https://doi.org/10.3390/en10121987>
- [19] H. Ramchoun, Y. Ghanou, M. Ettaouil, and M. A. J. Idrissi, “Multilayer perceptron: Architecture optimization and training,” *International Journal of Interactive Multimedia and Artificial Intelligence*, vol. 4, no. 1, 2016. [Online]. Available: <http://doi.org/10.9781/ijimai.2016.415>
- [20] A. S. Nazmul Huda, S. Taib, M. S. Jadin, and D. Ishak, “A semi-automatic approach for thermographic inspection of electrical installations within buildings,” *Energy and Buildings*, vol. 55, pp. 585–591, 2012. [Online]. Available: <https://doi.org/10.1016/j.enbuild.2012.09.014>
- [21] C. Yuan, X. Sun, and R. Lv, “Fingerprint liveness detection based on multi-scale OPQ and PCA,” *China Communications*, vol. 13, no. 7, pp. 60–65, 2016. [Online]. Available: <https://doi.org/10.1109/CC.2016.7559076>
- [22] H. Zou and F. Huang, “A novel intelligent fault diagnosis method for electrical equipment using infrared thermography,” *Infrared Physics & Technology*, vol. 73, pp. 29–35, 2015. [Online]. Available: <https://doi.org/10.1016/j.infrared.2015.08.019>
- [23] S.-S. Yu, S.-W. Chu, C.-M. Wang, Y.-K. Chan, and T.-C. Chang, “Two improved k-means algorithms,” *Applied Soft Computing*, vol. 68, pp. 747–755, 2018. [Online]. Available: <https://doi.org/10.1016/j.asoc.2017.08.032>
- [24] T. V. Phan, S. Sultana, T. G. Nguyen, and T. Bauschert, “Q - transfer: A novel framework for efficient deep transfer learning in networking,” in *2020 International Conference on Artificial Intelligence in Information and Communication (ICAIIIC)*, 2020, pp. 146–151. [Online]. Available: <https://doi.org/10.1109/ICAIIIC48513.2020.9065240>
- [25] M. Ebrahim, M. Al-Ayyoub, and M. A. Alsmirat, “Will transfer learning enhance imagenet classification accuracy using imagenet-pretrained models?” in *2019 10th International Conference on Information and Communication Systems (ICICS)*, 2019, pp. 211–216. [Online]. Available: <https://doi.org/10.1109/IACS.2019.8809114>
- [26] T. Alshalali and D. Josyula, “Fine-tuning of pre-trained deep learning models with extreme learning machine,” in *2018 International Conference on Computational Science and Computational Intelligence (CSCI)*, 2018, pp. 469–473. [Online]. Available: <https://doi.org/10.1109/CSCI46756.2018.00096>

- [27] G. Vrbančić and V. Podgorelec, “Transfer learning with adaptive fine-tuning,” *IEEE Access*, vol. 8, pp. 196 197–196 211, 2020. [Online]. Available: <https://doi.org/10.1109/ACCESS.2020.3034343>
- [28] T. Kaur and T. K. Gandhi, “Automated brain image classification based on vgg-16 and transfer learning,” in *2019 International Conference on Information Technology (ICIT)*, 2019, pp. 94–98. [Online]. Available: <https://doi.org/10.1109/ICIT48102.2019.00023>
- [29] R. L. Gálvez, E. P. Dadios, A. A. Bandalá, and R. R. P. Vicerra, “Threat object classification in X-ray images using transfer learning,” in *2018 IEEE 10th International Conference on Humanoid, Nanotechnology, Information Technology, Communication and Control, Environment and Management (HNICEM)*, 2018, pp. 1–5. [Online]. Available: <https://doi.org/10.1109/HNICEM.2018.8666344>
- [30] D. Xue, X. Zhou, C. Li, Y. Yao, M. M. Rahaman, J. Zhang, H. Chen, J. Zhang, S. Qi, and H. Sun, “An application of transfer learning and ensemble learning techniques for cervical histopathology image classification,” *IEEE Access*, vol. 8, pp. 104 603–104 618, 2020. [Online]. Available: <https://doi.org/10.1109/ACCESS.2020.2999816>
- [31] E. Cengil and A. Çınar, “Multiple classification of flower images using transfer learning,” in *2019 International Artificial Intelligence and Data Processing Symposium (IDAP)*, 2019, pp. 1–6. [Online]. Available: <https://doi.org/10.1109/IDAP.2019.8875953>
- [32] J. R. Rajayogi, G. Manjunath, and G. Shobha, “Indian food image classification with transfer learning,” in *2019 4th International Conference on Computational Systems and Information Technology for Sustainable Solution (CSITSS)*, vol. 4, 2019, pp. 1–4. [Online]. Available: <https://doi.org/10.1109/CSITSS47250.2019.9031051>
- [33] H. Shao, M. Xia, G. Han, Y. Zhang, and J. Wan, “Intelligent fault diagnosis of rotor-bearing system under varying working conditions with modified transfer convolutional neural network and thermal images,” *IEEE Transactions on Industrial Informatics*, vol. 17, no. 5, pp. 3488–3496, 2021. [Online]. Available: <https://doi.org/10.1109/TII.2020.3005965>
- [34] O. Janssens, R. Van de Walle, M. Locufier, and S. Van Hoecke, “Deep learning for infrared thermal image based machine health monitoring,” *IEEE/ASME Transactions on Mechatronics*, vol. 23, no. 1, pp. 151–159, 2018. [Online]. Available: <https://doi.org/10.1109/TMECH.2017.2722479>
- [35] T. Carneiro, R. V. Medeiros Da Nóbrega, T. Nepomuceno, G.-B. Bian, V. H. C. De Albuquerque, and P. P. R. Filho, “Performance analysis of google colab as a tool for accelerating deep learning applications,” *IEEE Access*, vol. 6, pp. 61 677–61 685, 2018. [Online]. Available: <https://doi.org/10.1109/ACCESS.2018.2874767>
- [36] A. S. N. Huda and S. Taib, “Suitable features selection for monitoring thermal condition of electrical equipment using infrared thermography,” *Infrared Physics & Technology*, vol. 61, pp. 184–191, 2013. [Online]. Available: <https://doi.org/10.1016/j.infrared.2013.04.012>
- [37] M. S. Jadin, S. Taib, and K. H. Ghazali, “Feature extraction and classification for detecting the thermal faults in electrical installations,” *Measurement*, vol. 57, pp. 15–24, 2014. [Online]. Available: <https://doi.org/10.1016/j.measurement.2014.07.010>
- [38] W. I. Technology, *ThermoProTP8S™ IR Thermal Camera. User Manual*. Wuhan Guide Infrared Technology Co., Ltd., 2007. [Online]. Available: <https://bit.ly/3bVGd0u>
- [39] L. Sandjakoska and F. Stojanovska, “How initialization is related to deep neural networks generalization capability: Experimental study,” in *2020 55th International Scientific Conference on Information, Communication and Energy Systems and Technologies (ICEST)*, 2020, pp. 163–166. [Online]. Available: <https://doi.org/10.1109/ICEST49890.2020.9232882>
- [40] C. Heghedus, A. Chakravorty, and C. Rong, “Neural network frameworks. comparison on public transportation prediction,” in *2019 IEEE International Parallel and Distributed Processing Symposium Workshops (IPDPSW)*, 2019, pp. 842–849. [Online]. Available: <https://doi.org/10.1109/IPDPSW.2019.00138>
- [41] A. A. Almisreb, N. Jamil, and N. M. Din, “Utilizing alexnet deep transfer learning for ear recognition,” in *2018 Fourth International Conference on Information Retrieval and Knowledge Management (CAMP)*, 2018, pp. 1–5. [Online]. Available: <https://doi.org/10.1109/INFRKM.2018.8464769>
- [42] S. Liu and W. Deng, “Very deep convolutional neural network based image classification using small training sample size,” in *2015 3rd IAPR Asian Conference on Pattern Recognition (ACPR)*, 2015, pp. 730–734. [Online]. Available: <https://doi.org/10.1109/ACPR.2015.7486599>

- [43] J. Xiao, J. Wang, S. Cao, and B. Li, "Application of a novel and improved VGG-19 network in the detection of workers wearing masks," *Journal of Physics: Conference Series*, vol. 1518, p. 012041, apr 2020. [Online]. Available: <https://doi.org/10.1088/1742-6596/1518/1/012041>
- [44] A. Budhiman, S. Suyanto, and A. Arifianto, "Melanoma cancer classification using resnet with data augmentation," in *2019 International Seminar on Research of Information Technology and Intelligent Systems (ISRITI)*, 2019, pp. 17–20. [Online]. Available: <https://doi.org/10.1109/ISRITI48646.2019.9034624>
- [45] K. Zhang, Y. Guo, X. Wang, J. Yuan, and Q. Ding, "Multiple feature reweight densenet for image classification," *IEEE Access*, vol. 7, pp. 9872–9880, 2019. [Online]. Available: <https://doi.org/10.1109/ACCESS.2018.2890127>
- [46] C. Szegedy, W. Liu, Y. Jia, P. Sermanet, S. Reed, D. Anguelov, D. Erhan, V. Vanhoucke, and A. Rabinovich, "Going deeper with convolutions," in *2015 IEEE Conference on Computer Vision and Pattern Recognition (CVPR)*, 2015, pp. 1–9. [Online]. Available: <https://doi.org/10.1109/CVPR.2015.7298594>
- [47] GeeksforGeeks. (2020) Understanding googlenet model - CNN architecture. [Online]. Available: <https://bit.ly/2RLmiuc>
- [48] K. Fu, L. Sun, X. Kang, and F. Ren, "Text detection for natural scene based on mobilenet V2 and U-net," in *2019 IEEE International Conference on Mechatronics and Automation (ICMA)*, 2019, pp. 1560–1564. [Online]. Available: <https://doi.org/10.1109/ICMA.2019.8816384>
- [49] C. Qiu, M. Schmitt, H. Taubenböck, and X. X. Zhu, "Mapping human settlements with multi-seasonal sentinel-2 imagery and attention-based resnext," in *2019 Joint Urban Remote Sensing Event (JURSE)*, 2019, pp. 1–4. [Online]. Available: <https://doi.org/10.1109/JURSE.2019.8809009>
- [50] S. Zagoruyko and N. Komodakis, "Wide residual networks," in *Proceedings of the British Machine Vision Conference (BMVC)*, E. R. H. Richard C. Wilson and W. A. P. Smith, Eds. BMVA Press, September 2016, pp. 87.1–87.12. [Online]. Available: <https://dx.doi.org/10.5244/C.30.87>
- [51] M. Tan, B. Chen, R. Pang, V. Vasudevan, M. Sandler, A. Howard, and Q. V. Le, "Mnasnet: Platform-aware neural architecture search for mobile," in *2019 IEEE/CVF Conference on Computer Vision and Pattern Recognition (CVPR)*, 2019, pp. 2815–2823. [Online]. Available: <https://doi.org/10.1109/CVPR.2019.00293>
- [52] Y. Li and C. Lv, "Ss-yolo: An object detection algorithm based on YOLOv3 and shufflenet," in *2020 IEEE 4th Information Technology, Networking, Electronic and Automation Control Conference (ITNEC)*, vol. 1, 2020, pp. 769–772. [Online]. Available: <https://doi.org/10.1109/ITNEC48623.2020.9085091>
- [53] PyTorch. (2019) TORCHVISION.MODELS. [Online]. Available: <https://bit.ly/2QSCIGe>
- [54] X. Song, Y. Du, and J. Jackson, "An empirical study on hyperparameters and their interdependence for RL generalization," *arXiv preprint arXiv*, vol. abs/1906.00431, 2019. [Online]. Available: <https://bit.ly/3ulY3zZ>
- [55] J. N. van Rijn and F. Hutter, "Hyperparameter importance across datasets," in *Proceedings of the 24th ACM SIGKDD International Conference on Knowledge Discovery & Data Mining*, ser. KDD '18. New York, NY, USA: Association for Computing Machinery, 2018, pp. 2367–2376. [Online]. Available: <https://doi.org/10.1145/3219819.3220058>
- [56] A. Aravkin, J. V. Burke, A. Chiuso, and G. Pillonetto, "On the estimation of hyperparameters for empirical bayes estimators: Maximum marginal likelihood vs minimum MSE," *IFAC Proceedings Volumes*, vol. 45, no. 16, pp. 125–130, 2012, 16th IFAC Symposium on System Identification. [Online]. Available: <https://doi.org/10.3182/20120711-3-BE-2027.00353>
- [57] A. Mikolajczyk and M. Grochowski, "Data augmentation for improving deep learning in image classification problem," in *2018 International Interdisciplinary PhD Workshop (IIPHDW)*, 2018, pp. 117–122. [Online]. Available: <https://doi.org/10.1109/IIPHDW.2018.8388338>
- [58] C. Shorten and T. M. Khoshgoftaar, "A survey on image data augmentation for deep learning," *Journal of Big Data*, vol. 6, no. 1, p. 60, Jul. 2019. [Online]. Available: <https://doi.org/10.1186/s40537-019-0197-0>
- [59] D. Avola, L. Cinque, G. L. Foresti, F. Lamacchia, M. R. Marini, L. Perini, K. Qorraj, and G. Telesca, "A shape comparison reinforcement method based on feature extractors and f1-score," in *2019 IEEE International Conference on Systems, Man and Cybernetics (SMC)*, 2019, pp. 2155–2159. [Online]. Available: <https://doi.org/10.1109/SMC.2019.8914601>
- [60] J. Amat Rodrigo. (2020) Validación de modelos predictivos: Cross-validation, one-leaveout, bootstrapping. [Online]. Available: <https://bit.ly/3bYgPHk>



# SIMPLIFIED MODEL OF A GRID-CONNECTION INTERFACE BASED ON POWER ELECTRONIC CONVERTER FOR GRID STUDIES IN DYNAMIC REGIME

## MODELO SIMPLIFICADO DE UNA INTERFAZ DE CONEXIÓN A LA RED BASADA EN UN CONVERTIDOR ELECTRÓNICO DE POTENCIA PARA ESTUDIOS DE RED EN RÉGIMEN DINÁMICO

Danny Ochoa<sup>1,\*</sup>

Received: 02-02-2021, Received after review: 09-04-2021, Accepted: 22-04-2021, Published: 01-07-2021

### Abstract

The paradigm change experienced by worldwide power systems has led to a massive participation of new energy agents: generation, storage, and consumption. In most cases, these agents are equipped with power electronic converters (PEC) to incorporate their energy to the grid. This reality has motivated the development of highly sophisticated and detailed PEC analytical models that accurately represent their dynamics and enable to study their impact on the grid in a simulation environment. However, when it comes to studying large-scale power systems or with all their components disaggregated, the huge computational burden required to simulate a detailed model could make these studies unfeasible. This paper proposes the design of a simplified model of a grid-connection interface based on PEC for power system analysis using MATLAB/Simulink®. The model is designed to represent, with reasonable numerical accuracy, the dynamic behavior of certain electrical variables of interest that would produce a detailed model and, at the same time, to achieve a noticeable reduction in the computation time. A comparative analysis of the numerical results, the dynamics generated, and the convergence time achieved by the two models enable to validate the proposal. These milestones make it possible to fulfill the objectives of this research.

**Keywords:** Computer Simulation, Energy Conversion, Power Electronic Converter, Power Systems, Pulse Width Modulation

### Resumen

El cambio de paradigma experimentado por los sistemas eléctricos a nivel mundial ha propiciado una participación masiva de nuevos agentes energéticos: generación, almacenamiento y consumo. En la mayoría de los casos, estos agentes están dotados de convertidores electrónicos de potencia (CEP) para verter su energía a la red. Esta realidad ha impulsado el desarrollo de modelos analíticos muy sofisticados y detallados de CEP para estudiar el impacto de su interacción con la red en un entorno de simulación. No obstante, cuando se trata de estudiar redes de gran dimensión o con sus componentes desagregados, la enorme carga computacional requerida para simular un modelo detallado podría suponer una limitante para la realización de tales estudios. En este artículo se propone el diseño de un modelo simplificado de una interfaz de conexión a la red basada en CEP, útil para estudios de red mediante MATLAB/Simulink®. El modelo está concebido para representar, con una precisión numérica razonable, el comportamiento dinámico que tendrían ciertas variables eléctricas de interés de un modelo detallado y, al mismo tiempo, para conseguir una reducción significativa del tiempo de cómputo. Un análisis comparativo de los resultados numéricos, las dinámicas generadas y el tiempo de convergencia de los dos modelos permite validar la propuesta. Estos hitos conseguidos permiten cumplimentar los objetivos planteados en esta investigación.

**Palabras clave:** convertidor electrónico de potencia, conversión de energía, modulación por ancho de pulso, simulación por computadora, sistemas eléctricos de potencia

<sup>1,\*</sup>Departamento de Ingeniería Eléctrica, Electrónica y Telecomunicaciones, Universidad de Cuenca, Ecuador.  
Corresponding author ✉: danny.ochoac@ucuenca.edu.ec.

Suggested citation: Ochoa, D. (2021). «Simplified Model of a Grid-Connection Interface Based on Power Electronic Converter for Grid Studies in Dynamic Regime». INGENIUS. N.º 26, (july-december). pp. 87-99. DOI: <https://doi.org/10.17163/ings.n26.2021.08>.

## 1. Introduction

In recent decades, electrical power systems have experienced a paradigm change that has forced them to go from a predominantly centralized generation model to a more distributed generation model and even to an intelligent electricity grid model, together with the inclusion of new energy generation, storage and consumption agents [1,2]. In the framework of this transition, renewable electric generators, electric vehicles, energy storage systems, among others, are being increasingly integrated, and their grid-connection interface is based on power electronic converters (Figure 1).

This is because the electricity generated/consumed by these agents is incompatible with the grid in terms of type of energy (direct current or alternating current), amplitude and frequency of the voltage, etc. The need to employ electronic converters to incorporate to the grid the energy coming from renewable generators (for instance, wind or photovoltaic), complies with criteria of obtaining the maximum efficiency in converting the primary energy resource into electrical energy [3,4]. In the case of charge stations of electric vehicles, the energy supplied to the batteries is handled by power electronic converters with the purpose of guaranteeing the efficiency of the process and safeguarding the useful life of such batteries [5].

A similar situation applies to battery energy storage systems, in which the energy flow may go from the battery to the grid or vice versa according to the need of the grid of having or storing energy [6]. The power electronic converters have a topology that enable the bidirectional flow of active and reactive power depending on the set points preestablished in the control systems that govern the firing logic of the semiconductors that constitute them. Therefore, from the perspective of the grid, these interfaces behave as current controlled sources [7].

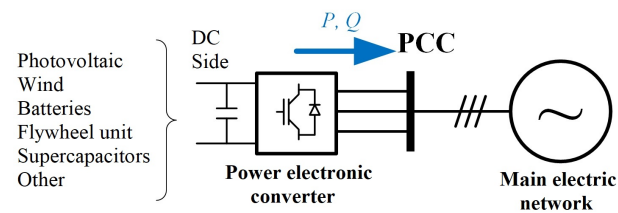


**Figure 1.** Power electronic converter connected to the grid

In the operation of a power electric system in dynamic regime, a reduced participation of renewable generators with grid-connection interface based on power electronic converters does not involve a severe stability problem (of frequency and voltage), since this task is successfully carried out by conventional synchronous generation. However, as this integration is

massified (substituting synchronous generation), the grid starts to show a decrease in its inertial characteristics and, consequently, the operating conventional electric generation may result insufficient to guarantee stability of the system in case that a fault or contingency occurs [8].

This situation is of great concern in weak and isolated electric systems, in which the participation quota of renewable generation in the energy mix is comparable or exceeds conventional generation, as demonstrated by studies published in [9–11]. However, many of the solutions proposed in the literature to mitigate the aforementioned problems are precisely based on the use of more electronic converters, usually associated to energy storage systems (batteries, flywheel units, supercapacitors, among others).

This initial presentation intends to show the relevance claimed by power electronic converters in the operation of an electric system, which has motivated the development of very detailed and complete models devised to emulate its dynamic behavior and interaction with the grid, and to be used in studies based on computer simulations [12,13]. However, when the object of a study is the dynamic analysis of large-scale power systems or of electric systems with all their components disaggregated, the huge computational load required to simulate detailed models of converters in a time range from few seconds up to a couple of minutes (time in which physical phenomena related with the frequency/voltage stability in the grid show up) might limit, to a large extent, conducting this type of studies.

This situation has motivated the search for methodological alternatives that enable modeling power electronic converters in a less complex way, without affecting its numerical accuracy with respect to results that might be provided by a traditional detailed model. For example, recent works published in [14–17] present effective techniques to achieve a significant simplification of the control logic of power electronic converters, all them based on the predictive control of finite states based on the FCS-MPC model.

The results reported in these contributions show that the control of converters through FCS-MPC enables reducing the execution time of control loops, compared to that associated to the implementation of classical linear controllers, without a degradation in its performance. However, this benefit brings along the need to perform a larger number of calculations to fulfill control objectives. To mitigate this situation, these papers propose different designs of matrix converters oriented to reduce the number of sectors necessary for the vector decomposition of the three-phase voltage in the point of common coupling, either by means of a simplification of the formulation used [15–17] or through the use of search tables that speed up the calculation process [14].

A common feature of these scientific contributions

is that the proposed simplifications focus on optimizing the control logic of the converter but maintaining a detailed representation of the three-phase inverter (bridge of 6 or 9 power transistors). In contrast, [18] states a simplification idea focused on the three-phase inverter, represented by means of a bridge of six controlled current sources, modulated through SPWM, whose computational gains are latent as evidenced by the reported results. They also envision that the goodness obtained by simplifying the analytic representation of the three-phase inverter are depleted, to a certain extent, when using a pulse-width modulation technique for controlling the controlled current sources, which demands an important computational effort for its implementation. It is here where the research gap that gave rise to the statement of the present proposal was identified.

With the purpose of achieving a larger degree of simplification, and at the same time maintaining a compromise between simplicity and accuracy, it is proposed the development of a simplified model of a grid-connection interface based on power electronic converters to be used for studies of grids in dynamic regime in the MATLAB/Simulink® simulation environment. The three-phase inverter is represented by three controlled current sources governed by a pair of linear controllers in the  $d - q$  coordinates designed for this research. For this purpose, it is taken as reference the theoretical basis of the operation principle of the detailed model of a complete power electronic converter and its implementation in the simulation program

## 2. Materials and methods

The research developed in this work is experimental, since the experiments, conducted in a computer simulation environment, are carried out under controlled conditions [19].

In the first instance, the theoretical basis and the implementation of a detailed model of a power electronic converter (PEC) are presented. Then, it is stated the development of the simplified model devised to emulate the dynamical behavior that would have the detailed model, from the point of view of the grid, within the time horizon of interest delimited in this research. At the same time, it is sought to achieve a significant reduction of the computational effort required to represent the dynamics of particular electrical variables handled by the PEC in the simulation. These are the main objectives of the research.

### 2.1. Detailed representation of a power electronic converter

Figure 2 shows the typical configuration of a PEC connected to the grid. In the illustration, it is possible

to distinguish two subsystems: the three-phase inverter and its power controller PQ. The inverter, constituted by a bridge of power semiconductors (SCR, MOSFET, IGBT, or others, according to the application), has the function of converting the energy coming from a direct current (DC) system into alternating current (AC) energy for its further incorporation in the three-phase grid, or vice versa. Based on the switches that are closed at each time instant, the bridge will be constructing a three-phase voltage signal at its terminals whose fundamental frequency will be inherited from the voltage established by the grid at the point of common coupling (PCC), and whose amplitude and phase will be defined by the current that is required to be injected to achieve a predetermined value of active and reactive power at the PCC by the converter.

The firing sequence applied to each of the six semiconductors of the inverter is implemented using pulse width modulation techniques, whose principle is described in section 2.1.1., whereas the tasks of controlling the injected active and reactive power are carried out by means of a PQ control scheme similar to the one shown in the lower subsystem in Figure 2, whose criteria are explained with more detail in section 2.1.2. In addition, it should be indicated that, with the purpose of reducing the harmonic content of the current signal injected by the PEC at the PCC, this topology is frequently used together with a first-order three-phase passive filter as seen in the figure.

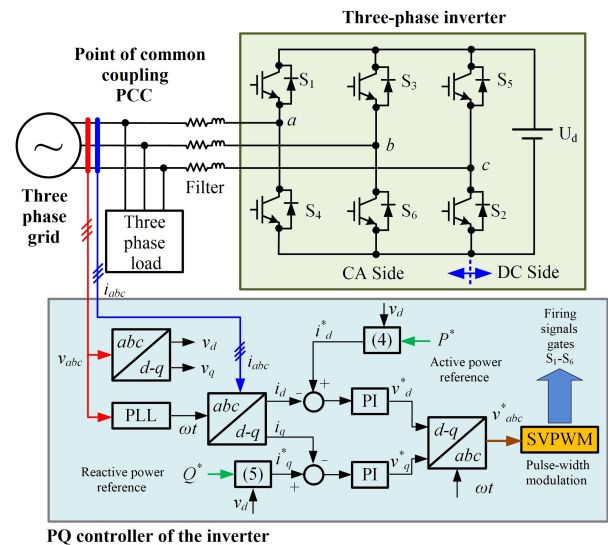


Figure 2. Typical configuration of a three-phase PEC connected to the grid

### 2.1.1. Space vectors pulse-width modulation (SVPWM)

For generating the firing signals of the gates of the transistors that constitute the PEC topology, there

are currently available many techniques with great applicability and high degree of maturity, such as: pulse-width modulation (PWM), selective harmonic eliminated pulse width modulation (SHE-PWM), sinusoidal pulse width modulation (SPWM) and space vectors pulse-width modulation (SVPWM) [20–22]. With the recent advances in the industry of semiconductors, microprocessors and in digital signal processing, the space vectors pulse-width modulation techniques are widely used in the PEC for applications of electric power generation due to their greater flexibility in the control, lower harmonic content and better dynamic performance [22, 23].

In general, the SVPWM is a digital modulation technique in which a sampled reference vector is synthesized through an appropriate number of state vectors switched at particular time instants. Both the reference vector and the vector of switched states are represented in a complex plane through a transformation from an abc three-phase reference framework to a reference framework in  $\alpha - \beta$  coordinates. In order to provide the reader a first approximation to the method, consider the three-phase inverter shown in Figure 2. This topology offers eight switching states, which are arranged according to the a, b, c sequence. Starting from the premise that in each of the three branches of the bridge of transistors only one of them can be active (or in conduction), it is defined as switching state 1 the case when the upper transistor in the branch is active, and 0 when it is active the lower transistor in the branch.

If the voltage at the DC side of the inverter is defined as  $U_d$ , such inverter is capable of offering at its terminals the volage values (phase voltages  $V_A$ ,  $V_B$  and  $V_C$ , and line voltages  $V_{AB}$ ,  $V_{BC}$ ,  $V_{CA}$ ) shown in Table 1. Now, the SVPWM technique is defined by the sequence in which each of the eight switching combinations is selected and the time for which each of them should remain active. Figure 3 gives a graphical idea of the mechanics for constructing the voltage vector  $V_n$  at the inverter terminals, on the stationary complex plane  $\alpha - \beta$ . This vector is decomposed in eight switching states, namely  $V_0$  to  $V_7$ , of which  $V_1$ - $V_6$  are active vectors that constitute a regular hexagon (six sectors), and  $V_0$  and  $V_7$  are null vectors that lie at the center of the hexagon. A detailed description of the theoretical framework of this modulation technique, calculation of switching times for each of the sectors and implementation criteria may be found in [12, 13, 24].

**Table 1.** Switching states of the three-phase inverter

State			Voltages at the inverter terminals						
<i>a</i>	<i>b</i>	<i>c</i>	$V_A$	$V_B$	$V_C$	$V_{AB}$	$V_{BC}$	$V_{CA}$	
0	0	0	0	0	0	0	0	0	
0	0	1	$-U_d/3$	$-U_d/3$	$2U_d/3$	0	$-U_d$	$U_d$	
0	1	0	$-U_d/3$	$2U_d/3$	$-U_d/3$	$-U_d$	$U_d$	0	
0	1	1	$-2U_d/3$	$U_d/3$	$U_d/3$	$-U_d$	0	$U_d$	
1	0	0	$2U_d/3$	$-U_d/3$	$-U_d/3$	$U_d$	0	$-U_d$	
1	0	1	$U_d/3$	$-2U_d/3$	$U_d/3$	$U_d$	$-U_d$	0	
1	1	0	$U_d/3$	$U_d/3$	$-2U_d/3$	0	$U_d$	$-U_d$	
1	1	1	0	0	0	0	0	0	

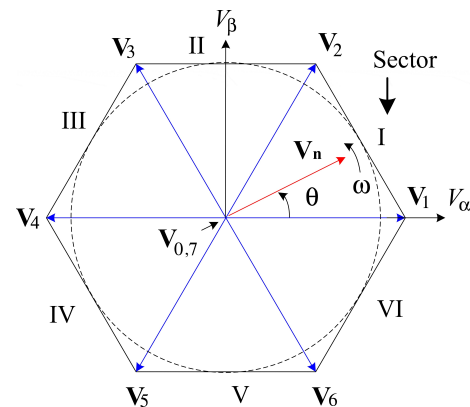


**Figure 3.** SVPWM modulation

### 2.1.2. Control of PQ power

For most industrial applications of PECs, the control of active and reactive power is carried out through the transformation of the three-phase voltage and current vectors expressed as components of a rotating coordinate system, where the vector of each variable is decomposed into vectors in the direct and quadrature ( $d-q$ ) axes [25]. From the theory of electrical power systems, Park transformation is the operator that enables transforming the abc representation of the three-phase electrical variables to a reference framework in the  $d-q$  coordinates, as indicated in (1). In this equation, expressed for the current,  $i_d$ ,  $i_q$  and  $i_0$  correspond to the components in the direct, quadrature and homopolar ( $dq0$ ) axes, respectively, of the  $i_a$ ,  $i_b$  and  $i_c$  three-phase currents;  $\omega$  is the angular frequency of the grid, which is the angular speed at which the  $d-q$  coordinate system rotates. Figure 4 shows an example in which the current vector  $I$  is decomposed into the  $I_d$  and  $I_q$  components. A similar reasoning may be applied to the voltage.

$$\begin{bmatrix} i_d \\ i_q \\ i_0 \end{bmatrix} = \frac{2}{3} \underbrace{\begin{bmatrix} \cos \omega t & \cos (\omega t - \frac{2\pi}{3}) & \cos (\omega t + \frac{2\pi}{3}) \\ -\sin \omega t & -\sin (\omega t - \frac{2\pi}{3}) & -\sin (\omega t + \frac{2\pi}{3}) \\ \frac{1}{2} & \frac{1}{2} & \frac{1}{2} \end{bmatrix}}_{\text{Park transform}} \begin{bmatrix} i_a \\ i_b \\ i_c \end{bmatrix} \quad (1)$$

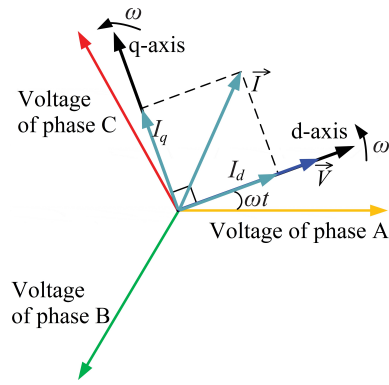


Figure 4.  $d - q$  coordinate system

It has been demonstrated in the literature that the instantaneous powers in a three-phase system, may be calculated through the computation of the instantaneous voltage and current variables expressed in  $d - q$  coordinates, as follows [26]:

$$P = \frac{3}{2} (v_d i_d + v_q i_q) \quad (2)$$

$$Q = \frac{3}{2} (-v_d i_q + v_q i_d) \quad (3)$$

Where:

$v_d$  and  $i_d$ : instantaneous voltage and current in the direct axis.

$v_q$  and  $i_q$ : instantaneous voltage and current in the quadrature axis

For analytical convenience, in this work it will be forced that the direct axis of the  $d-q$  coordinate system is aligned with the phase voltage vector, such that it is achieved that  $v_q = 0$  and moreover, that  $v_d = |\mathbf{V}| = V$ . With this arrangement, the instantaneous powers are defined as follows:

$$P = \frac{3}{2} V i_d \quad (4)$$

$$Q = -\frac{3}{2} V i_q \quad (5)$$

This last pair of expressions shows the advantages of using the  $d-q$  coordinates for controlling the power injected to the grid by the PEC, since regulation of active power will only depend on the manipulation of variable  $i_d$ , whereas regulation of reactive power will depend on  $i_q$ . This implies that the control of power  $P$  may be carried out decoupled from the set-points applied to the control of power  $Q$ , thus requiring for this purpose the design of a single controller for each variable. The lower box in Figure 2 shows an implementation example of the PQ controller for the three-phase inverter under study.

## 2.2. Implementation of the detailed model of the power electronic converter in MATLAB/Simulink®.

Based on the above, this section presents the implementation of the detailed model of a power electronic converter in the MATLAB/Simulink® simulation environment. The grid illustrated in Figure 2 is defined as test bench, whose implementation in the simulator is shown in Figure 5.

Since the scientific interest of this work is focused on studying the interaction of the power electronic converter with the grid; an ideal voltage source will be connected at the DC side of the inverter, which may represent the primary energy resource from different agents such as: wind or photovoltaic generation, inertia flywheels, supercapacitors, battery banks, etc.

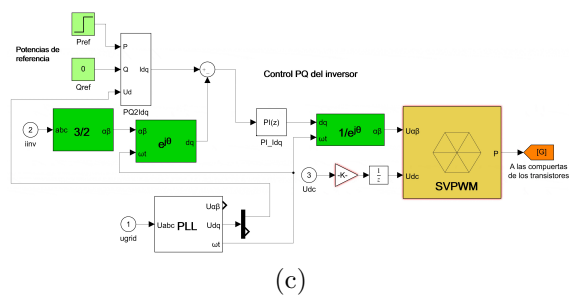
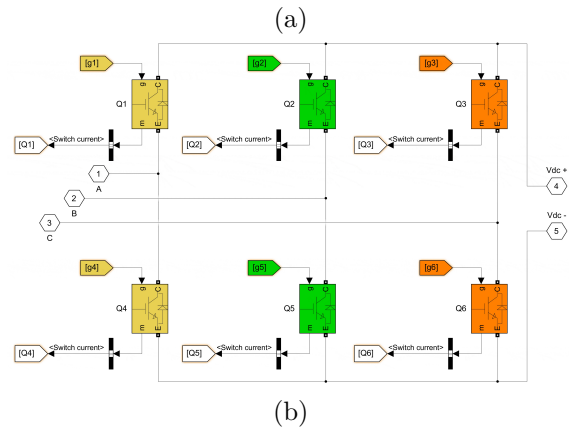
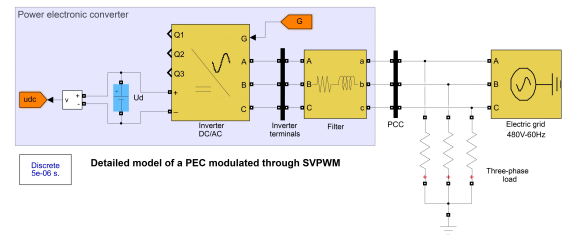


Figure 5. Implementation of the PEC in MATLAB/Simulink® (detailed model): a) test electric system; b) inverter configuration and; c) PQ controller and SVPWM modulator

The values assigned to the parameters of the different elements that constitute the test system are

provided in the Appendix. For more details about the implementation of the converter in the simulator, it is recommended to check [13].

In order to evaluate the performance of the detailed model of the power electronic converter in time domain in the simulation environment, a set-point is established for the active power that starts at a constant value of 10 kW, and changes to 20 kW after 0.4 s of simulation. In addition, a zero set-point has been set for the reactive power during the time horizon of the simulation, with the purpose of verifying the decoupled PQ control offered by the control philosophy through d-q coordinates. The following figures show the results obtained in the simulation.

Figure 6 illustrates the phase-neutral voltage signal constructed by the three-phase inverter through the application of SVPWM modulation and measured at the inverter terminals (before the filtering stage). As it is seen in these plots, this voltage oscillates at the grid fundamental frequency (60 Hz) and presents a high-frequency component (20 KHz) inherited from the carrier employed for the pulse-width modulation, which will be attenuated by the series R-L filter.

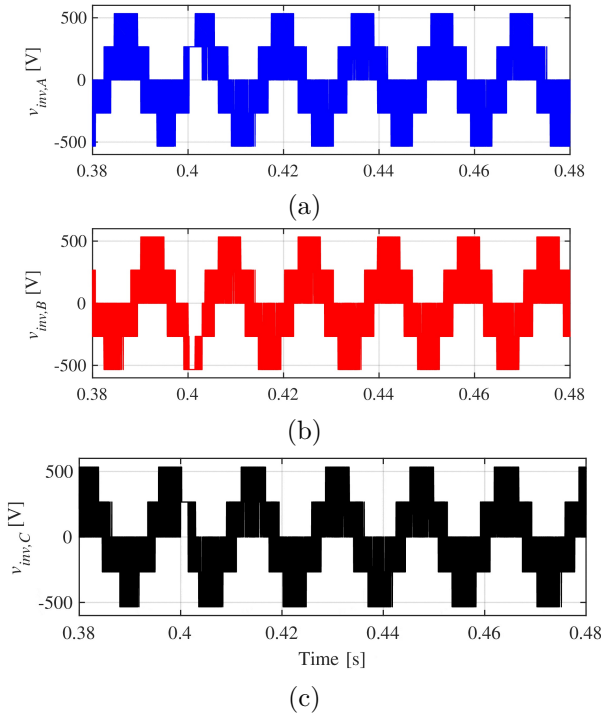


**Figure 6.** Three-phase generated at the inverter terminals

Figure 7(a) shows the wave shape of the current injected by the PEC at the PCC, which has been constructed by the PQ controller of the inverter to achieve the set-points established for active and reactive powers. The time domain dynamics shows the correct performance of the inverter and, moreover, the effectiveness of the filtering task (the values of total

harmonic distortion (THD) are shown in the same figure). Based on the voltage and current measurements at the terminals of the PEC, the active and reactive powers injected at the PCC have been also plotted (Figures 7b and 7c, respectively). Note in Figure 7b that the PEC correctly tracks the active power set-point established in the PQ control system. Similarly, Figure 7c enables assessing the effectiveness of reactive power control, since this variable is maintained virtually at zero for the entire interval simulated. Moreover, this evidences one of the advantages offered by the PEC in its integration to the grid: the decoupled control of the P and Q powers.

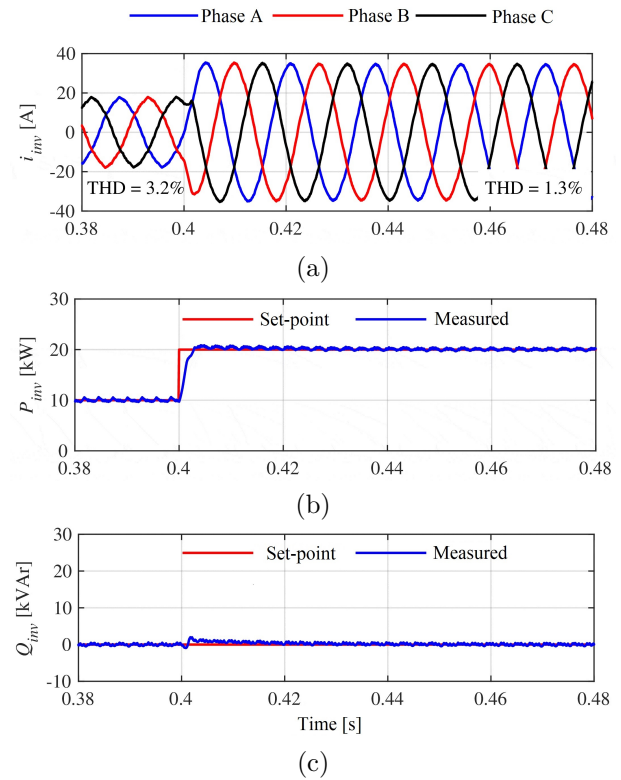


**Figure 7.** Electric variables measured at the output of the PEC: a) current; b) active power and; c) reactive power

For the scientific interest of this study, focused in those phenomena that occur in the time horizon from milliseconds to few seconds in the operating dynamics of an electric power system (as it was justified in the introduction of this work), the set-points of both active and reactive powers are achieved by the PEC virtually instantaneously. This feature will be the premise for the simplified modeling addressed in the following subsection.

### 2.3. Design of the simplified model

In studies of electric power systems in dynamic regime, whose objective is evaluating the impact of energy agents based on the grid-connection interface through

power electronic converters, the use of a detailed model focused in the inner architecture of the PEC, such as the one presented in the previous section, may demand a high computational effort for representing its internal and external variables, which would make inviable many studies in simulation environments in the case of multimachine or large-scale grids. The objective of this work is to develop a simplified model that correctly emulates the dynamic behavior of a PEC seen from the grid at the point of common coupling (PCC), measured in terms of its electric variables. For this purpose, the operating principle, control criteria and simulation results described in section 2.1, will serve as starting point for the statement of the proposal.

**2.3.1. Design criteria**

First, consider the diagram shown in Figure 8a. This illustration is a synthesized representation of the electric system shown in Figure 2. According to the operating mode of the PEC, it will inject at the PCC some values of active and reactive power,  $P_{inv}$  and  $Q_{inv}$ , respectively, according to the preestablished set-points. Since the three-phase voltage at the PCC is imposed by the grid (in amplitude and frequency), the PEC will have to inject the three currents that will enable achieving the reference powers  $P_{inv}^*$  and  $Q_{inv}^*$ , as it is seen in the results illustrated in Figure 7. Therefore, from the point of view of the grid at the PCC, the PEC behaves as a controlled source of three-phase current (Figure 7a) whose amplitude and phase will depend, as it has been mentioned already, on the set-points of power.

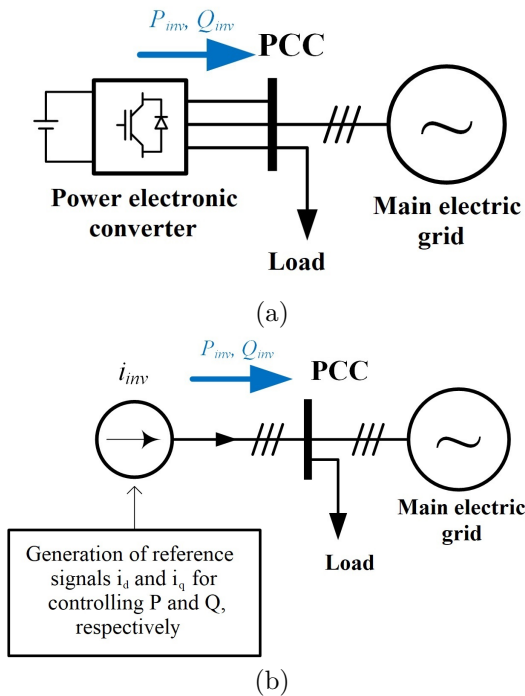


**Figure 8.** Simplification criterion of the PEC model: a) general diagram; b) simplified representation

Based on the theory of the  $d - q$  components (section 2.1.2), the injected three-phase currents are directly related with variables  $P_{inv}$  and  $Q_{inv}$ , given its dependence on current components  $i_d$  and  $i_q$ , respectively (equations 4 and 5). Figure 8b illustrates the simplification criterion of the PEC model, representing it as a controlled current source, whose control scheme is developed hereafter.

Figure 9 shows the three-phase representation of the diagram of Figure 8b, in which the PEC is modeled by means of a controlled current source. This source will have to inject three-phase currents  $i_{inv,A}$ ,  $i_{inv,B}$  and  $i_{inv,C}$  whose amplitude and phase will be defined according to the control criterion implemented and the applications assigned to the converter.

For generating the set-point signals of current, in this work it is proposed using the control scheme shown in Figure 10. According to this scheme, the three-phase signals applied to the controlled current source are generated based on the theory of the  $d - q$  coordinate system, as explained in the following:

- For controlling the active power  $P_{inv}^*$ , a closed-loop PI controller is employed which generates at its output the signal  $i_d^*$  that will be in charge of regulating such power (equation 4). This signal is applied to a first-order delay function, introduced to represent the time it takes for the converter to reach the value of the control variable,  $i_d$ , from the time it is specified at its input,  $i_d^*$ .
- A similar control scheme is proposed for regulating the reactive power  $Q_{inv}^*$ , whose regulation is carried out analogously to the scheme described previously, but in this case manipulating variable  $i_q$  (equation 5).

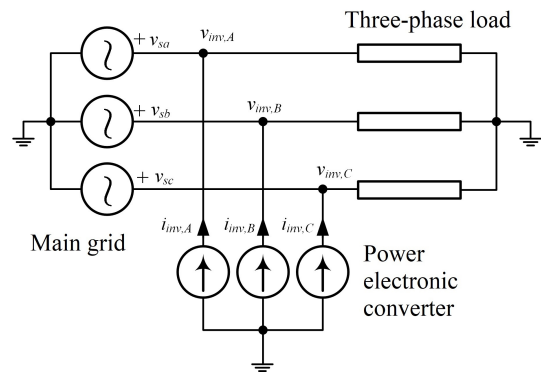


**Figure 9.** Proposed simplification of the PEC

Once signals  $i_d$  and  $i_q$  have been generated, they have to be transformed to an  $abc$  three-phase reference framework before being applied to the controlled source that represents the dynamics of the PEC. In order to carry out this transformation, the phase of the

voltage at the PCC is measured in real time through a phase lock loop (PLL), to further evaluate Park transformation by means of (1). At last, to feedback the PI controllers in each of the control loops, it is measured the instantaneous values of the active and reactive power injected by the controlled current sources at the PCC.

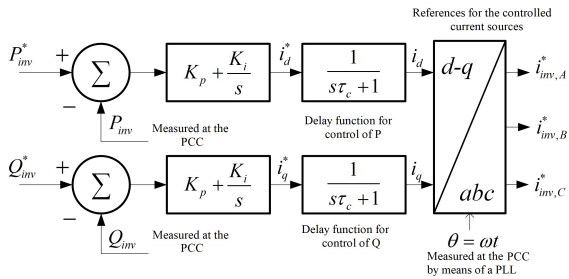


Figure 10. Proposed simplification for the PQ controller

### 2.3.2. Implementation of the proposal in MATLAB/Simulink®

Figure 11 shows the implementation of the PEC simplified model in the simulator on the same test bench used in section 2.1.3. It is noted the notorious simplification regarding complexity and number of elements necessary to represent the integration of the PEC to the grid, compared to the model of Figure 5.

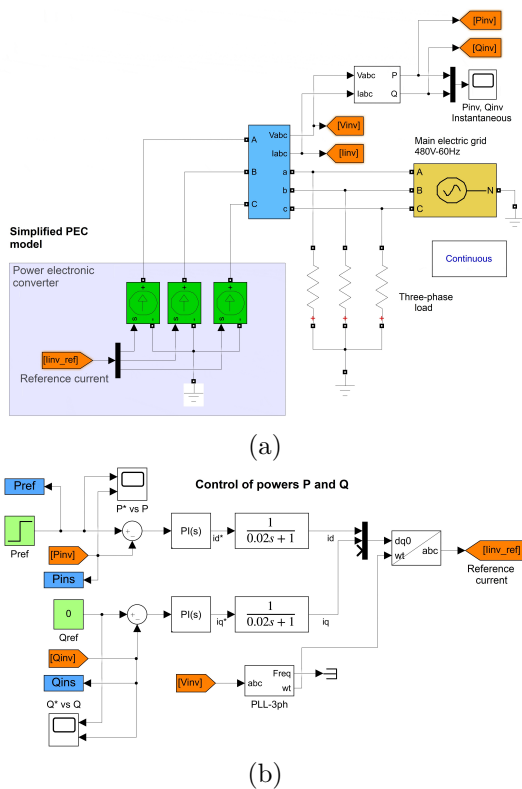


Figure 11. Implementation scheme of the simplified model: a) test electric system; b) PQ controller

In order to facilitate replicating the results of the simulation presented here, the reader is asked to review the values assigned to the different model parameters in the Appendix.

Hereafter, the proposed model is subject to the same operating conditions defined to simulate the detailed model: set-point signals for active and reactive power, time horizon for the simulation, main electric grid, load supplied, etc. The results illustrated in Figure 12a demonstrate that the three-phase current injected by the PEC is correctly generated, and that its amplitude and shape are very close to the ones obtained when simulating the detailed model (Figure 7a).

Figures 12b and 12c show the instantaneous active and reactive powers measured at the converter terminals. It is observed in these figures that the set-point values are successfully reached and faster than in the detailed model. Since the proposed simplified model is closer to the ideal operating conditions of a power electronic converter, the three-phase currents virtually lack of harmonic content, and moreover the instantaneous powers reach their target values almost immediately.

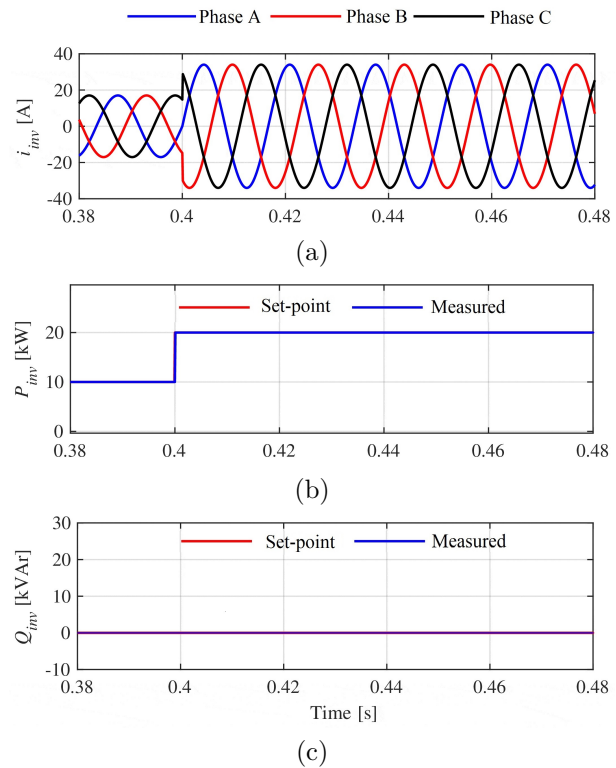
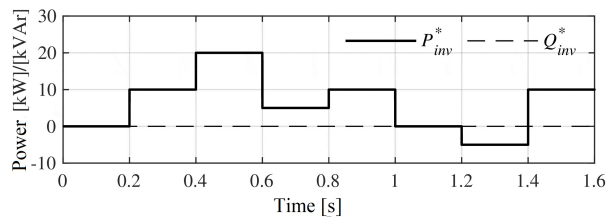


Figure 12. Electric variables measured at the output of the simplified model of the converter: a) current; b) active power and; c) reactive power

### 3. Results and discussion

This section presents a comparative analysis of the performance of the proposed simplified model (Figure 11), with respect to the detailed model taken as reference (Figure 5). For this purpose, the power set-point signals shown in Figure 13 were applied to both models, and they were subjected to the same operating conditions in the test bench designed in MATLAB/Simulink®.



**Figure 13.** Power set-point signals applied to the converter

Figure 14 shows the results obtained in the simulation. It is observed in this figure the correct performance of both models in tracking the power set-points. This is an important conclusion, because these varia-

bles result from quantifying the three-phase voltage and current at the PEC terminals, and are most interesting ones in the dynamic study of electric power systems. The three-phase current achieved by the proposed model has virtually the same envelope of the corresponding current generated by the detailed model. The similarity between the dynamics of the variables of interest for both models in the short time horizon used in the plots, enables verifying the versatility of the proposed model and that the simplification in the representation of the main components of a PEC does not penalize significantly the numerical precision. Note that the resulting dynamics corresponds to the ideal behavior of a converter: much more immediate power transitions, absence of ripple in the injected powers and lack of harmonic content in the current signal. As the time horizon considered in the grid study of the proposed model enlarges, the impact of these limitations on the generated numerical results is smaller.

At last, regarding the computational benefits obtained with the implementation of the proposal, the simulation of the simplified model gives results in 4 % percent of the total computation time that it takes the detailed model to converge.

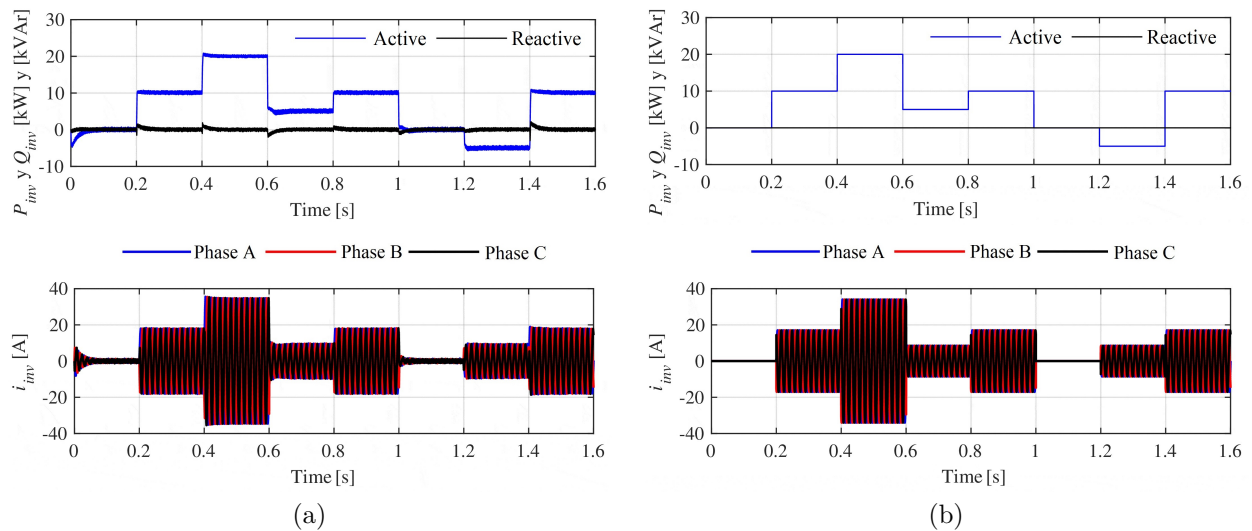


**Figure 14.** Simulation results: a) detailed model; b) simplified model

### 4. Conclusions

A simplified model of a grid-connection interface based on a power electronic converter for studies of grids in dynamic regime has been developed in this work. For this purpose, in the first instance an exhaustive review of the operating principle of a power electronic converter and its implementation in MATLAB/Simulink® was carried out.

Then, according to the theoretical basis described and analyzing the preliminary results of the simulation, a simplified model of the converter was developed such that it enables emulating a dynamic behavior similar to the one that would be obtained when simulating a detailed model.

The effort invested in the simplification and design tasks are justified after performing a comparative analysis of the dynamics generated by the two models, when being subject to the same operating conditions

in the simulation environment. The numerical results and the dynamics exhibited by particular variables of interest are very close to each other, also achieving a reduction in the order of 96 % in the numerical computation time. These milestones enabled accomplishing the main objectives of this research work.

It is important to indicate that the proposed model gives numerical results that are closer to the ideal behavior of a power electronic converter, and hence there is an open possibility of incorporating certain improvements in future research works, such as:

- Add some harmonic content to the three-phase current signal injected, as a function of its amplitude.
- Perform a more exhaustive tuning process of the proportional and integral gains of the PQ controller.
- Apply modeling techniques, such as «hardware-in-the-loop», to achieve a more realistic characterization of the delay function assigned to the control loops of active and reactive power, among others.

## Appendix

### A. Electric grid parameters:

Three-phase source:  $V_{ab(rms)} = 480$  V,  $f = 60$  Hz  
 Three-phase load:  $P_{LA} = P_{LB} = P_{LC} = 1,00$  kW.

### B. Detailed model parameters:

SVPWM modulation:  $f_{carrier} = 20$  kHz  
 PI controller:  $K_P = 50$  y  $K_I = 2500$   
 Series R-L filter:  $R_f = 0.1$   $\Omega$  y  $L_f = 12,7$  mH  
 DC voltage:  $U_d = 800$  V

### C. Simplified model parameters:

P controller:  $K_p = 5$  y  $K_i = 50$   
 Q controller:  $K_p = -5$  y  $K_i = -50$   
 Delay function time constant:  $\tau_C = 0,02$  s

### D. Simulator parameters

	Detailed model	Simplified model
Solver	ode3 (Bogacki-Shampine)	ode23tb (stiff/TR-BDF2)
Step size for numeric calculation	$5 \times 10^{-6}$ s (fixed)	$0,5 \times 10^{-3}$ s (variable max. )

## References

- [1] I. Alotaibi, M. A. Abido, M. Khalid, and A. V. Savkin, "A comprehensive review of recent advances in smart grids: A sustainable future with renewable energy resources," *Energies*, vol. 13, no. 23, 2020. [Online]. Available: <https://doi.org/10.3390/en13236269>
- [2] T. Sadamoto, A. Chakraborty, T. Ishizaki, and J.-i. Imura, "Dynamic modeling, stability, and control of power systems with distributed energy resources: Handling faults using two control methods in tandem," *IEEE Control Systems Magazine*, vol. 39, no. 2, pp. 34–65, 2019. [Online]. Available: <https://doi.org/10.1109/MCS.2018.2888680>
- [3] J. Baran and A. Jäderko, "An MPPT control of a PMSG-based WECS with disturbance compensation and wind speed estimation," *Energies*, vol. 13, no. 23, 2020. [Online]. Available: <https://doi.org/10.3390/en13236344>
- [4] C. González-Castaño, L. L. Lorente-Leyva, J. Muñoz, C. Restrepo, and D. H. Peluffo-Ordóñez, "An MPPT strategy based on a surface-based polynomial fitting for solar photovoltaic systems using real-time hardware," *Electronics*, vol. 10, no. 2, 2021. [Online]. Available: <https://doi.org/10.3390/electronics10020206>
- [5] O. Saadeh, A. Al Nawasrah, and Z. Dalala, "A bidirectional electrical vehicle charger and grid interface for grid voltage dip mitigation," *Energies*, vol. 13, no. 15, 2020. [Online]. Available: <https://doi.org/10.3390/en13153784>
- [6] A. R. Choudhury, S. Pati, A. Choudhury, and K. B. Mohanty, "Control of voltage frequency of a hybrid microgrid using a FLC based bidirectional converter equipped with BESS," in *2018 Technologies for Smart-City Energy Security and Power (ICSESP)*, 2018, pp. 1–6. [Online]. Available: <https://doi.org/10.1109/ICSESP.2018.8376666>
- [7] D. Li, F. Li, D. Rong, K. Zheng, D. Wang, and Q. Li, "An svpwm strategy for multifunction current source converter," in *2018 IEEE International Power Electronics and Application Conference and Exposition (PEAC)*, 2018, pp. 1–6. [Online]. Available: <https://doi.org/10.1109/PEAC.2018.8590656>
- [8] A. Fernández-Guillamón, E. Gómez-Lázaro, E. Muljadi, and A. Molina-García, "Power systems with high renewable energy sources: A review of inertia and frequency control strategies over time," *Renewable and Sustainable Energy Reviews*, vol. 115, p. 109369, 2019. [Online]. Available: <https://doi.org/10.1016/j.rser.2019.109369>
- [9] N. Bouzounierakis, Y. Katsigiannis, K. Fiorentzis, and E. Karapidakis, "Effect of hybrid

- power station installation in the operation of insular power systems,” *Inventions*, vol. 4, no. 3, 2019. [Online]. Available: <https://doi.org/10.3390/inventions4030038>
- [10] J. I. Sarasúa, G. Martínez-Lucas, C. A. Platero, and J. A. Sánchez-Fernández, “Dual frequency regulation in pumping mode in a wind–hydro isolated system,” *Energies*, vol. 11, no. 11, 2018. [Online]. Available: <https://doi.org/10.3390/en1112865>
- [11] D. Ochoa and S. Martínez, “Proposals for enhancing frequency control in weak and isolated power systems: Application to the wind-diesel power system of San Cristobal island-Ecuador,” *Energies*, vol. 11, no. 4, 2018. [Online]. Available: <https://doi.org/10.3390/en11040910>
- [12] A. Kocalmis and S. Sunter, “Simulation of a space vector pwm controller for a three-level voltage-fed inverter motor drive,” in *IECON 2006 - 32nd Annual Conference on IEEE Industrial Electronics*, 2006, pp. 1915–1920. [Online]. Available: <https://doi.org/10.1109/IECON.2006.347442>
- [13] S. Huang, D. C. Pham, K. Huang, and S. Cheng, “Space vector PWM techniques for current and voltage source converters: A short review,” in *2012 15th International Conference on Electrical Machines and Systems (ICEMS)*, 2012, pp. 1–6. [Online]. Available: <https://bit.ly/3fqdEdU>
- [14] M. Siami, D. A. Khaburi, M. Rivera, and J. Rodríguez, “A computationally efficient lookup table based FCS-MPC for PMSM drives fed by matrix converters,” *IEEE Transactions on Industrial Electronics*, vol. 64, no. 10, pp. 7645–7654, 2017. [Online]. Available: <https://doi.org/10.1109/TIE.2017.2694392>
- [15] M. Siami, D. Arab Khaburi, and J. Rodríguez, “Simplified finite control set-model predictive control for matrix converter-fed PMSM drives,” *IEEE Transactions on Power Electronics*, vol. 33, no. 3, pp. 2438–2446, 2018. [Online]. Available: <https://doi.org/10.1109/TPEL.2017.2696902>
- [16] T.-L. Nguyen, H.-N. Nguyen, T. D. Nguyen, and H.-H. Lee, “Simplified model predictive control for AC/DC matrix converters with fixed switching frequency,” in *2019 10th International Conference on Power Electronics and ECCE Asia (ICPE 2019 - ECCE Asia)*, 2019, pp. 1–6. [Online]. Available: <https://doi.org/10.23919/ICPE2019-ECCEAsia42246.2019.8797210>
- [17] J. Lei, S. Feng, P. Wheeler, B. Zhou, and J. Zhao, “Steady-state error suppression and simplified implementation of direct source current control for matrix converter with model predictive control,” *IEEE Transactions on Power Electronics*, vol. 35, no. 3, pp. 3183–3194, 2020. [Online]. Available: <https://doi.org/10.1109/TPEL.2019.2928874>
- [18] M. M. Bhesaniya and A. Shukla, “Computationally efficient method for simulating current source modular multilevel converter,” in *2016 18th European Conference on Power Electronics and Applications (EPE’16 ECCE Europe)*, 2016, pp. 1–10. [Online]. Available: <https://doi.org/10.1109/EPE.2016.7695490>
- [19] R. Hernández Sampieri, C. Fernández Collado, and P. Baptista Lucio, *Metodología de la investigación*. McGraw-Hill Education, 2014. [Online]. Available: <https://bit.ly/3vqDKD4>
- [20] A. Moeed Amjad and Z. Salam, “A review of soft computing methods for harmonics elimination PWM for inverters in renewable energy conversion systems,” *Renewable and Sustainable Energy Reviews*, vol. 33, pp. 141–153, 2014. [Online]. Available: <https://doi.org/10.1016/j.rser.2014.01.080>
- [21] K. Latha Shenoy, C. G. Nayak, and R. P. Mandi, “MPPT enabled SPWM based bipolar VSI design in photovoltaic applications,” *Materials Today: Proceedings*, vol. 5, no. 1, Part 1, pp. 1372–1378, 2018. [Online]. Available: <https://doi.org/10.1016/j.matpr.2017.11.223>
- [22] A. Arif, Y. Bekakra, D. B. Attous, and H. Bakini, “Comparative study between indirect power control and sliding mode control with SVPWM for DFIG driven by wind turbine,” in *2020 1st International Conference on Communications, Control Systems and Signal Processing (CCSSP)*, 2020, pp. 322–327. [Online]. Available: <https://doi.org/10.1109/CCSSP49278.2020.9151770>
- [23] R. Palanisamy, P. Aravindh, and K. Vijayakumar, “Experimental and numerical analysis on SVPWM based grid connected photovoltaic system,” *Materials Today: Proceedings*, 2020. [Online]. Available: <https://doi.org/10.1016/j.matpr.2020.08.382>
- [24] M. A. A. Badran, A. M. Tahir, and W. F. Faris, “Digital implementation of space vector pulse width modulation technique using 8-bit microcontroller,” *World Applied Sciences Journal*, no. 21, pp. 21–28, 2013. [Online]. Available: <https://bit.ly/2RPZF87>
- [25] L. Fan, *Control and Dynamics in Power Systems and Microgrids*. CRC Press, 2017. [Online]. Available: <https://bit.ly/3yDXpBt>
- [26] A. Yazdani and R. Iravani, *Voltage-sourced converters in power systems: modeling, control, and applications*. John Wiley & Sons, 2010. [Online]. Available: <https://bit.ly/3fQU7SP>



# INFLUENCE OF HOMOGENIZATION PRECEDING TO COLD-ROLLING ON THE MICROSTRUCTURE OF THE AA-3003

## INFLUENCIA DEL HOMOGENEIZADO PREVIO AL LAMINADO EN FRÍO EN LA MICROESTRUCTURA DEL AA3003

Gennifer Aparicio-Carrillo<sup>1</sup> , Marco Ciaccia-Sortino<sup>2,\*</sup> , Ricardo Jerez G<sup>3</sup>

Received: 09-06-2020, Received after review: 09-04-2021, Accepted: 11-05-2021, Published: 01-07-2021

### Abstract

The aluminum alloy AA3003 produced by a direct chill continuous casting process has a microstructure that significantly affects its potential use in engineering applications. This work studies the effects of the homogenizing heat treatment on the microstructure of AA3003 with cold working. Six conditions were studied, combining the variables initial condition (with and without homogenizing) and amount of cold working. All conditions were evaluated by means of optical and scanning electron microscopy, in combination with backscattered electrons and energy dispersive X ray spectroscopy techniques. Results suggest that for both initial conditions, the secondary phases present are  $Al_6(Mn,Fe)$  and  $\alpha-Al(Mn,Fe)Si$ , which vary in number, size, and shape. The homogenization caused the dissolution and precipitation of dispersoids, in addition to the spheroidization of primary particles, and minor variation of the size of secondary particles during cold working. Secondary phases are composed of primary and secondary particles, which differ in their Fe and Mn content, resulting in a lower Mn/Fe ratio for the primary particles (0,57 for the as-received condition and 0,80 for the homogenized condition), whereas the dispersoids have a higher Mn/Fe ratio (1,56 after the homogenization). Homogenization increased ductility and reduced the likelihood of cracking during cold working. This was evidenced by the results obtained for strength, hardness, and ductility.

**Keywords:** Microstructure, AA-3003, homogenized, cold work, continuous casting

### Resumen

La aleación de aluminio AA3003 proveniente de colada continua posee una microestructura que afecta significativamente su uso potencial en aplicaciones de ingeniería. Este trabajo estudia los efectos de la homogeneización sobre la microestructura del AA3003 con trabajo en frío. Se estudiaron seis condiciones combinando las variables: condición inicial (con y sin homogeneizado) y cantidad de trabajo en frío. Se evaluaron todas las condiciones mediante microscopía óptica y electrónica de barrido, combinadas con técnicas de electrones retrodispersados y espectroscopía de dispersión de rayos X. Los resultados sugieren que, para ambas condiciones iniciales, las fases secundarias presentes son  $Al_6(Mn,Fe)$  y  $\alpha-Al(Mn,Fe)Si$ . La homogeneización causó la disolución y precipitación de los dispersoides, la esferoidización de las partículas primarias y permitió que la variación del tamaño de las partículas secundarias fuese mínima durante el trabajo en frío. Además, se obtuvo que las fases secundarias están compuestas de partículas primarias y secundarias, que difieren en su contenido de Fe y Mn, lo que resulta en una relación Mn/Fe más baja para las partículas primarias (0,57 para la condición recibida y 0,80 para la condición homogeneizada), mientras que los dispersoides tienen una mayor relación Mn/Fe (1,56 después de la homogeneización). La homogeneización aumentó la ductilidad y redujo la probabilidad de agrietamiento del material durante el trabajo en frío, lo cual se evidenció en los resultados obtenidos de resistencia, dureza y ductilidad.

**Palabras clave:** microestructura, AA3003, homogeneizado, trabajo en frío, colada continua

<sup>1,\*</sup>Centro de Investigaciones en Mecánica, Universidad de Carabobo -Venezuela.

<sup>2</sup>Ingeniería Mecatrónica, Universidad Técnica del Norte, Ecuador

Corresponding author ✉: mciaccia@utn.edu.ec.

<sup>3</sup>Universidad de Carabobo, Escuela de Ingeniería Mecánica, Venezuela.

Suggested citation: Aparicio-Carrillo, G.; Ciaccia-Sortino, M. and Jerez G., R. (2021). «Influence of homogenization preceding to cold-rolling on the microstructure of the AA-3003». INGENIUS. N.º 26, (july-december). pp. 99-110. DOI: <https://doi.org/10.17163/ings.n26.2021.09>.

## 1. Introduction

The AA-3003 aluminum alloy is widely used in the industries of transportation vehicles body manufacturing, and food and beverage packaging, among other applications, and is commonly produced by continuous or semi continuous casting processes.

In the direct chill (DC) continuous casting process, a feed channel brings the molten metal to a rolling mill by a feed channel, at the end of which is a nozzle that distributes the metal throughout the width of the rollers. A water-cooling system maintain the rollers at a lower temperature than the molten metal, causing the solidification of the material in contact with the roller, with high cooling rates.

Therefore, the aluminum matrix becomes highly saturated with manganese and shows a variation of the microstructure with respect to the thickness, since the temperature gradients produce a faster cooling on the surfaces of the sheet than in the middle of the thickness [1].

After solidification, the microstructure is characterized by a heterogeneous solution with primary particles of  $Al_6(Mn,Fe)$  and smaller amounts of  $\alpha-Al(Mn,Fe)Si$  formed at the edges of the solidification cell or in the interdendritic areas. This microstructure significantly affects the mechanical properties of the alloy and its potential use in engineering applications [2].

To reduce this effect, a homogenization heat treatment is applied at temperatures between 500 °C and 650 °C, for a minimum of 8 h [3, 4]. This process reduces the concentration of manganese and controls the size, density, and distribution of the primary and dispersoid particles, which are some of the factors that affect the phenomenon of recrystallization, the texture, and mechanical properties of the alloy in forming stages [5, 6].

This work presents a comparative study of the microstructure of the AA-3003 aluminum alloy from continuous casting with and without homogenization, and with subsequent application of cold working (CW) by rolling, using optical and scanning electron microscopy in combination with back scattered electron and energy dispersive X-ray spectroscopy techniques, and the evaluation of its mechanical properties (microhardness and strength).

The results obtained will allow the comparison of the shape and distribution of the primary and secondary (dispersoids) particles present in the alloy in both initial conditions and after the application of cold work, to evaluate the relevance, from the microstructural point of view, of the homogenization for the subsequent forming of the alloy.

## 2. Materials y methods

### 2.1. Experimentation

A sheet of AA 3003 alloy, 1350 mm wide, 250 mm long (rolling direction) and an average thickness of 6.2 mm, coming from the double roller continuous casting process of CVG ALUCASA (Venezuela) was used. The chemical composition, obtained by optical emission spectroscopy, was (Wt. %): Mn 1.170, Fe 0.666, Si 0.357, Cu 0.133, Zn 0.012, Al 97.600.

Six samples were cut from the sheet. Three cuts, labeled as H samples, were subjected to a homogenization heat treatment in an electrical resistance oven, at 600 °C for 8 h as suggested by [7]., and then cooled slowly, while the other three, called DC samples, were left in its as-received condition. One of each H and DC samples were reserved for reference and labeled as initial condition (IC) samples (0 % cold work). One H sample and one DC sample were cold rolled with 30 % reduction in thickness, and the remaining samples were subjected to a 60 % reduction. The cold working process was carried out in an experimental rolling mill at a speed of 1.5 m/min, maintaining the original rolling direction of the sheet and making several passes. Afterwards, samples were cut for tensile testing specimen preparation and other cuts were made for microstructural evaluation.

The specimens for tensile tests were prepared as specified by the ASTM E8 [8]. standard with a rectangular cross section, 25 mm calibrated length and 100 mm total length. They were cut using the waterjet process to avoid microstructural changes in the cutting zone.

The samples for microstructural evaluation were finally embedded in polymethylmethacrylate to facilitate their handling and preparation, as well as to avoid possible contamination of the surface. Were prepared in accordance with the ASTM E3 [9]. and ASTM E407 [10]. standards, roughed down in water with sandpaper No. 240, 320, 400, 600 and 800. Afterwards, they were polished in two stages; first, with 1  $\mu$ m alumina, and then in a Buehler Electromet 4 electrolytic polishing machine with an electrolyte composed of 800 cm<sup>3</sup> of ethanol, 140 cm<sup>3</sup> of distilled water and 60 cm<sup>3</sup> of 60 % perchloric acid, applying a tension of 17 V for 25 seconds. Finally, samples were etched by immersion in a solution composed of 50 cm<sup>3</sup> of distilled water and 5 g of NaOH at 70 °C for 10 seconds.

#### 2.1.1. Optical microscopy (OM)

A preliminary exploration by optical microscopy is necessary in every microstructural characterization of materials, since it provides a general idea of the microstructure, distribution and morphology of the phases, and other features of interest in which to focus

with the electron microscopy techniques.

Samples were analyzed with an Olympus PMG3 microscope with magnifications from 100X to 1000X, and images were taken with an Olympus DP12 camera.

In this study, the expected variation of the microstructure due to deformation gradients was evaluated in three points cross section of the samples. These positions were termed «outer», «middle» and «center», as shown in Figure 1.

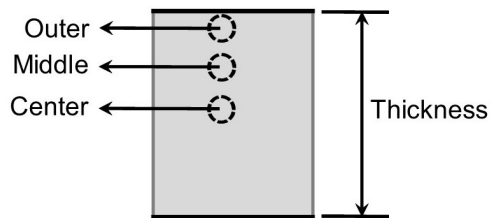


**Figure 1.** Positions to evaluate the variation of the microstructure cross section of the sample

### 2.1.2. Scanning electron microscopy (SEM)

This visualization technique was used to locate phases and precipitates in the microstructure to be identified later. This technique was selected because it is capable of greater image magnification (more than 1000X) compared with optical microscopy.

The sample surface was covered with gold dust, since this is a highly conductive material, enabling the electron scanning on the whole surface of the sample and obtaining images with improved resolution.

A JEOL JSM-6390 scanning electron microscope was used in the backscattered electron (BSE) configuration, a technique that highlights the contrast between phases, making them lighter or darker depending on the atomic weight of its components. In this method, the specific energy of the beam depends on the atomic number of the material, that is, the higher the average atomic number, the higher the intensity. The visualization was performed according to the pattern shown in Figure 1.

### 2.1.3. Energy dispersive X-ray spectroscopy (EDX) analysis

With this technique, it is possible to perform a semi quantitative chemical analysis of specific points or lines in the selected area of the sample. It gives values of the relative amount of the constituent elements expressed as weight percentage and as atomic weight, hence allowing the provisional identification of the observed phase. This analysis was performed with an Oxford Instruments 7582 EDX device.

### 2.1.4. Evaluation of the phases in the AA 3003 alloy

A tentative evaluation of the phases was performed with the results obtained from the SEM studies using a BSE detector, and the EDX analyzes, in conjunction with the investigations of [6, 7], [11, 12]. These authors have been able to identify, using TEM, two types of phases, both in the as-received and in the homogenized conditions:

- The primary phase, formed by the dendritic matrix of aluminum.
- The secondary phases  $Al_6(Mn,Fe)$  and  $\alpha-Al(Mn,Fe)Si$ , which may be part of the primary particles coming from the solidification of liquid with high content of alloying elements, and of the secondary particles (dispersoids, with size less than  $1 \mu m$ ), originating from the decomposition and precipitation of the alloying elements in supersaturated solid solution in the dendritic matrix.

### 2.1.5. Mechanical properties evaluation

Tensile tests were performed at a displacement rate of 5 mm/min using a 25-ton capacity MTS universal materials tester and a 1 in Instron extensometer. Five replications were carried out for each test condition, considering the longitudinal, transverse, and diagonal directions with respect to the rolling direction, evaluating a total of 90 specimens.

Vickers microhardness tests were performed on the samples used in optical microscopy, applying three penetrations for each study condition, according to the ASTM E384 [13]. standard. with a load of 50 g and 15 seconds of application. A Buehler Identamet 1104 Vickers - Knoop microhardness tester was used.

## 3. Results and discussion

### 3.1. Optical microscopy

This technique was used to identify points of interest, as well as the arrangement and preliminary morphology of the precipitates. For this reason, only results for the IC samples are presented. Figure 2 shows a scanning of the microstructure of the AA-3003 in the outer, middle, and center positions of the thickness, in the DC initial condition.

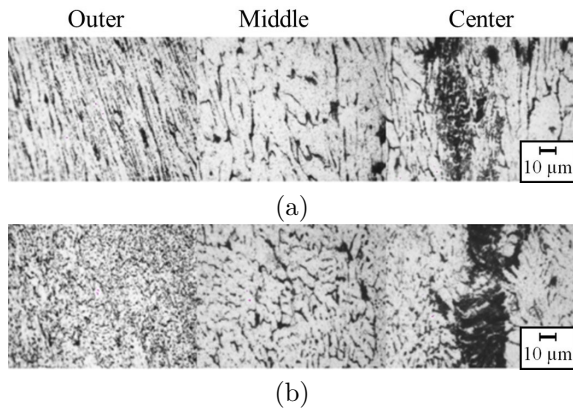


**Figure 2.** OM micrographs showing the microstructure of DC IC samples of AA 3003 alloy: (a) rolling direction, (b) transverse direction

It can be observed in Figure 2 (a) that the precipitates in the outer area are stretched in the direction of rolling. In contrast, in Figure 2(b) they show as dots, which is consistent with the stretching of the precipitates in the direction normal to the plane of the micrograph.

A characteristic of the DC continuous casting process is the temperature gradient across the thickness of the sheet, causing different cooling and solidification rates and producing a change of the microstructure, see Figures 2 (a) and (b). It can be observed that the precipitates are finer and are present in greater quantity at the outer areas of the samples, while in the middle zone the precipitates are larger and with lower density. A central segregation line (CSL) was observed towards the center area of the samples, which consists of a high concentration of precipitates aligned in the rolling direction. This defect, characteristic of aluminum alloys obtained by DC continuous casting, has been observed by other researchers [14, 15].

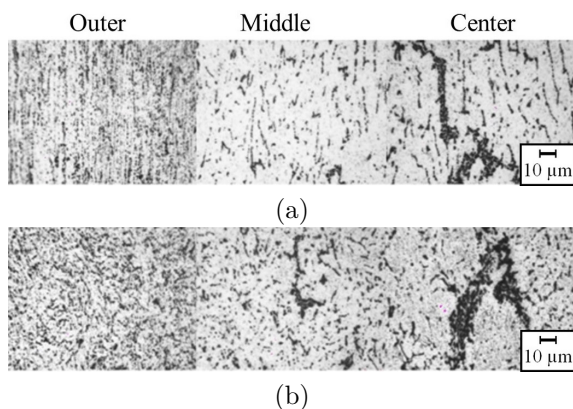


**Figure 3.** OM micrographs showing the microstructure of H IC samples of AA 3003 alloy: (a) rolling direction, (b) transverse direction

An expected result of the homogenization is the uniform distribution of the second phase particles, and

the absence of the CSL. However, although Figure 3 shows that the concentration of the precipitates in the CSL has been reduced, the distribution of the precipitates across the thickness is similar to that of the DC initial condition, see Figure 2. These facts lead to the conclusion that it is necessary to optimize the homogenization heat treatment parameters.

An additional effect of the homogenization is a change in the morphology of the precipitates. The micrograph of the as-received IC specimen in Figure 4 (a) shows the precipitates stretched in the direction of rolling, whereas Figure 4 (b) clearly shows the spheroidization of the precipitates in the homogenized IC specimen.

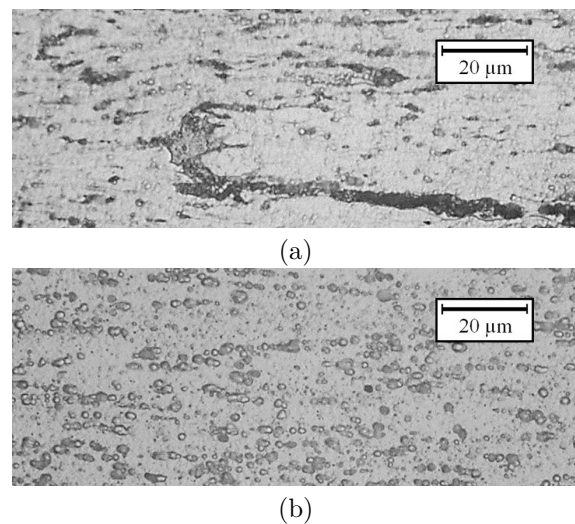


**Figure 4.** OM micrographs showing the effect of the homogenization in the morphology of the precipitates in the IC samples of AA 3003 alloy: (a) Stretched precipitates in the DC specimen, (b) spheroidized precipitates in the H specimen

### 3.2. Evaluation of phases by SEM

The evaluation of the phases of the IC specimens was performed using SEM with the BSE technique. The lighter regions in the images indicate the possible presence of the  $\alpha$ -Al(Mn,Fe)Si phase due to its high average atomic number (rich in Mn, Fe and Si), while the  $Al_6$ (Mn,Fe) phase has a smaller amount of Mn and Fe, thus a lower average atomic number and lower brightness than the  $\alpha$  phase. The matrix is the opaqueness phase, as it has the lowest concentration of the alloying elements.

Figure 5 and Table 1 show the microstructure of the alloy in the as received condition. According to [16], the constituent particles  $Al_6$ (Mn,Fe) and  $\alpha$ -Al(Mn,Fe)Si are formed mainly as interdendritic eutectic networks.

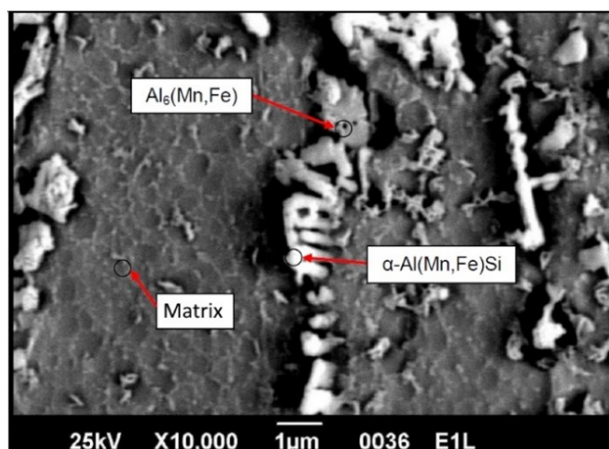


**Figure 5.** SEM micrograph showing the tentative identification of the phases of the AA-3003 alloy in the as received condition

**Table 1.** BSE chemical microanalysis of the AA-3003 alloy in the as-received condition

Phases	Weight percentage				Atomic percentage			
	Al	Mn	Fe	Si	Al	Mn	Fe	Si
Matrix	97	1,9	0,8	–	99	0,9	0,4	–
$\alpha$ -Al(Mn,Fe)Si	87	2,7	4,1	2	88	1,3	2	2
$Al_6$ (Mn,Fe)	89	3,1	5,3	–	90	1,5	2,6	–

It can be seen in Figure 5 that two phases coexist in eutectic networks, which are presumed to be those suggested by [16]. The semi quantitative chemical analysis and the analysis of EDX spectra performed at the points indicated in Figure 5 provide the following results:

- The evaluation in the area pointed as the matrix presents lower amounts of alloying elements compared to the other two, and absence of silicon.
- The phase marked as  $Al_6$ (Mn,Fe) has the highest iron content of the three zones evaluated, and there is no presence of silicon.
- The phase marked as  $\alpha$ -Al(Mn,Fe)Si is the only zone that has silicon.

These results show that the material in the DC condition has a microstructure that could be composed of  $Al_6$ (Mn,Fe) and  $\alpha$ -Al(Mn,Fe)Si.

Figure 6 and Table 2 show the microstructure of the homogenized material. The secondary phases appear as individual particles, in contrast to the eutectic networks shown in the material in the as-received condition. These particles, around 1  $\mu$ m in size, are classified as dispersoids.

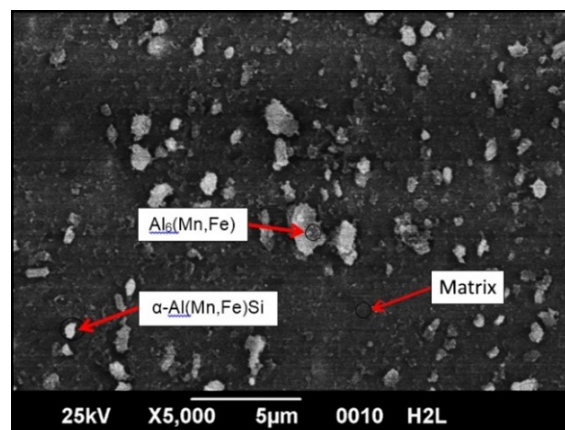


**Figure 6.** SEM micrograph showing the tentative identification of the phases of the AA-3003 alloy in the homogenized, 0 % cold work condition.

**Table 2.** BSE chemical microanalysis of the AA-3003 alloy in the homogenized, 0 % cold work condition

Phases	Weight percentage				Atomic percentage			
	Al	Mn	Fe	Si	Al	Mn	Fe	Si
Matrix	100	–	–	–	100	–	–	–
$\alpha$ -Al(Mn,Fe)Si	79,9	4,72	3,20	2,34	76,5	2,18	1,48	2,15
$Al_6$ (Mn,Fe)	86,3	3,47	3,94	–	84,2	1,66	1,88	–

Throughout the SEM evaluation of the homogenized material, it was difficult to locate particles whose chemical composition corresponded to the  $Al_6$ (Mn,Fe) phase. Therefore, it can be inferred that most of this phase transformed into the  $\alpha$ -Al(Mn,Fe)Si phase as a result of the heat treatment, as suggested by [6] and [11]. This effect increases the ductility of the alloy, improving its performance in plastic forming processes [6] [11].

The results obtained from the chemical analysis and the EDX spectra, presented in Figure 6, show that, as was the case with the as-received material, the dark phase contains the highest quantity of iron, and only the bright phase contains silicon. However, it can be noticed that the matrix is composed of 100 % aluminum, which evidences a decrease of the alloying elements in the supersaturated solid solution as a consequence of the applied heat treatment. Hence, the alloy reaches an equilibrium state through the precipitation of manganese and iron.

### 3.3. Structure and composition of the phases

During the heating to the homogenization temperature, the dispersoids precipitate in the matrix; afterwards, most of the primary particles composed of the  $Al_6$ (Mn,Fe) phase are transformed to the  $\alpha$ -Al(Mn,Fe)Si phase due to the high diffusion of the silicon contained in the solid and eutectics solutions [17–19]. Since transference of the silicon atoms does not

occur from one constituent to another (from primary particles to dispersoids or vice versa), neither interstitially nor by substitution, these researchers have proposed to study the evolution of primary and dispersoid particles through the ratio of the atomic percentages of Mn and Fe, obtained by the EDX spectra.

Li and Arnberg [16]. found that this ratio varies according to the temperature and time of homogenization, since the iron and manganese atoms mutually substitute in the primary and dispersoid particles. Based on this methodology, EDX and semiquantitative chemical analyzes were performed to primary and dispersoids particles located in the center and middle positions (see Figure 1) of both initial condition samples. Figures 7 and 8 show examples of the obtained EDX spectra, and Table 3 presents the elemental chemical composition and average Mn/Fe ratio.

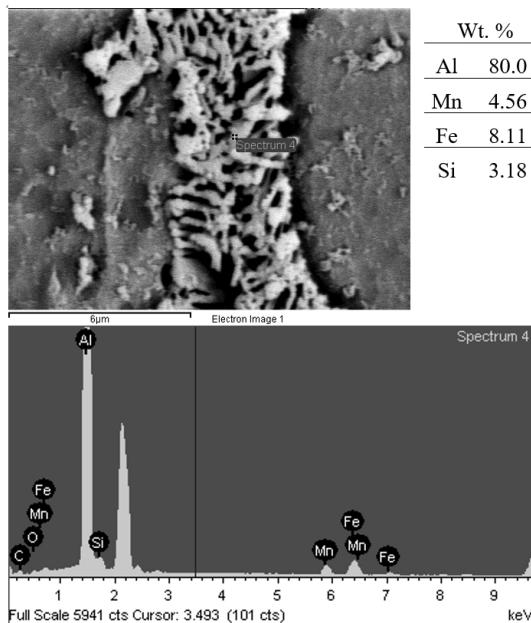


**Figure 7.** SEM micrograph and EDX spectrum of a primary particle in the as-received condition

**Table 3.** Elemental chemical composition obtained by EDX of the primary and dispersoid particles of the AA 3003 alloy in the DC and H initial conditions (Two samples per condition)

Particles	Initial condition	Weight percentage				Average Mn/Fe ratio
		Al	Mn	Fe	Si	
Primary	DC	80	4,6	8,1	3,2	0,57
		82	4,9	8,6	4,5	
	H	77	5,2	6,6	4,1	0,8
Dispersoids	H	77	6	4	3,1	1,56
		79	5,7	3,6	3,8	

Note: Two samples per condition

These results are similar to those found by [15], who obtained Mn/Fe ratios, for the primary particles,

of 0.57 in the DC condition, and 0.79 for the homogenized material; in the case of the dispersoids, a value of 1.70 was found.

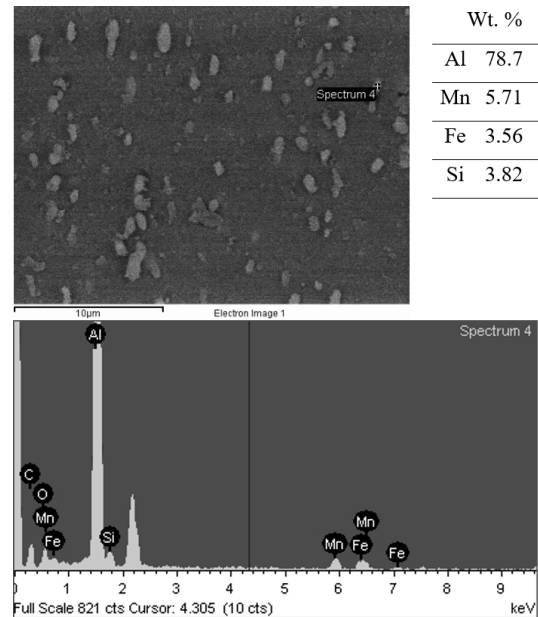


**Figure 8.** SEM micrograph and EDX spectrum of a dispersoid particle in the homogenized condition

Based on the similarity between our results and those found in the literature, it is presumed that there exist two types of  $\alpha$ -Al(Mn,Fe)Si phases in the homogenized condition:

- The primary  $\alpha$  phase, coming from the transformation of  $\text{Al}_6(\text{Mn,Fe})$  and from the rupture of eutectic networks during heating, which, similarly to the primary particles in the DC condition, have a high iron content.
- The secondary  $\alpha$  phase, coming from the precipitation and subsequent thickening of the dispersoids, differentiated from the primary  $\alpha$  phase due to its lower iron content, higher Mn/Fe ratio and smaller size. In this work, the few dispersoids that could be observed had a size that was always slightly larger than  $1 \mu\text{m}$  due to the thickening process during homogenization.

Since iron has very little solubility in solid aluminum, the decrease of the iron content in the primary particles for the homogenized material might indicate that not all the dispersoids in contact with the primary particles are dissolved and absorbed, but some of them may be exchanging manganese atoms for iron atoms with the primary particles. This could be the reason by which some dispersoids grew larger than  $1 \mu\text{m}$  in size and even became primary particles.

The compound tentatively identified as  $\alpha$ -Al(Mn,Fe)Si was the highest weight fraction phase

found in the alloy in the H condition, as was verified through the SEM evaluation as well as in the DC condition. This might be due to the high amount of silicon (0.357 % by weight) contained in the alloy employed in this work compared to those used by other authors (0.1 % to 0.2 % by weight), since a silicon content exceeding a weight percentage of 0.07 favors the precipitation of the  $\alpha$  phase; in contrast, a lower silicon content will promote the precipitation of the  $\text{Al}_6(\text{Mn,Fe})$  phase [17].

Another finding in some areas of the samples in the DC condition was the presence of rectangular shaped precipitates identified, with the help of EDX analyses, as  $\text{Al}_{6-7}\text{Mn}$ , see Figure 9. Similar precipitates, in shape and composition, were observed by [15] and [19], in samples of sheets of AA 3003 obtained by continuous casting. Therefore, this might be a characteristic precipitate morphology of this material.

Moreover, note in Figure 9 that the length of these precipitates is less than  $1 \mu\text{m}$ ; therefore, they can be classified as dispersoids. These particles precipitate in the dendritic zones during the continuous casting process at approximately  $350 \text{ }^\circ\text{C}$ , temperature at which the precipitation of dispersoids initiates.

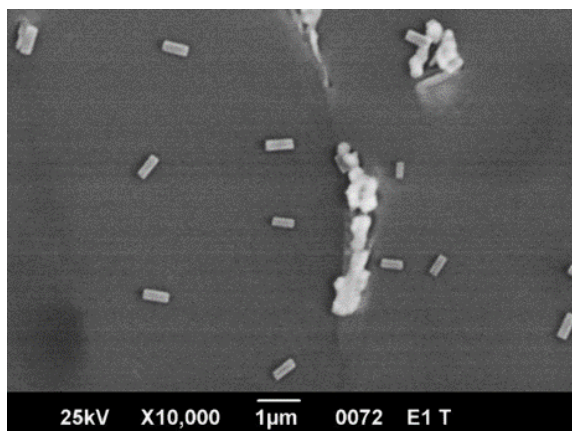


**Figure 9.** SEM micrograph showing  $\text{Al}_{6-7}\text{Mn}$  precipitates in DC samples

### 3.4. Variation of the microstructure with cold working

The sheets of aluminum alloys obtained by continuous casting exhibit a higher concentration of alloying elements in supersaturated solid solution, and smaller intermetallic (eutectic) particles, as compared to other types of casting. These characteristics affect the thermo-mechanical behavior of the alloy during the forming processes. SEM micrographs of the DC and H samples, subjected to cold working as described in the Experimental section, were acquired to investigate this phenomenon and to determine the influence of both the cold working and the homogenization heat treatment on the distribution of the phases. Figure 10 shows the SEM micrographs for the DC material, with and without cold working, of the outer and center positions of the samples.

It can be observed in Figure 10 (a) the formation of eutectic networks in its initial stage, and columnar dendritic structures, both elongated in the direction of lamination, in the outer zone of the sample. This is caused by the direct contact of the surface of the sheet with the roller during the casting process; therefore, it is the zone subjected to the highest cooling rate and pressure.

The variation of the microstructure distribution with the amount of cold work applied is shown in Figure 10 (b) and (c). As the cold deformation increases, so does the separation of the primary and secondary particles contained in the interdendritic and dendritic regions, respectively. Furthermore, the number of primary particles is also increased, but their size is reduced.

Figure 11 shows an image of the central zone in a DC sample, where a CSL can be noticed. This line was observed in all samples of the DC material, which confirms an appropriate control of the process and a good efficiency in the extraction of the heat by both rollers. It was found in an EDX line profile analysis performed to the CSL that as the central zone is approached, there is a reduction of the aluminum concentration and an increase of the alloying elements, mainly iron, due to its low solubility in solid aluminum.

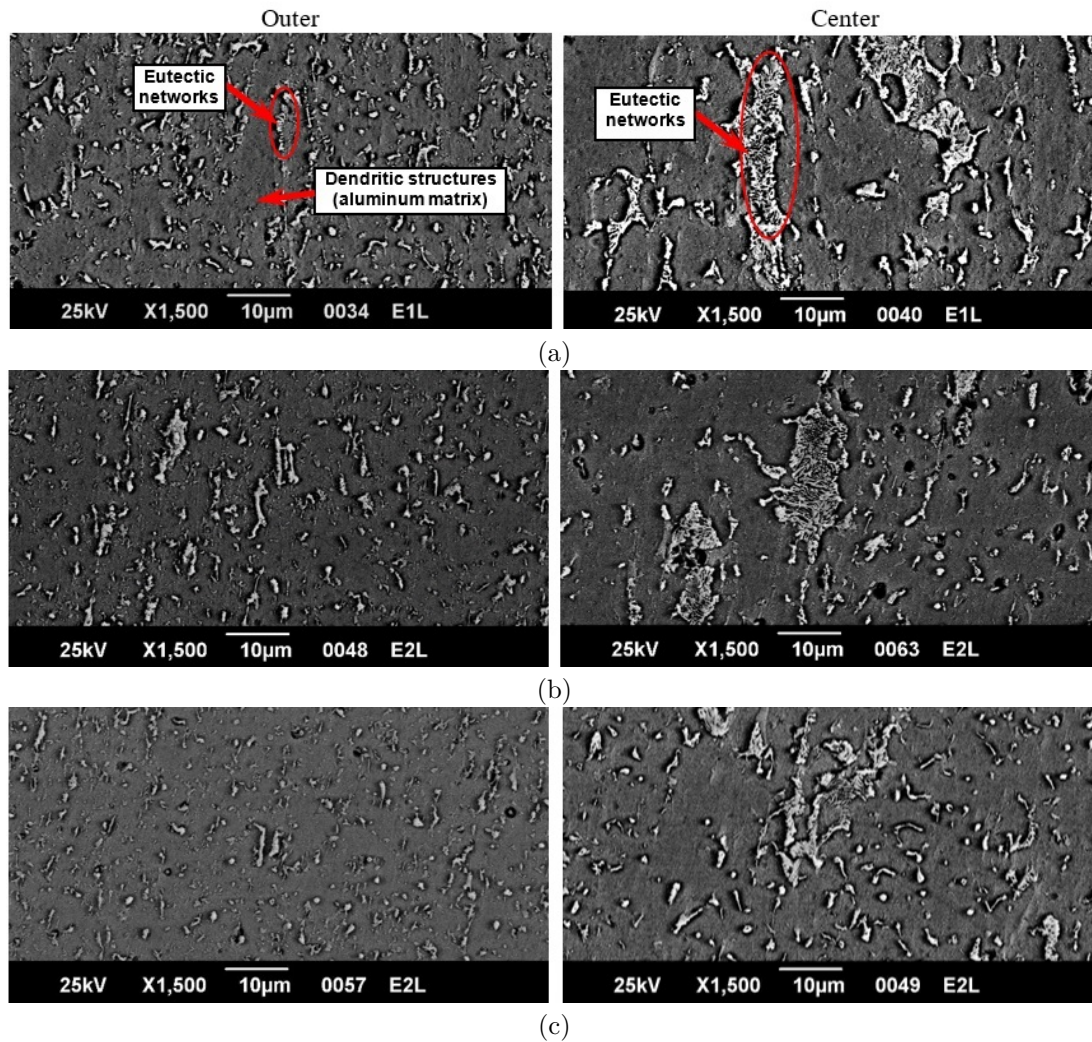


**Figure 10.** SEM micrographs showing the variation of the microstructure of the AA-3003 as-received sample with cold working, at the outer and center positions: (a) 0 % CW, (b) 30 % CW, and (c) 60 % CW

Figure 12 shows the CSL after homogenization, confirming the decrease in the number of segregates, as compared to Figure 11.

Figure 13 shows the SEM micrographs for the homogenized material, with and without cold working, of the outer and center zones of the samples. In this case, particles with an average size of 2 to 3  $\mu\text{m}$  were observed at the outer position of the sample, while in the center they have a larger size, from 3 to 5  $\mu\text{m}$ . This occurs because the formers originate from the rupture of eutectic networks which are much smaller than those observed in the middle and center positions.

In Figure 13 (a), the particles are grouped in the form of what previously were the eutectic networks located in the interdendritic regions. As the level of cold working increases, these particles are displaced by the effect of the movement of the sliding planes, leading to the loss of these clusters and showing further alignment of the precipitates with the direction of lamination (See Figures 12, 13 (a) and 13 (b)).

Note in Figure 13 that, in contrast to the variation of the microstructure for the DC condition, no substantial change in the size of the secondary phase particles was observed with the increase of the cold working in the homogenized samples. This condition contributes to the homogeneity of the mechanical properties, which is an evidence of the effectiveness of the application of the homogenization heat treatment prior to a cold forming process.

Torres *et al.* [20]. determined that a higher diffusion rate, which increases with the time of homogenization, induces a greater localized dissolution of the CSL and, at the same time, a redistribution of the segregates in the aluminum matrix, producing a more uniform microstructure.

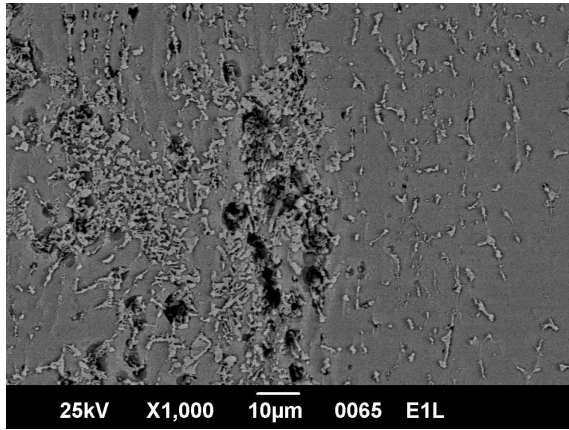


Figure 11. SEM micrographs showing the CSL for the as-received material

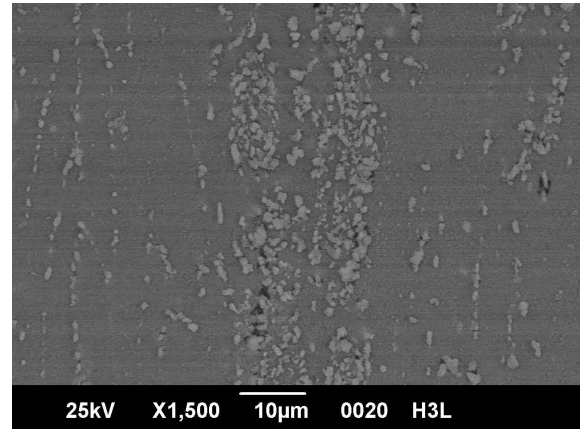


Figure 12. SEM micrographs showing the CSL for the homogenized material

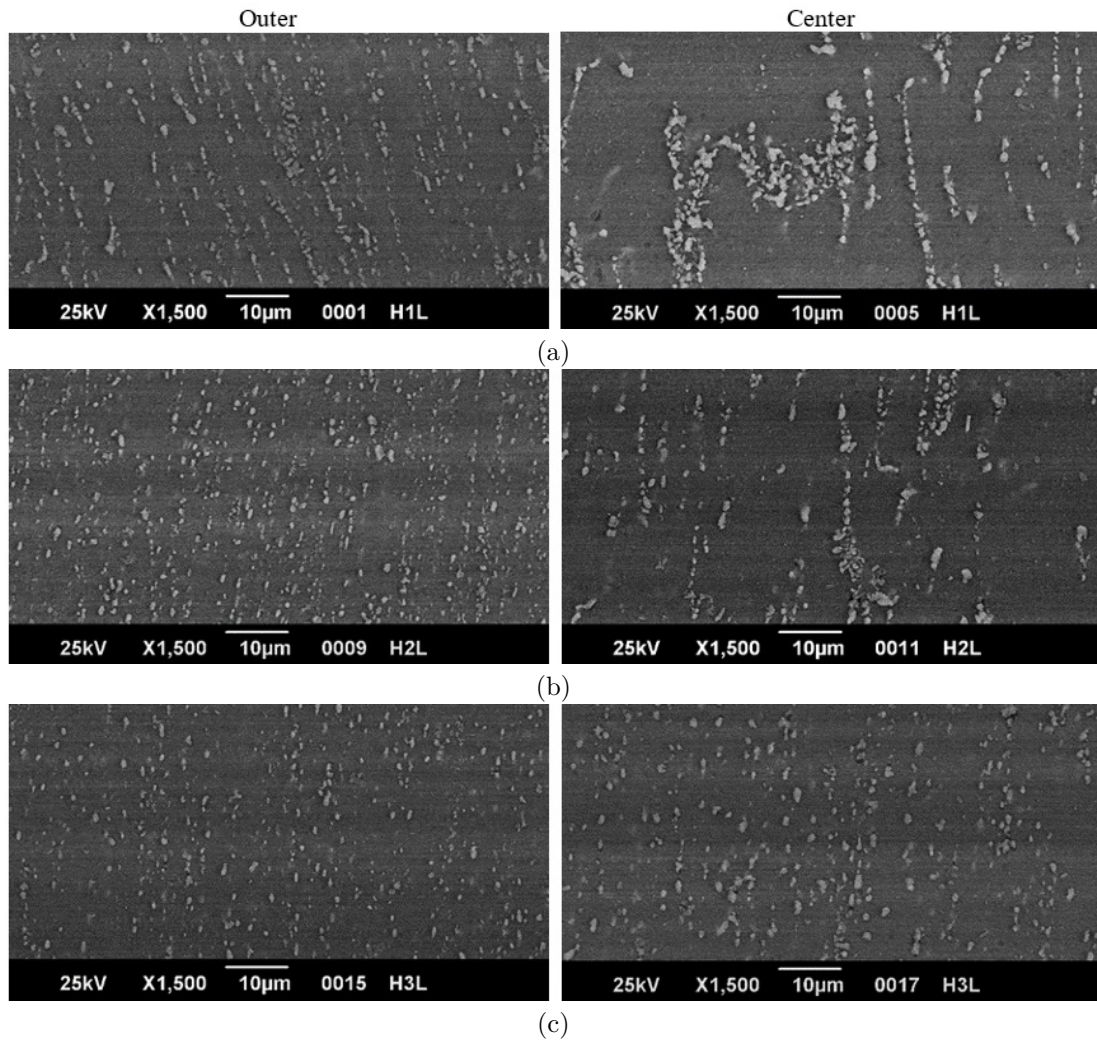


Figure 13. SEM micrographs showing the variation of the microstructure of the AA-3003 homogenized sample with cold working, at the outer and center positions: (a) 0 % CW, (b) 30 % CW, and (c) 60 % CW

### 3.5. Mechanical properties

Table 4 shows the mean and standard deviation of the mechanical properties obtained from the tensile and microhardness tests. Yield strength ( $S_{0,2}$ ), tensile strength ( $S_u$ ), ductility as a function of percent reduction in area (RA) and Vickers microhardness (HV) are reported.

**Table 4.** Mechanical properties of AA3003 in the DC and H conditions as a function of cold work

Initial Cond.	Properties	Cold Work (%), mean (SD)		
		0	30	60
DC	$S_{0,2}$ (MPa)	102 (1,99)	200 (3,10)	243 (4,30)
	$S_u$ (MPa)	161 (0,054)	209 (0,920)	251 (1,50)
	RA (%)	53,9 (1,64)	43,1 (2,56)	28,6 (4,32)
	HV	52,8 (4,65)	70,8 (4,30)	78,4 (3,92)
H	$S_{0,2}$ (MPa)	44,5 (2,17)	148 (1,01)	187 (2,40)
	$S_u$ (MPa)	112 (0,360)	155 (1,14)	195 (1,74)
	RA (%)	64,1 (2,59)	59,9 (0,480)	46,3 (5,63)
	HV	38,3 (2,03)	51,7 (4,96)	62,1 (2,75)

Table 4 shows the increase in strength and hardness, and the decrease in ductility, as the cold work is increased regardless of the initial condition of the material, which is due to the strain hardening mechanism of this alloy and is related to the generation, movement and stacking of dislocations at the grain boundaries or different obstacles that the crystal may present.

The differences in strength and hardness between the as-received and homogenized materials are mainly due to two mechanisms: the first and dominant one is the constraining of the movement of dislocations by the presence of more alloying element atoms in supersaturated solid solution in the DC condition, which was confirmed by the EDS spectrum shown in Figure 7; the second mechanism is the hardening by the dispersion of small particles in the matrix, such as the Al<sub>6</sub>-7Mn precipitates found in the DC condition and shown in Figure 9 which, according to some researchers, are incoherent with the matrix and promote the formation of dislocation rings around them, thus further hardening the aluminum matrix [19], [21].

Table 5 shows the percentage difference of the mechanical properties relative to the maximum amount of cold work, which was 60%. Comparing these results, for the homogenized material prior to cold working (H) a much higher increase in strength (320 % compared to 138 % for the DC material) and hardness (62.1 % compared to 48.5 % for the DC material), and a smaller decrease in ductility (-27.8 % compared to -46.9 % for the DC material) were obtained.

These results indicate that homogenization prior to cold working considerably improves the cold plastic deformation capacity of the alloy, since the decrease in ductility measured as a function of area reduction is

much lower than that obtained without prior homogenization. On the other hand, although the homogenized material does not reach the strength and hardness of the direct cast alloy, by making a comparison for the same deformation percentages, the increases in these properties are more significant, which indicates that by continuing the cold plastic deformation process, a material with higher strength and hardness would be obtained, in addition to the higher cold deformation capacity.

These results correlate with those obtained in section 3.4, showing that the homogenization process of the AA3003 alloy from continuous casting improves its plastic deformation capacity and decreases the probability of cracking during subsequent cold working.

**Table 5.** Percentage differences of the mechanical properties of AA3003 for the DC and H conditions with respect to the maximum amount of cold work (60 % CW).

Properties	Percentage difference	
	DC	H
$S_{0,2}$ (MPa)	138	320
$S_u$ (MPa)	55,9	74,1
RA (%)	-46,9	-27,8
HV	48,5	62,1

## 4. Conclusions

Based on the results obtained for the different evaluated conditions, the secondary phases were tentatively identified as Al<sub>6</sub>(Mn,Fe) and  $\alpha$ -Al(Mn,Fe)Si, which varied in quantity, size, and shape. A conclusive identification requires a TEM analysis, which was not possible at the time of this investigation.

Secondary phases are composed of primary and secondary particles, which differ in their Fe and Mn content, resulting in a lower Mn/Fe ratio for the primary particles (0.57 for the as received condition and 0.80 for the homogenized condition), whereas the dispersoids have a higher Mn/Fe ratio (1.56 after the homogenization).

The homogenization should be adjusted to a longer exposure time, since the secondary phase particles, aligned with the lamination direction, could still be observed in the microstructure.

The homogenization produces the decomposition of the supersaturated solid matrix through the dissolution and precipitation of dispersoids, in addition to spheroidizing the primary particles contained in the interdendritic zones. Because of these effects, the ductility of the material is expected to increase, thus producing favorable conditions for the application of cold forming processes. The application of the cold

working to the unhomogenized material caused the division and separation of the particles of the secondary phases. In contrast to this behavior, the particles of the previously homogenized material showed minor variation of their size. This is a desirable condition for subsequent metal forming applications because of the lower probability of cracking of the material during cold working.

The above was confirmed by the results obtained for strength, hardness, and ductility, which showed an increase of 320 % in yield strength and a decrease in ductility of 27.8 % for the homogenized material, compared to 138 % and 46.9 %, respectively, for the untreated material, thus demonstrating that the homogenized material has a greater capacity for cold plastic deformation.

## Acknowledgements

To the CDCH of Universidad de Carabobo for funding this research.

To the Scanning Electron Microscopy and Optical Microscopy laboratories of Universidad Simón Bolívar, and Materials Laboratory of Universidad de Carabobo, for allowing the use of the equipment used in this work.

## References

- [1] G. Aparicio, "Evaluación del comportamiento mecánico de la aleación de aluminio 3003 proveniente de colada continua," Master's thesis, 2010.
- [2] M. Dehmas, E. Aeby-Gautier, P. Archambault, and M. Serrière, "Interaction between eutectic intermetallic particles and dispersoids in the 3003 aluminum alloy during homogenization treatments," *Metallurgical and Materials Transactions A*, vol. 44, no. 2, pp. 1059–1073, Feb. 2013. [Online]. Available: <https://doi.org/10.1007/s11661-012-1473-1>
- [3] Y. J. Li and L. Arnberg, "Quantitative study on the precipitation behavior of dispersoids in DC-cast AA3003 alloy during heating and homogenization," *Acta Materialia*, vol. 51, no. 12, pp. 3415–3428, 2003. [Online]. Available: [https://doi.org/10.1016/S1359-6454\(03\)00160-5](https://doi.org/10.1016/S1359-6454(03)00160-5)
- [4] Y. Li and L. Arnberg, *Precipitation of Dispersoids in DC-Cast AA3103 Alloy during Heat Treatment*. Grandfield J.F., Eskin D.G. (eds) Essential Readings in Light Metals. Springer, Cham, 2016. [Online]. Available: [https://doi.org/10.1007/978-3-319-48228-6\\_129](https://doi.org/10.1007/978-3-319-48228-6_129)
- [5] M. Velandia and B. Hidalgo, "Evolución estructural de la aleación AA-3003 sometida a tratamiento térmico de homogenización," in *7th Latin American and Caribbean Conference for Engineering and Technology, San Cristóbal, Venezuela*, 2009. [Online]. Available: <https://bit.ly/3fofH1V>
- [6] H.-W. Huang and B.-L. Ou, "Evolution of precipitation during different homogenization treatments in a 3003 aluminum alloy," *Materials & Design*, vol. 30, no. 7, pp. 2685–2692, 2009. [Online]. Available: <https://doi.org/10.1016/j.matdes.2008.10.012>
- [7] Y. J. Li and L. Arnberg, "Precipitation of dispersoids in DC-cast 3003 alloy," in *Aluminium Alloys 2002 - ICAA8*, ser. Materials Science Forum, vol. 396. Trans Tech Publications Ltd, 7 2002, pp. 875–880. [Online]. Available: <https://doi.org/10.4028/www.scientific.net/MSF.396-402.875>
- [8] ASTM, *ASTM E8 / E8M-21, Standard Test Methods for Tension Testing of Metallic Materials*. ASTM International, West Conshohocken, 2004. [Online]. Available: [http://doi.org/10.1520/E0008\\_E0008M-21](http://doi.org/10.1520/E0008_E0008M-21)
- [9] —, *ASTM E3-01, Standard Practice for Preparation of Metallographic Specimens*. ASTM International, West Conshohocken, 2001. [Online]. Available: <http://doi.org/10.1520/E0003-01>
- [10] —, *ASTM E407-07(2015)e1, Standard Practice for Microetching Metals and Alloys*. ASTM International, West Conshohocken, 1999. [Online]. Available: <http://doi.org/10.1520/E0407-07R15E01>
- [11] M. Dehmas, P. Weisbecker, G. Geandier, P. Archambault, and E. Aeby-Gautier, "Experimental study of phase transformations in 3003 aluminium alloys during heating by in situ high energy X-ray synchrotron radiation," *Journal of Alloys and Compounds*, vol. 400, no. 1, pp. 116–124, 2005. [Online]. Available: <https://doi.org/10.1016/j.jallcom.2005.03.062>
- [12] G. E. Totten and D. S. MacKenzie, *Handbook of Aluminum: Vol. 1: Physical Metallurgy and Processes*. CRC Press, 2003. [Online]. Available: <https://bit.ly/2SqMkTE>
- [13] ASTM, *ASTM E384-17, Standard Test Method for Microindentation Hardness of Materials*, ASTM International, West Conshohocken ed., 2002. [Online]. Available: <http://doi.org/10.1520/E0384-17>
- [14] J. Pérez-Illzarbe Uriz, J. Faustmann Salas, and A. Suárez Sanabria, "Recristalización de bandas de aluminio procedentes de colada continua, laminadas en frío," *Revista de Metalurgia*, vol. 36, no. 6, pp. 435–451, 2000. [Online]. Available: <https://dx.doi.org/10.3989/revmetalm.2000.v36.i6.594>

- [15] M. Slámová, M. Karlík, F. Robaut, P. Sláma, and M. Véron, “Differences in microstructure and texture of Al-Mg sheets produced by twin-roll continuous casting and by direct-chill casting,” *Materials Characterization*, vol. 49, no. 3, pp. 231–240, 2002. [Online]. Available: [https://doi.org/10.1016/S1044-5803\(03\)00011-1](https://doi.org/10.1016/S1044-5803(03)00011-1)
- [16] Y. J. Li and L. Arnberg, “Evolution of eutectic intermetallic particles in DC-cast AA3003 alloy during heating and homogenization,” *Materials Science and Engineering: A*, vol. 347, no. 1, pp. 130–135, 2003. [Online]. Available: [https://doi.org/10.1016/S0921-5093\(02\)00555-5](https://doi.org/10.1016/S0921-5093(02)00555-5)
- [17] M. Poková, M. Cieslar, and J. Lacaze, “Enhanced aw3003 aluminum alloys for heat exchangers,” in *WDS’11 Proceedings of Contributed Papers, Part II*, 2011, pp. 141–146. [Online]. Available: <https://bit.ly/3bYehcj>
- [18] M. M. R. Jaradeh and T. Carlberg, “Solidification studies of 3003 aluminium alloys with Cu and Zr additions,” *Journal of Materials Science & Technology*, vol. 27, no. 7, pp. 615–627, 2011. [Online]. Available: [https://doi.org/10.1016/S1005-0302\(11\)60116-3](https://doi.org/10.1016/S1005-0302(11)60116-3)
- [19] J. P. Martins, A. L. M. Carvalho, and A. F. Padilha, “Microstructure and texture assessment of Al-Mn-Fe-Si (3003) aluminum alloy produced by continuous and semicontinuous casting processes,” *Journal of Materials Science*, vol. 44, no. 11, pp. 2966–2976, Jun. 2009. [Online]. Available: <https://doi.org/10.1007/s10853-009-3393-z>
- [20] T. Torres, R. Bisbala, S. Cameroa, and C. Llanos, “Estudio del efecto del tratamiento térmico de homogeneización en la microestructura y propiedades mecánicas de una aleación de aluminio AA8011,” *Acta Microscópica*, vol. 20, no. 2, pp. 165–173, 2011. [Online]. Available: <https://bit.ly/3wCbT2K>
- [21] S. Y. Paredes-Dugarte and B. Hidalgo-Prada, “Micromecanismo de deformación durante la laminación en frío de la aleación comercial de aluminio 3003,” *Suplemento de la Revista Latinoamericana de Metalurgia y Materiales*, no. 2, pp. 778–781, 2009. [Online]. Available: <https://bit.ly/2SpEYQh>



# NUMERICAL ANALYSIS OF FLOW PATTERN MAP OF R600A IN A COLLECTOR/EVAPORATOR OF A SOLAR-ASSISTED HEAT PUMP

## ANÁLISIS NUMÉRICO DE LOS MAPAS DE PATRONES DE FLUJO DEL REFRIGERANTE R600A EN UN COLECTOR/EVAPORADOR DE UNA BOMBA DE CALOR ASISTIDA POR ENERGÍA SOLAR

William Quitiaquez<sup>1,\*</sup> , Eduardo Cortez<sup>2</sup> , Karen Anchapaxi<sup>2</sup> ,  
 C.A. Isaza-Roldán<sup>3</sup> , César Nieto-Londoño<sup>4</sup> , Patricio Quitiaquez<sup>1</sup> ,  
 Fernando Toapanta-Ramos<sup>1</sup>

Received: 30-10-2020, Received after review: 26-05-2021, Accepted: 08-06-2021, Published: 01-07-2021

### Abstract

This research work presents a detailed description of the flow patterns maps generated in a horizontal pipe of the collector/evaporator of a direct-expansion solar-assisted heat pump, using R600a refrigerant as working fluid. The study was performed in a pipe with an internal diameter of 3.8 mm and a length of 1000 mm, mass velocities varying between 197.59 and 267.26 kg·m<sup>-2</sup>·s<sup>-1</sup> and heat flux between 72.83 and 488.27 W·m<sup>-2</sup>; during the experimental tests, an incident solar radiation between 0 and 652.9 W·m<sup>-2</sup> was present. The Wojtan, Ursenbacher and Thome correlation was considered for the analysis and the model used does not require iterative calculations; moreover, it carries out a detailed analysis of the different zones present along the pipe. The predominant zones in this study are intermittent, annular and dryout, found in the five tests, however, due to the working conditions in all tests with the exception of test A, mist and stratified-wavy flow were found.

**Keywords:** Flow patterns, two-phase flow, heat transfer, R600a

### Resumen

En la presente investigación se detallan los mapas de patrones de flujo que se generan en una tubería horizontal de un colector/evaporador componente de una bomba de calor de expansión directa asistida por energía solar, utilizando el refrigerante R600a como fluido de trabajo. El estudio se realizó en una tubería de 3,8 mm de diámetro interno y 1000 mm de longitud, las velocidades de masa variaron entre 197,59 y 267,26 kg·m<sup>-2</sup>·s<sup>-1</sup>, el flujo de calor entre 72,83 y 488,27 W·m<sup>-2</sup>, durante las pruebas experimentales se presentó una radiación solar incidente entre 0 y 652,9 W·m<sup>-2</sup>. Se consideró para el análisis la correlación de Wojtan, Ursenbacher y Thome, el modelo utilizado no requiere de cálculos iterativos, además, plantea un análisis detallado de las diferentes zonas presentes a lo largo de la tubería, evidenciando una mayor precisión en los resultados. Las zonas predominantes en los resultados de este estudio son: intermitente, anular y secado, encontrados en las cinco pruebas, sin embargo, por las condiciones de trabajo en todas las pruebas a excepción de la prueba A, se encontró el flujo niebla y estratificado-ondulado.

**Palabras clave:** patrones de flujo, flujo bifásico, transferencia de calor, R600a

<sup>1,\*</sup>Carrera de Ingeniería Mecánica - Programa de Maestría en Producción y Operaciones Industriales / GIERIMP, Universidad Politécnica Salesiana, Quito, Ecuador. Corresponding author ✉: wquitiaquez@ups.edu.ec.

<sup>2</sup>Carrera de Ingeniería Mecánica, Universidad Politécnica Salesiana, Quito, Ecuador.

<sup>3</sup>Centro de Investigación en Refrigeración y Aire Acondicionado, Universidad Pontificia Bolivariana, Colombia.

<sup>4</sup>Facultad de Ingeniería Aeroespacial, Universidad Pontificia Bolivariana, Colombia.

Suggested citation: Quitiaquez, W.; Cortez, E.; Anchapaxi, K.; Isaza-Roldán, C.A.; Nieto-Londoño, C.; Quitiaquez, P. and Toapanta-Ramos, F. (2021). «Numerical analysis of flow pattern map of R600a in a collector/evaporator of a solar-assisted heat pump». INGENIUS. N.º 26, (july-december). pp. 111-121. DOI: <https://doi.org/10.17163/ings.n26.2021.10>

## 1. Introduction

From past decades until now different protocols have been implemented to help mitigate environmental problems [1, 2]. Abas *et al.* [3] indicate that refrigeration systems are under a prescribed permission period of the Kyoto Protocol which, together with the European Union and the Paris Agreement, emphasize on the elimination of refrigerants that harm the ozone layer and proposes to replace them by natural refrigerants. For this purpose, research studies are conducted across the globe using hydrocarbon refrigerants, such as R290 and R600a, which show an ozone depletion potential (ODP) of 0 and a global warming potential (GWP) of 3 [4].

Yu *et al.* [5] use the R290 and R600a refrigerants as an alternative to R134a. Results indicate that refrigeration systems consume less electricity and the refrigerant load is 30 to 60 % smaller compared to the load of the R134a, concluding that it improves the energy factor of refrigeration systems reducing the refrigerant load with the R600a and decreasing even more the direct emissions to the environment produced by refrigerants [6].

The flow patterns predict the hydrodynamics of the flow and the heat transfer between a pipe and the fluid that it transports; due to its larger heat transfer rate, the refrigerant will rapidly change phase and enter the compressor in pure vapor phase [7]. The flow regime that predicts an almost total phase change is the mist flow pattern visualized at the outlet of the collector/evaporator, which is present in research works such as the one conducted by Wojtan *et al.* [8].

The Wojtan *et al.* correlation [8] is analyzed to determine the flow patterns that may appear in horizontal pipes, since they propose various modifications to the map proposed by Kattan *et al.* [9]. The correlation by Wojtan *et al.* [8] does not involve iterative calculations and indicates that the stratified-wavy zone is further subdivided in three zones, namely slug, slug + stratified-wavy and stratified-wavy; in addition, it is mentioned an extra analysis in the transition of the zones from annular to dryout and from dryout to mist, and likewise it is known the beginning and the end of the dryout zone that may appear in this type of pipes.

Mashouf *et al.* [10] conducted a research working with horizontal tubes and R600a refrigerant; they showed different flow patterns at mass velocities between 114 and 368  $\text{kg}\cdot\text{m}^{-2}\cdot\text{s}^{-1}$ , with saturation temperature between 38 and 42 °C and quality of 0.8 for the boiling process of the refrigerant. The results obtained were an intermittent and annular flow in a dimpled tube, whereas for a smooth tube it was observed an intermittent, annular and stratified-wavy flow. Similarly, Vahabi *et al.* [11] conducted a study of the flow patterns in a copper tube with an internal diameter of 8.7 mm and a length of 1200 mm, using

R600a refrigerant. The test was carried out with mass velocities (GA) between 155 and 470  $\text{kg}\cdot\text{m}^{-2}\cdot\text{s}^{-1}$  and quality between 0.05 and 0.78, finding the flows intermittent, annular and stratified-wavy for the smooth tube.

De Oliveira *et al.* [12] determined the pressure drop and the flow patterns when using R600a refrigerant, in a horizontal tube with an internal diameter of 1 mm. The heat flux conditions fluctuated between 5 and 60  $\text{kW}\cdot\text{m}^{-2}$ , mass velocities between 240 and 480  $\text{kg}\cdot\text{m}^{-2}\cdot\text{s}^{-1}$  and a saturation temperature of 25 °C during the boiling process; they were able to determine that the predominant flows are plug, slug and annular.

Yang *et al.* [13] studied the two-phase flow patterns that may appear in a horizontal pipe with an internal diameter of 6 mm, using the R600a refrigerant. The values obtained experimentally were: heat fluxes ( $q$ ) between 10.6 and 75  $\text{kW}\cdot\text{m}^{-2}$ , mass velocities between 67 and 194  $\text{kg}\cdot\text{m}^{-2}\cdot\text{s}^{-1}$  and saturation pressures between 0.215 and 0.415 MPa. Using a high-speed camera, they observed plug, stratified-wavy, slug and annular flows.

Zhu *et al.* [14] investigated the flow patterns during the boiling process of R32 refrigerant in horizontal mini channels, working with internal diameters of 1 and 2 mm, saturation temperatures between 10 and 20 °C, mass velocities between 500 and 600  $\text{kg}\cdot\text{m}^{-2}\cdot\text{s}^{-1}$ , heat fluxes between 10 and 30  $\text{kW}\cdot\text{m}^{-2}$  and vapor qualities between 0 and 1. The flows observed were slug, annular, dryout, mist and stratified. They determined that the slug flow region is small when the mass velocity increases and is larger when the tube diameter, the saturation temperature or the heat flux increase. For the annular region, it is smaller when the tube diameter, the saturation temperature, the heat flux or the mass velocity increase. The mist flow region has a larger presence when the saturation temperature, the mass velocity or the heat flux increase, and it is reduced when the tube diameter increases.

Zhuang *et al.* [15] observed the flows: plug, slug, intermittent and annular, where they concluded that vapor qualities decrease as the mass velocity increase, whereas the variation of the saturation pressure does not have larger influence in the zones that may be present in the analyses. In their research work about flow patterns, Liu *et al.* [16] identified six zones where the stratified flow only exists when the mass velocity is low, whereas, for the transition from intermittent to annular flow, it will depend on the mass velocity and on the heat flux, i.e., if they increase the transition line will change to a lower quality.

De Oliveira *et al.* [17] studied the boiling heat transfer using R600a refrigerant as working fluid in a horizontal pipe with an internal diameter of 1 mm. The tests were conducted using ranges of heat flux and mass velocity from 5 to 60  $\text{kW}\cdot\text{m}^{-2}$  and from 240 to 480  $\text{kg}\cdot\text{m}^{-2}\cdot\text{s}^{-1}$ , respectively, and also a saturation temperature of 25 °C. The flow patterns observed

in the tests conducted were annular-wavy, annular smooth, slug and plug, with the annular flows being the predominant ones in all experimental tests.

Nasr *et al.* [18] investigated the heat transfer during the boiling of R600a in a horizontal tube with an internal diameter of 8.7 mm. The tests were conducted varying the ranges of mass velocity and heat flux from 130 to 380  $\text{kg}\cdot\text{m}^{-2}\cdot\text{s}^{-1}$  and from 10 to 27  $\text{kW}\cdot\text{m}^{-2}$ , respectively. For quality values up to 0.7 the predominant flow patterns in all experimental tests were intermittent and annular.

The present study was conducted to investigate the flow pattern maps in a collector/evaporator on which there is incident solar radiation, using R600a refrigerant as working fluid during the boiling process. For this purpose, five experimental tests were carried out at different times, where the flow transition will be determined based on the correlation proposed by Wojtan *et al.* [8].

## 2. Materials and methods

The combination of a heat pump and solar energy is known as solar-assisted heat pump (SAHP) system. When collector and evaporator are merged in a single component, the system becomes a direct expansion solar-assisted heat pump (DX-SAHP) [19]. The coefficient of operation (COP) of DX-SAHP systems is above the one corresponding to conventional heat pump systems, due to the high temperatures generated by its solar energy source [20]. The DX-SAHP systems have a great potential in different applications, such as heating rooms and water, and are constituted by a collector/evaporator, a compressor, a condenser and an expansion valve [21].

The working cycle starts when the refrigerant at low temperature and pressure enters the collector/evaporator from the expansion valve, and then vaporizes when receiving the incident solar radiation. Upon arrival to the compressor the fluid is compressed increasing its temperature and pressure, and subsequently the vapor flows to the condenser and releases heat to its container [22]. Afterwards, the expansion valve reduces the temperature and pressure of the refrigerant coming

from the condenser, and finally the refrigerant enters the collector/evaporator and the process is repeated. Figure 1 shows a scheme of the DX-SAHP system constructed [23].

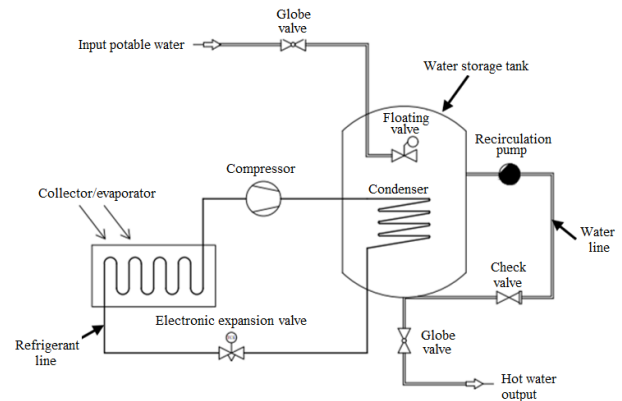


Figure 1. Proposed DX-SAHP system

### 2.1. Collector/evaporator

Figure 2 shows a scheme of the collector/evaporator used for analyzing the flow pattern maps, from which the experimental data for the analysis were obtained. The dimensions of the horizontal pipe used inside the collector/evaporator are: inner diameter 3.8 mm, pipe length 1000 m, collector width 223.4 mm and collector cross-sectional area 223400  $\text{mm}^2$ .

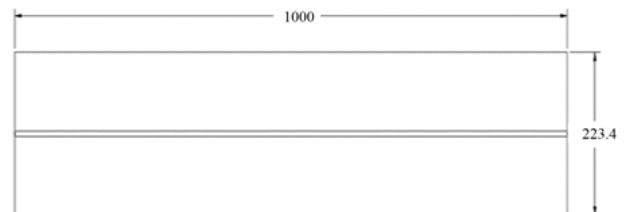


Figure 2. Schematic diagram of the collector/evaporator [2]

Operating tests were conducted at different times; Table 1 presents the most relevant experimental data.

Table 1. Experimental data for 5 different tests

Variables	Test A	Test B	Test C	Test D	Test E
Time	12:15	12:40	12:30	16:45	20:40
Ambiente temperature [°C]	17,6	18,3	17,9	15,4	12
Average incident solar radiation [ $\text{W}\cdot\text{m}^{-2}$ ]	464,1	652,9	582,6	123,22	0
Mass Flow [ $\text{kg}\cdot\text{s}^{-1}$ ]	0,00268	0,00303	0,00295	0,0026	0,00224
Vapor quality[-]	0,176	0,256	0,215	0,2305	0,2325
Superface temperature [°C]	14,5	14,5	14,5	12,6	9,5

## 2.2. Correlation by Wojtan, Ursenbacher and Thome

The equations for determining each of the zones that may be present in the collector/evaporator, are identified from the study conducted by Wojtan *et al.* [8], which is an update of the Kattan *et al.* [9] correlation. The advantage of using this correlation is that it involves no iterative calculation, being its study reliable and one of the most up-to-date and implemented in several research works, such as the ones conducted by Singh *et al.* [24] and Yang and Hrnjak [25].

### 2.2.1. Void fraction and stratified flow

Wojtan *et al.* [8] propose equation (1) as the way to obtain the void fraction, whereas the stratified angle is obtained from equation (2), moreover, it is necessary to know the height of liquid and the nondimensional perimeter of the interface, shown in equations (3) and (4), respectively [26].

$$\alpha = \frac{x}{\rho_v} \left\{ [1 + 0.12(1-x)] \left( \frac{x}{\rho_v} + \frac{1-x}{\rho_L} \right) \dots \right\}^{-1} \quad (1)$$

$$\theta_{strat} = 2\pi - 2 \left\{ \dots \left[ 1 - 2(1-\alpha) + (1-\alpha)^{\frac{1}{3}} - \alpha^{\frac{1}{3}} \right] \dots \right. \\ \left. \dots - \frac{1}{200} (1-\alpha) \alpha [1 - 2(1-\alpha)] \dots \right. \\ \left. \dots [1 + 4 [(1-\alpha)^2 + \alpha^2]] \right\} \quad (2)$$

$$h_{Ld} = 0.5 \left[ 1 - \cos \left( \frac{2\pi - \theta_{strat}}{2} \right) \right] \quad (3)$$

$$P_{id} = \sin \left( \frac{2\pi - \theta_{strat}}{2} \right) \quad (4)$$

### 2.2.2. Stratified to stratified-wavy flow

Wojtan *et al.* [8] propose equation (5) as the calculation required to obtain the stratified flow, where  $G_{strat} = G_{strat}(x_{IA})$  a ( $x < x_{IA}$ ) and indicates that the flow is stratified when  $G_A < G_{strat}$ .

$$G_{strat} = \left[ \frac{(226.3)^2 A_{Ld} A_{vd}^2 \rho_v (\rho_L - \rho_v) g \mu_L}{x^2 (1-x) \pi^3} \right]^{\frac{1}{3}} \quad (5)$$

### 2.2.3. Limit between stratified-wavy to intermittent annular flow

Equation 6 indicates the analysis necessary for the calculation in the wavy zone, indicating that three different zones may be found, namely:

$$\text{Slug zone: } G > G_{wavy}(x_{IA})$$

Slug/stratified-wavy zone:

$$G_{strat} < G_A < G_{wavy}(x_{IA}) \text{ and } x < x_{IA}$$

Stratified-wavy zone:  $x \geq x_{IA}$

$$G_{wavy} = \left\{ \frac{16 A_{vd}^3 g D \rho_L \rho_v}{x^2 \pi^2 [1 - (2h_{Ld} - 1)^2]^{0.5}} \dots \right\}^{0.5} \\ + 50 \left\{ \dots \left[ \frac{\pi^2}{25 h_{Ld}^2} \left( \frac{We}{Fr} \right)_L^{-1} + 1 \right] \right\} \quad (6)$$

### 2.2.4. Transition from intermittent to annular

Wojtan *et al.* [8], Yang *et al.* [27], indicate that equation (7) is necessary to determine the transition from intermittent to annular flow.

$$x_{IA} = \left\{ \left[ 0.34^{\frac{1}{0.875}} \left( \frac{\rho_v}{\rho_L} \right)^{-\frac{1}{1.75}} \left( \frac{\mu_v}{\mu_L} \right)^{\frac{1}{7}} \right] + 1 \right\}^{-1} \quad (7)$$

### 2.2.5. Annular to dryout

Equation (8) shows the analysis that should be considered when determining the dryout zone, proposed by Wojtan *et al.* [8] and used by Yang *et al.* [27].

$$G_{dryout} = \left\{ \frac{1}{0.235} \left[ \ln \left( \frac{0.58}{x} \right) + 0.52 \right] \left( \frac{D}{\rho_v \sigma} \right)^{-0.17} \dots \right\}^{0.926} \\ \dots \left[ \frac{1}{g D \rho_v (\rho_L - \rho_v)} \right]^{-0.37} \dots \\ \dots \left( \frac{\rho_v}{\rho_L} \right)^{-0.25} \left( \frac{\dot{q}}{\dot{q}_{crit}} \right)^{-0.70} \quad (8)$$

### 2.2.6. Dryout to mist

The calculation for the change from dryout to mist flow is determined from the equation (9) proposed by Wojtan *et al.* [8].

$$G_{mist} = \left\{ \frac{1}{0.0058} \left[ \ln \left( \frac{0.61}{x} \right) + 0.57 \right] \left( \frac{D}{\rho_v g} \right)^{-0.38} \dots \right\}^{0.926} \\ \dots \left[ \frac{1}{g D \rho_v (\rho_L - \rho_v)} \right]^{-0.15} \dots \\ \dots \left( \frac{\rho_v}{\rho_L} \right)^{0.09} \left( \frac{\dot{q}}{\dot{q}_{crit}} \right)^{-0.27} \quad (9)$$

In order to define the transitions in the quality range it is necessary to know the following conditions [8]:

$$\text{If: } G_{strat} \geq G_{dryout} \Rightarrow G_{dryout} = G_{strat}$$

$$\text{If: } G_{wavy} \geq G_{dryout} \Rightarrow G_{dryout} = G_{wavy}$$

However, for the dryout and mist equations, the maximum value of quality is 0.99 specified by Wojtan *et al.* [8]- [28] and De Oliveira *et al.* [12]- [29].

### 3. Results and discussion

The flow pattern maps corresponding to each of the tests conducted at different times are obtained from experimental data and the correlation proposed by Wojtan *et al.* [8].

Each of the zones present in the flow pattern maps are identified according to the following nomenclature: Intermittent (I), Annular (A), Stratified (S), Stratified-wavy (SW), Dryout (D) and Mist (M). As the refrigerant circulates along the pipe of the collector/evaporator its quality increases, giving rise to the presence of the different flow patterns.

#### 3.1. Flow pattern maps in different experimental tests

##### 3.1.1. Flow pattern map for test A

Figure 3 shows the flow pattern map obtained at 12:15.

The mass velocity of  $236.5 \text{ kg}\cdot\text{m}^{-2}\cdot\text{s}^{-1}$  indicates that the zones present in this pipe of the collector/evaporator are intermittent, annular and dryout, with quality ranges 0.176-0.2686, 0.2686-0.9484 and 0.9484-0.99, respectively. It is shown the largest visualization range in the annular zone, whereas the dryout zone is the one with the smallest visualization.

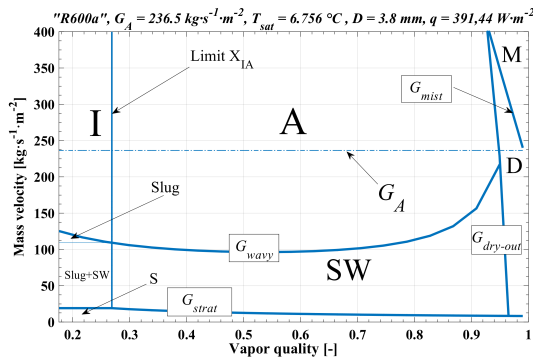


**Figure 3.** Flow pattern map for test A for the R600a refrigerant with  $T_{\text{sat}} = 6,756 \text{ }^\circ\text{C}$ ,  $D = 3,8 \text{ mm}$ ,  $q = 391,44 \text{ W}\cdot\text{m}^{-2}$  and  $G_A = 236,5 \text{ kg}\cdot\text{m}^{-2}\cdot\text{s}^{-1}$

##### 3.1.2. Flow pattern map for test B

Test B was conducted at 12:40, obtaining intermittent, annular, dryout and mist flow patterns, which are visualized in Figure 4. Compared to test A, a new zone appears with a mass velocity of  $267.26 \text{ kg}\cdot\text{m}^{-2}\cdot\text{s}^{-1}$  and quality ranges 0.256-0.283, 0.283-0.941, 0.98-0.979 and 0.979-0.99, respectively, for the four zones present.

The zone with largest visualization is the annular, due to the extended quality range, whereas the intermittent zone is the one that shows the smallest visualization due to its reduced quality range.

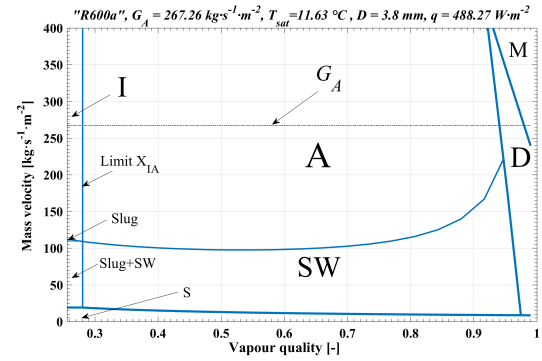


**Figure 4.** Flow pattern map for test B for the R600a refrigerant with  $T_{\text{sat}} = 11,63 \text{ }^\circ\text{C}$ ,  $D = 3,8 \text{ mm}$ ,  $q = 488,27 \text{ W}\cdot\text{m}^{-2}$  and  $G_A = 267,26 \text{ kg}\cdot\text{m}^{-2}\cdot\text{s}^{-1}$

##### 3.1.3. Flow pattern map for test C

Figure 5 shows the flow patterns for test C from the data obtained at 12:30, with a mass velocity of  $260.115 \text{ kg}\cdot\text{m}^{-2}\cdot\text{s}^{-1}$ . Four zones are present, namely: intermittent, annular, dryout and mist, located at the quality ranges 0.215-0.275, 0.275-0.943, 0.943-0.982 and 0.982-0.99, respectively.

In both tests A and B, the zone with largest visualization is the annular, and a small range is shown by the intermittent flow and the dryout zone.

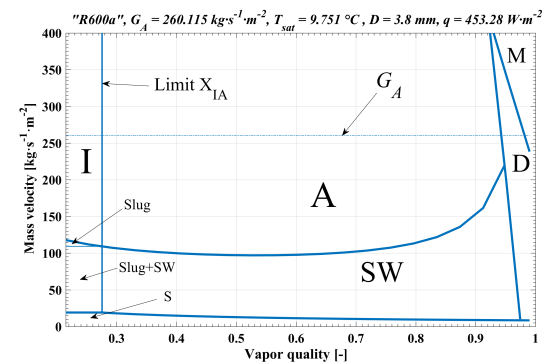


**Figure 5.** Flow pattern map for test B for the R600a refrigerant with  $T_{\text{sat}} = 9,751 \text{ }^\circ\text{C}$ ,  $D = 3,8 \text{ mm}$ ,  $q = 453,28 \text{ W}\cdot\text{m}^{-2}$  and  $G_A = 260,115 \text{ kg}\cdot\text{m}^{-2}\cdot\text{s}^{-1}$

##### 3.1.4. Flow pattern map for test D

The flow pattern map obtained from the experimental data taken at 16:45 with a mass velocity of  $229.43 \text{ kg}\cdot\text{m}^{-2}\cdot\text{s}^{-1}$ , shows the zones: intermittent, annular, stratified-wavy and dryout, as indicated in Figure 6.

The quality ranges present according to the flows are 0.231-0.267, 0.267-0.952, 0.952-0.961 and 0.961-0.99, respectively. The zone with the largest visualization is the annular, due to its quality range, whereas the remaining zones are present in smaller quality ranges. The operating conditions are different, and

both the mass velocity and the time for taking the data have influence, which results in the presence of a new zone, the stratified-wavy.

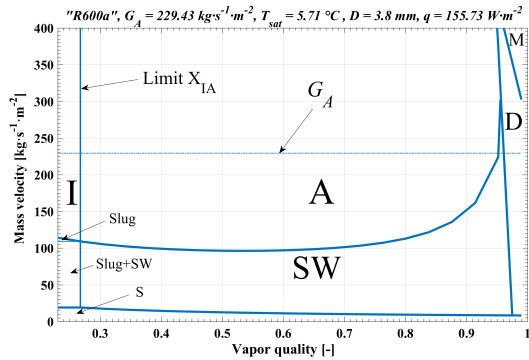


**Figure 6.** Flow pattern map for test B for the R600a refrigerant with  $T_{sat} = 5,71$  °C,  $D = 3,8$  mm,  $q = 155,73$   $W \cdot m^{-2}$  and  $G_A = 229,43$   $kg \cdot m^{-2} \cdot s^{-1}$

### 3.1.5. Flow pattern map for test E

Figure 7 indicates the flow pattern map for test E, obtained from the experimental data taken at 20:40 with a mass velocity of  $197.59$   $kg \cdot m^{-2} \cdot s^{-1}$ , where the flow patterns that appear in this test are intermittent, annular, stratified wavy and dryout.

The range with the largest visualization is the one corresponding to the annular zone, whereas the intermittent and dryout zones are smaller. As it was the case for test D, the stratified-wavy zone appears because the mass velocity is smaller than in previous cases.

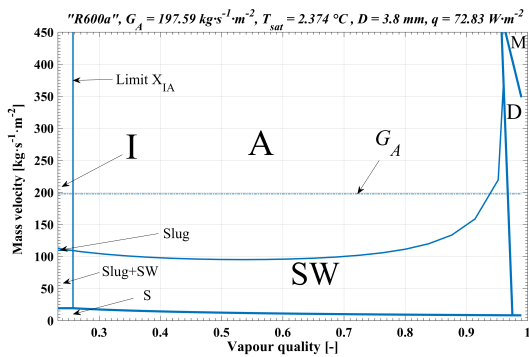


**Figure 7.** Flow pattern map for test E for the R600a refrigerant with  $T_{sat} = 2,374$  °C,  $D = 3,8$  mm,  $q = 72,83$   $W \cdot m^{-2}$  and  $G_A = 197,59$   $kg \cdot m^{-2} \cdot s^{-1}$

All tests indicate that flow patterns vary depending on the operating conditions, and thus it is determined that for a larger mass velocity the mist flow tends to be present, while if it decreases the stratified-wavy zone may appear. In addition, of the zones present in the five tests, the one with the best visualization and a larger quality range is the annular flow, which is the

predominant one in this study, as well as the intermittent and dryout zones, but with a smaller quality range.

## 3.2. Comparison of the flow patterns at different times

Hereafter, an analysis is conducted based on times and on the results obtained regarding the flow patterns, as well as the difference in their operating conditions.

### 3.2.1. Comparison between test A and test B

Figure 8 shows a comparison of the results between test A carried out at 12:15 and test B at 12:40. The incident solar radiations were  $464.1$  and  $652.9$   $W \cdot m^{-2}$ , respectively, and the mass velocities were  $236.5$  and  $267.26$   $kg \cdot m^{-2} \cdot s^{-1}$ , respectively. It may be observed that the limits between the annular flow and the stratified-wavy and mist flows do not vary, whereas there is a small mismatch in the limit of the dryout zone, as well as the intermittent-annular limit, in which the initial qualities vary from  $0.176$  to  $0.256$ .

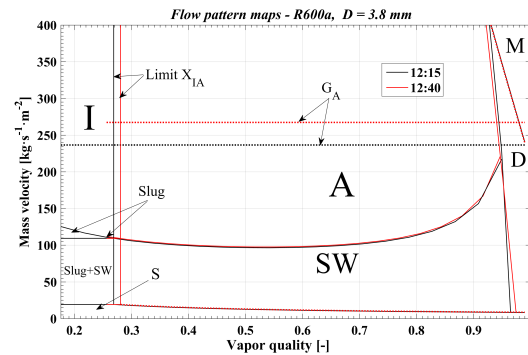


**Figure 8.** Comparison of the maps corresponding to tests A and B at 12:15 and 12:40, respectively

### 3.2.2. Comparison between test A and test D

Figure 9 shows a comparison between tests A and D, with data taken at 12:15 and 16:45, with incident solar radiations of  $391.44$  and  $155.73$   $W \cdot m^{-2}$ , respectively, and mass velocities of  $236.5$  and  $229.43$   $kg \cdot m^{-2} \cdot s^{-1}$ , respectively. The limits between stratified and wavy do not vary, which is not the case for the remaining limits.

In case of test B, the mass velocity does not indicate that the stratified-wavy flow appears in this test, however, in test D the mass velocity is smaller and the stratified-wavy zone is present. On the other hand, the limits of the dryout and mist zones move to the right due to the increment of the incident solar radiation.

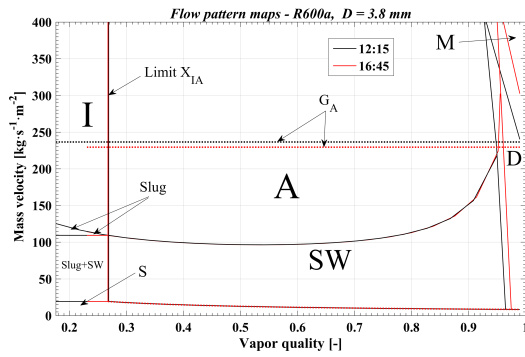


Figure 9. Comparison of the maps corresponding to tests A and D at 12:15 and 16:45, respectively

### 3.2.3. Comparison between test D and test E

Figure 10 shows a comparison between tests D and E, with experimental data taken at 16:45 and 20:40, incident solar radiations of 123.22 and 0 W·m<sup>-2</sup> and mass velocities of 229.43 and 197.59 kg·m<sup>-2</sup>·s<sup>-1</sup>, respectively. The limits of the stratified-wavy line show no variation, whereas the limits of the dryout and mist zones show a trend to the right when the incident solar radiation decreases at high quality values. Both tests indicate the presence of the stratified-wavy zone with the aforementioned values of mass velocity, however, for test D there is a better visualization of the flow because the mass velocity decreases due to the incident solar radiation of 0 W·m<sup>-2</sup>.

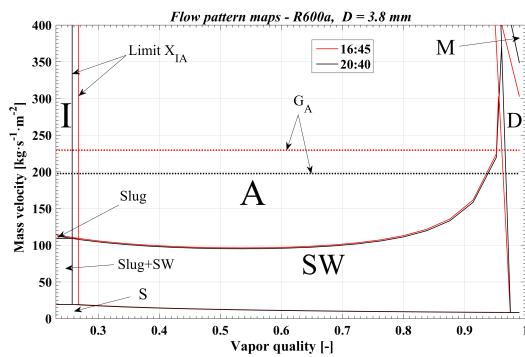


Figure 10. Comparison of the maps corresponding to tests D and E at 16:45 and 20:40, respectively

### 3.2.4. Comparison between test A and test E

Figure 11 displays a comparison of the flow pattern maps between tests A and E, with working hours of 12:15 and 20:40, incident solar radiations of 464.1 and 0 W·m<sup>-2</sup> and mass velocities of 236.5 and 197.59 kg·m<sup>-2</sup>·s<sup>-1</sup>, respectively. The stratified-wavy limit shows no variation, whereas the dryout and mist limits move to the right compared to the resulting limits at noon. The difference between tests A and E for the

aforementioned velocities indicate that the stratified-wavy flow appears only in test E, not in test A.

### 3.2.5. Comparison of tests A, D and E

Figure 12 shows a comparison between tests A, D and E with working hours 12:15, 16:45 and 20:40, and incident solar radiations of 464.1, 123.22 and 0 W·m<sup>-2</sup>, respectively. It is analyzed that the mass velocity in the plot is directly proportional to the solar radiation.

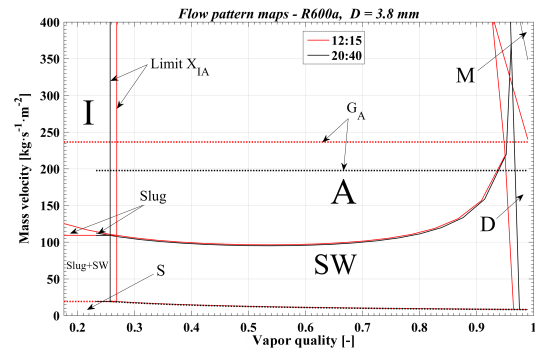


Figure 11. Comparison of the maps corresponding to tests A and E

When reducing both variables, the dryout and mist zones extend to the right with high quality values, whereas the stratified-wavy limits show no variation. It is indicated how the  $x_{IA}$  limit varies at the initial qualities. Zones that are present in the pipe according to each condition may be identified based on the mass velocity, if it is higher it will correspond to test A and if it is lower it corresponds to tests D and E. The zones present in test A are intermittent, annular and dryout, whereas for tests D and E the zones present are intermittent, annular, stratified-wavy and dryout.

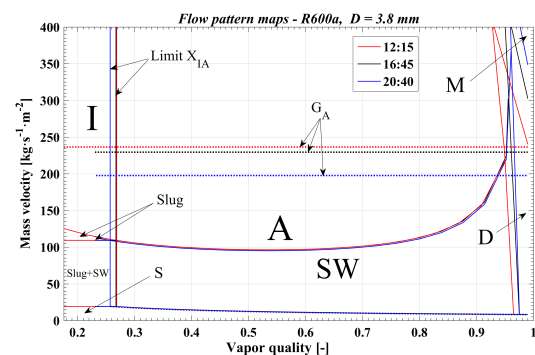
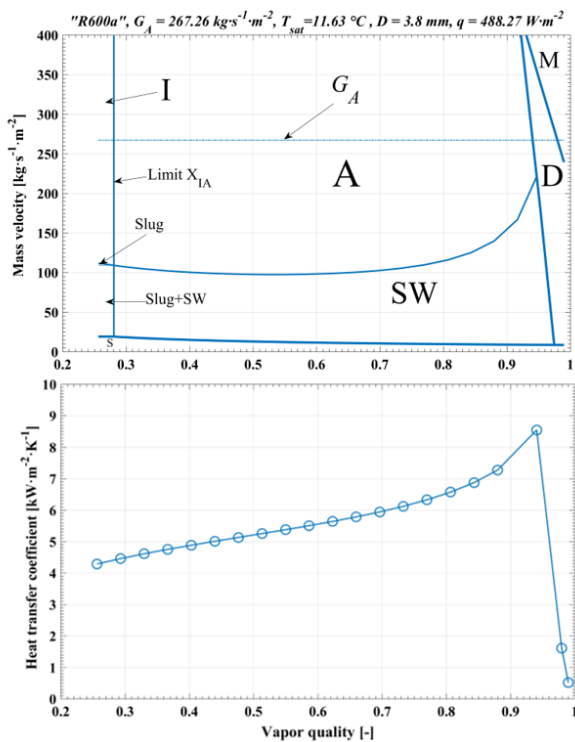


Figure 12. Comparison of the flow pattern maps with incident solar radiation at different times

In the different maps obtained, test A shows the best results due to its lower initial quality, the limits within the plot observed in Figure 3 are similar to the model by Wojtan *et al.* [8] considered for the analysis of the boiling fluid. In addition, one of the

predominant conditions in a DX-SAHP system is to have a working fluid in vapor phase at the outlet of the collector/evaporator; the flow patterns that meet this condition are dryout and mist, which are present in the larger quality range 0.941-0.99 for test B observed in Figure 4.

It is evidenced in Figure 13 the relationship between flow patterns and heat transfer coefficient (HTC); the flow patterns base their importance indicating the phase change of a refrigerant that flows within a pipe. This figure shows the intermittent, annular, dryout and mist zones. For flow patterns such as intermittent and annular the behavior of the heat transfer coefficient shows an increasing trend; at the beginning of the dryout zone the HTC tends to decrease for increasing vapor quality [8]. The working fluid reaches a quasi-total caloric balance with the pipe, and when reaching the mist zone, it completely changes its phase from liquid to vapor, and thus the HTC in the dryout and mist zones tends to decrease to minimum values of  $516.37 \text{ W}\cdot\text{m}^{-2}\cdot\text{K}^{-1}$  for the example shown.



**Figure 13.** Contrasting of flow pattern maps vs. heat transfer coefficient for the Wojtan *et al.* [8], [28] mathematical model

## 4. Conclusions

The flow pattern maps obtained in the experimental tests conducted represent the behavior of the phase change of the R600a refrigerant, in response to the solar energy gained by the system. The plots and the

limits of the different flow regimes showed a variation based on the different operating parameters, namely: mass velocity, incident solar radiation, heat flux, mass flow [23] and initial quality of the working fluid. Similarly, the flow pattern maps enable studying the different configurations of the distribution of two phases in a fluid, and indicate which zone predicts its almost total phase change; for that purpose, the following conclusions were obtained:

The predominant zones in this study are intermittent, annular and dryout, since these are the flows present in all tests, and the dryout and mist zones present in different opportunities. This is the case of the mist zone, which will be present when the heat flux and the mass velocity are  $488.27 \text{ W}\cdot\text{m}^{-2}$  and  $267.26 \text{ kg}\cdot\text{m}^{-2}\cdot\text{s}^{-1}$ , respectively, whereas for the stratified-wavy zone the heat flux and the mass velocity will be  $72.83 \text{ W}\cdot\text{m}^{-2}$  and  $197.59 \text{ kg}\cdot\text{m}^{-2}\cdot\text{s}^{-1}$ , respectively.

The stratified-wavy zone was present in tests D and E, at quality ranges 0.952-0.961 and 0.939-0.968, respectively. Whereas, the mist zone is present in test B with quality range 0.979-0.99 and in test C with quality range 0.982-0.99. In addition, tests D and E were obtained with incident solar radiation values of  $123.22$  and  $0 \text{ W}\cdot\text{m}^{-2}$ , respectively.

Since test A has an initial quality of 0.176, it is more similar to the model of flow pattern map considered as base for this study. However, in tests B and C it is visualized the largest dryout and mist zones, thus fulfilling the condition that the fluid must enter the compressor in vapor phase.

The present research work was conducted using an environmentally friendly refrigerant, such as R600a isobutane, which has an ODP of 0 and a GWP of 3; moreover, its use presents larger thermal conductivities compared to conventional refrigerants such as R22 and R134a.

## Acknowledgements

The authors thank to the Research Group in Renewable Energies and Mechanical Implementation of SMEs of the Universidad Politécnica Salesiana and to the Research Group in Energy and Thermodynamics of the Universidad Pontificia Bolivariana de Medellín.

## References

- [1] J. Calle-Sigüencia and O. Tinoco-Gómez, "Obtención de ACS con energía solar en el cantón Cuenca y análisis de la contaminación ambiental," *Ingenius*, no. 19, pp. 89–101, 2018. [Online]. Available: <https://doi.org/10.17163/ings.n19.2018.09>
- [2] W. Quitiaquez, J. Estupiñán Campos, C. Isaza Roldán, F. Toapanta-Ramos, and A. Lobato-Campoverde, "Análisis numérico de

- un sistema de calentamiento de agua utilizando un colector solar de placa plana,” *Ingenius*, no. 24, pp. 97–106, 2020. [Online]. Available: <https://doi.org/10.17163/ings.n24.2020.10>
- [3] N. Abas, A. R. Kalair, N. Khan, A. Haider, Z. Saleem, and M. S. Saleem, “Natural and synthetic refrigerants, global warming: A review,” *Renewable and Sustainable Energy Reviews*, vol. 90, pp. 557–569, 2018. [Online]. Available: <https://doi.org/10.1016/j.rser.2018.03.099>
- [4] K. Nawaz, B. Shen, A. Elatar, V. Baxter, and O. Abdelaziz, “R290 (propane) and R600a (isobutane) as natural refrigerants for residential heat pump water heaters,” *Applied Thermal Engineering*, vol. 127, pp. 870–883, 2017. [Online]. Available: <https://doi.org/10.1016/j.applthermaleng.2017.08.080>
- [5] C.-C. Yu and T.-P. Teng, “Retrofit assessment of refrigerator using hydrocarbon refrigerants,” *Applied Thermal Engineering*, vol. 66, no. 1, pp. 507–518, 2014. [Online]. Available: <https://doi.org/10.1016/j.applthermaleng.2014.02.050>
- [6] X. Zhuang, M. Gong, X. Zou, G. Chen, and J. Wu, “Experimental investigation on flow condensation heat transfer and pressure drop of R170 in a horizontal tube,” *International Journal of Refrigeration*, vol. 66, pp. 105–120, 2016. [Online]. Available: <https://doi.org/10.1016/j.ijrefrig.2016.02.010>
- [7] J. C. Pérez Angulo, C. Simancas, and N. Santos Santos, “Modelamiento y simulación de un sistema no convencional de levantamiento multifásico,” *Fuentes, el reventón energético*, vol. 14, no. 1, pp. 19–34, 2016. [Online]. Available: <https://doi.org/10.18273/revfue.v14n1-2016002>
- [8] L. Wojtan, T. Ursenbacher, and J. R. Thome, “Investigation of flow boiling in horizontal tubes: Part I—A new diabatic two-phase flow pattern map,” *International Journal of Heat and Mass Transfer*, vol. 48, no. 14, pp. 2955–2969, 2005. [Online]. Available: <https://doi.org/10.1016/j.ijheatmasstransfer.2004.12.012>
- [9] N. Kattan, J. R. Thome, and D. Favrat, “Flow boiling in horizontal tubes: Part 1—Development of a diabatic two-phase flow pattern map,” *Journal of Heat Transfer*, vol. 120, no. 1, pp. 140–147, Oct. 1998. [Online]. Available: <https://doi.org/10.1115/1.2830037>
- [10] H. Mashouf, M. Shafae, A. Sarmadian, and S. Mohseni, “Visual study of flow patterns during evaporation and condensation of R-600a inside horizontal smooth and helically dimpled tubes,” *Applied Thermal Engineering*, vol. 124, pp. 1392–1400, 2017. [Online]. Available: <https://doi.org/10.1016/j.applthermaleng.2017.06.125>
- [11] A. Vahabi, M. Shafae, A. Sarmadian, and H. Mashouf, “Discovering an empirically new relation and obtain the flow pattern map for dimpled tubes in two-phase flow for refrigerant R600-a,” *Modares Mechanical Engineering*, vol. 17, no. 7, 2017. [Online]. Available: <http://dorl.net/dor/20.1001.1.10275940.1396.17.7.25.7>
- [12] J. D. de Oliveira, J. B. Copetti, and J. C. Passos, “Experimental investigation on flow boiling pressure drop of R-290 and R-600a in a horizontal small tube,” *International Journal of Refrigeration*, vol. 84, pp. 165–180, 2017. [Online]. Available: <https://doi.org/10.1016/j.ijrefrig.2017.08.004>
- [13] Z.-Q. Yang, M. Gong, G. Chen, Z. Lin, H. Huang, and H. Feng, “A new diabatic two phase flow pattern transition model of R600a,” *International Journal of Refrigeration*, vol. 99, pp. 138–144, 2019. [Online]. Available: <https://doi.org/10.1016/j.ijrefrig.2018.12.025>
- [14] Y. Zhu, X. Wu, and R. Zhao, “R32 flow boiling in horizontal mini channels: Part I. Two-phase flow patterns,” *International Journal of Heat and Mass Transfer*, vol. 115, pp. 1223–1232, 2017. [Online]. Available: <https://doi.org/10.1016/j.ijheatmasstransfer.2017.07.101>
- [15] X. Zhuang, M. Gong, G. Chen, X. Zou, and J. Shen, “Two-phase flow pattern map for R170 in a horizontal smooth tube,” *International Journal of Heat and Mass Transfer*, vol. 102, pp. 1141–1149, 2016. [Online]. Available: <https://doi.org/10.1016/j.ijheatmasstransfer.2016.06.094>
- [16] J. Liu, J. Liu, and X. Xu, “Diabatic visualization study of R245fa two phase flow pattern characteristics in horizontal smooth and microfin tube,” *International Journal of Heat and Mass Transfer*, vol. 152, p. 119513, 2020. [Online]. Available: <https://doi.org/10.1016/j.ijheatmasstransfer.2020.119513>
- [17] J. Diehl de Oliveira, J. Biancon Copetti, and J. C. Passos, “An experimental investigation on flow boiling heat transfer of R-600a in a horizontal small tube,” *International Journal of Refrigeration*, vol. 72, pp. 97–110, 2016. [Online]. Available: <https://doi.org/10.1016/j.ijrefrig.2016.08.001>
- [18] M. Nasr, M. Akhavan-Behabadi, M. Momenifar, and P. Hanafizadeh, “Heat transfer characteristic of r-600a during flow boiling inside horizontal plain tube,” *International Communications in Heat and Mass Transfer*, vol. 66, pp. 93–99, 2015. [Online]. Available: <https://doi.org/10.1016/j.icheatmasstransfer.2015.05.024>

- [19] Z. Wang, P. Guo, H. Zhang, W. Yang, and S. Mei, "Comprehensive review on the development of sahp for domestic hot water," *Renewable and Sustainable Energy Reviews*, vol. 72, pp. 871–881, 2017. [Online]. Available: <https://doi.org/10.1016/j.rser.2017.01.127>
- [20] D. Zhang, Q. Wu, J. Li, and X. Kong, "Effects of refrigerant charge and structural parameters on the performance of a direct-expansion solar-assisted heat pump system," *Applied Thermal Engineering*, vol. 73, no. 1, pp. 522–528, 2014. [Online]. Available: <https://doi.org/10.1016/j.applthermaleng.2014.07.077>
- [21] G.-H. Shi, L. Aye, D. Li, and X.-J. Du, "Recent advances in direct expansion solar assisted heat pump systems: A review," *Renewable and Sustainable Energy Reviews*, vol. 109, pp. 349–366, 2019. [Online]. Available: <https://doi.org/10.1016/j.rser.2019.04.044>
- [22] X. Kong, P. Sun, Y. Li, K. Jiang, and S. Dong, "Experimental studies of a variable capacity direct-expansion solar-assisted heat pump water heater in autumn and winter conditions," *Solar Energy*, vol. 170, pp. 352–357, 2018. [Online]. Available: <https://doi.org/10.1016/j.solener.2018.05.081>
- [23] W. Quitiaquez, I. Simbaña, R. Caizatoa, C. Isaza, C. Nieto, P. Quitiaquez, and F. Toapanta, "Análisis del rendimiento termodinámico de una bomba de calor asistida por energía solar utilizando un condensador con recirculación," *Revista Técnica Energía*, vol. 16, no. 2, pp. 111–125, 2020. [Online]. Available: <https://doi.org/10.37116/revistaenergia.v16.n2.2020.358>
- [24] G. K. Singh, S. Pradhan, and V. Tanna, "Experimental studies of two phase flow characteristics and void fraction predictions in steady state horizontal two-phase nitrogen flow," *Cryogenics*, vol. 100, pp. 77–84, 2019. [Online]. Available: <https://doi.org/10.1016/j.cryogenics.2019.04.007>
- [25] C.-M. Yang and P. Hrnjak, "A new flow pattern map for flow boiling of R410a in horizontal micro-fin tubes considering the effect of the helix angle," *International Journal of Refrigeration*, vol. 109, pp. 154–160, 2020. [Online]. Available: <https://doi.org/10.1016/j.ijrefrig.2019.09.013>
- [26] M. Shafae, H. Mashouf, A. Sarmadian, and S. Mohseni, "Evaporation heat transfer and pressure drop characteristics of R-600a in horizontal smooth and helically dimpled tubes," *Applied Thermal Engineering*, vol. 107, pp. 28–36, 2016. [Online]. Available: <https://doi.org/10.1016/j.applthermaleng.2016.06.148>
- [27] Z.-Q. Yang, G.-F. Chen, X.-R. Zhuang, Q.-L. Song, Z. Deng, J. Shen, and M.-Q. Gong, "A new flow pattern map for flow boiling of R1234ze(E) in a horizontal tube," *International Journal of Multiphase Flow*, vol. 98, pp. 24–35, 2018. [Online]. Available: <https://doi.org/10.1016/j.ijmultiphaseflow.2017.08.015>
- [28] L. Wojtan, T. Ursenbacher, and J. R. Thome, "Investigation of flow boiling in horizontal tubes: Part II—Development of a new heat transfer model for stratified-wavy, dryout and mist flow regimes," *International Journal of Heat and Mass Transfer*, vol. 48, no. 14, pp. 2970–2985, 2005. [Online]. Available: <https://doi.org/10.1016/j.ijheatmasstransfer.2004.12.013>
- [29] J. D. de Oliveira, J. C. Passos, J. B. Copetti, and C. van der Geld, "Flow boiling heat transfer of propane in 1.0 mm tube," *Experimental Thermal and Fluid Science*, vol. 96, pp. 243–256, 2018. [Online]. Available: <https://doi.org/10.1016/j.exptthermflusci.2018.03.010>

## GUIDELINES FOR PUBLICATION IN INGENIUS JOURNAL

### 1. General Information

INGENIUS is a scientific publication of the *Universidad Politécnica Salesiana* of Ecuador, published since January 2007, with a fixed biannual periodicity, specialized in Mechanical Engineering, Electrical Engineering, Electronics, Computer Science and its integration in what is now known as Mechatronics; these lines of action strengthen areas such as automation, control, robotics, among others..

It is a scientific journal, which uses the peer-review system, under double-blind review methodology, according to the publication standards of the Institute of Electrical and Electronics Engineers (IEEE). Compliance with this system allows authors to guarantee an objective, impartial and transparent review process, which facilitates the publication of their inclusion in reference databases, repositories and international indexing.

INGENIUS is indexed in the directory and selective catalog of the Regional Online Information System for Scientific Journals of Latin America, the Caribbean, Spain and Portugal (Latindex), in the Directory of Journals of Open Access DOAJ, In the Information Matrix for the Analysis of Journals, MIAR, In the Ibero-American Network of Innovation and Scientific Knowledge, REDIB and in repositories, libraries and specialized catalogs of Latin America.

The journal is published in a double version: printed (ISSN: 1390-650X) and digital (e-ISSN: 1390-860X), in Spanish, each work being identified with a DOI (Digital Object Identifier System). The articles sent to INGENIUS magazine must comply with the following criteria:

### 2. Scope and policy

#### 2.1. Theme

Original contributions in Mechanical Engineering, Electrical and Electronic Engineering, Computer Science and its integration in what is now known as Mechatronics, as well as related areas: Automation, Control, Domotics, Robotics in their different fields of action and all those related disciplines with the same central theme.

All the work carried out by national or foreign researchers may be published once they meet the required scientific quality criteria.

#### 2.2. Contributions

INGENIUS Journal preferably publishes articles related to empirical research, and also reports of technological development, proposals for models and innovations, products for the elaboration of graduate and postgraduate thesis that contribute to the field of science and technology, as well as select revisions of literature. (state-of-the-art).

- **Research:** 5,000 to 6,500 words of text, including title, abstracts, descriptors, charts and references.
- **Reports:** 5,000 to 6,500 words of text, including title, abstracts, charts and references.
- **Reviews:** 6,000 to 7,000 words of text, including charts and references. Current, selective and justified references, would be specially valued from among 40 works

The INGENIUS Journal publishes original and unpublished works written in Spanish and English, they may not have been published

through any printed or electronic media, nor be in the process of arbitration or publication.

Every article will be subjected to a rigorous arbitration process; the evaluation of the article will be made according to criteria of originality, relevance, relevance, contributions, scientific rigor and compliance with established editorial guidelines.

Being an arbitrated publication, the Editorial Board approves its publication based on the concept of specialized pairs. The reception of a document does not imply commitment of publication.

It is essential to present a letter of presentation and grant of rights which can be downloaded from: [urlhttps://goo.gl/ZNkMRD](https://goo.gl/ZNkMRD).

Contributions must be exclusively sent and through the OJS (Open Journal System) [urlhttps://goo.gl/JF7dWT](https://goo.gl/JF7dWT). In which all authors must previously register as a user. For any consultation of the procedure you should contact:

[revistaingenius@ups.edu.ec](mailto:revistaingenius@ups.edu.ec),  
[jcalles@ups.edu.ec](mailto:jcalles@ups.edu.ec) ó  
[mquinde@ups.edu.ec](mailto:mquinde@ups.edu.ec).

### 3. Presentation and structure of the manuscripts

For those works that are empirical investigations, the manuscripts will follow the IMRDC structure (Introduction, Materials and Methods, Results and Discussion and Conclusions), being optional the Notes and Supports. Those papers that, on the contrary, deal with reports, studies, proposals and reviews may be more flexible in their epigraphs, particularly in material and methods, analysis, results, discussion and conclusions. In all typologies of works, references are mandatory.

Articles may be written on Microsoft Word (.doc or .docx) or L<sup>A</sup>T<sub>E</sub>X(.tex). The template to

be used can be downloaded from the journal's website, a, [urlhttps://goo.gl/gtCg6m](https://goo.gl/gtCg6m), while for L<sup>A</sup>T<sub>E</sub>X in [urlhttps://goo.gl/hrHzzQ](https://goo.gl/hrHzzQ), it is necessary that the file be anonymised in Properties of File, so that the author(s) ID is not displayed.

Figures, Graphs and/or Illustrations, as well as Charts shall be numbered sequentially including an explanatory description for each. The equations included in the article must also be numbered; the figures, charts and equations must be cited in the text.

Use space after point, commas and question marks.

Use “enter” at the end of each paragraph and title heading. Do not use .<sup>enter</sup>.<sup>anywhere</sup> else, let the word processor program automatically break the lines.

Do not center headings or subheadings as they should be aligned to the left.

Charts must be created in the same program used for the document body, but must be stored in a separate file. Use tabs, not spaces, to create columns. Remember that the final size of printed pages will be 21 x 28 cm, so the tables must be designed to fit the final print space.

#### 3.1. Structure of the manuscripts

##### 3.1.1. Presentation and cover letter

1. **Título (español) / Title (inglés):** Concise but informative, in Spanish on the front line and in English on the second, when the article is written in Spanish and vice versa if it is written in English.
2. **Authors and affiliations:** Full name and surname of each author, organized by order of priority and their institutional affiliation with reference to the end of the first sheet, where it must include: Dependency to which belongs within the

institution, Institution to which he/she belongs, country, ORCID. A maximum of 5 authors will be accepted, although there may be exceptions justified by the complexity and extent of the topic.

3. **Abstract (Spanish) / Abstract (English):** It will have a maximum extension of 230 words, first in Spanish and then in English. : 1) Justification of the topic; 2) Objectives; 3) Methodology and sample; 4) Main results; 5) Main conclusions.
4. **Keywords (Spanish) / Keywords (English):** 6 descriptors must be presented for each language version directly related to the subject of the work. The use of the key words set out in UNESCO's Thesaurus will be positively valued.
5. **Presentation (Cover Letter):** A statement that the manuscript is an original contribution, not submission or evaluation process in another journal, with the confirmation of the signatory authors, acceptance (if applicable) of formal changes in the manuscript according to the guidelines and partial assignment of rights to the publisher, according to the format established in: <<https://goo.gl/ZNkMRD>>

### 3.1.2. Manuscript

1. **Título (español) / Title (inglés):** Concise but informative, in Spanish on the front line and in English on the second, when the article is written in Spanish and vice versa if it is written in English.
2. **Authors and affiliations:** Full name and surname of each author, organized by order of priority and their institutional affiliation with reference to the end of the first sheet, where it must include: Dependency to which belongs within the institution, Institution to which he/she belongs, country, ORCID. A maximum of 5 authors will be accepted, although

there may be exceptions justified by the complexity and extent of the topic.

3. **Abstract (Spanish) / Abstract (English):** It will have a maximum extension of 230 words, first in Spanish and then in English. : 1) Justification of the topic; 2) Objectives; 3) Methodology and sample; 4) Main results; 5) Main conclusions.
4. **Keywords (Spanish) / Keywords (English):** 6 descriptors must be presented for each language version directly related to the subject of the work. The use of the key words set out in UNESCO's Thesaurus will be positively valued.
5. **Introduction:** It should include the problem statement, context of the problem, justification, rationale and purpose of the study, using bibliographical citations, as well as the most significant and current literature on the topic at national and international level.
6. **Material and methods:** It must be written so that the reader can easily understand the development of the research. If applicable, it will describe the methodology, the sample and the form of sampling, as well as the type of statistical analysis used. If it is an original methodology, it is necessary to explain the reasons that led to its use and to describe its possible limitations.
7. **Analysis and results:** It will try to highlight the most important observations, describing, without making value judgments, the material and methods used. They will appear in a logical sequence in the text and the essential charts and figures avoiding the duplication of data.
8. **Discussion and Conclusions:** It will summarize the most important findings, relating the observations themselves to relevant studies, indicating contributions

and limitations, without adding data already mentioned in other sections. It should also include deductions and lines for future research.

9. **Supports and acknowledgments (optional):** The Council Science Editors recommends the author (s) to specify the source of funding for the research. Priority will be given to projects supported by national and international competitive projects.

10. **The notes (optional):** will go, only if necessary, at the end of the article (before the references). They must be manually annotated, since the system of footnotes or the end of Word is not recognized by the layout systems. The numbers of notes are placed in superscript, both in the text and in the final note. The numbers of notes are placed in superscript, both in the text and in the final note. No notes are allowed that collect simple bibliographic citations (without comments), as these should go in the references.

11. **References:** Bibliographical citations should be reviewed in the form of references to the text. Under no circumstances should references mentioned in the text not be included. Their number should be sufficient to contextualize the theoretical framework with current and important criteria. They will be presented sequentially in order of appearance, as appropriate following the format of the IEEE.

### 3.2. Guidelines for Bibliographical references

#### *Journal articles:*

- [1] J. Riess, J. J. Abbas, "Adaptive control of cyclic movements as muscles fatigue using functional neuromuscular stimulation". IEEE Trans. Neural Syst. Rehabil. Eng

vol. 9, pp.326–330, 2001. [Online]. Available: <https://doi.org/10.1109/7333.948462>

#### *Books:*

- [1] G. O. Young, "Synthetic structure of industrial plastics" in *Plastics*, 2nd ed., vol. 3, J. Peters, Ed. New York: McGraw–Hill, 1964, pp. 15–64.

#### *Technical reports:*

- [1] M. A. Brusberg and E. N. Clark, "Installation, operation, and data evaluation of an oblique–incidence ionosphere sounder system," in "Radio Propagation Characteristics of the Washington–Honolulu Path," Stanford Res. Inst., Stanford, CA, Contract NOBSR–87615, Final Rep., Feb. 1995, vol. 1

#### *Articles presented in conferences (unpublished):*

- [1] Vázquez, Rolando, Presentación curso "Realidad Virtual". National Instruments. Colombia, 2009.

#### *Articles of memories of Conferences (Published):*

- [1] L. I. Ruiz, A. García, J. García, G. Taboada. "Criterios para la optimización de sistemas eléctricos en refinerías de la industria petrolera: influencia y análisis en el equipo eléctrico," IEEE CONCAPAN XXVIII, Guatemala 2008.

#### *Thesis:*

- [1] L.M. Moreno, "Computación paralela y entornos heterogéneos," Tesis doctoral, Dep. Estadística, Investigación Operativa y Computación, Universidad de La Laguna, La Laguna, 2005.

#### *Guidelines:*

- [1] IEEE Guide for Application of Power Apparatus Bushings, IEEE Standard C57.19.100–1995, Aug. 1995.

#### *Patents:*

- [1] J. P. Wilkinson, "Nonlinear resonant circuit devices," U.S. Patent 3 624 125, July 16, 1990.

*Manuals:*

- [1] Motorola Semiconductor Data Manual, Motorola Semiconductor Products Inc., Phoenix, AZ, 1989.

*Internet resources:*

- [1] E. H. Miller, "A note on reflector arrays" [Online]. Available. <https://goo.gl/4cJkCF>

**3.3. Epigraphs, Figures and Charts**

The epigraphs of the body of the article will be numbered in Arabic. They should go without a full box of capital letters, neither underlined nor bold. The numbering must be a maximum of three levels: 1. / 1.1. / 1.1.1. At the end of each numbered epigraph will be given an enter to continue with the corresponding paragraph.

The charts must be included in the text according to order of appearance, numbered in Arabic and subtitled with the description of the content, the subtitle should go at the top of the table justified to the left.

Figures can be linear drawings, maps or black and white halftone or color photographs in 300 dpi resolution. Do not combine photographs and line drawings in the same figure.

Design the figures so that they fit eventually to the final size of the journal 21 x 28 cm. Make sure inscriptions or details, as well as lines, are of appropriate size and thickness so that they are not illegible when they are reduced to their final size (numbers, letters and symbols must be reduced to at least 2.5 mm in height After the illustrations have been reduced to fit the printed page). Ideally, the linear illustrations should be prepared at about a quarter of their final publication size.

Different elements in the same figure should be spelled a, b, c, etc.

Photographs should be recorded with high contrast and high resolution. Remember that

photographs frequently lose contrast in the printing process. Line drawings and maps should be prepared in black.

The text of the figures and maps must be written in easily legible letters.

If the figures have been previously used, it is the responsibility of the author to obtain the corresponding permission to avoid subsequent problems related to copyright.

Each figure must be submitted in a separate file, either as bitmap (.jpg, .bmp, .gif, or .png) or as vector graphics (.ps, .eps, .pdf).

**4. Submission process**

The manuscript must be sent through the OJS system of the journal, <<https://goo.gl/JF7dWT>>, the manuscript should be uploaded as an original file in .pdf without author data and anonymized according to the above; In complementary files the complete manuscript must be loaded in .doc or .docx (Word file), that is to say with the data of the author (s) and its institutional ascription; Also the numbered figures should be uploaded in independent files according to the corresponding in the manuscript (as bitmap .jpg, .bmp, .gif, or .png or as vector graphics .ps, .eps, .pdf). It is also obligatory to upload the cover letter and grant of rights as an additional file.

All authors must enter the required information on the OJS platform and only one of the authors will be responsible for correspondence.

Once the contribution has been sent the system will automatically send the author for correspondence a confirmation email of receipt of the contribution.

**5. Editorial process**

Once the manuscript has been received in OJS, a first check by the editorial team of the following points:

- The topic is in accordance with the criteria of the journal.
- Must have the IMRDC structure.
- Must be in the INGENIUS format.
- Must use the IEEE citation format.
- All references should be cited in the text of the manuscript as well as charts, figures and equations.
- The manuscript is original; for this, software is used to determine plagiarism.

The assessment described above can take up to 4 weeks.

If any of the above is not complete or there is inconsistency, an email will be sent to the author to make the requested corrections.

The author will make the corrections and re-send the contribution through an email in response to the notification and will also upload the corrected manuscript into OJS supplementary files.

The editorial team will verify that the requested corrections have been incorporated, if it complies, the manuscript will start the second part of the process that may be followed by the author through OJS, otherwise the author will be notified and the manuscript will be archived.

The second phase of the process consists of the evaluation under the methodology of double-blind review, which includes national and foreign experts considering the following steps:

- The editor assigns two or more reviewers for the article.

- After reviewing the article, the reviewers will submit the evaluation report with one of the following results.
  - Publishable
  - Publishable with suggested changes
  - Publishable with mandatory changes
  - Non publishable
- The editor once received the evaluation by the reviewers will analyze the results and determine if the article is accepted or denied.
- If the article is accepted, the author will be notified to make corrections if required and the corresponding editorial process will be continued.
- If the article is denied, the author will be notified and the manuscript will be archived.
- In the two previous cases the result of the evaluation of the reviewers and their respective recommendations will be sent.

The second phase of the process lasts at least 4 weeks, after which they will be notified to the author giving instructions to continue with the process.

## 6. Publication

The INGENIUS Journal publishes two issues per year, on January 1st and July 1st, so it is important to consider the dates for sending the articles and their corresponding publication. Articles received until October will be considered for the January publication and those received until April for the July publication.

**UNIVERSIDAD POLITÉCNICA SALESIANA DEL ECUADOR**

Juan Cárdenas Tapia, sdb,  
Rector

©Universidad Politécnica Salesiana  
Turuhuayco 3-69 y Calle Vieja  
Postal code 2074  
Cuenca, Ecuador  
Teléfono: (+593 7) 205 00 00  
Fax: (+593 7) 408 89 58  
Email: srector@ups.edu.ec

**Exchange**

Exchange with other periodicals is accepted.

Address:

Secretaría Técnica de Comunicación  
Universidad Politécnica Salesiana  
Turuhuayco 3-69 y Calle Vieja  
Postal code 2074  
Cuenca, Ecuador  
Phone: (+593 7) 205 00 00 Ext. 1182  
Fax: (+593 7) 408 89 58  
Email: rpublicas@ups.edu.ec  
www.ups.edu.ec  
Cuenca – Ecuador

INGENIUS, Journal Science of Technology,  
Semester publication, N.º 26, july/december 2021  
John Calle Sigüencia, Editor in chief  
revistaingenius@ups.edu.ec

**Printed**

Centro Gráfico Salesiano: Antonio Vega Muñoz 10-68 y General Torres.  
Phone: (+593 7) 283 17 45  
Cuenca – Ecuador  
Email: centrograficosalesiano@lms.com.ec

OTHER PERIODIC PUBLICATIONS OF THE UNIVERSITY  
UNIVERSITAS, Journal of Social and Human Sciences.

LA GRANJA, Journal of Life Sciences.

ALTERIDAD, Journal of Education.

RETOS Journal of Administration Sciences and Economics.

UTOPIA, University Youth Ministry Magazine.

SOPHIA, Collection of Philosophy of Education.



ABYA  
YALA | UNIVERSIDAD  
POLITÉCNICA  
SALESIANA

